Universidade de Aveiro
2014

Departamento de Engenharia de Materiais e Cerâmica

Ermelinda da Conceição Portela Salgueiredo

Revestimentos multicamada de diamante CVD micro/nanocristalino para biotribologia

Multilayered micro/nanocrystalline CVD diamond coatings for biotribology

Universidade de Aveiro
2014

Departamento de Engenharia de Materiais e Cerâmica

Ermelinda da Conceição Portela Salgueiredo

Revestimentos multicamada de diamante CVD micro/nanocristalino para biotribologia

Multilayered micro/nanocrystalline CVD diamond coatings for biotribology

Tese apresentada à Universidade de Aveiro para cumprimento dos requisitos necessários à obtenção do grau de Doutor em Ciência e Engenharia de Materiais, realizada sob a orientação científica do Doutor Rui Ramos Ferreira e Silva, Professor Associado do Departamento de Engenharia de Materiais e Cerâmica da Universidade de Aveiro e sob a co-orientação científica do Doutor Filipe José Alves de Oliveira, Investigador Auxiliar do Laboratório Associado CICECO da Universidade de Aveiro

Apoio financeiro da FCT (bolsa SFRH/BD/41757/2007, projetos PTDC/EME-TME/100689/2008 e PTDC/EME-PME/112910/2009).

Aos meus pais. À minha prima Açucena. À minha filha Maria.

Sísifo

Recomeça…
Se puderes,
Sem angústia e sem pressa.
E os passos que deres,
Nesse caminho duro
Do futuro,
Dá-os em liberdade.
Enquanto não alcances
Não descanses.
De nenhum fruto queiras só metade.

E, nunca saciado,
Vai colhendo
Ilusões sucessivas no pomar
E vendo
Acordado,
O logro da aventura.
És homem, não te esqueças!
Só é tua a loucura
Onde, com lucidez, te reconheças.

Miguel Torga, *Diário XIII*

o júri

presidente

Prof. Doutor Carlos Manuel Martins da Costa
professor catedrático da Universidade de Aveiro

Prof. Doutor Rui Ramos Ferreira e Silva
professor associado da Universidade de Aveiro

Prof. Doutor Albano Augusto Cavaleiro Rodrigues de Carvalho
professor catedrático da Faculdade de Ciências e Tecnologia da Universidade de Coimbra

Prof. Doutora Sandra Maria Fernandes Carvalho
professora auxiliar da Escola de Ciências da Universidade do Minho

Prof. Doutor João Miguel Maia Carrapichano
professor adjunto do Instituto Superior de Engenharia de Coimbra

Doutor Victor Fernando Santos Neto
professor auxiliar convidado da Universidade de Aveiro

agradecimentos

Agradeço ao Prof. Doutor Rui Silva pela orientação científica, apoio, compreensão e incentivo ao longo desta jornada. Ao Doutor Filipe Oliveira pelo rigor técnico e científico e colaboração. À Prof. Doutora Florinda Costa pelo apoio. Ao Dr. António José Fernandes pela colaboração (e fantástico sentido de humor). Aos meus colegas de trabalho pelo auxílio e amizade.

À Flávia Almeida por tudo. Por tanto. Por me dar a força, através do apoio técnico, mas sobretudo da amizade, de acreditar que nada é impossível. E o melhor ainda está para vir!

Ao Miguel Neto, Diogo Mata, Tiago Holz, Merche Vila, Isa Branco, Simone Rodrigues, Ana Horovistiz e Filipa Neves agradeço por, nos momentos mais difíceis me presentearem com lições de amizade e generosidade sem fim. Pela partilha do dia-a-dia, pelas gargalhadas e lágrimas ao longo destes anos, o meu mais sentido agradecimento.

Ao Prof. Doutor Cristiano Abreu da Universidade do Minho agradeço pelo enorme contibuto nos ensaios tribológicos, pelas discussões e sugestões que enriqueceram este trabalho, mas sobretudo pela disponibilidade e amizade. A ele e ao Prof. Doutor José Gomes agradeço também a cordial recepção que fez com que as deslocações a Guimarães fossem sempre realizadas com agrado. Ao Prof. Doutor João Miguel Carrapichano agradeço o trabalho incansável nos ensaios tribológicos em Coimbra, o incentivo e optimismo, sobretudo nos momentos mais difíceis.

Agradeço aos funcionários do Departamento de Engenharia de Materiais e Cerâmica. Aos Srs. Octávio Contente e Jacinto Alves agradeço a eficiência e a rapidez com que sempre tentaram responder aos meus inúmeros pedidos! Um agradecimento especial vai para a D. Luísa Costa, pelo exemplo de coragem, espírito positivo e amizade, em todos os momentos. Aos Mestres Bruno Almeida e Marta Ferro agradeço o rigor, profissionalismo, mas acima de tudo a constante disponibilidade e paciência. À Marta Ferro agradeço reconhecidamente a partilha, dedicação e o carinho, que alegraram as longas horas de trabalho.

À equipa da UATEC por um ano de profundo enriquecimento profissional, mas sobretudo pessoal. A alegria e espírito de equipa partilhados ficarão para sempre comigo. A todas as pessoas que, de forma directa ou indirecta, contribuíram para este trabalho, muitas vezes através de um simples sorriso ou palavra de incentivo (na impossibilidade de nomear todas) agradeço aqui reconhecidamente.

À Marta, Rita, Dina e Cristina. Por serem o meu porto seguro e certeza que nunca estou só. Obrigada por serem as minhas companheiras em todas as "viagens" ao longo destes anos. Estamos juntas. Sempre.

A todos os meus amigos que, por estarem na minha vida, fazem de mim uma pessoa feliz. Aos meus "filhos e sobrinhos do coração" por enriquecerem a minha vida com a sua inesgotável alegria, incontáveis sorrisos e abraços.

Aos meus pais por todos os sacrifícios e apoio em tantas horas difíceis. Por um amor que não tem medida. À minha prima Açucena e família pelo amor incondicional e abrigo quando não tive força para caminhar sozinha.

À minha filha Maria, luz e farol em todos os momentos. Por ser a minha companheira de equipa, o meu amor maior.

palavras-chave

Revestimentos de diamante, multicamadas, deposição química em fase vapor assistida por filamento quente, biotribologia

resumo

No presente trabalho desenvolveram-se revestimentos de diamante micro/nanocristalino (MCD/NCD) em multicamadas obtidos por deposição química em fase vapor (CVD) assistida por filamento quente. Pretendeu-se minimizar a rugosidade através de um camada superficial de NCD, maximizar a adesão com um filme inicial de MCD sobre substratos cerâmicos de nitreto de silício (Si_3N_4) e incrementar a resistência mecânica pela presença de interfaces MCD/NCD nestes revestimentos compósitos. Este conjunto de características garante elevada resistência ao desgaste e baixo coeficiente de atrito, o que somado à biocompatibilidade do diamante, configuram este material como ideal para aplicações em biotribologia.

Os parâmetros de deposição do MCD foram otimizados usando o método de Taguchi e utilizaram-se duas variedades de NCD: NCD-1 crescido numa atmosfera com sobressaturação de metano e NCD-2 crescido na presença de árgon. A melhor combinação de pré-tratamentos nos substratos de Si_3N_4 consiste num polimento com suspensão de diamante (15 µm), seguido de ataque por plasma de CF_4 durante 10 minutos e riscagem em suspensão de pó de diamante em etanol durante 1 hora.

As interfaces das multicamadas de diamante foram caracterizadas em detalhe por HRTEM, STEM-EDX e EELS. Os resultados mostram que na transição de diamante MCD para NCD ocorre a formação de um filme fino de carbono amorfo, inexistente na transição de NCD para MCD, como resultado da maior percentagem de hidrogénio atómico na mistura de gases e do incremento da temperatura do substrato para a deposição de MCD. Uma característica comum nas interfaces nos dois tipos de NCD é a presença de partículas esféricas de carboneto de tungsténio, devido à contaminação pelos filamentos, estando também presentes na interface entre a camada de MCD e o substrato de nitreto de silício.

A adesão e resistência mecânica dos filmes de diamante foram avaliadas por ensaios de indentação, erosão com partículas de carboneto de silício e ensaios tribológicos em movimento recíproco, com pares próprios. Por indentação verificou-se que as multicamadas suportam uma carga de 800N, sem delaminação, valor superior ao atingido pelas mono- e bicamadas. Nos ensaios de erosão, as multicamadas apresentaram igualmente melhor comportamento, devido à ação das interfaces MCD/NCD como defletoras das fissuras, sendo estes resultados confirmados por uma análise de distribuição de tensões de von Mises. As multicamadas apresentam também as cargas críticas de delaminação máximas nos ensaios tribológicos a seco (200 N para multicamadas com NCD-2). Os valores do coeficiente de atrito variam na gama µ=0.02-0.09, para coeficientes de desgaste ~10^{-7} $mm^3 N^{-1} m^{-1}$ para a esfera e placa, indicando um regime de desgaste moderado. Sob lubrificação de líquidos fisiológicos (HBSS e FBS) descem para ~10^{-9}-10^{-8} $mm^3 N^{-1} m^{-1}$, valores determinados pela rugosidade de partida e pelo regime de pressão de contato efetiva.

keywords

Diamond coatings, multilayers, hot filament chemical vapour deposition, biotribology

abstract

In the present work multilayered micro/nanocrystalline (MCD/NCD) diamond coatings were developed by Hot Filament Chemical Vapour Deposition (HFCVD). The aim was to minimize the surface roughness with a top NCD layer, to maximize adhesion onto the Si_3N_4 ceramic substrates with a starting MCD coating and to improve the mechanical resistance by the presence of MCD/NCD interfaces in these composite coatings. This set of features assures high wear resistance and low friction coefficients which, combined to diamond biocompatibility, set this material as ideal for biotribological applications.

The deposition parameters of MCD were optimized using the Taguchi method, and two varieties of NCD were used: NCD-1, grown in a methane rich gas phase, and NCD-2 where a third gas, Argon, was added to the gas mixture. The best combination of surface pre-treatments in the Si_3N_4 substrates is obtained by polishing the substrates with a 15 µm diamond slurry, further dry etching with CF_4 plasma for 10 minutes and final ultrasonic seeding in a diamond powder suspension in ethanol for 1 hour.

The interfaces of the multilayered CVD diamond films were characterized with high detail using HRTEM, STEM-EDX and EELS. The results show that at the transition from MCD to NCD a thin precursor graphitic film is formed. On the contrary, the transition of the NCD to MCD grade is free of carbon structures other than diamond, as a result of the richer atomic hydrogen content and of the higher substrate temperature for MCD deposition. At those transitions, WC nanoparticles were found due to contamination from the filament, being also present at the first interface of the MCD layer with the silicon nitride substrate.

In order to study the adhesion and mechanical resistance of the diamond coatings, indentation and particle jet blasting tests were conducted, as well as tribological experiments with homologous pairs. Indentation tests proved the superior behaviour of the multilayered coatings that attained a load of 800 N without delamination, when compared to the mono and bilayered ones. The multilayered diamond coatings also reveal the best solid particle erosion resistance, due to the MCD/NCD interfaces that act as crack deflectors. These results were confirmed by an analytical model on the stress field distribution based on the von Mises criterion. Regarding the tribological testing under dry sliding, multilayered coatings also exhibit the highest critical load values (200N for Multilayers with NCD-2). Low friction coefficient values in the range µ=0.02-0.09 and wear coefficient values in the order of $\sim 10^{-7}$ $mm^3 N^{-1} m^{-1}$ were obtained for the ball and flat specimens indicating a mild wear regime. Under lubrication with physiological fluids (HBSS e FBS), lower wear coefficient values $\sim 10^{-9}$-10^{-8} $mm^3 N^{-1} m^{-1}$) were achieved, governed by the initial surface roughness and the effective contact pressure.

Index

Nomenclature

A - Hertzian contact radius
AC – alternating current
AFM – atomic force microscopy
AJCVD - arc-jet plasma chemical vapour deposition
BEN - bias enhanced nucleation
BOF - ball-on-flat
c-BN - cubic boron nitride
CoC - ceramic-on-ceramic
CoP – ceramic-on-polyethylene
CTEM - conventional transmission electron microscopy
CVD – chemical vapor deposition
CW - continuous wave
d – density
D – disordered graphite
DC – direct current
DCGD - direct current glow discharge
DLC - diamond-like carbon
$\dot{E}$ – erosion rate
E - Young's modulus
E_1 - Young's modulus of the half-space material
E_2 - Young's modulus of the impact particle material
ECR - electron cyclotron resonance
EDX - energy-dispersive X-ray spectroscopy
EELS - electron energy loss spectroscopy
E_k – impact energy
F – friction force
F_a – adhesion force
FBS - fetal bovine serum
F_d – deformation force
FE-SEM - field emission scanning electron microscopy
FIB – focused ion beam
FL - flat lapped
F_m - maximum load
FOM - figure-of-merit
G - average grain size
G band - crystalline graphite
H - hardness of the target material
H° - atomic hydrogen
HAADF - high angle annular dark field
HBSS - Hank's balanced salt solution
H_e - hardness of erodent material
HFCVD – hot filament chemical vapor deposition

H_m - target material hardness
HPHT - high pressure and high temperature
HRTEM - high resolution transmission electron microscopy
ICP - inductively coupled plasma
I_D - integrated intensity of the 1332cm^{-1} diamond peak
IFFT - inverse fast Fourier transform
IT - induction time
I_T - total integrated intensity of the Raman spectrum
$J_2^{1/2}$ - von Mises parameter
k - wear coefficient
K_{Ic} - fracture toughness
LFA - low friction arthroplasty
LIBAD - low incident beam angle X-ray diffraction
LP-CVD - low pressure chemical vapour deposition
LPLT - low temperature and low pressure
MCD – microcrystalline diamond
MoM – metal-on-metal
MoP - metal-on-polyethylene
MPCVD - microwave plasma chemical vapour deposition
NCD - nanocrystalline diamond
NIRIM - National Institute of Research in Inorganic Materials
P – total gas pressure
P_0 - maximum contact pressure
PE - Plasma etching
P_m - mean contact pressure
PP - pre-polishing
PTFE - polytetrafluoroethylene
PVD - physical vapor deposition
PW - pulsed microwave
Q - diamond structural quality
r - ball radius
R - impact particle radius
Ra – average surface roughness
RF – radio frequency
RI - refractive index
RIE - parallel plate reactive ion etching
RMS=R_q – root mean square roughness
SAED - selected-area electron diffraction
sccm - standard cubic centimeters per minute
SEM – scanning electron microscopy
STEM - scanning transmission electron microscopy
THA - total hip arthroplasty
THR – total hip replacement
TPA - trans-polyacetylene
T_s - substrate temperature

UHMWPE - ultra high molecular weight polyethylene
UNCD - ultra-nanocrystalline diamond
UV – ultra violet
V - particle velocity
V_L - volumetric erosion loss per impact
W - normal applied load
W_C - critical load
X - sliding distance
XRD – X-ray diffraction
Z - distance to the surface (depth)
α – thermal expansion coefficient
μ - friction coefficient
$\Delta\upsilon$ - difference between the measured and the natural stress-free diamond peak shifts
ν_1 - Poisson coefficient of the half-space material
ν_2 - Poisson coefficient of the impact particle material
σ_r - residual stress
σ_{xx}; σ_{yy}; σ_{zz} – principal stresses in the half-space
τ_{xy}; τ_{yz}; τ_{zx} – shear stresses
ω – normal load in contact

Motivation, objectives and thesis organization

Nowadays, more and more human natural functions are being replaced by artificial devices, to repair or enhance disabilities due to several causes, namely aging or trauma. Thus, it is mandatory to develop materials that fulfil the highest standards regarding design, structural and mechanical requirements, and biocompatibility. One of the most commonly known applications of biomaterials is the hip joint prosthesis for total hip replacement (THR). In this specific case, wear of the tribosystem composed by the femoral head and the acetabular cup is the main issue addressed.

This work aimed at the development and application of excel tribosystems for such biotribological application based on multilayered micro/nanocrystalline (MCD/NCD) diamond coated silicon nitride (Si_3N_4) ceramic surfaces with superior friction and wear properties.

Monolayered microcrystalline diamond structures were already developed and characterized by our group, which demonstrated an excellent adhesion to Si_3N_4, due to their good thermal and chemical compatibility but at the cost of high surface roughness, limiting its use in some tribological applications. This was the motivation to shift efforts in the last years towards nanocrystalline diamond coatings with reduced surface roughness, providing lower friction coefficients than MCD, although presenting a lower adhesion to the ceramic substrates.

The deposition of MCD/NCD coatings in a multilayer configuration is thus foreseen, to combine the superior adhesion of MCD and the surface properties of NCD. Moreover, alternating MCD and NCD thin layers will prevent MCD grains to grow excessively, allowing a smooth surface by depositing a top NCD layer. Another envisaged advantage is the enhanced coating fracture toughness achieved by careful interlayer design. These ultra-hard biocompatible MCD/NCD multilayered films anticipate outstanding wear and bio-resistance, which may result in significant improvements when used in articular prosthetic devices.

This thesis is based on a compilation of five scientific papers published in relevant journals of this research area, and a final one to be submitted. Before their presentation, a bibliographic survey is addressed in Chapter I, reporting the most relevant issues on biotribology and briefly reviewing the fundamental concepts of tribology and diamond coatings biocompatibility for biotribological applications. Diamond coatings obtained by chemical vapour deposition (CVD), namely by hot filament technique (HFCVD), and the importance of the nucleation and growth in the development of the microcrystalline and nanocrystalline varieties for the design of multilayered composite coatings, are also included subjects. The basic concepts on adhesion evaluation of the diamond coatings by static indentation and erosive wear testing are also reviewed in this chapter.

Chapter II starts with a description of the use of silicon nitride based ceramics as substrates for diamond deposition, including the substrate preparation prior to diamond deposition, highlighting its importance to the adhesion of the films. The work on the optimization of the growth parameters of the home-built HFCVD reactor, the development and physical characterization of mono-, bi- and multilayered coatings were reported on three SCI papers, presented as three main sections of Chapter II.

Unlubricated and lubricated with physiological fluids (HBSS and FBS) reciprocating sliding experiments with homologous pairs (pin-on-plate) of diamond monolayers, bilayers and multilayers were then conducted. Their wear behaviour under erosion testing was also evaluated. The results are presented in three papers in Chapter III.

In Chapter IV the main conclusions of the work are summarized and the perspectives on future work are proposed.

Chapter I

Bibliographic overview

The literature survey presented in Chapter I starts with an overview on biotribology, namely on the fundamental aspects of tribology and on the particular case of the hip joint biotribosystem. Then, a concise revision on diamond structure and applications, presents the state of the art in the production of chemical vapour deposition (CVD) diamond films by various techniques, focusing on the hot filament (HFCVD) method used in this work. Nucleation and growth steps and the microcrystalline and nanocrystalline diamond coatings structure for the design of multilayered composite coatings are also addressed. The basic concepts of static indentation and erosive wear testing as adhesion evaluation methods are finally presented.

I.1. Biotribology - Wear, friction and lubrication in synovial joints

Biotribology is a multidisciplinary research field that gathers biomechanics, materials science and tribology. According to Jin *et al*. the term was coined in 1973 by Dowson and Wright to cover "all aspects of tribology related to biological systems". The most common example of a biotribological system is the natural synovial joint. There are numerous studies dedicated to the design, manufacturing and testing of the joint replacements, trying to mimic the natural bearing system [1].

I.1.1. Fundamental background on tribology

The main object of tribology, a relatively new discipline in science, relates to surfaces that interact in relative motion. The nature and consequence of interactions that take place at the interface control the friction, wear and lubrication phenomena [2].

Tribology was first defined in 1966 by a committee of the Organization for Economic Cooperation and Development and derivates from the Greek word "tribos", which means rubbing, so tribology could also be named, in literal translation, as the science of rubbing. Although the word tribology is relatively recent, the interest in this science comes from ancient history. During the Paleolithic period, the drills used for drilling holes or producing fire were fitted with bearings made from antlers or bones. Another example is the stones for grinding cereals, which also require some kind of bearings. In Lake Nimi, near Rome, was found a ball-thrust bearing dated about AD 40. To transport large stone building blocks and monuments, our ancestors already used some kind of lubricants, such as water-lubricated sleds. The first scientific considerations in wear and lubrication were made by Leonardo da Vinci (1452-1519), who postulated the first approach to friction. The tremendous industrial growth, since the beginning of the twentieth century, has led to the demand for better tribological solutions, leading to an enormous expansion in all areas of tribology [2].

The main purpose of research in tribology is the minimization and elimination of losses that result from friction and wear, in technologies involving the rubbing of surfaces. [2] This area of investigation plays a crucial role several fields in all modern

machinery that incorporates sliding and rolling surfaces, from aeronautics to household appliances. Therefore, it is not difficult to understand that friction reduction and wear control are major objectives, for economic reasons and long-term reliability.

Wear

Wear is a phenomenon of progressive removal of a substance from the surface of a solid, as a result of its motion relatively to the adjacent moving part [3]. The wear in bearings, namely the hip joint, can be the combination of abrasive, adhesive, corrosive or surface fatigue modes [3, 4].

Abrasive wear relates to the case in which hard asperities in one body that is moving across a softer or brittle body, under a certain load, removes material from its surface, leaving a groove. Since the most evident expression of this kind of wear are the grooves produced in the surface, abrasive wear is also classified as grooving wear [5]. The most important entities involved in abrasive wear can be classified in three groups [3, 4]:

1) First body – the body or bodies being worn, the wear of which is of most concern;

2) Second body – any counterface body, in motion relative to the first body, and in direct or indirect contact in such way that the forces can be transmitted to the first body. Second body is frequently the major cause of the wear to the first body;

3) Interfacial elements (third body): any materials (autogenously generated or foreign matter) and other special conditions that may be present in the interface between the first and second bodies. Wear debris, lubricants, entrained solid particles and reactive chemicals are examples.

The adhesive wear mechanism involves the transference of material from one surface to another, due to the shearing or junctions between contacting asperities. With the applied load, deformation occurs until the contact area is large enough to support the applied force. Adhesive wear is the most common wear mechanism in bearing couples [3, 4].

Corrosive wear occurs due to the chemical interaction of the material with the surrounding medium (external environment). This phenomenon is enhanced by friction, as it causes the removal of passivation layers and further corrosion of the material surfaces [3, 4].

Surface fatigue wear is the loss of material resulting from cyclic stress variation. In contact fatigue surface damage occurs by a repeated rolling contact. It depends on the number of performed cycles, the level of stress and the friction acting at the surface during the lifetime of the material [3, 4].

Friction

Friction is defined as the resistance to movement when two bodies move tangentially over one another, and it is the principal cause of wear and energy dissipation [6]. Friction is not a material property. It is a system response in the form of a reaction force. The fundamental experimental laws of friction are usually called Coulomb laws. These laws include the following aspects:

- static friction is greater than kinetic friction;
- kinetic friction is independent of sliding velocity;
- friction force is directly proportional to the applied load;
- friction force is independent of the apparent contact area.

Coulomb suggested that friction was caused by mechanical interlocking of asperities, like in abrasive interaction. The “interlocking” model had many limitations, and there were some objections to this theory, then adhesion, cohesion, atomic attraction, molecular attraction, and similar terms were also used to explain friction [7].

The coefficient of friction, μ, is the tangential friction force, F, divided by the normal load, ω, in contact [8]:

$$\mu = \frac{F}{\omega} \qquad \text{(Eq. 1)}$$

Friction can be divided into two components: an adhesion force, F_a, due to the adhesion between the two surfaces, and a deformation force, F_d, so that:

$$F = F_a + F_d \quad \text{(Eq. 2)}$$

In the macroscale, the deformation force is called “ploughing force” and “asperity deformation” when it occurs in a microscale [8]. Friction depends on several mechanisms, namely the hardness, surface roughness and thickness of the coatings and the wear debris that result of the contact between the opponent surfaces. The contact conditions for the mechanisms that influence friction when a hard spherical slider moves on a coated flat surface are schematically illustrated in Figure 1 [8].

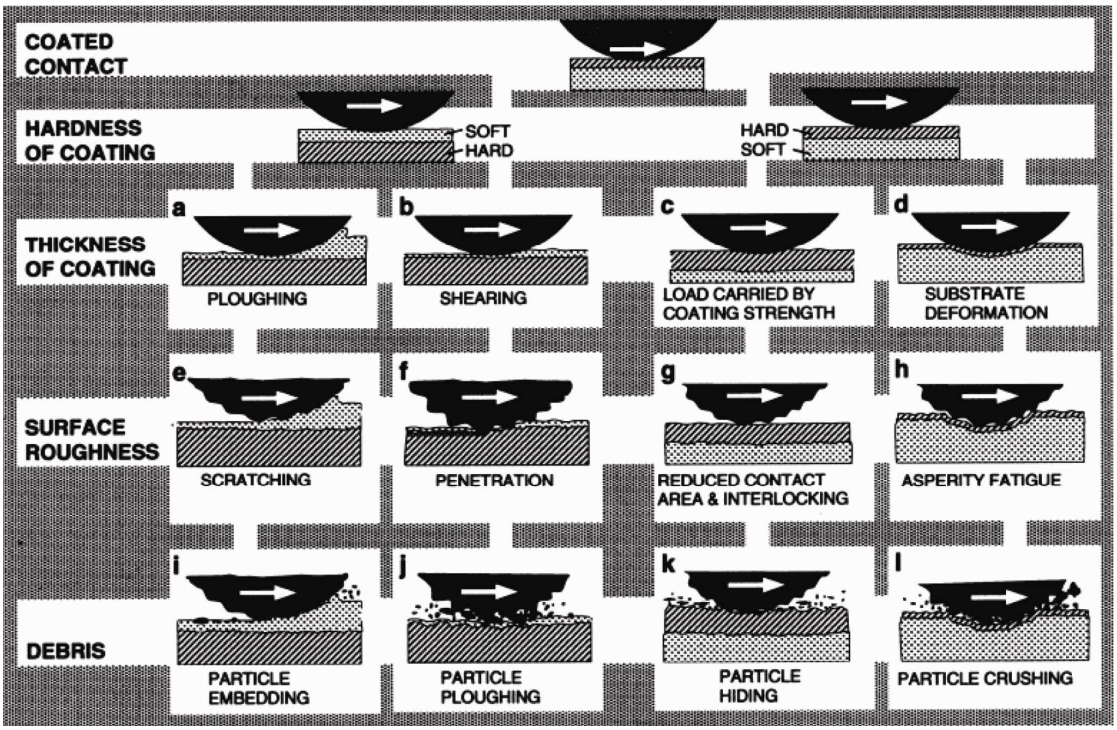

Figure 1 - Macromechanical contact conditions for different mechanisms that influence friction when a hard spherical slider moves on a coated flat surface (adapted from [8]).

It is fundamental to bear in mind that during the dry tribological contact, the composition and tribological properties of the original interface will change during use. These modifications may comprise topography changes (smoothening or roughing), formation of micro-cracks, phase transformations, deformation hardening, formation of oxides, formation of solid films by reactions with lubricant additives, transfer of

material from the counter surface, among others. A schematic representation of these phenomena is depicted in Figure 2 [9]. The film thickness ranges from atomic monolayers (e.g., hydrogen termination of diamond surfaces) to tens of microns (e.g., plastic deformation of metals) [9].

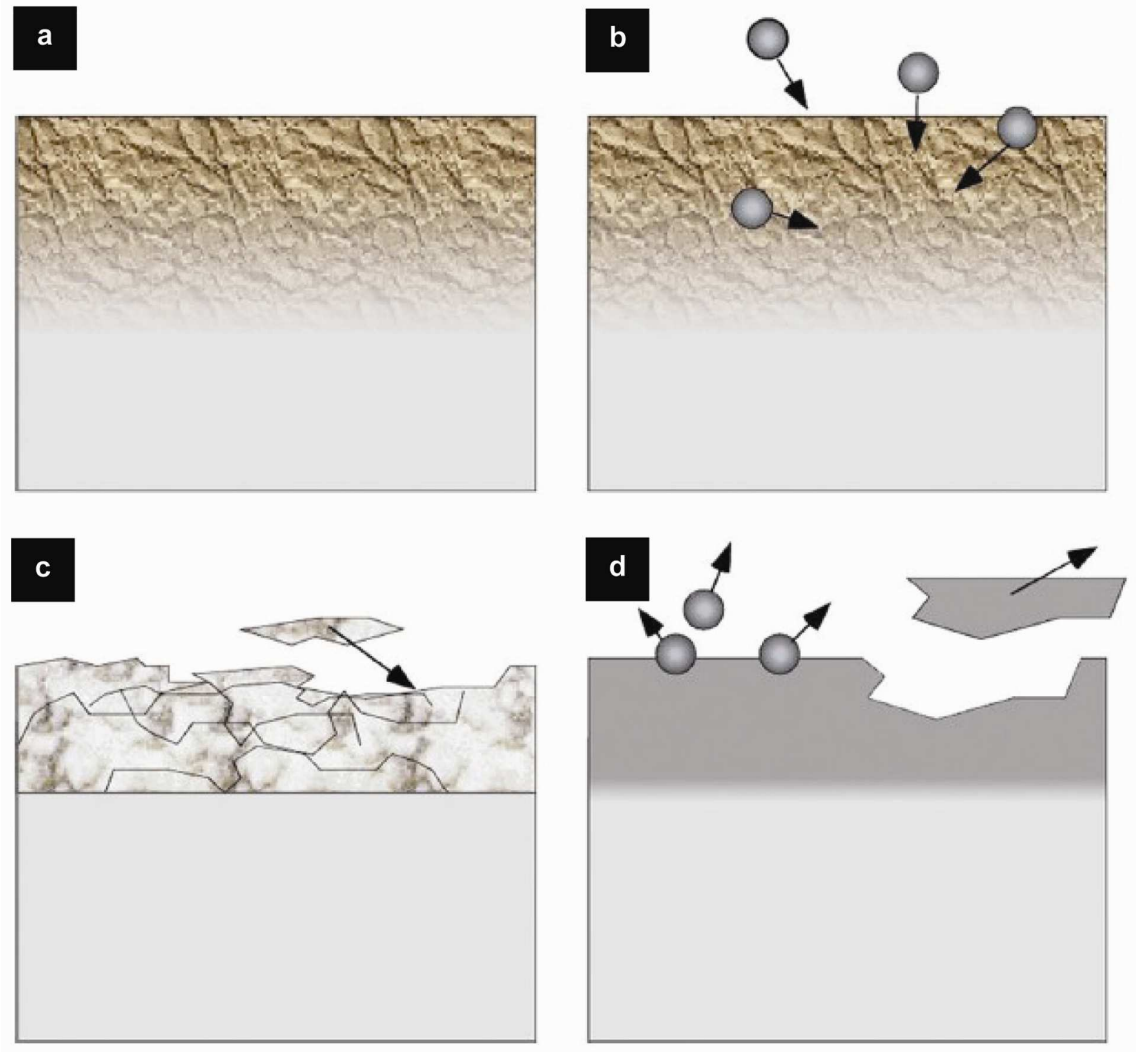

Figure 2 - Tribological surface modification: (a) modification without any material transfer; (b) modification involving material transfer; (c) formation of tribofilm or coating; (d) wear (loss of particles or atoms from the surface) (adapted from [9]).

Lubrication

Lubrication consists in the addition of a material between two surfaces able to undergo relative movement, aiming to reduce, or ultimately prevent, friction and wear [10]. Lubricants are thin, low shear strength, layers of liquid, gas or solid. In

engineering, three lubrication regimes are considered: fluid-film lubrication, boundary lubrication and mixed lubrication, which are directly dependent on the ratio between the thickness of the lubricating film and the roughness of the surface. The articular cartilage presents a roughness in the range 2-5 μm, which is approximately three orders of magnitude higher than the man-made ceramic surfaces [10].

Fluid-film or hydrodynamic lubrication corresponds to the lowest wear regime. In boundary lubrication significant contact between asperities takes place, with high wear and friction. Mixed lubrication presents a mixture of characteristics between boundary and fluid-film lubrication regimes [1]. This behaviour is schematically described in Figure 3.

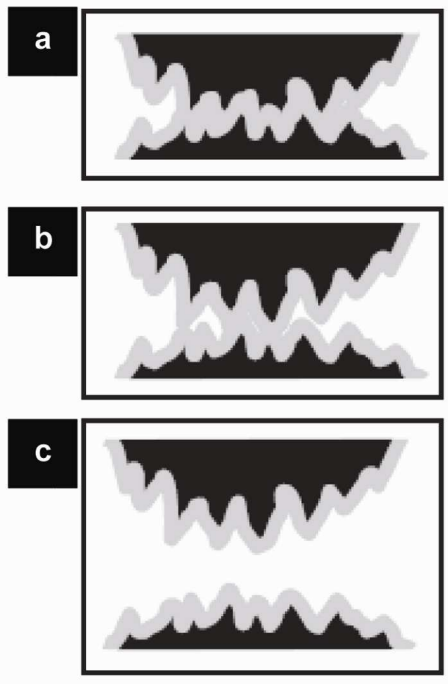

Figure 3 - Schematic lubrication regimes: a) Boundary lubrication, b) Mixed lubrication and c) fluid-film lubrication. The dark regions correspond to solid surfaces, while the light grey ones stand for boundary film (adapted from [1]).

At a microscopic level, the main feature that determines the characteristic of bearing is whether or not exist prevailing conditions that can maintain full fluid film lubrication thus preventing the contact between the two articulating surfaces. In these circumstances, the load is supported by the fluid between the bearing surfaces, resulting in the reduction of the frictional resistance and wear. But, when contact between the two surfaces occurs, there is an increase in friction and in the amount of

generated wear debris, which can originate an unfavorable response from the host system [11].

I.1.2. The natural hip joint and Total Hip Replacements (THR)

The hip joint is a synovial joint that connects the lower limb to the trunk. It is formed by a synovial ball (femoral head) and a socket (acetabulum), allowing a wide range of movements [12]. The strength of the joint capsule, the shape of the articular surface and the ligaments, depicted in Figure 4, establish the stability of the hip joint. During normal gait, forces up to five times the body weight were estimated in the hip joint.

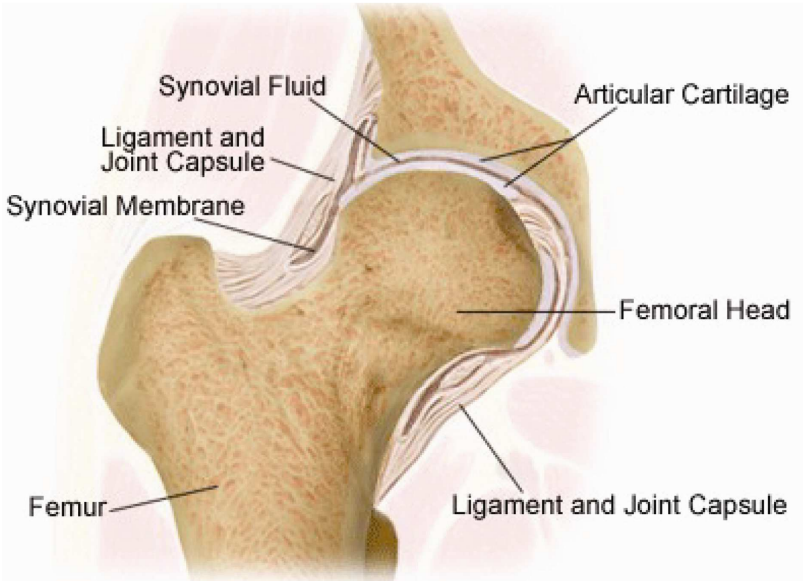

Figure 4 - Lateral view of a natural hip joint trybosystem (adapted from [13]).

The most common disorders of the hip joint are osteoarthritis, rheumatoid arthritis and avascular necrosis. Osteoarthritis is the degeneration of the articular cartilage, especially in weight bearing joints such as ankles, knees, spine and hips. The breakdown of cartilage tissue induces severe pain, caused by the rubbing of the bones against each other [14]. Rheumatoid arthritis is a systemic inflammatory disorder that can cause destruction of the articular cartilage and ultimately of the joint [14, 15]. Avascular necrosis, or ischemic bone necrosis, results from the loss of blood supply to the bone. In the case of the hip joint, the cells start to die, leading to the destruction of the articular cartilage and collapse of the joint [16].

A total hip replacement (THR) is the most common procedure to solve hip joint disorders since 1938 by Philip Wiles, that used a stainless steel cup, fixated by screws, and a head fixated using a stem, which was fixed to the neck of the femur by a bolt [17-19]. In THR the acetabulum is separated from the femoral head by introducing a bearing surface between the two parts of the joint aiming to reduce the pain and restore motion [20]. Fixation can be accomplished by using bone cement (cemented prosthesis) or with a porous sintered coating that allows bone growth (non-cemented prosthesis) [21]. The most common bearing couples used by surgeons are divided into two groups:

1) hard-on-soft bearings: metal-on-polyethylene (MoP) and ceramic-on-polyethylene (CoP);

2) hard-on-hard bearings: metal-on-metal (MoM) and ceramic-on-ceramic (CoC) bearings.

The first MoP (steel – PTFE) bearing was implanted by Charnley in 1958, named low friction arthroplasty (LFA), but only lasted two years. PTFE was replaced by Ultra High Molecular Weight Polyethylene (UHMWPE), being use to date in less active and older patients [22]. MoP bearings suffer long term failure due to osteolysis induced by polyethylene wear debris [23-25]. Osteolysis is a result of the biomechanical and biological interactions between the environment and the produced wear debris that are responsible for severe inflammatory responses, leading to periprosthetic osteolysis and aseptic loosening, incomplete osseointegration and severe stress shielding of the implants [26]. It has been reported that submicron polyethylene wear particles generate more intense biological activities than larger particles [27]. Loosening can also occur due to the fluid pressure in the fibrous membrane that will develop around the cement securing the prosthesis [27]. McEvoy and co-workers concluded that both particles and pressure contribute to osteolysis, and their combined effect accelerates aseptic loosening [28]. This drawback has led to intense research on polyethylene-free hard-on-hard bearings, more adequate in several solicitations, namely in younger and more active patients.

Boutin developed the first CoC total hip replacement in the early 1970s [29]. These were widely spread in Europe due to the inertness, good surface finishing and

high resistance to wear *in vivo* of the ceramics [30]. CoC bearing couples present extremely low wear rates, under standard simulation conditions, compared to MoM, MoP and CoP [31]. Nevertheless, there are still some concerns about the incidental fracture of the ceramic materials, correlated with its fracture toughness [32].

Si_3N_4 as a biomaterial

Silicon nitride (Si_3N_4) ceramics possess an outstanding set of properties, namely hardness and fracture toughness, which makes them suitable for tribological applications, namely for automotive and aerospace industry [33]. But Si_3N_4 is also a chemically inert, biocompatible material [34] used in several medical applications, namely for osteointegration, where it presented superior bone growth (new bone formation) and superior resistance to bacterial infection, when compared to poly (ether ether ketone) and titanium implants [35].

Si_3N_4 also finds applications in spinal implants [36] as well as subcutaneous implanted sensors [37]. The advantageous use of Si_3N_4 in artificial hip joints goes back to works as the ones performed by Zhou and colleagues [38] and Kusaka *et al*. [39]. More recently Sonntag and colleagues pointed out the applicability of this ceramic for high load medical applications, specifically in total joint replacement, as an attempt to reduce the wear debris found in the most commonly used metal-PE system [40]. Silicon nitride Total Hip Arthroplasty (THA) bearings have already been developed by Bal and co-workers [41]. Mechanical testing showed that Si_3N_4 had improved fracture toughness and fracture strength over alumina (Al_2O_3) ceramic. When tested with Si_3N_4 cups in a hip simulator, both cobalt-chromium (CoCr) and Si_3N_4 femoral heads produced low wear rates that were comparable to Al_2O_3-Al_2O_3 bearings in THA [41].

Bal and Rahaman recently reviewed the applicability of Si_3N_4 for orthopedic implants [42]. Dense Si_3N_4 ceramics prepared by in situ toughening proved to have superior mechanical properties then Al_2O_3-based ceramics and composites, which are currently used as bearings for total hip and knee joint replacement. Also, silicon nitride ceramics are being used to promote bone fusion in spinal surgery and to develop bearings that can improve the wear and longevity of prosthetic hip and knee joints.

Si_3N_4 has been implanted in human patients and clinical trials with Si_3N_4 femoral heads in prosthetic hip replacement are contemplated [42].

Diamond: a biocompatible material

Earlier studies on protein adsorption, cell adhesion and implantation have proven that diamond coatings are biocompatible, opening a large window of opportunities for biomedical applications [43]. Since then, intense research on this field has been carried on [e.g. 44, 45].

One solution for the problem of osteolysis, caused by the wear debris in articular prosthetic devices, is to coat the articulating surfaces with a harder material, such as diamond. This will improve wear resistance and reduce the number and size of the particles generated [46]. Diamond possesses a high chemical resistance and diamond particles are harmless when compared to UHMWPE, bone cement and chromium-cobalt particles [44]. The diamond surface can also be tailored in its chemical composition to be more biocompatible to proteins [47, 48] or cells [49, 50].

Among diamond coatings, the nanocrystalline diamond (NCD) variety has attracted interest for tribological applications due to its high hardness and low surface roughness, when compared to the microcrystalline diamond variety (MCD) [51]. Titanium alloys are among the most used substrates for NCD deposition, aiming its use on the biomedical field [52]. Also, NCD nanophase topography approaches the bone surface roughness and mimics the nanometric structures and molecules found in bones, potentially reducing the chances of rejection of the hip or knee prosthesis [53]. NCD is non-toxic [54, 55] and exhibit a higher resistance to bacterial colonization than medical steel and titanium [56], a relevant issue since bacterial infection resulting from implantation still is a significant clinical problem.

TiN-NCD composite layers on Ti-6Al-4V were tested on pin-on-disc experiments against polyethylene, in conditions aiming to simulate the joint implant in the human body (contact pressure, 4 MPa). NCD films diminished friction in a specific way via a “third body” lubricant, proving their ability to coat titanium alloys for use in hip prosthesis [57]. Papo *et al*. successfully tested a three layer NCD/MCD/NCD coated

temporomandibular Ti-6Al-4V joint [45]. For these synovial joints, the free diamond working surface in multilayer films should be terminated with smooth NCD layers.

NCD coatings over Si_3N_4 substrates for tribological applications has been the object of intense research by our group, both in dry as in lubricated sliding, envisaging applications such as the hip prostheses. NCD coatings have shown adequate tribological behaviour in dry conditions [58-62]. Using a ball-on-flat configuration, lubricated tests in water [63] and physiological fluids (HBSS and FBS) [64] were conducted. In all cases, high threshold load values before coating delamination were obtained, as well as very low friction coefficients (μ~0.02-0.10) and a high wear resistance (10^{-9} to 10^{-8} $mm^3N^{-1}m^{-1}$), indicating a mild to very mild wear regime.

I.2. Chemical vapour deposition of diamond

I.2.1. Historical background

P. W. Bridgman from Harvard University first reported the phase diagram of carbon in 1939, evidencing the need for high temperature and high pressure conditions under which carbon could exist in molten state and diamond crystals could be grown from this melt. He developed a high pressure and high temperature (HPHT) apparatus to grow crystals of several materials, but those attempts were not successful [65].

In 1953 investigators at Allemanna Svenska Elektriska in Sweden successfully achieved the synthesis of diamond from graphite. This work was done in parallel at General Electric in USA, being reported in 1954 [66]. This method proved to be rather expensive and does not allow the development of diamond coatings. It was therefore necessary to develop a more economic method where diamonds could be grown using low temperature and low pressure (LPLT). Intense studies on the thermodynamics of diamond formation suggested that diamond could be nucleated and grown at low pressures and low temperatures in an ambient of supersaturated carbon vapour [67].

In a simplified version of the phase diagram for carbon (Figure 5) it is visible that, when temperature and pressure are high enough, diamond is the minimum energy state of carbon atoms, while, at lower pressures and temperatures, graphite is

the stable form. At ~1 atm and room temperature diamond may be considered a metastable form of carbon. Although diamond is not the minimum energy state, it does not convert spontaneously to graphite [68]. Therefore, under these LPLT condition, either of them can nucleate and grow simultaneously [69].

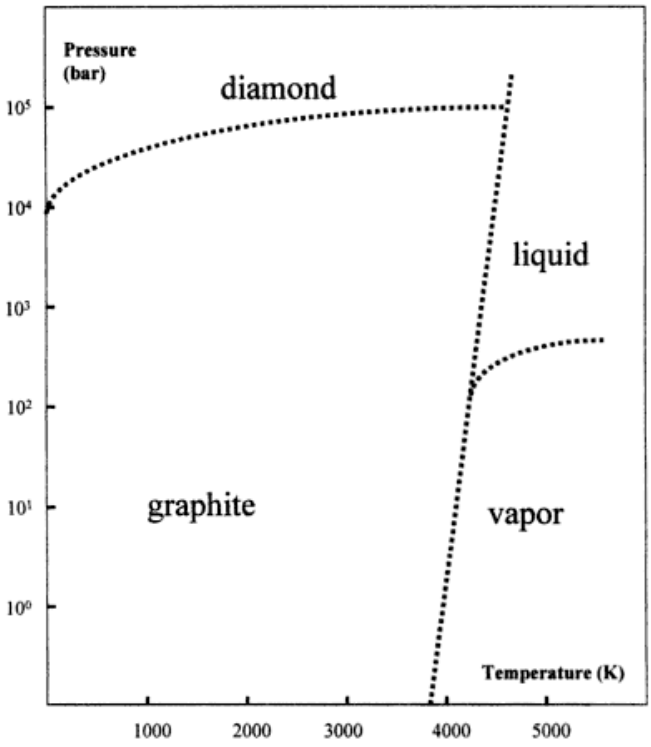

Figure 5 - Simplified phase diagram for carbon (adapted from [68]).

Eversole of Union Carbide Corp and Derjaguin and Fedoseev from USSR conducted the first successful attempts to grow diamond particles from organic species by decomposition of hydrocarbon gases under LPLT conditions, giving rise to the a new technology named "CVD Diamond Technology" [68]. Derjaguin and co-workers demonstrated, in the late 1970s, the possibility of enhancing the nucleation density and growth rate of diamond particles in presence of atomic hydrogen during the hydrocarbon pyrolysis. They were also successful in depositing diamond particles on non-diamond substrates [70]. Later on, Angus and co-workers in USA and a group of scientists from the National Institute of Research in Inorganic Materials (NIRIM) in Japan conducted systematic and detailed analysis of the nucleation and growth mechanism of diamond particles [66]. The latter grew diamond particles forming a polycrystalline coating on several non-diamond substrates by low pressure chemical

vapour deposition techniques involving various agents for decomposition of the hydrocarbon source gases. Driven by these discoveries, a worldwide research has been conducted over the last decades, focusing on the synthesis of diamond coatings by a variety of deposition techniques involving CVD processes.

I.2.2. CVD techniques for diamond

Chemical vapour deposition occurs from the dissociation, sometimes along with chemical reactions, of the reactant gases in an atmosphere activated by heat, light or plasma, with subsequent formation of a solid and stable product. Those homogeneous gas-phase reactions, that occur in the gas phase and/or heterogeneous chemical reactions that occur on/near the vicinity of a heated surface, originate powders or films, respectively. The temperature gradient and the gas flow processes are responsible for the transport of the carbon-bearing species. Since the diamond is formed by covalent bonding sp^3 hybridized orbitals of depositing carbon-species, the substrate or the environment near the substrate surface needs to be favorable to the formation of sp^3 bonds and should suppress the formation of other bonds and/or hybridization [71-73]. A simplified model of the CVD process is shown in Figure 6 [73].

The CVD techniques used to grow diamond films basically differ on the way the gases are activated: by plasma or thermally. The most used are: microwave plasma (MPCVD), hot filament (HFCVD), arc-jet plasma (AJCVD), RF-enhanced plasma and combustion flame. Along with HFCVD, hybrid methods involving the application of bias to the substrate and direct current (DC) have been developed [68]. Their working principles are discussed briefly in the following paragraphs, emphasizing on the HFCVD technique, used in this work.

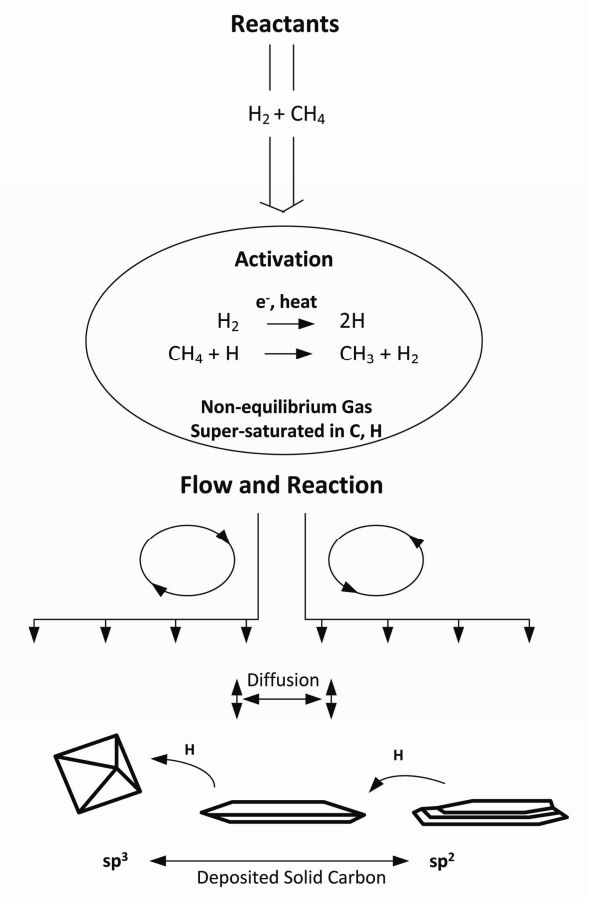

Figure 6 – Schematic representation of the chemical vapour deposition process (adapted from [71]).

Microwave Plasma Chemical Vapour Deposition (MPCVD)

A research group at NIRIM in Japan firstly grew polycrystalline diamond films in 1981 on non-diamond substrates using this technique [74]. In this method, a microwave plasma is used to activate the gas mixture of a carbon-bearing species (e.g. methane) and hydrogen. The general schematic diagram of a microwave reactor is shown in Figure 7 [75].

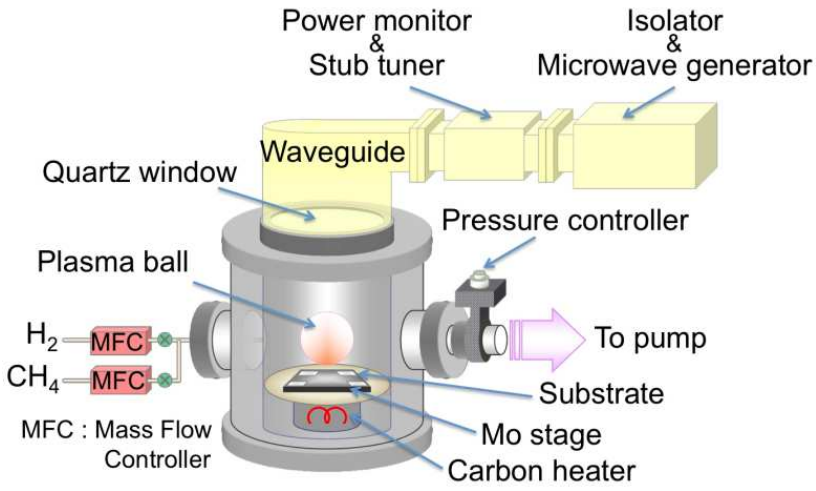

Figure 7 - Schematic representation of a ASTeX type Microwave Plasma assisted CVD reactor (adapted from [75]).

Microwaves (2.45 GHz) generated by a magnetron are introduced from the top of the reactor by a rectangular metal waveguide. The electron density is typically of ~10^{20} electrons.m^{-3} [73]. The waves are then picked up by an antenna and are emitted centre-symmetrically into the circular waveguide that contains the evacuated chamber. The plasma is generated at the point of highest electrical field strength inside it. The plasma shape, size and also its stability are dependent on the deposition conditions, power, pressure and gas composition. If correct conditions are chosen, a ball-shaped, stable plasma is formed in the centre of the chamber, as illustrated in Figure 7. In this method, the typical deposition pressure is between 1 and 400 torr and the substrate temperature is between 400 °C and 1000 °C. The substrate can be heated by the plasma alone or with a separate heating source. The heated substrate is kept below a plasma ball and the activated gas radicals are condensed on it [76].

By using this method, uniform and good quality diamond films can be obtained. The growth rate is usually in the range of 1 µm.h^{-1} to 10 µm.h^{-1}, depending on the selected growth parameters but also on the microwave power [77]. MPCVD requires expensive equipment, being therefore difficult to scale up to an industrial level. Also, the deposition area is restricted to the area of the plasma ball.

Combustion flame CVD

In this method, a gaseous mixture of oxygen and acetylene is used as starting material, producing a flame at atmospheric pressure [78, 79]. This flame is comprised of three regions, as shown in the schematic set-up of this method in Figure 8 [79].

I) The inner core that limits the O_2-C_2H_2 flame front;

II) The acetylene feather zone where the excess acetylene burns with the oxygen that diffuses into the flame from the surrounding air;

III) The outer flame where the CO and H_2 produced in the inner zone and the feather zone are burnt to produce CO_2 and H_2O.

The growth of diamond is observed when the substrate is in the feather zone. Synthesis of diamond by combustion flame CVD was first reported by Hirose *et al*. [64]. An advantage of this method is that diamond films can be grown in the open atmosphere. For the high quality diamond coatings over large areas, combustion flame technique is a good choice. The main disadvantage of this method is the requirement of high substrate temperature (> 1000 °C) which causes limitations on the type of usable substrates. This method also suffers from poor uniformity of the film.

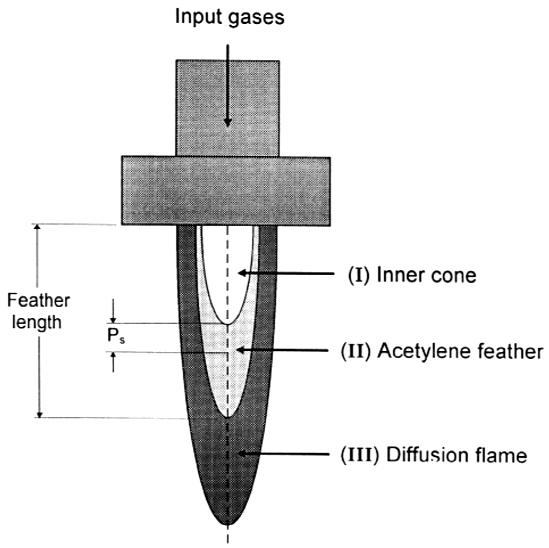

Figure 8 - Schematic set-up of a Combustion Flame CVD system (adapted from [79]).

Radio frequency plasma enhanced CVD

Radio-frequency power can be used to produce plasma when applied either to a capacitively coupled parallel plate reactor or by induction through an induction coil coupled to the reactor [80]. Frequency is usually 13.56 MHz. These two methods are schematically shown in the Figure 9 [81, 82].

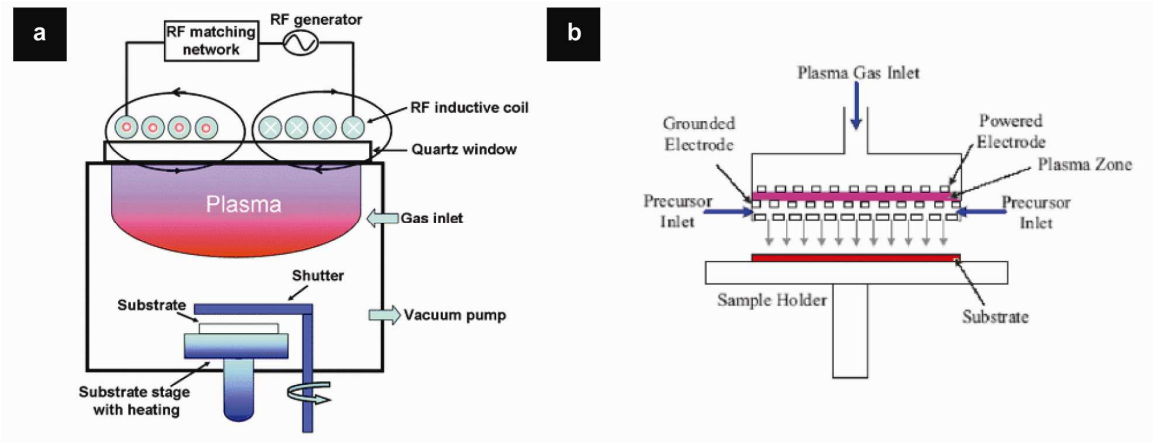

Figure 9 - A schematic representation of the low-frequency inductively coupled (a) and a parallel plate capacitively coupled (b) plasma-assisted chemical vapor deposition system (adapted from [81, 82]).

In order to maximize plasma stability, an impedance matching network is connected between the RF generator and the electrode assembly in order to match the plasma load to that of the RF power supply. Since ion bombardment from the plasma can destroy the sp^3 bonded nuclei and stabilize them as sp^2 bonded nuclei, capacitively coupled RF plasmas produce mainly hydrocarbon films, such as diamond-like carbon (DLC). Wood *et al*. [83] reported the synthesis of diamond films by a parallel plate, capacitively coupled RF plasma reactor. RF plasmas can be generated over larger areas, when compared to MPCVD [84, 85], being easy to scale up for industrialization of diamond deposition, but the films present poor crystalline quality and low growth rates.

Arc-Jet plasma (AJ-CVD)

Arc-jet Plasma or Plasma Jet designates a high-pressure direct current plasma discharge. Konig and Helwig [86] reported, in 1951, the deposition of hydrocarbon films form DC plasma excited benzene molecules. Kurihara *et al*. [87] used this technique to produce an arc discharge between the two electrodes, naming it the DC Plasma Jet process. A representation of this technique is shown in Figure 10 [88]:

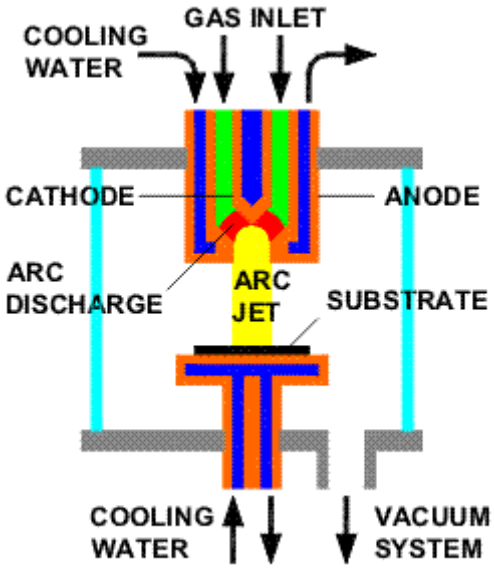

Figure 10 – Schematic representation of an Arc-Jet system (adapted from [88]).

Due to the pressure gradients and high gas flows, the formed DC plasma arc expands into a reactor vessel, where a substrate is mounted onto a water-cooled holder. Inside the plasma arc, heavy ions, molecules and free electrons are submitted to very high temperatures (1000 – 5000K) so that all molecules injected in that hot zone are decomposed into atoms or even ionized, depending on the energy supplied to the arc [89]. This technique allows high diamond growth rates of up to ~1 $mm.h^{-1}$ [90] and also the simultaneous deposition of metals and ceramics, along with diamond, by introducing the various powders in the plasma stream. This approach was used by Kurihara and co-workers, enabling the deposition of diamond films onto tungsten-molybdenum substrates, with a tungsten carbide interlayer, followed by a

diamond-tungsten carbide composite layer [91]. The use of this multilayered system allowed an increase of an order of magnitude of the adhesion strength, when compared to the diamond coatings without the tungsten carbide interlayer.

Hot Filament Chemical Vapour Deposition (HFCVD)

The first report on this method was published in 1982 by Matsumoto *et al*. [92]. In this method, the gas mixture (usually hydrogen and methane) flows towards the hot filament, reaching the substrate surface. Refractory metals like tungsten, tantalum, and rhenium are the most commonly used filament materials, heated from 2000 °C up to 2400 °C. At pressures in the range 10 to 100 torr, the heated filament transforms the hydrocarbon in the gas mixture (e.g. CH_4, 0.3 to 5 vol%) in acetylenic species, methyl radicals and other hydrocarbons, while H_2 decomposes into atomic hydrogen (H°). The H° and the hydrocarbon radicals diffuse from the filament to the substrate surface, which is usually at ~5-10 mm from the filament. The formation of atomic hydrogen at the activation region and the formation of the carbon growth precursors can be generically described by equations (3) and (4), respectively [77, 93-95]:

$$H_2 \leftrightarrow H^\circ + H^\circ \qquad \text{(Eq. 3)}$$

$$CH_4 + H^\circ \leftrightarrow CH_3{}^\circ + H_2 \qquad \text{(Eq. 4)}$$

The temperature gradient between the filament and substrate provides the driving force for the diffusion of these species [96]. The substrate is heated by the hot filament and, if necessary by a separate heater to 800 °C - 1000 °C allowing the deposition of polycrystalline diamond films. Growth rates between 0.1 µm.h^{-1} up to 15 µm.h^{-1} have been reported [97]. The deposition area is dependent of the number of filaments and varies from a few square millimetres up to more than 500 mm x 1000 mm for commercial reactors [98]. The HFCVD reactor used in the present work is shown in Figure 11.

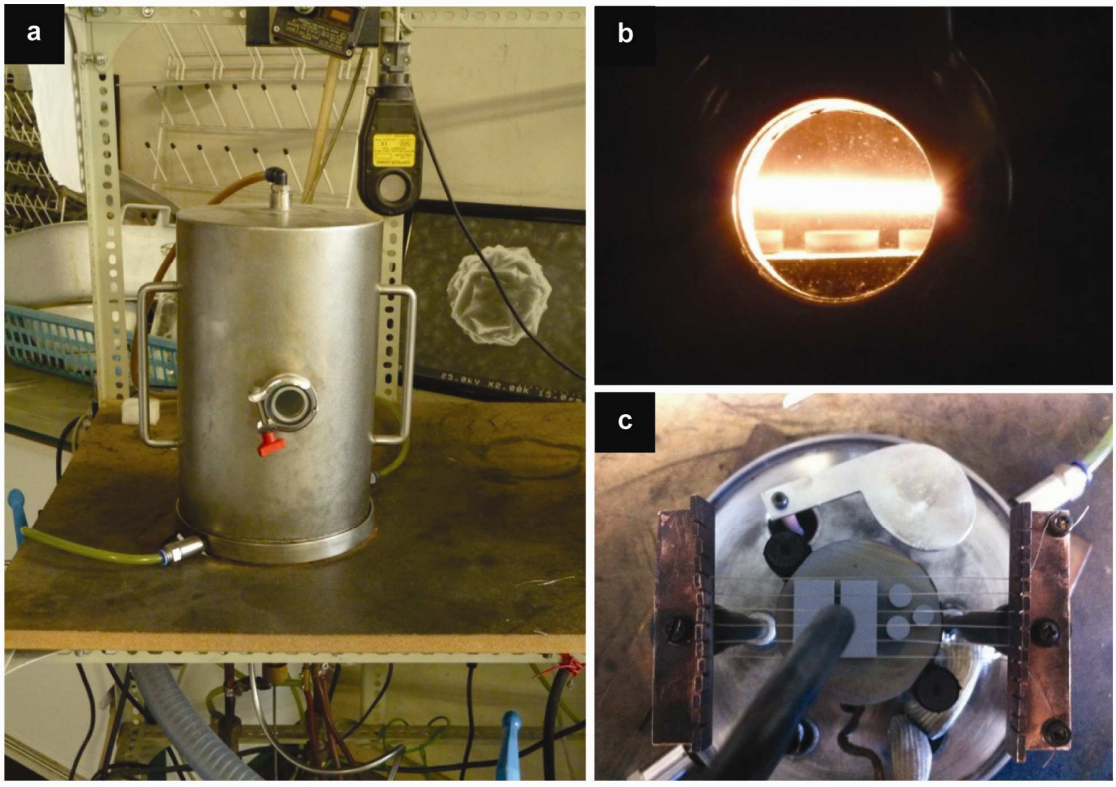

Figure 11 - HFCVD reactor used in this work (a); heated filaments over the Si_3N_4 substrates (b); general top view inside the reactor (c).

Due to its simplicity, comparatively low capital and operating cost, possibility to deposit over large areas and onto 3D shapes, hot filament assisted CVD has become popular in industry [99, 100] and it is abundantly reported in literature [e.g. 101-112]. Along with HFCVD, hybrid methods involving the application of bias to the substrate and direct current (DC) have been developed [68]. A drawback of this technique is the smaller deposition rate, when compared to other CVD plasma assisted techniques, such as MPCVD [113].

I.2.3. Diamond structure, properties and applications

A total of a dozen different allotropic forms of carbon structures are known, including graphite, graphene, carbon nanotubes, fullerenes and DLC. Our interest is focused in the diamond allotrope, as follows. Solids with only covalent C-C bonds form 3D structures that are rigid and isotropic and their allotropic form is diamond. Isolated C atoms have distinct 2s and 2p atomic orbitals. When these atoms condense to form

diamond electronic admixtures occur, resulting in four equal hybridized sp^3 molecular orbitals. Each C atom is covalently attached to four C atoms in tetragonal bonds 1.54 Å long creating a cubic structure, as shown in Figure 12 [114]. Due to its high density, diamond is the stable form at high pressure (d=3.51 $g.cm^{-3}$ in comparison to 2.26 $g.cm^{-3}$ for graphite or 1.72 $g.cm^{-3}$ for solid fullerenes) but it is metastable at room temperature and when heated to 1000 °C in the absence of air, it becomes covered with a layer of graphite.

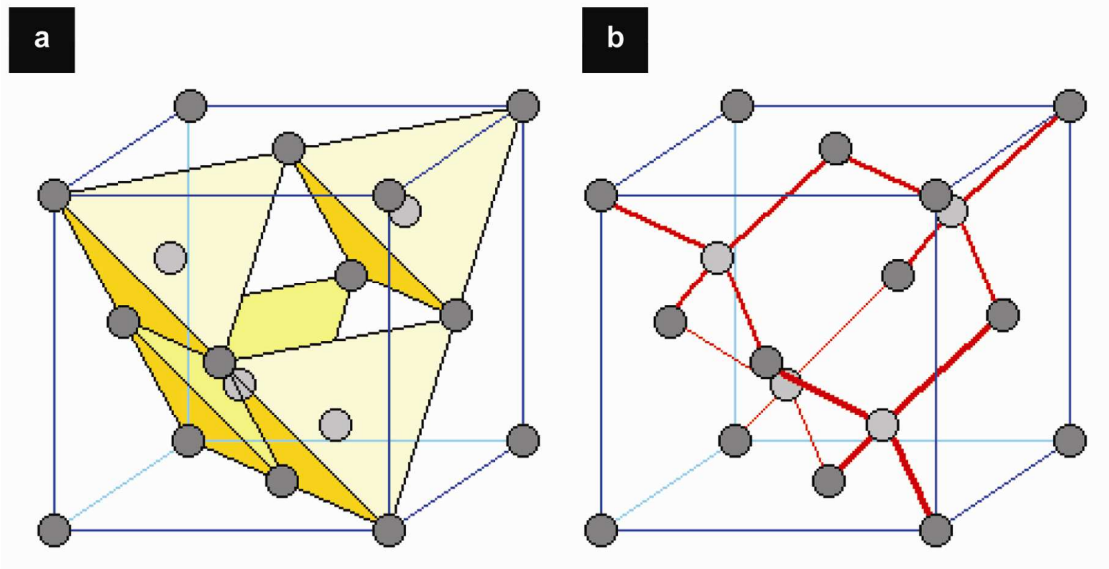

Figure 12 - Schematic structure of cubic diamond: (a) image depicts the position of the carbon atoms in the tetrahedral; (b) the carbon-carbon bonds are shown (adapted from [115]).

The high strength of the covalent bond (347 $kJ.mol^{-1}$) turns diamond into a very hard and abrasion resistant material, where a great amount of energy is required to remove a carbon atom from the diamond lattice. A comparison between diamond, graphite and DLC is presented in Table 1.

Table 1 - Comparing graphite, diamond and DLC (adapted from [73, 116]).

	Graphite	Diamond	DLC
Composition	Pure carbon	Mostly carbon (<1 at %)	0 – 60 at. % hydrogen
Microstructure	Crystalline	Crystalline	Amorphous
Atom-bonding state	sp^2 only	sp^3 only	sp^2, sp^3, sp^1 (variable ratio)
Stability	Stable	Metastable	Metastable
Raman Spectrum	Sharp peak at 1580 cm^{-1}	Sharp peak at 1332 cm^{-1}	Broad humps at 1330 and 1550 cm^{-1}
Electrical conductivity	Conductor (*ab* direction)	Insulator	Insulator

These allotropic forms can be distinguished using Raman spectroscopy. Microcrystalline diamond, graphite and DLC coatings display the distinctive Raman features mentioned in Table 1. For nanocrystalline diamond coatings there are additional bands located at 1180 cm^{-1} and 1540 cm^{-1}, that can be attributed to C-H modes in *trans*-polyacetylene (TPA) segments [117-119]. A band detected at 1240 cm^{-1} might also derive from *trans*-polyacetylene which has a small Raman peak in this region [117, 120]. There are two more bands located at 1370 cm^{-1} and 1585 cm^{-1} related to disordered (D) and crystalline (G) graphite, respectively, which is an indication of sp^2 carbon phases incorporated in the grain boundaries [121-125].

Diamond displays an extraordinary set of physical, chemical and mechanical properties attracting a considerable scientific and technological interest for a wide range of applications [126]. Either in bulk or as thin films, diamond is used in semiconductor, optical, computer and mechanical industries [127-130], among others. Some of the most relevant diamond properties and its possible applications, in comparison with some competing materials, are listed in Table 2 [68, 126].

Table 2 - Diamond properties and possible fields of applications (adapted from [68, 126]).

	Diamond Properties	Comparison with other materials	Applications (examples)
Vickers Hardness (Pa)	120 -150 ($x10^9$)	Hardest material known	Cutting tools, drill bits, wear resistant coatings, polishing material
Self- friction coefficient	0.1	In air	
Chemical stability	Inert	Resistant to all acids, bases and solvents, at room temperature	Coatings for reactor vessels
Young´s Modulus (GPa)	1.2×10^3	Highest mechanical strength; twice the modulus of alumina	Stiff membranes for lithography masks; lightweight coatings for audio devices
Sound propagation ($km.s^{-1}$)	18.2	1.6x the velocity in alumina	
Thermal conductivity ($W.m^{-1}.K^{-1}$)	2000	4x Cu or Ag, when compared to type IIa natural diamond	Insulting heat sinks for electronic devices
Thermal expansion coefficient ($1.K^{-1}$)	0.8×10^{-6}	Close to silica (0.57×10^{-6}), at room temperature	X-ray lithography masks
Band Gap (eV)	5.45	1.1 Si 1.43 GaAs	High frequency semiconducting devices; lasers; detectors; hot thermistors; hot transistors
Electron/ hole mobility ($cm^2.V^{-1}.s^{-1}$)	1900/1600	1500/600 for Si 8500/600 for GaAs	
Dielectric constant	5.5	11 Si 12.5 GaAs	
Refractive Index (RI)	2.41	1.6x higher than silica	Optical wave guides

Due to its extreme hardness, diamond is commonly used for cutting and drilling tools, where the edge of a non-diamond tool can be coated increasing the cutting performance by several orders of magnitude [131-135]. Diamond also found applications in optical windows [136, 137], wear-resistant coatings [138], surface acoustic-wave devices [139], field emission displays [140, 141], and heat spreaders [142, 143].

I.2.4. Diamond films: nucleation and growth

CVD diamond growth from a vapour phase starts with nucleation, which is the early stage of crystal formation, has been the subject of intense research [144]. Diamond growth on a diamond surface is likely to occur, with the nucleation sites being provided by the surface vacancies and broken bonds. In the absence of such diamond spots, nucleation has a very low probability to take place on non-diamond substrates [145]. CVD diamond nucleation has been reported to occur as a result of a combination of reactions that lead to [146]:

(a) suppression of formation of graphite nuclei;

(b) stabilization of diamond nuclei at the surfaces;

(c) preferential etching of sp^2 bonded carbon.

This is usually achieved by using large amounts of molecular hydrogen compared to the carbon source gas, allowing the supersaturation of atomic hydrogen produced by activation sources such as a hot filament or electric discharge. Nucleation is processed in two steps that depend on the substrate type, its pretreatment and the deposition parameters. In the first step, the carbon species impinge on the substrate and diffuse into the bulk, originating a carbide layer in most substrates with a low carbon diffusion coefficient. When carbon diffusion stops, the surface carbon concentration increases and eventually exceeds the necessary level for the second step of diamond nucleus stabilization [147, 148]. In the second step, nucleation depends on the surface pre-treatment and diamond seeds that are most commonly obtained by abrasive scratching with diamond powder, in a dry form or dispersed in an organic solvent, [149] or by bias enhanced nucleation (BEN) [150], the latter limited for use in conducting substrates.

When using abrasive scratching with a diamond powder, very small diamond fragments get locked into the scratches, providing the nucleation sites. The carbon species thus diffuse into the existing nucleation sites. Further diffusion of carbon and bonding of carbon species results into the formation of critical nuclei and the growth process begins. A schematic drawing of the relative importance of the primary and secondary nucleation is depicted in Figure 13 [151].

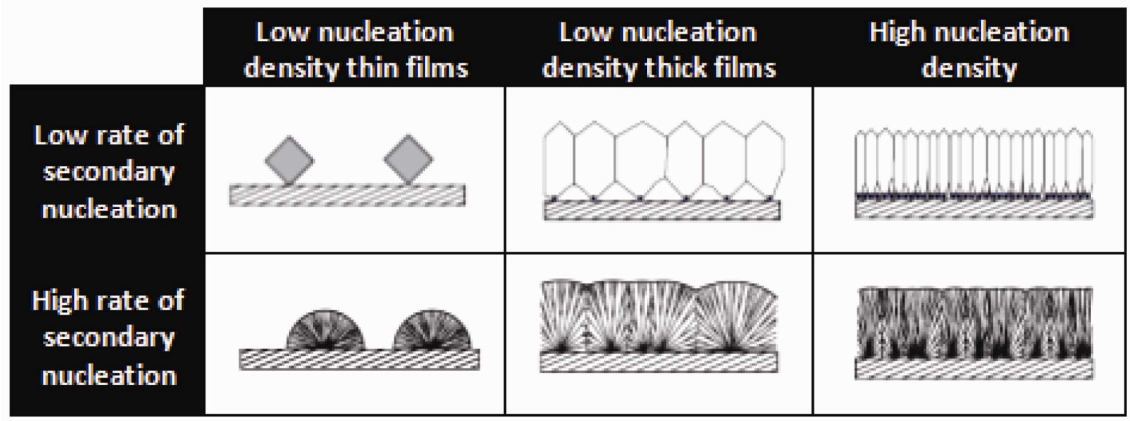

Figure 13 - Schematic drawing of the growth of diamond in dependence of the primary nucleation density and the rate of secondary nucleation (adapted from [151]).

Cicala *et al*. used diamond powder sizes in the range 0.125 to 45 µm, showing that powder size strongly affects the nucleation density, but has no effect on the growth rate and cristallinity of the films [152]. Although scratching improves nucleation density, it contributes to the loss in transmittance of diamond films due to the damage of the substrate surface [150]. Nucleation rates in the range of 10^{7}-10^{10} cm^{-2} have been reported, using hexane as a dispersion medium, for diamond deposition on a silicon wafer by microwave plasma-enhanced CVD [153, 154].

The reactions that take place after nucleation and during the growth step at the gas substrate surface interface have been studied by several investigators [155-160]. Besides atomic hydrogen and methane, radical species derived from methane can be found in the gas mixture, namely CH_3, C_2H, CH and C_2H. The chemistry of diamond deposition involves the competition for deposition among sp^2 and sp^3 carbon on the surface. The atomic hydrogen in the mixture erodes the sp^2 components, reducing the amount of graphitic or amorphous carbon that will be deposited in the substrate, thus allowing the building of sp^3 carbon as diamond crystals.

The importance of the scratching time with a diamond powder (seeding) procedure is highlighted in the SEM micrographs of MCD in Figure 14, grown in our HFCVD reactor with the same deposition time. After ultrasonication in a diamond powder suspension in ethanol for 20 min only individual diamond crystallites appear (Figure 14a), while a continuous, homogeneous MCD film is obtained in the substrates that were scratched for 1h (Figure 14b).

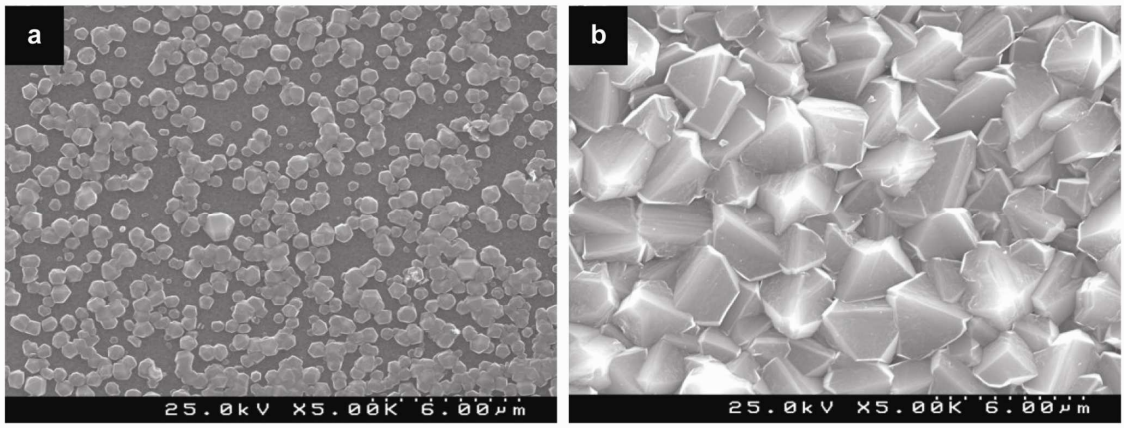

Figure 14 - Diamond crystallites and continuous MCD film after ultrasonication for a) 20 min and b) 1h, respectively, in a diamond powder suspension in ethanol.

I.2.5. Microcrystalline and nanocrystalline diamond coatings

Polycrystalline diamond films consist of diamond crystals with a minor fraction of non-diamond phases incorporated. However, there are substantial differences when considering film morphology, film texture, crystal size distribution and incorporation of non-crystalline phases, which depend of the selected growth conditions [161]. CVD polycrystalline diamond growth can lead to the following microstructures [162]:

- Columnar: consisting of columnar grains of preferred orientation that grow from the first nucleated, equiaxed layer deposited on the substrate. This is a result of a high supersaturation and low substrate temperature and hence more limited diffusion. This morphology is typical of microcrystalline (MCD) diamond films.

- Equiaxed: consisting of fine and randomly oriented grains, typical of nanocrystalline (NCD) diamond. This microstructure results from even higher supersaturation. This enables the rapid supply of reactants to re-nucleate new grains, and lower substrate temperature which limits surface diffusion and restrains the migration of monomers to preferred crystal lattice sites. This change in microstructure is caused by the rate of secondary nucleation, which is low for MCD but very high for NCD diamond deposition.

The columnar structure of MCD and of the equiaxed NCD deposited on silicon nitride ceramic substrates, using the HFCVD reactor shown in Figure 11, are visible in the cross-sectional SEM micrographs in Figure 15.

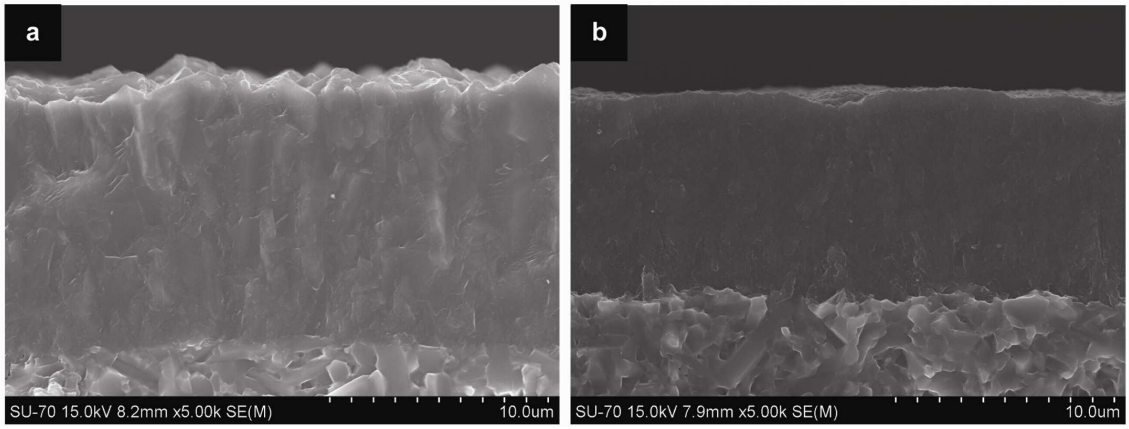

Figure 15 - Cross-sectional SEM micrographs of a) MCD and b) NCD evidencing the columnar and equiaxed structures, respectively.

NCD films are normally described as nanocrystalline diamond grains embedded in an amorphous carbon network [163], with diamond grains typically in the range 3 nm to 100 nm and surface roughness (Rq) from 15 nm to 40 nm, much smaller than that of MCD [163-166]. This is related to the almost non dependence of roughness on thickness of NCD, while for MCD crystallite size increases with film thickness. Thus, NCD coatings present low surface roughness, attracting considerable interest in applications that require very smooth surfaces like tribology [167] and electronic applications [168], among others.

In the so-called Ultra-Nanocrystalline Diamond (UNCD) variety, diamond grains are less than 5 nm [169]. The electronic properties of NCD and UNCD are very different. NCD is essentially very fine microcrystalline diamond and can be doped with boron. It is intrinsically transparent, with absorption increasing with doping level. UNCD is highly absorbing due to its higher sp^2 content, and exhibits a reduced bandgap due to disorder. By adding nitrogen to the gas phase, the density of states within the bandgap increases and ultimately metallic conductivity can be achieved. [170].

Due to the amount of sp^2-bonded nature of the grain boundaries, NCD is often called *ballas* diamond or *cauliflower* or ball-shaped diamond [171]. Ballas diamond possesses a strongly twinned microstructure and grows at the transition from faceted diamond to graphitic deposition [172]. NCD can be deposited by several CVD techniques, namely HFCVD, using different gas mixtures, such as H_2/CH_4 [99, 173], CH_4/N_2 [151, 174], $Ar/N_2/CH_4$ [175], CH_4/TMB for boron doping and H_2S for sulfur incorporation, in high hydrogen dilution chemistry [176], CH_3COCH_3 / H_2 [177].

NCD growth is achieved by favouring the secondary nucleation rate and disabling the growth of diamond to the micrometer scale. A key issue is the reduction of atomic H density that can be accomplished by increasing the carbon source gas amount and/or by partial substitution of H_2 by noble gases or nitrogen [112, 178, 179].

Some authors claim that NCD can still be grown even without any H_2 addition [180] but adding hydrogen to the feed gas permits stabilising the plasma, improving the process reproducibility [181, 182]. Argon is often found in the gas mixtures for NCD depositon as it is known to ensure high re-nucleation rate of secondary nuclei [183, 184] and to produce smoother NCD films when compared to other gases [178].

In MPCVD, using high concentrations of Ar, C_2 dimer species formation is favoured which is crucial for the growth of UNCD [112]. The same mechanism is advanced for the HFCVD technique, as C_2 was detected for amounts of Ar above 90% [112]. Nevertheless, the C_2 mechanism of NCD formation is not consensual and some authors postulate that C_1 species are the main responsible for the growth of nanocrystallites [178, 185]. By negatively biasing the substrate in a HFCVD system, the deposition becomes plasma-assisted, increasing the growth rate to values as high as 3 $\mu m \cdot h^{-1}$ [186]. In HFCVD, nitrogen is believed to behave as a catalyst to convert atomic H into H_2, allowing NCD to grow [187].

I.2.6. CVD diamond multilayers

Over the last decades a considerable effort has been dedicated to the increase of the wear resistance of tool materials and machine elements by applying thin, hard coatings. These coating materials must possess several different properties in order to work successfully in tribological applications. Key properties are: good adhesion to the substrate, low tendency to adhere to the counterpart material, high thermal and chemical stability good abrasive wear resistance (high hardness) and high fracture toughness. The improvement in the tribological properties can be achieved decreasing the friction coefficient, increasing surface hardness, altering the surface chemistry and by changing the surface roughness [188]. Thus, the wear resistance of surfaces is improved and the lifetime of relevant components is extended. Generally speaking, there are several different ways of increasing the toughness of coatings, such as

ductile phase toughening, grain boundary strengthening and grain boundary sliding, composition and structure grading, carbon nanotube toughening, phase transformation toughening, compressive stress toughening and finally, multilayer designs [189, 190].

In multilayered structures, micro-cracks tend to branch and deflect at the interface between two alternating layers of different materials [191, 192], while in single-layer coatings the cracks propagate directly to the coating-substrate interface. In these multilayered composites, depending on the layer properties and loading conditions, besides crack deflection, delamination at interfaces and crack reinitiation from flaws on the surfaces of the hard layer ahead of the primary crack may occur, with the material behind the latter either fully or intermittently detached. The variety of geometric and material parameters involved, e.g., thickness, stiffness and toughness of the layer or interlayer, and some control over the quality of the joining surfaces and residual thermal stresses, offers means for improving damage tolerance and energy absorption capabilities. [193].

Besides crack deflection at interface between layers, ductile interlayer ligament bridging and crack tip blunting due to nanoplasticity at interface are mechanisms for toughness improvement in a multilayer structure [194-198]. The three mechanisms are schematically depicted in Figure 16.

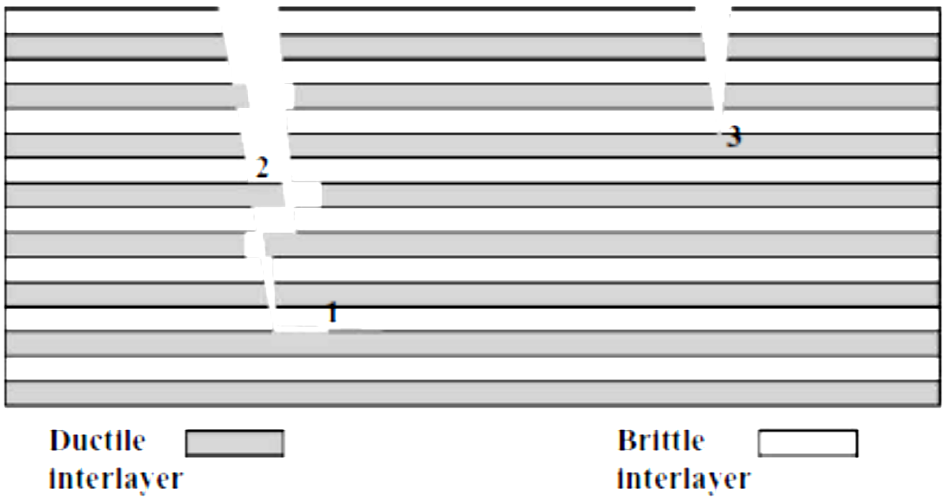

Figure 16 - Schematic representation of toughening mechanism in multilayer films: (1) crack deflection, (2) ductile interlayer ligament bridging, and (3) crack tip blunting due to nanoplasticity at interlayer (adapted from [199]).

The multilayer design approach for improving the mechanical behaviour of a coating is one of the few compatible with continuous CVD diamond processes, as composition, structure and internal stresses can be adjusted by changing the deposition conditions and interlayer thickness [189, 200]. It is of interest that the free diamond working surface in multilayer films is terminated with smooth nanocrystalline diamond (NCD) layers that are much more appropriate for tribological purposes than rougher ones. NCD coatings present a suitable combination of high hardness and reduced surface roughness for mechanical applications [59, 201, 202]. On the other hand, the threshold load for delamination is constrained by the lower NCD adhesion to the substrate, when comparing to that of the microcrystalline diamond (MCD) variety [59, 203, 204] that normally presents excellent adhesion but a high surface roughness. For tribological applications MCD coatings present high initial friction peaks, due to the interlocking of the asperities, somehow limiting is use [205]. To overcome these drawbacks, a consistent solution is a CVD diamond multilayer combination, starting with MCD to assure a superior adhesion to the substrate, and ending with a smooth nanocrystalline diamond (NCD) top coating.

A multi-step Hot Filament Chemical Vapour Deposition (HFCVD) deposition strategy was conducted based on a substrate negatively biased relatively to the filament, leading to a multi-layer coating where the diamond layers have different properties due to their morphological structures [206]. These composite, layered films, exhibit an excellent adhesion to the substrate, and a notable decrease in the surface roughness from 650 nm to 50 nm was achieved. The multilayered coatings present better wear resistance than the corresponding micro-structured, rougher monolayer coatings. A similar work was conducted by Takeuchi and colleagues [207], but without the use of bias current. A 30% increase in bending strength was obtained for the multilayers, when compared to the monolayered coatings. By controlling the processing parameters, namely methane concentration and gas pressure, Dumpala *et al*. [208] designed an integrated composite diamond consisting of a NCD layer over MCD with a coating architecture of NCD/transition layer/MCD/WC–Co. The transition layer, of about 1 μm in thickness, was deposited in order to integrate the MCD and NCD layers. Köpf and co-workers studied the possibility of combining diamond as a basic layer with protective CVD layers of TiC, TiN, Ti(C,N) and Al_2O_3 in a multilayered

structure, onto WC–Co hardmetal substrates, showing that, under optimal conditions, the layers present good adherence amongst each other and on the substrate [209] .

Multiple layers of NCD on top of a MCD coating, combining HFCVD and polishing was proposed by Shen and Sun. Tribological testing in dry and lubricated conditions was performed against ball-bearing steel, copper and silicon nitride balls, revealing a substantial increase in the friction properties, when compared to the WC-Co or MCD samples in both solicitations [210].

Crack propagation on cemented carbide cutting inserts was reduced by using alternating layers of fine- and coarse-grained MCD, as reported by Schäfer *et al.*[211]. A considerable improvement on the working lifetime of drawing dies by a factor of above 15, when compared to the uncoated substrates, was achieved by Sun *et al*. [212] on MCD/NCD bilayered coatings using bias-assisted hot-filament CVD. Kadlečíková *et al.* also grew diamond bilayered structures on WC-Co substrates using the same technique [200].

A two-step diamond deposition method was used to coat hardmetal drawing and stranding dies, where the first layer, of MCD, ensured a good adhesion to the substrate while the top NCD coating provided a low surface roughness (Ra < 100 nm) [213]. Bias assisted MPCVD technique was used by Jiang and co-workers to deposit nano/micro diamond overlayer films. The formation of a diamond nanocrystalline structure on microcrystalline diamond surface was due to the frequent generation of diamond secondary nuclei under the bias conditions [214].

A multilayered structure consisting on diamond grains agglutinated with electroplated nickel to serve as anchors for the diamond film, a chromium nitride layer and a CVD diamond film were developed for use in abrasive tools, increasing the tool life without compromising the cutting speed [215].

The structural influence of composite polycrystalline/nanocrystalline diamond, with a top smooth surface on dielectric properties was evaluated. The multilayerd structures presented better dielectric properties, compared to polycrystalline and nanocrystalline diamond films, being adequate for the fabrication of diamond semiconductor devices [216].

I.3. Adhesion evaluation of CVD diamond coatings

Diamond films adhesion to the substrate is a key issue that is strongly influenced by several factors, namely the surface roughness, surface reactivity and by the stresses developed at the bonding surface due to the thermal expansion coefficient mismatch between the coating and the substrate material [217]. In CVD diamond coatings the film adhesion is commonly evaluated by static indentation tests, and not by scratching experiments as usual in other types of coatings, as diamond is a very hard material and rapidly leads to tip breakage. A complementary adhesion evaluation test can be derived from the impact of hard particles on the coatings in erosion wear experiments.

Indentation testing

Indentation hardness characterizes the resistance of a material to permanent deformation. The first widely used and standardized testing method was developed in 1900 by J. A. Brinell [218]. Another method, known as the Rockwell hardness testing uses several indentation loads and is based on the penetration depth to evaluate hardness. Although used for hardness measurement, it can be applied to evaluate the adhesion between two surfaces [219], as one of the major sources of failure in adhesive joints, thin films, and composite materials is the propagation of cracks between the constituent materials [220].

There are two main types of Rockwell hardness tests, *regular* and *superficial*, which mainly differ in the loads applied, and the geometry of the indenters used. For the regular Rockwell hardness testing method, a minor load of 10 kgf is applied to set up a base or zero point. After this initial tuning, a major load of 60, 100 or 150 kgf is first applied, and then removed. In this method, the hardness number is inversely proportional to the depth of the indentation, and the indenters are shaped as diamond cones or hardened steel balls of various sizes [218].

The Rockwell hardness testing method uses different indenters such as 1/16” (1.5875 mm) diameter or 1/8” (3.175 mm) diameter hardened steel balls according to the scale used in the test. Another indenter used in the Rockwell C scale is the Brale

indenter. It is a diamond cone with a 120 ° ± 0.35 ° included angle and a spherical tip with a mean radius of 0.200 mm ± 0.010 mm. Figure 17 illustrates these features [218].

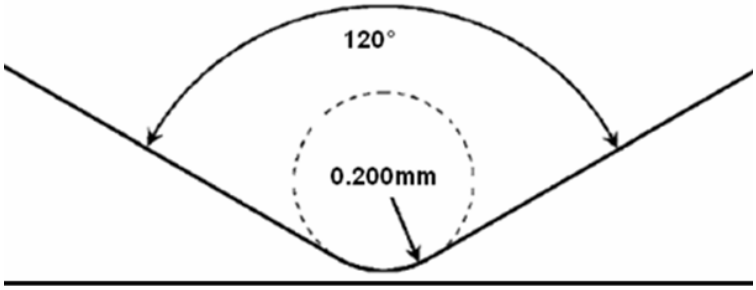

Figure 17 - Profile of Brale Diamond indenter tip (adapted from [218]).

Belmonte *et al.* investigated the adhesion behaviour of diamond coated silicon nitride ceramics using a Brale indentation test. [221]. As the indenter penetrates through the film and leaves the sample, the following events occur:

i) in the silicon nitride ceramic substrate: elastic and quasi-plastic deformation, lateral and radial/median vents nucleation at the elastic/plastic transition and their growth towards the film/substrate interface;

ii) at the film/substrate interface: propagation of the radial and lateral (circumferential) cracks. According to the Marshal and Evans model, the propagation of radial and lateral (circumferential) cracks along the film/substrate interface are due to the combination of a set of factors: residual stresses, mechanical properties of both the film and substrate and interfacial fracture resistance [222].

iii) propagation of the former vents along the film and its spalling-off when both crack systems meet.

Due to the brittle nature of the silicon nitride substrate, the cracks initiate in the substrate bulk. Film spalling-off occurs when radial and circumferential cracks meet, after emerging from the coating/substrate interface [221].

Almeida *et. al.* [204] grew diamond films, from nanometric to microcrystalline grain sizes and evaluated their adhesion levels to a silicon nitride ceramic by Brale tip indentation testing. MCD attained a normal load of 1600N without spalling-off, much higher than the nanocrystalline diamond variety (400N) [204]. This is due to the sp^2 amorphous carbon phases at the grain boundaries in NCD, responsible for the

decrease in the mechanical properties, when compared to MCD [223]. Also, NCD revealed a poorer adhesion to the ceramic substrate, due to the lower deposition temperature. The combination of harder and thicker coating upholds the applied load and reduces the plastic deformation volume in the substrate [217].

Erosive wear performance

Solid particle erosion occurs when solid particles carried by a stream of liquid or gas impinge/impact against a target material, causing the target material to deform, fracture or be removed completely [224]. Erosive wear testing is also a way to assess film adhesion [225-227], and presents itself as an alternative solution to static indentation or scratch tests, therefore avoiding the problem of indenter tip wear.

It is important to clarify the difference between impingement and erosion, as impingement does not always result in erosion. However, impingement is necessary for erosion to occur. Impingement refers to the impact of the droplet or particulate on the target. Erosive wear is a general name for a number of erosive mechanisms. The mechanisms differ based on the impact velocity, orientation, size and properties of the impacting droplets or particles [4]. Predictive models aiming to quantify material loss during erosion can be found in literature. An exhaustive review in this matter was conducted by Meng and Ludema [228], that emphasizes the variety of existing models and the difficulty in the data analysis in this type of wear tests, due to high number of existing factors influencing erosion.

Erosion studies on several materials caused by impacting particles are reported on literature [229-233]. A common feature is the variation in wear behaviour with properties such as hardness, toughness, stress levels, temperature, surface roughness, ductility and brittleness, emphasizing the crucial role played by the material properties in the overall wear.

B. Karunamurthy and co-authors conducted an experimental study on the mechanism of cavitation erosion in silicon nitride ceramics showing that multiple intergranular and transgranular fracture occurred at the initial stages followed by the formation of grain dislodging and removal which, due to proliferating and coalescing, encouraged further damage. Also, crack initiation and propagation were visible,

showing that cavitation erosion is a surface fatigue process and concluding that the rate of erosion largely depended on the microstructure of the material [234].

Velocity and the impact angle of the erodent particles are key factors influencing the erosion performance of materials. The local particle impact angle can be defined as the angle subtended by the velocity vector of a particle to the surface just prior to imminent collision. For an air-borne erosion system, this angle can be considered to be similar to the angle subtended by the impinging jet to the target surface. This is an important factor in modeling solid particle erosion, for it determines the nature of the erosion mechanism. In the case of a brittle material, the maximum overall wear was observed for 90° impingement angles and reduced to zero at low angles of impingement [235].

Chen and Li [236] used mathematical deformation models to predict erosion losses on two different materials (ductile and brittle) using similar abrasives (material property, geometrical feature and orientation) at exact local particle impact conditions and observed the variation of erosion loss with impact angles. For the ductile material type, maximum erosion occurred at an impact angle around 30° whereas for the brittle type material erosion rate peaked at 90° impact angle, as illustrated in Figure 18 [236].

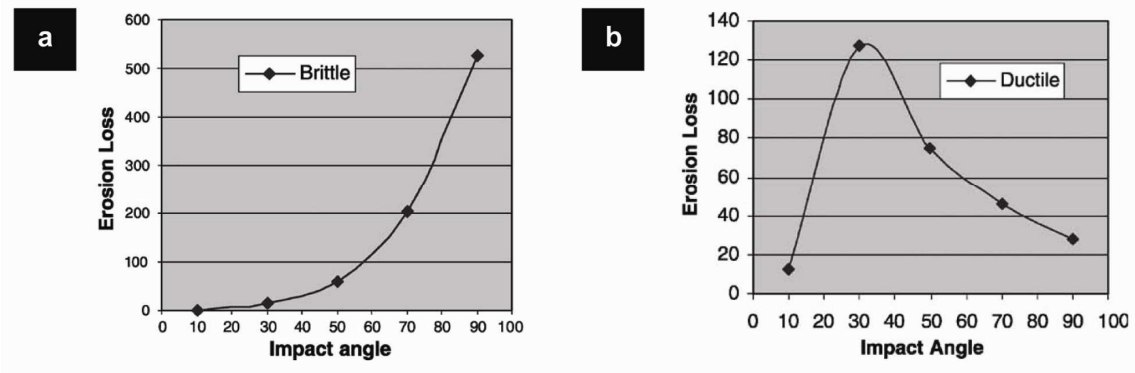

Figure 18 - Relationship between the impact angle and the erosion loss for brittle (a) and ductile (b) materials (adapted from [236]).

The erosion resistance of a range of polymeric, ceramic and metallic coatings on carbon steel substrates using sand/water slurry jets impinging at 30° and 90° and at velocities between 10 and 28.5 ms^{-1} was investigated by R.J.K. Wood [237]. For both angles of jet impingement, the performance of the coating relatively to carbon steel is

dependent on impact energy, E_k, and the tested coatings presented a range of erosion behaviour from purely ductile to purely brittle with some mixed behaviour.

One of the factors to address when predicting erosion of a material is the particle size effect. Lynn *et al*. and Clark and Hartwick studied erosion using a range of particle sizes, concluded that the collision efficiency of the particles decreased with decreasing particle size. According to the authors, collision efficiency can be defined as the "ratio of the number of particles striking a unit area of the surface in unit time, to the number of particles contained within the volume of suspension swept by that area in unit time" [238, 239].

Erodent shape is another important parameter when describing the erosion mechanism of solid particles. The cutting mechanism is the most effective in angular particles, while ploughing and deformation is the dominant mechanism in spherical particles [224]. However, the shape angle of the particles is difficult to determine, being usually described as angular or rounded [240]. The author demonstrated that particle angularity causes an increase in abrasion and erosion rates. Stachowiak used the Spike Parameter (SP) to define the particle angularity, representing the particle boundary by a set of triangles, as depicted in Figure 19 [240]. A more erosive particle would correspond to sharper and bigger triangles. However, this did not take into account the influence of other material properties such as fracture toughness on the increase of the wear rate.

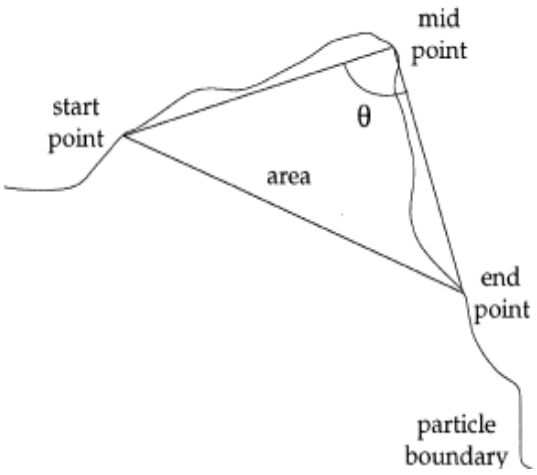

Figure 19 - Schematic illustration of calculation method for Spike Parameter, SP (adapted from [240]).

When describing the erosion resistance of a material, fracture toughness of the erodent must be considered [240]. When particles impact the target, the tip or cutting edge of angular particles can break off during impact, thus reducing the effectiveness of cutting on the surface. Another important characteristic in erosion resistance is the target material hardness.

In erosive wear tests, several erodent particles can be used with SiO_2, Al_2O_3, sand and SiC among the most commonly used [241-244]. In the present work SiC particles with ~75 µm diameter as the one depicted in Figure 20, for a particle impact angle of 90° were tested against diamond coated silicon nitride ceramics.

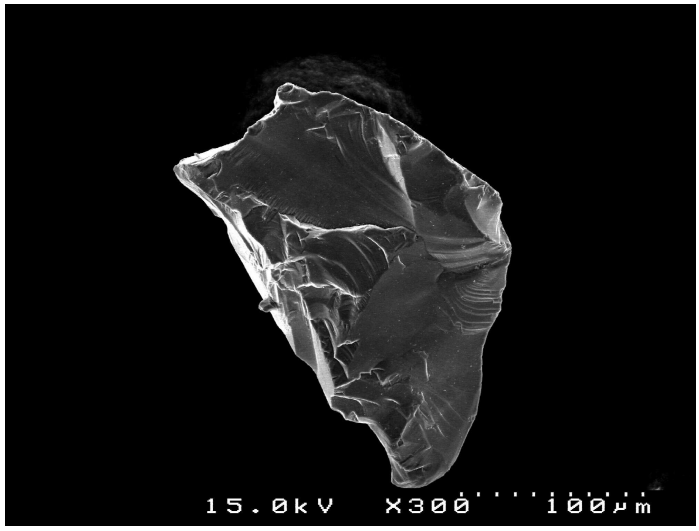

Figure 20 - SEM micrograph of a SiC erodent particle used in this work.

Material hardness is a major factor which affects erosion rates. Erosion wear usually occurs if the particle hardness is greater that the target surface hardness and increased target surface hardness can enhance erosion endurance [245-247]. Particles with lower hardness than the target material cause less wear, compared to particles which are significantly harder. The wear rate depends on the ratio between the hardness of erodent, H_e, and the target material hardness, H_m [224]. The relative hardness of the SiC particles used in this work is 28.5 GPa, while for CVD, according to Wheeler and Wood [225], is 80 GPa, thus, the H_e/H_m ratio is 0.35.

In solid particle erosion, it is important to consider not only the properties of the particles and the target material, but also the fluid flow characteristics. In a

simplified approach it would be expected that increasing the erodent concentration would increase the erosion rate, due to the higher number of particles impinging the target material [224].

The volumetric erosion loss per impact V_L, in a brittle and homogeneous material, based on the elastic plastic theory, can be written as [248]:

$$V_L = \frac{\lambda\left(\vartheta^2 m\right)^{\frac{7}{6}}}{K_{Ic}H^{\frac{1}{6}}} \times \left(\frac{E}{H}\right)^{\frac{4}{5}} \quad \text{(Eq. 5)}$$

In Equation 5, λ is a material independent coefficient, ν is the aerial speed of the erodent, m is the mass of the erodent, K_{Ic} is the fracture toughness, and E and H are the Young's modulus and hardness of the target, respectively. The erosion rate is proportional to the volumetric erosion loss, $\dot{E} \propto V_L$. For brittle materials, material removal occurs by intersection and propagation of cracks, while for ductile ones a process of displacement and cutting takes place [249]. In 1881 Hertz studied the formation of cone cracks in brittle materials by the use of spherical indenters. According to the contact equations by Hertz, the maximum tensile stress occurs at the edge of the contact circle. This stress on the specimen surface is responsible for the formation of Hertzian cone cracks following an impact.

The cracks initiate normal to the substrate surface and extend downwards into the material prior to full widening into a fully developed cone [250]. Upon sufficient intersections of the formed cone and ring cracks, chunks of material break out, resulting in mass loss. As a consequence, radial cracking occurs and the material degrades [251].

Erosion of diamond

The superior resistance of diamond to erosion damage by solid impact particles is well known [52, 225, 225, 252]. Heinrich and co-workers [52] coated titanium alloys with MPCVD diamond films, grown with 1, 4 and 8% methane. A standard sand-blast rig under an incidence angle of 90° was used to access the solid particle erosion behaviour. The diamond coated samples showed a superior wear resistance, when

compared to the TiAlN PVD hard coatings [52]. For diamond layers grown with 1% methane, intercrystalline cracking along the grain boundaries was found while a CH_4 content of 4% resulted in transcrystalline cleavage of diamond grains. In coatings deposited with a process gas concentration of 8% methane a mixture of both mechanisms was detected.

Amirhaghi *et al*. [226] tested sintered tungsten carbide (WC) with different binder percentages (5 and 6%) coated with MPCVD diamond in a high velocity air-sand erosion testing. The diamond coated substrates proved to have a better erosion resistance compared to uncoated substrates, with the erosion rate being lowered by up to a factor between ~5 and 20 for particle test velocities of 148 and 63 $m.s^{-1}$, respectively. The authors stated that the probable source of crack initiation are the voids present at the diamond grain boundaries close to the interface, and it is the propagation of these interfacial cracks by the repeated particle impacts that determines the coating life.

Diamond is very resistant to plastic deformation, so microcracks are nucleated by multiple particles impacts, where Hertzian ring and cone cracks develop in the elastic regime. Erosion tests in natural diamond show that the material removal mechanism is caused by the intersection of those cracks, leading to the separation of small volumes of diamond from the bulk [252], while for CVD diamond coatings, abrupt adhesion failure usually occurs before a detectable weight loss [225, 252]. According to Wheeler [3] a three-stage mechanism controls the erosion process: 1) initial period prior to steady-state erosion where micro-chipping takes place; 2) steady-state period where the micro-chipping is augmented by the nucleation of pin-holes and development of disbonded areas at the coating-substrate interface and 3) failure of the coating. After adhesion, the most important parameter that controls the erosion resistance is the diamond coating thickness [226, 253].

References

[1] Z.M. Jin, M. Stone, E. Ingham, J. Fisher, Current Orthopedics 20 (2006) 32.

[2] B. Bhushan, Handbook of Micro/Nano Tribology, CRC Press, USA (1995) 3.

[3] J.A. Williams, Engineering Tribology, Cambridge University Press, Cambridge (2005).

[4] G.W. Stachowiak, A.W. Batchelor, Engineering Tribology, Elsevier Butterworth-Heinemann, Amesterdam (2005).

[5] J.D. Gates, Wear 214 (1998) 139.

[6] E. Rabinowicz, Friction and Wear of Materials, John Wiley and Sons, New York (1965).

[7] B. Bhushan, Modern tribology Handbook, CRC Press, London (2001).

[8] K. Holmberg, A. Matthews, Coatings Tribology: Properties, Techniques and Applications in Surface Engineering, Elsevier, Amsterdam (1994).

[9] S. Jacobson, S. Hogmark, Wear 266 (2009) 370.

[10] J.J. Ramsden *et al*., CIRP Ann. 56 (2007) 687.

[11] R.M. Hall, M.J.K. Bankes, G. Blunn, Current Orthopaedics 15 (2001) 281.

[12] N.P. Palastanga, D. Field, R. Soames, Phys Ther. 86 (2006) 1450.

[13] http://www.iospak.com/hipjoint.html, February 2014

[14] A. Charlish, The Complete Arthritis Handbook, Carnell Ltd, London (1994).

[15] M. Corr, Rheumatoid arthritis: Introduction, Springer Semin. Immunopathol. 25 (2003) 1.

[16] T.L. Fagerson, The Hip Handbook, Butterworth-Heinemann, London (1998).

[17] A. Ravaglioli, A. Krajewski, Bioceramics: Materials, Properties, Applications,

Chapman & Hall, London (1992).

[18] N.J. Hallab, J.J. Jacobs, L. Katz, Orthopedic Applications. In Ratner B, Hoffman A., Schoen F., Lemons J. editors, Biomaterials Science – An Introduction to Materials in Medicine, Second Edition, Elsevier Academic Press (2004).

[19] L. Ambrosio, G. Peluso, P.A. Davis, Biomaterials and their Biocompatibilities. *in* D.L. Wise, D.J. Trantolo, D.E. Altobelli, M.J. Yaszemski, J.D. Gresser editors, Human Biomaterials Applications, Humana Press (1996).

[20] A. Buford, T. Goswami, Mater. Des. 25 (2004) 385.

[21] K. S. Katti, Colloids Surf. B 39 (2004) 133.

[22] J. Charnley, Lancet, 1 (1961) 1129.

[23] A. Wang, D.C. Sun, C. Stark, J.H. Dumbleton, Wear 181-183 (1995) 241.

[24] A. Sargeant, T. Goswani, Mater. Des. 27 (2006) 287.

[25] G. Willmann, Adv. Eng. Mater. 3 (2001) 135.

[26] E. Ingham, J. Fisher, Proc Inst Engr J Eng Med 214 (2000) 21.

[27] P. Aspenberg, H. Van der Vis, Clin. Orthop. 352 (1998) 75.

[28] A. McEvoy, M. Jeyam, G. Ferrier, C.E. Evans, J.G. Andrew, Bone 30 (2002) 177.

[29] P. Boutin *et al*., J. Biomed. Mater. Res 22 (1988) 1203.

[30] P. Bizot, R. Nizard, S. Lerouge, F. Prudhommeaux, L. Sedel, J. Orthop. Sci. 5 (2000) 622.

[31] J.E. Nevelos, E. Ingham, C. Doyle, A.B. Nevelos, J. Fisher, J. Mater. Sci. Mater. Med. 12 (2001) 144.

[32] B. Cales, Clinical Orthopaedics and Related Research 379 (2000) 94.

[33] R. C. Dante, C.K. Kajdas, Wear 288 (2012) 27.

[34] R. Kue, A. Sohrabi, D. Nagle, C. Frondoza, D. Hungerford, Biomaterials 20 (1999) 1195.

[35] T.J. Webster, A.A. Patel, M.N. Rahaman, B. Sonny Bal, Acta Biomater. 8 (2012) 4447.

[36] R.M. Taylor, J.P. Bernero, A.A. Patel, D.S. Brodke, A.C. Khandar, J. Bone Joint Surg. Br 92-B (2010) 133.

[37] P.R. Hernández, C. Taboada, L. Leija, V. Tsutsumi, B. Vázquez, F. Valdés-Perezgasga, J.L. Reyes, Sens. Actuators B 46 (1998) 133.

[38] Y.S. Zhou, M. Ohashi, N. Tomita, K. Ikeuchi, K. Takashima, Mater. Sci. Eng., C 5 (1997) 125.

[39] J. Kusaka, K. Takashima, D. Yamane, K. Ikeuchi, Wear 225-229 (1999) 734.

[40] R. Sonntag, J. Reinders, J.P. Kretzer, Acta Biomater. 8 (2012) 2434.

[41] B.S. Bal, A. Khandkar, R. Lakshminarayanan, I. Clarke, A.A. Hoffman, M.N. Rahaman, J. Arthroplasty 24 (2009) 110.

[42] B.S. Bal, M.N. Rahaman, Acta Biomater. 8 (2012) 2889.

[43] L. Tang, C. Tsai, W.W. Gerberich, L. Kruckeberg, D.R. Kania, Bioamterials 16 (1995) 483.

[44] P. Aspenberg *et al*., Biomaterials 17 (1996) 807.

[45] M.J. Papo, S.A. Catledge, Y.K. Vohra, C. Machado, J. Mater. Sci. Mater. Med. 15 (2004) 773.

[46] V. Thomas, B.A. Halloran, N. Ambalavanan, S.A. Catledge, Y.K. Vohra, Acta Bioamater. 8 (2012) 1939.

[47] B. Rezek, E. Ukraintsev, L. Michalíková, A. Kromka, J. Zemek, M. Kalbacova, Diamond Relat. Mater. 18 (2009) 918.

[48] L. Grieten, S.D. Janssens, A. Ethirajan, N. Vanden Bon, M. Ameloot, L. Michiels, K. Haenen, P. Wagner, Phys. Status Solidi A 208 (2011) 2093.

[49] P. Ariano, O. Budnyk, S. Dalmazzo, D. Lovisolo, C. Manfredotti, P. Rivolo, E. Vittone, Eur. Phys. J. E: Soft Matter. Biol. Phys. 30 (2009) 149.

[50] B. Rezek, L. Michalíková, E. Ukraintsev, A. Kromka, M. Kalbacova, Sensors 9 (2009) 3549.

[51] M.D. Fries, Y. K. Vohra, Diamond Relat. Mater. 13 (2004) 1740.

[52] G. Heinrich, T. Grijgler, S.M. Rosiwal, R.F. Singer, Surf. Coat. Technol. 94-95 (1997) 514.

[53] E. Palin, H. Liu, T.J. Webster, Nanotechnology 16 (2005) 1828.

[54] M. Amaral, P.S. Gomes, M.A. Lopes, R.F. Silva, J.D. Santos, M.H. Fernandes, Acta Biomater. 5 (2009) 755.

[55] M. Amaral, P.S. Gomes, A.G. Dias, M.A. Lopes, R.F. Silva, J.D. Santos, M.H. Fernandes, J. Biomed. Mater. Res. A 87 (2008) 91.

[56] W. Jakubowski, G. Bartosz, P. Niedzielski, W. Szymanskia, B. Walkowiak, Diamond Relat. Mater. 13 (2004) 1761.

[57] A. Sokoyowska, J. Rudnicki,T.P. Niedzielski, A. Boczkowska, G. Bogusyawski, T. Wierzchon, S. Mitura, Surf. Coat. Technol. 200 (2005) 87.

[58] K.L. Yarina, D.S. Dandy, E. Jensen, Diamond Relat. Mater. 7 (1998) 1491.

[59] C.S. Abreu, M. Amaral, F.J. Oliveira, A.J.S. Fernandes, J.R. Gomes, R.F. Silva, Diamond Relat. Mater. 15 (2006) 2024.

[60] M. Belmonte, A.J.S. Fernandes, F.M. Costa, F.J. Oliveira, R.F. Silva, Diamond Relat. Mater. 12 (2003) 733.

[61] A. Erdemir, G.R. Fenske, A.R. Krauss, D.M. Gruen, T. McCauley, R.T. Csencsits, Surf. Coat. Technol. 120-121 (1999) 565.

[62] C. Popov, W. Kulisch, M. Jelinek, A. Bock, J. Stmad, Thin Solid Films 494 (2006) 92.

[63] C.S. Abreu, M. Amaral, F.J. Oliveira, J.R. Gomes, R.F. Silva, Diamond Relat. Mater. 18 (2009) 271.

[64] M. Amaral, C.S. Abreu, F.J. Oliveira, J.R. Gomes, R.F. Silva, Diamond Relat. Mater. 17 (2008) 848.

[65] M.N. Yoder, MRS Proceedings 97 (1987) 315.

[66] P.K. Bachmann, R. Meisser, Chem. Eng. News 15 (1989) 24.

[67] A.H. Deutchman, R.J. Partykay, Adv. Mater. Processes 6 (1989) 29.

[68] J. Asmussen, D.K. Reinhard, Diamond Film Handbook, Marcel Dekker Inc., New York 2 (2002).

[69] R.F. Davis, Diamond Films Coat., Noyes Publications, Park Ridge, USA (1993) 435.

[70] B.V. Spitsyn, L.L. Bouilov, B.V. Derjaguin, J. Crystal Growth 52 (1981) 219.

[71] P.E. Pehrsson, F.G. Celii, J.E. Butler, in R.F. Davis editor, Diamond Films and Coatings, Noyes Publications, Park Ridge, New Jersey 3 (1993).

[72] J. E. Butler, H. Windischmann, Mater. Res. Bull. 23 (1998) 22.

[73] H.O. Pierson, Handbook of Carbon, Graphite, Diamond and Fullerenes – Properties, Processing and Applications, Noyes Publications (1993).

[74] S. Matsumoto, in J. P. Dismukes *et al*. editors, Diamond and Diamond-like Films, The Electrochemical Society, Pennington, New Jersey (1989) 50.

[75] M. Hiramatsu, M. Hori, *in* S. Yellampalli editor, Carbon Nanotubes - Synthesis, Characterization, Applications, InTech Publisher, 10 (2011).

[76] P. K. Bachmann, W. Drawe, D. Knight, R. Weimer, R. Meisser, *in* M. Geis, G. H. Johnson, A. R. Badzian editors, Diamond and Diamond-like Materials Synthesis (Extended Abstracts) (1988) 99.

[77] V. J. Trava-Airoldi, E. J. Corat, V. Baranauskas, Key Eng. Mater. 138 (1998) 195.

[78] K. V. Ravi, C. A. Koch, H. S. Hu, A. Joshi, J. Mater. Res. 5 (1990) 2356.

[79] R. T. Rozbicki, V. K. Sarin, Thin Solid Films 332 (1998) 87.

[80] C. V. Deshpande, R. F. Bunshah, J. Vac. Sci. Technol. A 7 (1989) 2294.

[81] Q. Cheng, E. Tam, S. Xu, K. K. Ostrikov, Nanoscale 2 (2010) 594.

[82] M. Atanasova, E. A. D. Carbone, D. Mihailova, E. Benova, G. Degrez, J. J. A. M. van der Mullen, J. Phys. D: Appl. Phys. 45 (2012) 145202.

[83] P. Wood, T. Wydeyen, O. Tsuji, Programs and Abstracts of the First International Conference on New Diamond Science and Technology, New Diamond Forum, Tokyo, Japan (1988) 100.

[84] J. C. Angus, C. C. Hayman, Science 241 (1988) 913.

[85] J. C. Angus, F. A. Buck, M. Sunkara, T. F. Groth, C. C. Hayman, R. Gat, Mater. Res. Bull. 14 (1989) 38.

[86] H. Konig, G. Helwig, Zeitschrift Fur Physik 129 (1951) 491.

[87] K. Kurihara, K. Sasaki, M. Kawarada, N. Koshono, Appl. Phys. Lett. 52 (1988) 437.

[88] http://www.plasma.inpe.br/LAP_Portal/LAP_Site/Text/Plasma_Processing.htm, accessed in November 2013.

[89] S. Matsumoto, M. Hino, T. Kobayashi, Appl. Phys. Lett. 51 (1987) 737.

[90] Q.Y. Han, T.W. Or, Z.P. Lu, J. Heberlein E. Pfender. High rate deposition of diamond using liquid organic precursors in atmospheric plasmas. Proceedings of the 2nd Int. Symp. on Diamond Materials, Pennington, NJ: The Electrochemical Society 91 (1991) 115.

[91] K. Kurihara, K. Sasaki, M. Kawarada, Y Goto, in Y. Tzeng *et al*. (ed.), Application of Diamond Films and Related Materials, Elsevier Science Publishers, (1991) 461.

[92] S. Matsumoto, Y. Sato, M. Kamo, N. Sekata, Jpn. J. Appl. Phys. 21 (1982) L183.

[93] M. Frenklach, *in* R. E. Clausing *et al*. editors. Diamond and diamond-like films and coatings, New York: Plenun Press (1991) 499.

[94] D.S. Dandy, M.E. Coltrin in J. Asmussen, D.K. Reinhard editors, Diamond thin films Handbook, Marcell Dekker, New York, 4 (2001).

[95] B.K. Gupta, B. Bhushan, IEEE Trans. Magn. 31 (1995) 3012.

[96] C.H. Wu, M.A. Tamor, T.J. Potter, E.W. Kaiser, Diamond, SiC and Related Wide Bandgap Semiconductors, in J. T. Glass, R. Meisser, N. Fujimori editors Mater. Res. Soc. Proc., Pittsburg, Pennsylvania,USA, 162 (1990).

[97] V.J. Trava-Airoldi, E.J. Corat, A.F.V. Pena, N.F. Leite, V. Baranauskas, M.C. Salvadori, Diamond Relat. Mater. 4 (1995) 1255.

[98] J. Herlinger, Thin Solid Films 501 (2006) 65.

[99] T. Hao, H. Zhang, C. Shi, G. Han, Surf. Coat. Technol. 201 (2006) 801.

[100] S. Schwarz, S.M. Rosiwal, M. Frank, D. Breidt, R.F. Singer, Diamond Relat. Mater. 11 (2002) 589.

[101] C. Popov, S. Bliznakov, W. Kulisch, Diamond Relat. Mater. 16 (2007) 740.

[102] X. Liang, L. Wang, H. Zhu, D. Yang, Surf. Coat. Technol. 202 (2007) 261.

[103] G. Soto, G. Silva, O. Contreras, Surf. Coat. Technol. 201 (2006) 2733.

[104] J. Wei, Y. Tzeng, Diamond Films Technol. 5 (1995) 79.

[105] P.M. Menon *et al*., Diamond Relat. Mater. 8 (1999) 101.

[106] G.H. Song, J.H. Yoon, H.S. Kim, C. Sun, R.F. Huang, L.S. Wen, Mater. Lett. 56 (2002) 832.

[107] L. Schäfer, M. Höfer, R. Kröger, Thin Solid Films 515 (2006) 1017.

[108] S.A. Redman, C. Chung, M.N.R. Ashfold, Diamond Relat. Mater. 8 (1999) 1383.

[109] M.S. Kang, W.S. Lee, Y.J. Baik, Thin Solid Films 398 –399 (2001) 175.

[100] S. Yang, Z. He, Q. Li, D. Zhu, J. Gong, Diamond Relat. Mater. 17 (2008) 2075.

[111] A. Amorim, P.A.P. Nascente, V.J. Trava-Airoldi, E.J. Corat, A.R. Alves, J.R. Moro, Vacuum 83 (2009) 1054.

[112] Y.F. Zhang, F. Zhanga, Q.J. Gao, X.F. Peng, Z.D. Lin, Diamond Relat. Mater. 10 (2001) 1523.

[113] X. Qi, Z. Chen, Z. Wang, J. Mater. Sci. Technol. 19 (2003) 235.

[114] X. Bourrat, Structure in Carbon and Carbon Artifacts, in H. Marsh, F.R. Reinoso editors, Sciences of Carbon Materials, Publicaciones Universidad de Alicante (2000).

[115]https://www.uwgb.edu/DutchS/Petrology/Diamond%20Structure.HTM, accessed in January 2014.

[116] J. Robertson, Mat. Sci. Eng. R 37 (2002) 129.

[117] A.C. Ferrari, J. Robertson, Phys. Rev. B 63 (2001) 121405.

[118] H. Kuzmany, R. Pfeiffer, N. Salk, B. Günther, Carbon 42 (2004) 911.

[119] R.J. Nemanich, J.T. Glass, G. Lucovsky, R.E. Shroder, J. Vac. Sci. Technol. A 6 (1988) 1783.

[120] M. Roy, V.C. George, A.K. Dua, P. Raj, S. Schulze, D.A. Tenne, G. Salvan, D.R.T. Zahn, Diamond Relat. Mater. 11 (2002) 1858.

[121] D.S. Knight, W.B. White, J. Mater. Res. 4 (1989) 385.

[122] A.C. Ferrari, J. Robertson, Phys. Rev. B 64 (2001) 075414.

[123] M. Rybachuk, J.M. Bell, Carbon 47 (2009) 2481.

[124] S.R. Sails , D.J. Gardiner, M. Bowden, J. Savage, D. Rodway, Diamond Relat. Mater. 5 (1996) 589.

[125] G. Gouadec, P. Colomban, Prog. Cryst. Growth Charact. Mater. 53 (2007) 1.

[126] K.E. Spear, J.P. Dismukes, Synthetic Diamond, John Wiley & Sons, New York (1994) 4.

[127] E. Gheeraert, S. Koizumi, T. Teraji, H. Kanda, M. Nesladek, Diamond Relat. Mater. 9 (2000) 948.

[128] F. Deuerlera, H. Grunerb, M. Pohlc, L. Tikanac, Surf. Coat. Technol. 142–144 (2001) 674.

[129] H. Okazaki *et al*., Appl. Phys. Lett. 98 (2011) 082107.

[130] M. Werner, R. Locher, Rep. Prog. Phys. 61 (1998) 1665.

[131] F. Qin, J. Hu, Y.K. Chou, R.G. Thompson, Wear 267 (2009) 991.

[132] P.U. Arumugam, A.P. Malshe, S.A. Batzer, Surf. Coat. Technol. 200 (2006) 3399.

[133] H. Gomez *et al*., J. Mater. Process. Technol. 212 (2012) 523.

[134] E. Salgueiredo *et al*., Diamond Relat. Mater 18 (2009) 264.

[135] K. Bouzakis, N. Michailidis, G. Skordaris, E. Bouzakis, D. Biermann, R. M'Saoubi, CIRP Ann. 61 (2012) 703.

[136] K. Meykens, K. Haenen, M. Nesladek, L.M. Stals, C.S.J. Pickles, R.S. Sussmann, Diamond Relat. Mater. 9 (2000) 1021.

[137] Y. Kawano, S. Chiba, A. Inoue, Rev. Sci. Instrum. 75 (2004) 279.

[138] J. Li *et al*., J. Appl. Phys. 92 (2002) 6275.

[139] M.B. Assouar, O. Elmazria, P. Kirsch, P. Alnot, V. Mortet, C. Tiusan, J. Appl. Phys. 101 (2007) 114507.

[140] O. Ternyak *et al*., J. Appl. Phys. 98 (2005) 123522.

[141] K. Subramanian, W.P. Kang, J.L. Davidson, J. Vac. Sci. Technol. B 25 (2007) 532.

[142] G.B. Kim *et al*., Appl. Phys. Lett. 89 (2006) 181106.

[143] J.Y. Kim *et al*., Electron. Lett. 43 (2007) 105.

[144] H. Liu, D.S. Dandy. Diamond Relat. Mater. 4 (1995) 1173.

[145] Y. Lifshitz, Th. Kohler, Th. Frauenheim, I. Guzmann, A. Hoffman, R.Q. Zhang, X.T. Zhou, S.T. Lee, Science 297 (2002) 1531.

[146] W. A. Yarbrough, R. Messier, Science 247 (1990) 688.

[147] R. Lux, R. Haubner, Pure Appl. Chem. 66 (1994) 1783.

[148] R. S. Edelstein, I. Gouzman, M. Folman, S. Rotter, A. Hoffman, Diamond Relat. Mater. 8 (1999) 139.

[149] T. Hao, C. Shi, Diamond Relat. Mater. 13 (2004) 465.

[150] Y.K. Liu, P.L. Tso, I.N. Lin, Y. Tzeng, Y.C. Chen, Diamond Relat. Mater. 15 (2006) 234.

[151] W. Kulisch, C. Popov, Phys. Stat. Sol. A 203 (2006) 203.

[152] G. Cicala, P. Bruno, F. Bénédic, F. Silva, K. Hassouni, G.S. Senesi, Diamond Relat. Mater. 14 (2005) 421.

[153] P. Ascarelli, S. Fontana, Appl. Surf. Sci., 64 (1993) 307.

[154] T. Okubo, S. Nakata, H. Nakamoto, M. Ihara, H. Komiyama, Jpn. J. Appl. Phys. 32 (1993) L1767.

[155] J.W. Kim, Y.J. Baik, K.Y. Eun, D.N. Yoon, Thin Solid Films 212 (1992) 104.

[156] M. Sommer, F.W. Smith, J. Mater. Res. 5 (1990) 2433.

[157] J.E. Butler, F.G. Celii, Proc. Electrochem. Soc. 89 (1989) 317.

[158] S.J. Harris, Appl. Phys. Lett. 56 (1990) 2298.

[159] M. Frenklach, K.E. Spear, J. Mat. Res. 3 (1988) 133.

[160] F.G. Celii, P.E. Pehrsson, H.T. Wang, J.E. Butler, Appl. Phys. Lett. 52 (1988) 2043.

[161] Ch. E. Wild, N. Herres, P. Koidl, J. Appl. Phys. 68 (1990) 973.

[162] K.L. Choy, Prog. Mater. Sci. 48 (2003) 57.

[163] N. Toprani, S.A. Caledge, R. Thompson, Y.K. Vohra, J. Mater. Res. 15 (2000) 1052.

[164] D.M. Gruen, S. Liu, A.R. Krauss, X. Pan, J. Appl. Phys. 75 (1994) 1758.

[165] X. Liu *et al*., Diamond Relat. Mater. 16 (2007) 1463.

[166] P.W. May, M.N.R. Ashfold, Y.A. Mankelevich, J. Appl. Phys. 101 (2007) 053115.

[167] A.A. Talin, L.S. Pan, K.F. McCarty, T.E. Felter, H.J. Doerr, R.F. Bunshah, W.K. Wong, X.M. Meng, C.Y. Chan, I. Bello, Y. Lifshitz, S.T. Lee, Appl. Phys. Lett. 83 (2003) 3365.

[168] E.C. Almeida, A.F. Azevedo, M.R. Baldan, N.A. Braga, J.M. Roselen, N.G. Ferreira, Chem. Phys. Lett. 438 (2007) 47.

[169] O.A. William, S. Curat, J. Gerbi, D.M. Gruen, R.B. Jackman, Appl. Phys. Lett. 85 (2004) 1680.

[170] O.A. Williams, M. Nesladek, M. Daenen, S. Michaelson, A. Hoffman, E. Osawa, K. Haenen, R.B. Jackman, Diamond Relat. Mater. 17 (2008) 1080.

[171] R. Haubner, B. Lux, Int. J. Refract. Met. Hard Mater. 20 (2002) 93.

[172] T. Yang, C. Cheng, M. Wong, Diamond Relat. Mater. 10 (2001) 2161.

[173] M. You, F. Chau-Nan Hong, Y. Jeng, S. Huang, Diamond Relat. Mater. 18 (2009) 155.

[174] T. Liu, D. Raabe, Appl. Phys. Lett. 94 (2009) 021119.

[175] S.A. Rakha, Z. Xintai, D. Zhu, Y. Guojun, Curr. Appl. Phys. 10 (2010) 171.

[176] S. Gupta, O.A. Williams, R.J. Patel, K. Haenen, J. Mater. Res. 21 (2006) 3037.

[177] T. Wang, H.W. Xin, Z.M. Zhang, Y.B. Dai, H.S. Shen, Diamond Relat. Mater. 13 (2004) 6.

[178] J.R. Rabeau, P. John, J.I.B Wilson, Y. Fan, J. Appl. Phys. 96 (2004) 6724.

[179] T. Lin, G.Y. Yu, A.T.S. Wee, Z.X. Shen, K.P Loh, Appl. Phys. Lett. 77 (2000) 2692.

[180] Y. Tzeng, Y.K. Liu, Diamond Relat. Mater. 14 (2005) 261.

[181] T.G. McCauley, D.M. Gruen, A.R. Krauss, Appl. Phys. Lett. 73 (1998) 1646.

[182] D. Zhou, T.G. McCauley, L.C. Qin, A.R. Krauss, D. Gruen, J. Appl. Phys. 83 (1998) 540.

[183] P.W. May, J.A. Smith, Yu. A. Mankelevich, Diamond Relat. Mater. 15 (2006) 345.

[184] M. Marton, T. Iák, M. Vesely´, M. Vojs, M. Michalka, J. Bruncko, Vacuum 82 (2008) 154.

[185] P.W. May, J.N. Harvey, J.A. Smith, J. App. Phys. 99 (2006) 104907.

[186] S.M. Huang, F.C.N. Hong, Surf. Coat. Technol. 200 (2006) 3160.

[187] V. Baranauskas, B.B. Li, A. Peterlevitz, M.C. Tosin, S.F. Durrant, J. Appl. Phys. 85 (1999) 7455.

[188] Y. Fu, J. Wei, A.W. Batchelor, J. Mater. Process. Technol. 99 (2000) 231.

[189] S. Takeuchi, O. Sumitsugu, M. Murakawa, Thin Solid Films 398 –399 (2001) 238.

[190] K. Holmberg, H. Ronkainen, A. Matthews, Ceram. Int. 26 (2000) 787.

[191] S.J. Bull, A.M. Jones, Surf. Coat. Technol. 78 (1996) 173.

[192] P. Panjan, M. Čekada, B. Navinšek, Surf. Coat. Technol. 174 –175 (2003) 55.

[193] H. Chai, G. Ravichandran, Int. J. Fract. 145 (2007) 299.

[194] S. Hogmark, S. Jacobson, M. Larsson, Wear 246 (2000) 20.

[195] H. Holleck, H. Schulz, Surf. Coat. Technol. 36 (1988) 707.

[196] S. PanDey, S.C. Deevi, Mater. Sci. Eng., A Struct. Mater., Prop. Microstruct. Process. 342 (2003) 58.

[197] H. Holleck, V. Schier, Surf. Coat. Technol. 76–77 (1995) 328.

[198] G.S. Was, T. Foecke, Thin Solid Films 286 (1996) 1.

[199] S. Zhang, D. Sun, Y. Fu, H. Du, Surf. Coat. Technol. 198 (2005) 2.

[200] M. Kadlečíková *et al.*, Microelectron. J. 38 (2007) 20.

[201] Q. Wei, Z.M. Yu, M.N.R. Ashfold, J. Ye, L. Ma, Appl. Surf. Sci. 256 (2010) 4357.

[202] S.C. Tjong, H. Chen, Mater. Sci. Eng. R. 45 (2004) 1.

[203] R. Ikeda, M. Hayashi, A. Yonezu, T. Ogawa, M. Takemoto, Diamond Relat. Mater. 13 (2004) 2024.

[204] F.A. Almeida, M. Amaral, F.J. Oliveira, A.J.S. Fernandes, R.F. Silva, Vacuum 81 (2007) 1443.

[205] C.S. Abreu, E. Salgueiredo, F.J. Oliveira, A.J.S. Fernandes, R.F. Silva, J.R. Gomes, Wear 265 (2008) 1023.

[206] M. Vojs *et al*., Diamond Relat. Mater. 14 (2005) 613.

[207] S. Takeuchi, M. Kojima, S. Takano, K. Kazutaka, M. Murakawa, Thin Solid Films 469-470 (2004) 190.

[208] R. Dumpala, M. Chandran, N. Kumar, S. Dash, B. Ramamoorthy, M.S. Ramachandra Rao, Int. J. Refract. Met. Hard Mater. 37 (2013) 127.

[209] A. Köpf, R. Haubner, B. Lux, Int. J. Refract. Met. Hard Mater. 20 (2002) 107.

[210] B. Shen, F. Sun, Z. Zhang, H. Shen, S. Guo, Trans. Nonferrous Met. Soc. China 23 (2013) 161.

[211] L. Schäfer, M. Höfer, R. Kröger, Thin Solid Films 515 (2006) 1017.

[212] F. Sun, Y. Ma, B. Shen, Z. Zhang, M. Chen, Diamond Relat. Mater. 18 (2009) 276.

[213] F.H. Sun, B. Shen, Surf. Eng. 19 (2003) 461.

[214] N. Jiang, K. Sugimoto, K. Nishimura, Y. Shintani, A. Hiraki, J. Cryst. Growth 242 (2002) 362.

[215] L.W. Resende, E.J. Corat, V.J. Trava-Airoldi, N.F. Leite, Diamond Relat. Mater 10 (2001) 332.

[216] H.W. Xin *et al*., Diamond Relat. Mater. 11 (2002) 228.

[217] N. Nesladek, K. Vandierendonck, C. Quaeyhaegens, M. Kerkhofs, L.M. Stals, Thin Solid Films 270 (1995) 184.

[218] V. Vander, Metallography Principles and Practice, Material Science and Engineering Series, McGraw-Hill, Inc., New York (1984).

[219] W.C Oliver, G.M. Pharr, J. Mater. Res. 17 (1992) 1564.

[220] L. Marsavina, T. Sadowski, Int. J. Fract. 148 (2007) 79.

[221] M. Belmonte, A.J.S. Fernandes, F.M. Costa, F.J. Oliveira, R.F. Silva; Diamond Relat. Mater. 12 (2003) 733.

[222] D.B. Marshall, A.G. Evans, J. Appl. Phys. 56 (1984) 2632.

[223] H.D. Espinosa, B. Peng, B.C. Prorok, N. Moldovan, O. Auciello, J.A. Carlisle, D.M. Gruen, D. C. Mancini, J. Appl. Phys. 94 (2003) 6076.

[224] I.M. Hutchings, Tribology – Friction and Wear of Engineering Materials, Edward Arnold, United Kingdom (1992).

[225] D.W. Wheeler, R.J.K. Wood, Wear 233–235 (1999) 306.

[226] S. Amirhaghi, H.S. Reehal, R.J.K. Wood, D.W. Wheeler, Surf. Coat. Technol. 13 (2001) 126.

[227] J.C. Bareiβ, G. Hackl, N. Popovska, S.M. Rosiwal, R.F. Singer, Surf. Coat. Technol. 20 (2006) 718.

[228] H.C. Meng, K.C. Ludema, Wear, 181-183 (1995) 443.

[229] A.V. Levy, Solid Particle Erosion and Erosion-Corrosion of Materials , ASM International, Materials Park, Ohio (1995).

[230] G. Sundararajan, P.G. Shewmon, Wear 149 (1991) 111.

[231] A.V. Levy, N. Jee, P. Yau, Wear 117 (1987) 115.

[232] I. Finnie, Wear 186-187 (1995) 1.

[233] B.E. MacMillin, C.D. Roll, P. Funkenbusch, Wear 269 (2010) 875.

[234] B. Karunamurthy, M. Hadfield, C. Vieillard, G. Morales, Tribol. Int. 43 (2010) 2251.

[235] H.M. Clark, K.K. Wong, Wear 186-187 (1995) 454.

[236] Q. Chen, D.Y. Li, Wear 254 (2003) 203.

[237] N. Symonds, B.G. Mellor, R.J.K. Wood, S. Groves, Mater. Des. 20 (1999) 179.

[238] R.S. Lynn, K.K. Wong, H.M. Clark, Wear 149 (1991) 55.

[239] H.M. Clark, R.B. Hartwick, Wear 248 (2001) 55.

[240] G.B. Stachowiak, G.W. Stachowiak, Wear 241 (2000) 214.

[241] F.X. Lu, Q. He, S.B. Guo, F.L. Zhang, Y.M. Tong, Diamond Relat. Mater. 19 (2010) 936.

[242] I.P. Shapiro, R.I. Todd, J.M. Titchmarsh, S.G. Roberts, J. Eur. Ceram. Soc. 31 (2011) 85.

[243] W.D. Cellota *et al*., Wear 263 (2007) 278.

[244] I. Hussainova, M. Antonov, A. Zikin, Tribol. Int. 46 (2012) 254.

[245] M. Divakar, V.K. Agarwal, and S.N. Singh, Wear 259 (2004) 110.

[246] J.G. Chacon Nava, F.H. Stott, M.M. Stack, Corros. Sci. 35 (1993) 1045.

[247] S.G. Sapate, A.V.R. Rao, Mater. Manuf. Processes 17 (2002) 187.

[248] A.G. Evans, Impact damage and erosion in infrared materials. In Emerging optical materials, San Diego, CA, United States (1981) 99.

[249] I. Finnie, Wear 3 (1960) 87.

[250] A.C. Fischer-Cripps, Introduction to contact mechanics, Springer-Verlag, Berlin (2007).

[251] G. Schmitt Jr., Wear Control Handbook: Liquid and Solid Particle Impact Erosion, American Society of Mechanical Engineers (1980) 231.

[252] J.E. Field, Q. Sun, H. Gao, G.H. Jilbert, Wear 186–187 (1995) 195.

[253] A. Alahelisten, P. Hollman, S. Hogmark, Wear 177 (1994) 159.

Chapter II

Development and characterization of mono-, bi- and multilayered diamond coatings on Si_3N_4

This chapter starts with an overview on silicon nitride based ceramics used as substrates for diamond deposition, Chapter II.1.

The work on the optimization of the growth parameters of the new home-built HFCVD reactor, the development and characterization of the mono-, bi- and multilayered coatings as well the characterization using HRTEM, STEM-EDX and EELS of the interfaces between layers in the multilayered structure were reported on three SCI papers, presented here as three main sections:

- Chapter II.2. reports the use of the Taguchi Matrix approach for the experimental design of the study of the combined effects of gas composition, total gas pressure, total mass flow and substrate temperature on the quality and growth rate of CVD diamond films in a new home-built HFCVD reactor, used throughout this thesis.

- Chapter II.3. is focused on a comparative study of different combinations of MCD and NCD varieties: monolayers, bi-, tri- and fourfold layers. The Hertzian stress states under static indentation were estimated and compared on the basis of the von Mises stress parameter, revealing the superior performance of the multilayered composite structures.

- The characterization with high detail using HRTEM, STEM-EDX and EELS done on the interfaces of the multilayered diamond films is presented in Chapter II.4. The formation of a thin precursor graphitic film in the transition from the MCD to NCD layer and the presence of WC nanoparticles in the interfaces due to contamination from the filament are the main issues addressed in this section.

II.1. Silicon nitride ceramics

In order to minimize thermal mismatch, a key issue for good adhesion, a substrate material with a thermal expansion coefficient similar to that of diamond ($0.8x10^{-6}$ $K^{-1}<\alpha<4.5x10^{-6}$ K^{-1}, for 20<T<800 °C) must be selected. One of the most suitable materials is Si_3N_4 ceramic ($2.9x10^{-6}$ $K^{-1}<\alpha<3.6x10^{-6}$ K^{-1}, for 20<T<1500 °C) [1, 2]. XRD results proved that MCD intrinsic stresses are nearly zero (~0.15 GPa), which is corroborated by a negligible μ-Raman diamond peak deviation [3]. Si_3N_4 ceramic is a refractory material that endures the CVD diamond deposition temperatures and possesses a carburising nature that favours diamond nucleation and chemical bonding. Work by the proponent group demonstrated the excellent MCD diamond film adhesion on Si_3N_4 ceramic substrates [4].

Ceramics

Hill [5] reports “ceramic” as a general designation for four groups of inorganic materials which are produced by the application of pressure and heat to their base ingredients. These materials have a wide range of applications, from building blocks to devices used in medicine. The four groups are:

- Bonded ceramics: which oxide, nitride or carbide crystals are bonded together by a glassy matrix;
- Amorphous ceramics: also known as glasses;
- Cements: a group that may contain either crystalline or amorphous phases;
- Crystalline ceramics as single phase materials [5].

In many cases, they are also used as coatings due to their excellent wear and high temperature mechanical resistance, among other properties. In this wide class of materials we can find rocks and minerals glasses, cement and concrete, traditional and engineering ceramics and ceramic composites. Ceramics are characterized as brittle solids with typical fracture toughness ranging from 1 to 12 $MPa.m^{1/2}$ and high elastic

modulus (usually much greater than metals). They also possess good creep resistance, chemical inertness high melting point, high hardness and exceptional compressive strength, but are very weak in torsion and bending. Their coefficient of thermal expansion and coefficient of self-friction are lower than those of metals, which means lower running temperatures and less consumption of lubricant if used in engines. Ceramic parts can be produced in diverse ways. Their manufacture starts by powder consolidation into green compacts, using different techniques such as mechanical pressing, extrusion, slip casting or injection moulding. Once compacted, the material is sintered to bring out the full physical, chemical properties, namely the thermomechanical ones [5].

Classical ceramics materials consist mostly of oxides, which are mainly ionic materials. The bonds are nondirectional and the sintering of these ceramics occurs by volume or grain boundary diffusion, enhanced by vacancy formation, due to non-stoichiometry. In other ceramics, like silicon nitride (Si_3N_4), the highly covalent and strongly directional chemical bonds cause very low self-diffusion coefficients. Therefore, the conditions for the bulk diffusion are unfavourable and sintering of such covalent substances is usually difficult [6]. In fact, silicon nitride ceramics is a generic term that covers a variety of alloys of Si_3N_4, that incorporate additional compounds (sintering aids) necessary for the complete densification of the Si_3N_4 starting powder. These are heterogeneous, multicomponent materials characterized by the inherent properties of the crystalline modifications of α- and β- Si_3N_4 and the significant influence of the densification additives. [7]

Properties and applications of Si_3N_4

Silicon nitride ceramics have been developed for use at higher temperatures than those allowed by metallic superalloys [8]. Specifically, silicon nitride was developed for use in gas turbines that operated at elevated temperatures and to obtain greater efficiencies in space, automotive and electric power generating applications [9]. Si_3N_4 is a ceramic material that possesses an outstanding set of chemical, physical and mechanical properties, [6, 7, 10] such as wear and corrosion resistance, resistance to thermal shock, high hardness and fracture toughness, high

temperature stability, chemical inertness, low self-friction coefficient, high Young´s modulus and resistance to oxidation.

Some properties of the Si_3N_4 ceramics are shown in Table 1 [1, 7, 11].

Table 1 - Properties of the Si_3N_4 ceramics [1, 11, 12].

Cristal structure	
α-phase, hexagonal	a-axis: 0.775-0.777 nm c-axis: 0.516-0.569 nm c/a ~ 0.70
β-phase, hexagonal	a-axis: 0.759-0.761 nm c-axis: 0.271-0.292 nm c/a ~ 0.37
Decomposition temperature (°C)	1900
Theoretical density ($g.cm^{-3}$)	
α-phase	3.168 – 3.188
β-phase	3.19 – 3.202
Density ($g.cm^{-3}$)	
Dense Si_3N_4	90-100% th.d.*
Reaction-bonded Si_3N_4	70-88% th.d.
Coefficient of thermal expansion (20-1500 °C) (10^{-6} °C^{-1})	2.9 – 3.6
Thermal conductivity (RT) ($Wm^{-1}K^{-1}$)	
Dense Si_3N_4	15-50
Reaction-bonded Si_3N_4	4-30
Thermal diffusivity (RT) (cm^2sec^{-1})	
Dense Si_3N_4	0.08-0.29
Reaction-bonded Si_3N_4	0.02-0.22
Specific heat (Jkg^{-1} °C^{-1})	700
Electrical resistivity (RT) (Ωcm)	~10^{14}
Microhardness (Vickers, MPa)	1600-2200
Young´s modulus (RT) (GPa)	
Dense Si_3N_4	300-330
Reaction-bonded Si_3N_4	120-220
Flexural Strenght (RT) (MPa)	
Dense Si_3N_4	400-950
Reaction-bonded Si_3N_4	150-350
Fracture toughness ($MPa.m^{1/2}$)	
Dense Si_3N_4	3.4 - 8.2
Reaction-bonded Si_3N_4	1.5 - 2.8
***** theoretical density is dependent on the type and composition of consolidation aids (th.d. of pure Si_3N_4= 3.2 $g.cm^{-3}$)	

Due to this unique set of properties, Si_3N_4 can be used in a wide range of applications [6, 7], namely:

- Cutting tools;
- Ball bearings and sealing parts;
- Engine components;
- Metal forming and processing devices;
- Gas turbines;
- Automotive industry (fuel injector parts, turbocharger rotors,…);
- Aircraft engines (ceramic turbine nozzles, cutter pins,…);
- Space technology (turbo pump of the space nozzle, radar windows for rockets);
- Household (cooking plates with integrated heater).

Because of silicon nitride strength at elevated temperatures, it appears to be a good candidate for tribological applications such as roller bearings, presenting a better behaviour than those of steel. [11, 13]. A drawback in the application of silicon nitride parts is that they cannot be applied in oxidizing environments, for temperatures above 1200-1300 °C. Above these temperatures, the material creeps and is oxidized, even in the bulk, because the sintering aids (like MgO, Al_2O_3 or Y_2O_3) react with SiO_2 that is formed during the oxidation reaction, originating low viscosity silicates [6, 14].

Crystalline structures of Si_3N_4

Silicon nitride has the composition Si_3N_4 with a predominant covalent bonding (70% covalent) with a density of 3.2 $g.cm^{-3}$ [6, 7]. The most common crystalline modifications of Si_3N_4 are α-Si_3N_4 and β-Si_3N_4, produced under normal nitrogen pressure (Table 1). A third one is γ-Si_3N_4, present at high temperature and pressure. The α modification is dominant in the commonly produced Si_3N_4 powders. The lattice parameters of the α phase depend on the content of oxygen dissolved in the structure. The melting point of α-Si_3N_4 was observed under a nitrogen pressure of 120 MPa and a temperature of 2560 K. The β modification is the main constituent of most Si_3N_4

ceramics. The atomic coordinates in the unit cell are kept almost constant up to 1633 K. The solubility of oxygen in the β structure can reach a maximum of 0.258% in the absence of other elements [6, 7]. The hexagonal crystal structures of α-Si_3N_4 and β-Si_3N_4 are represented in Figure 1.

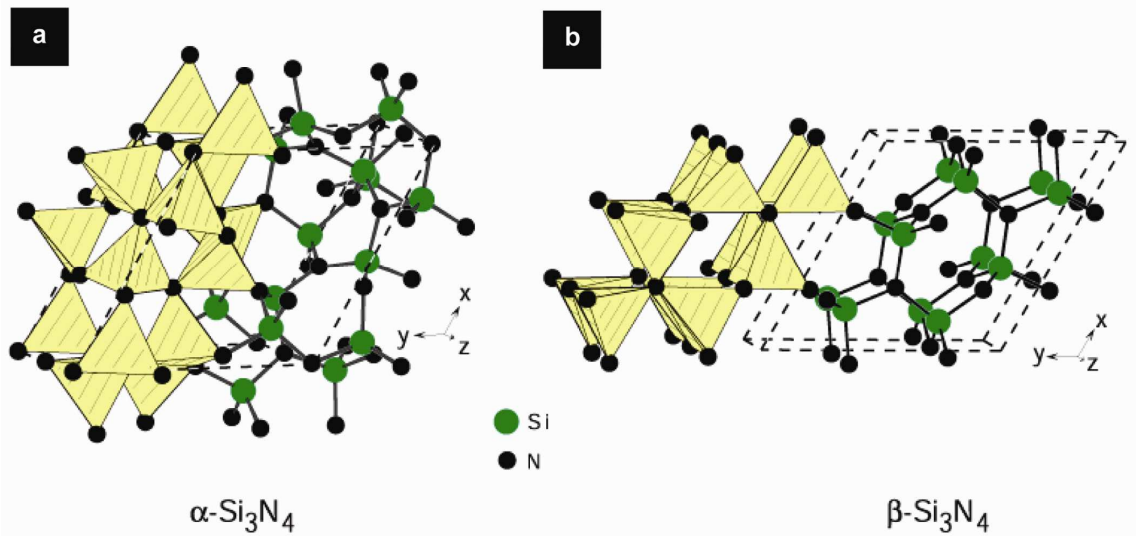

Figure 1 - Crystal structure of α-Si_3N_4 (a) and β-Si_3N_4 (b) in a view nearly along the z-axis [15].

The cubic γ modification was registered under a temperature higher than 2000 K and a pressure of 15 GPa, using the laser heating technique in a diamond cell. In fact, this modification is often designated as the c-modification, in comparison to cubic boron nitride (c-BN) [6]. This cubic modification was reported in 1999 by Zerr *et al.* [16], with results showing that this structure was metastable at ambient pressure, for a temperature that could go up to 700 K.

β- Si_3N_4 ceramics were reported as providing the best fracture resistance through the development of a microstructure that contains whisker-like grains, capable of deflecting or bridging a crack [14, 16].

Preparation of Si_3N_4 substrates

Almost all the commercial grades of silicon nitride are made with sintering aids e.g., Al_2O_3, MgO, Y_2O_3 and SiO_2 that support the liquid-phase sintering at temperatures ranging from 1650 °C to 2080 °C. The main role of the sintering aids is to react with

Si_3N_4 particles and its adhered silica to produce a liquid at high temperatures. This liquid allows mass transport trough solution-reprecipitation to consolidate the solid silicon nitride by rearrangement. The Si_3N_4 powder (α or β) dissolves into a transient liquid phase, precipitating in the polymorph β-Si_3N_4, which is stable at high temperature. The liquid phase sintering favours the acicular growth of the β-Si_3N_4 crystals. With the cooling process the liquid phase leads to an amorphous phase, present in pockets at triple junctions and in films along the grain boundaries, or to crystalline oxynitrides [8].

The first stage of the experimental work of this thesis was thus devoted to the processing of dense silicon nitride based ceramics, in order to produce convenient substrates for CVD diamond deposition. The mixture was prepared using commercial powders: α-Si_3N_4 (Starck grade C), Y_2O_3 (Starck grade M11) and Al_2O_3 (ALCOA CT-3000SG) in a 89.3/7.0/3.7% weight proportion, respectively. Powders were them planetary milled (Retsch PM 400) for 8h in a isopropyl alcohol media using Si_3N_4 balls as milling agents in agate jars, and the homogeneous suspension was dried at 60 °C for 48h and sieved with a 100 μm mesh.

After consolidation of the powder by uniaxial pressing at 30 MPa, the substrates were isostatically pressed at 200 MPa and then placed in a graphite crucible covered by a powder bed of Si_3N_4/BN (1:1). The sintering was performed in a graphite furnace (Thermal Technologies Inc.) at 1750 °C for 2 h in a nitrogen atmosphere.

References

[1] G. Ziegler, J. Heinrich, G. Wotting, J. Mater. Sci. 22 (1987) 3041.

[2] V.G. Ralchenko *et al.*, Diamond Relat. Mater. 4 (1995) 754.

[3] M.R. Soares, M. Belmonte, R.F. Silva, J. Appl. Phys. 94 (2003) 5633.

[4] M. Amaral, F.J. Oliveira, M. Belmonte, A.J.S. Fernandes, F.M. Costa, R.F. Silva, Surf. Eng. 19 (2003) 410.

[5] D. Hill, Design Engineering of Biomaterials for Medical Devices, John Wiley & Sons (1998).

[6] W. Dressler, R. Riedel, Int. Journal of Refractory Metals and Hard Materials 15 (1997) 13.

[7] G. Petzow, M. Herrmann, Silicon Nitride Ceramics, Structure and Bonding, Springer-Verlag Berlin Heidelberg 102 (2002).

[8] J.L. Besson, T. Rouxel, P. Goursat, Scripta Materialia 39 (1998) 1339.

[9] S.M. Wiederhorn, B.J. Hockey, J.D. French, J. Am. Ceram. Soc. 19 (1999) 2273.

[10] A. Olszyna, J. Smolik, J. Thin Solid Films 459 (2004) 224.

[11] S. Hampshire, Journal of Materials and Manufacturing Engineering 24 (2007).

[12] G. Ziegler, J. Heinrich, G. Wötting, J. Mater. Sci. 22 (1987) 3041.

[13] J. Takadoum, H. Houmid-Bennani, D. Mairey, J. Eur. Ceram. Soc. 18 (1999) 553.

[14] A. Rosenflanz, Curr. Opin. Solid State Mater. Sci. 4 (1999) 453.

[15] Handbook of Ceramic hard Materials, Ralf Riedel Editor, Wiley – VCH, Edition 1 (2000) 24.

[16] A. Zerr *et al.*, Nature 400 (1999) 340.

II.2. HFCVD Diamond Deposition Parameters Optimized by a Taguchi Matrix

E. Salgueiredo[1], M. Amaral[2], M.A. Neto[1], A.J.S. Fernandes[2], F.J. Oliveira[1], R.F. Silva[1]

[1]CICECO, Ceramics and Glass Eng. Dep., University of Aveiro, Campus de Santiago, P-3810-193 Aveiro, Portugal
[2]I3N, Physics Department, University of Aveiro, Campus de Santiago, P-3810-193 Aveiro, Portugal

Vacuum, 85 (2011) 701-704
DOI:10.1016/j.vacuum.2010.10.010

Abstract

A Taguchi Matrix was used for the experimental design to study the CVD diamond deposition parameters in a cold-wall HFCVD reactor. Gas composition, total gas pressure, total mass flow and substrate temperature were considered as controllable factors, and three levels for each of these factors were selected, in a L9 orthogonal array. A new Figure-of-Merit (FOM) is proposed to assess the best combination of film properties: grain size, residual stress, structural quality and growth rate. Substrate temperature affects mostly grain size and diamond quality, while methane content mostly determines residual stresses and the growth rate. The latter is also mainly affected by the total pressure as well as is grain size, while total gas flow has a neutral effect. Under the limits of deposition conditions, the best FOM is obtained at the highest total gas pressure and mass flow, average CH_4 content, and lowest substrate temperature.

Keywords: CVD diamond, Taguchi matrix, HFCVD.

1. Introduction

Modifications made to Hot Filament Chemical Vapour Deposition (HFCVD) reactor chambers for diamond deposition, namely in the chamber volume and gas flow trajectories inside the reactor and over the substrates, deeply account for local chemistry and temperature alterations that affect the nucleation, growth and morphology of the diamond films.

Gas composition, total gas pressure, total mass flow and substrate temperature are the main parameters that influence the film quality and deposition rate, thus deserving a careful evaluation [1], especially their combined influence. The Taguchi Matrix appears as a very adequate approach to rapidly achieve a practical outcome. It is a powerful tool for the study of the main variables and interactions in a minimum number of trials and it has been used in study of deposition parameters in many CVD methods [2, 3].

Many diamond features can characterize the film quality, but, for tribological applications, surface roughness, film cohesion and adhesion to the substrate are crucial. These are related to grain size, diamond purity and residual stress properties that are further aggregated in a new figure of merit (FOM) that also includes the film growth rate. The study of the FOM dependence on the deposition parameters using the Taguchi Matrix constitutes the focus of the present work.

2. Experimental

(100) oriented silicon (Si) samples (10x10x1 mm^3) were used as substrates for diamond deposition by HFCVD. Before deposition, the samples were scratched to improve the nucleation density by a 1 μm diamond powder suspension ultrasonically agitated for 1 hour.

A home-built 3 kW HFCVD reactor, comprising cylindrical water cooled stainless steel base and chamber, with a 6x5 cm^2 deposition area, was used for film growth. Six tungsten wires (∅=0.25 mm, 7.5 mm length) were kept at a constant distance of ~7 mm from the substrate. The gases were supplied through mass flow controllers. The filament temperature was measured with a two-colour pyrometer while the substrate

temperature was measured by a K-type thermocouple inserted on the substrate holder, placed on the back side of the substrate. The samples were heated at approximately 630 °C by thermal radiation. The additional heating of the substrate was provided by a DC external power supply.

The filament temperature and deposition time were kept constant at 2250 °C and 2.5 hours, respectively. Gas composition (%vol. CH_4), total gas pressure (P), total mass flow (F) and substrate temperature (T_s) were considered as Controllable Factors in the Taguchi Matrix, while three Levels for each of these factors were selected in a L9 orthogonal array (Table I). Average grain size (G), growth rate (R), residual stress (σ_r) and diamond structural quality (Q) were evaluated by SEM (top views and cross-sections) and μ-Raman spectroscopy (He-Cd, 325 nm).

Table I - Taguchi experimental array of deposition conditions and values of grain size (G), growth rate (R), residual stress (σ_r) and diamond quality factor (Q).

	P (kPa)	F ($ml \cdot m^{-1}$)	CH_4 (vol%)	T_s (°C)	G (μm)	R ($\mu m \cdot h^{-1}$)	σ_r (GPa)	Q (%)
L1	7.5	100	1.25	750	0.45	0.24	-0.65	10
L2	7.5	150	2.0	800	0.70	0.48	-0.65	15
L3	7.5	200	2.5	850	0.84	0.68	-1.23	24
L4	12.5	100	2.0	850	0.75	0.60	-0.83	21
L5	12.5	150	2.5	750	0.48	0.72	-0.91	18
L6	12.5	200	1.25	800	0.61	0.64	-0.63	15
L7	17.5	100	2.5	800	0.33	1.08	-0.99	12
L8	17.5	150	1.25	850	0.54	0.60	-0.65	22
L9	17.5	200	2.0	750	0.13	1.04	-0.95	12

3. Results and discussion

Based on previous work conducted by this group on diamond deposition but in a smaller HFCVD reactor [4], a first set of experiments using a Taguchi Matrix was conducted. The total mass flow, F, was set at 20, 100 and 200 $ml.m^{-1}$ and total gas pressure, P, at 2.0, 7.5 and 12.5 kPa. The substrate temperature, T_s, was established for 750, 800 and 900 °C, while the methane content, CH_4, was set at 0.5, 1.25 and 2.0 vol%. No continuous films were produced for values of P=2.0 kPa, F=20 $ml.min^{-1}$, Ts=900 °C and methane content of 0.5 vol%, irrespectively of the other factors. Therefore, these results suggested that an increase of the total gas pressure, total mass flow and methane content should be made, while decreasing the substrate

temperature. The lowest substrate temperature of 750 °C was chosen because preliminary work showed that using 700 °C no continuous films were produced. Thus, a new set of experiments was designed according to the L9 Taguchi Orthogonal Array in Table I.

For all the deposition conditions, continuous microcrystalline diamond films were obtained. Fig.1 presents a complete set of SEM micrographs, the columns from left to right with increasing substrate temperature, and the rows from top to bottom for increasing pressures. For the set of samples L1, L2 and L3 (first row, P=7.5 kPa) it is possible to observe that an increase in the substrate temperature, along with the total mass flow and CH_4 content increase, induces a noticeable augment in the diamond grain size. The average grain size (G) in Table I was calculated by image analysis from SEM micrographs. For samples L5, L6 and L4 grown at P=12.5 kPa (second row in Fig. 1), as well as for the set L9, L7 and L8 (third row, P=17.5 kPa), it is clear that, at constant pressure, increasing temperature results in larger grain sizes. Similarly, at a constant total mass flow of 200 $ml.m^{-1}$, the increase in temperature gives rise to an increase in the diamond grain size (see the set of samples L9, L6 and L3 in Fig. 1 diagonal, following this order).

When observing Fig. 1 micrographs from top to bottom, column by column, i.e. with increasing total gas pressure, an opposite trend to temperature influence is observed: the grain diminishes with increasing pressure at constant temperature. The correspondent G values are given in Table I. Contrarily to the major influence of substrate temperature and total gas pressure, the other deposition parameters, total mass flow and methane concentration, do not seem to play a crucial role in the morphology of the remaining films as no grain size trend is detectable.

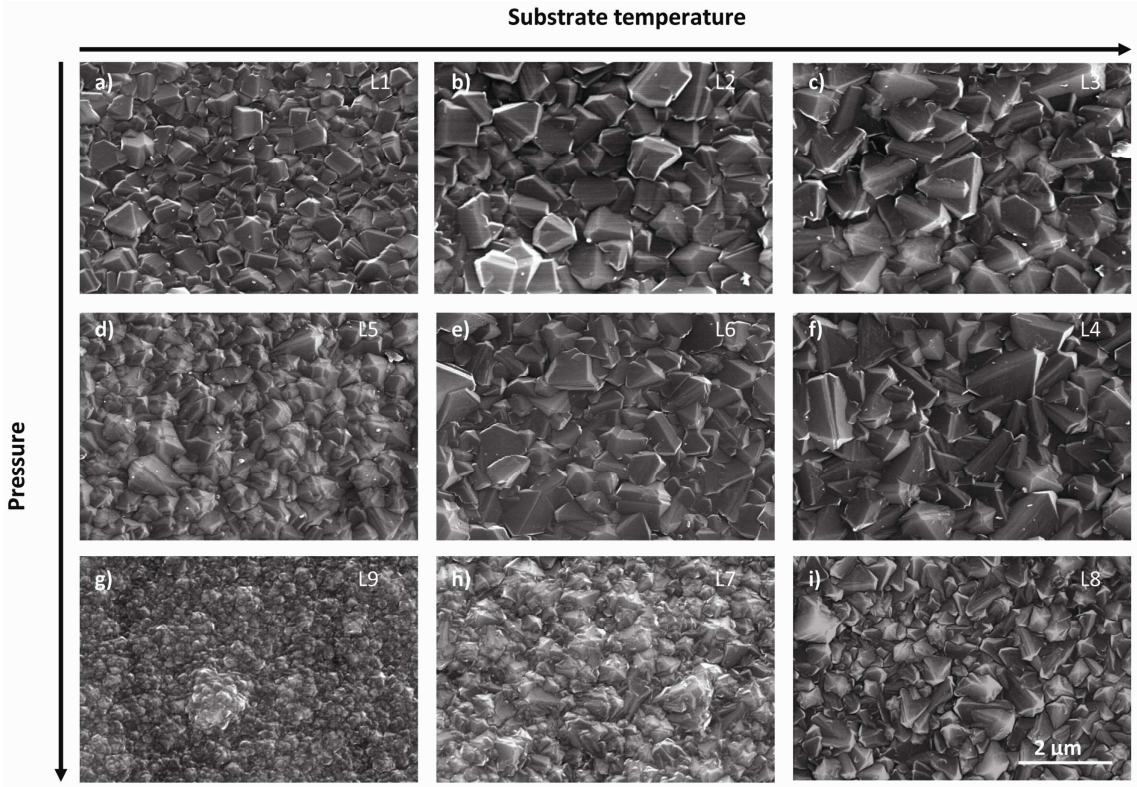

Figure 1 - SEM micrographs of CVD diamond obtained for each of the Taguchi experiments. The arrows indicate the increasing pressure and substrate temperature. All micrographs were taken at the same magnification.

The Raman spectra of the samples are similar to the one presented in Fig. 2. The plots were best fitted using a linear two point line for the photoluminescence baseline subtraction plus a Lorentzian curve for the diamond 1332 cm^{-1} peak and four Gaussian shapes. These are the graphitic D band at ~1380 cm^{-1}, the graphitic G band at ~1570 cm^{-1}, a band located at ~1300 cm^{-1}, probably due to scattering in disordered diamond [5], and another at ~1500 cm^{-1}, attributed to intergranular transpolyacetylene [6]. The dispersive bands are shifted to higher wavenumbers from its common positions in visible Raman, as a result of the 325 nm UV excitation wavelength [7].

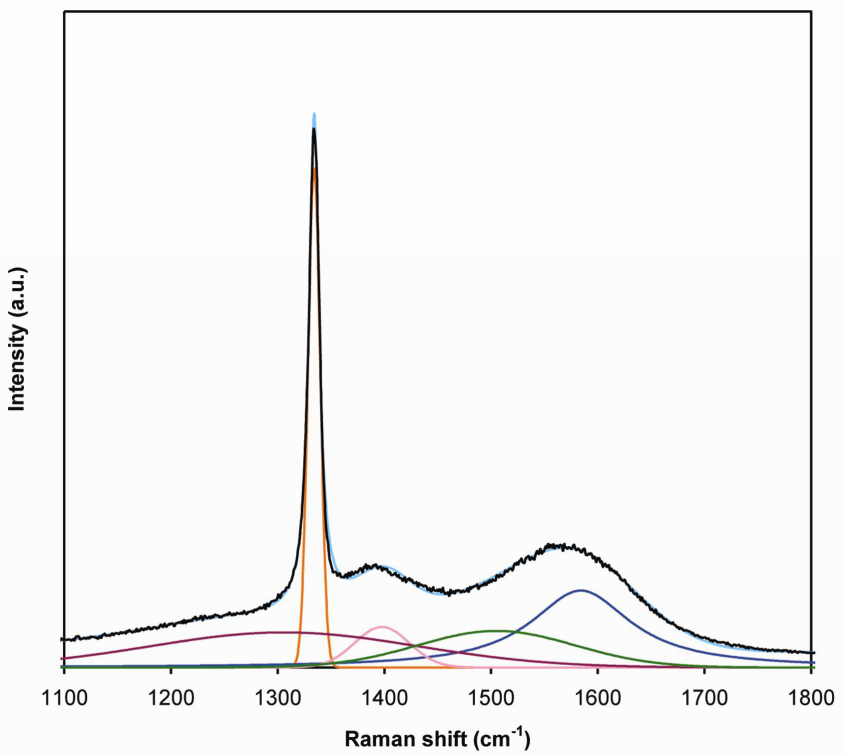

Figure 2 - Curve fitting for the Raman spectrum of sample L3, representative of all samples.

Diamond films usually present residual stresses extrinsically induced by the difference in the coefficients of thermal expansion between the substrate and the film. These are expressed mainly during cooling down from the deposition to room temperature. Also, intrinsic residual stresses arise from the non-diamond material at the grain boundaries and to structural defects, like microtwins, dislocations, impurities, among others [8]. Raman spectroscopy allowed the assessment of the total residual stress of the films, by analysing the diamond peak shifts, and then using Eq. 1 [9]:

$$\sigma_r = 0.567\ \Delta\vartheta\ (cm^{-1}) \qquad \text{(Eq. 1)}$$

where Δυ is the difference between the measured and the natural stress-free diamond peak shifts.

For all the films, a positive shift from the value of bulk diamond was obtained, indicating a compressive stress between the Si substrate and the diamond film (Table I) [10].

The Raman spectra also allowed a relative indication of the structural quality of the film (Q) from the ratio I_D/I_T, where I_D represents the integrated intensity of the 1332 cm^{-1} diamond peak and I_T the total integrated intensity of the Raman spectrum. The later comprises both diamond and non-diamond contributions. From Table I it can be noticed that the most notable influence on the structural quality is that of the substrate temperature: for each set of samples grown at constant pressure, the highest T_s leads to the best Q.

Fig. 3 graphically presents the influence of all the controllable factors on the specified film's characteristics, taking the average values at each individual level. It is clear that the chosen deposition parameters do not influence in the same manner the various film characteristics. In this plot it is visible that, within the temperature range used in this work (750-850 °C), the grain size (G) increased with substrate temperature. This unexpected result contradicts the model proposed by May *et al*. [11], but is in line with the results by Haitao *et al*. [12], even though the latter included Ar in the gas mixture.

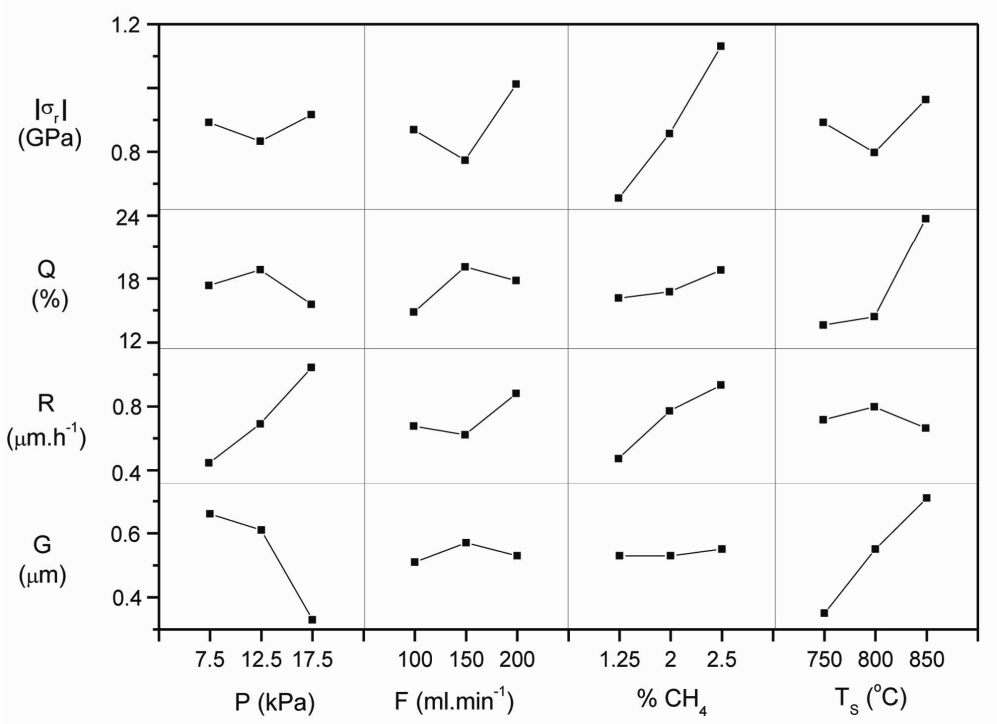

Figure 3 - Influence of the Controllable Factors on the grain size (G), growth rate (R), diamond quality factor (Q) and residual stress (σ_r).

Still from Fig. 3 it is also possible to conclude that the rise in pressure induces a decrease in the diamond grain size, as stated above. Concomitantly, Kang *et al*. [13] reported that by increasing pressure at a constant temperature, the diamond crystallite size decreased, eventually reaching a nano-crystalline growth mode.

The increase on the total gas pressure and methane content were identified as the main growth rate (R) enhancing factors. This behavior was already reported in HFCVD experiments using medium-high pressure levels and substrate temperatures comparable to the present work [14]. This trend is also common in other CVD techniques, such as microwave plasma [15]. It was argued in this case that, for a given temperature and pressure, the number of carbon radicals arriving at the growth surface depended only on the methane concentration (partial pressure) in the source gas and, as a consequence, the growth rate increased with carbon concentration.

For the structural quality (Q) also the substrate temperature seems to play the major role, especially from 800 °C to 850 °C. High substrate temperatures induce the deposition of highly pure diamond films, with low non-diamond carbon impurity content [1].

The residual stress (σ_r) is especially sensitive to the increase in the methane content. This is probably related to the well known trend of non-diamond phases development with methane increase [16]. These phases tend to concentrate at the grain boundaries and are the main source of internal compressive stress, as a consequence of their higher specific volume compared to diamond [17].

As seen above, the dependence of the film properties on the deposition conditions (controllable factors of the Taguchi Matrix) is diverse. The goal should be to obtain a diamond film with the highest diamond quality factor (Q) and growth rate (R), while minimizing the residual stress (σ_r) and the grain size (G). Bearing that in mind, a Figure-of-Merit (FOM) was designed to access the film valuation, based on these parameters, as stated in Eq. 2:

$$\mathrm{FOM} = \frac{|\mathrm{R}\times\mathrm{Q}|}{|\sigma_{\mathrm{R}}\times\mathrm{G}|} \qquad \text{(Eq. 2)}$$

The combined influence of all the parameters on the FOM normalized to the highest value is presented in Fig. 4. It is clearly shown that the total gas pressure has

the foremost influence on the film valuation parameter. Although having a positive influence on the grain size (G) and diamond quality factor (Q), the chosen substrate temperatures diminished the proposed film valuation (FOM). From this plot, the best film is probably obtained at the highest total gas pressure and mass flow, average CH_4 content, and lowest substrate temperature, within the considered deposition condition ranges. These are exactly the parameters used for sample L9, which presents the highest individual FOM.

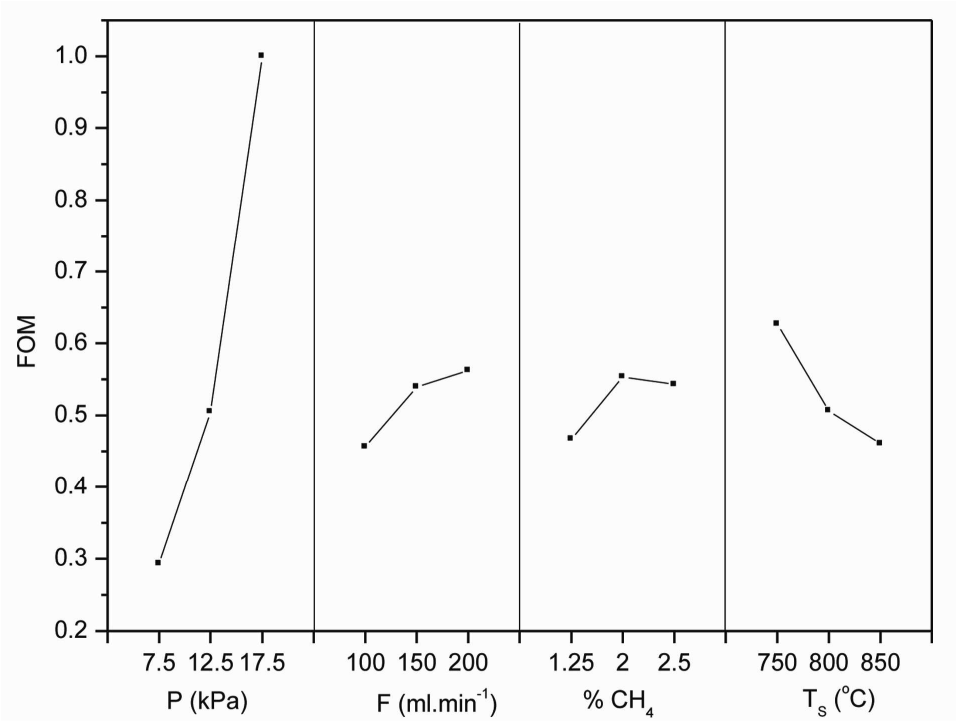

Figure 4 - Influence of the Controllable Factors on the film Figure-of-Merit (FOM).

4. Conclusions

Based on a Taguchi Matrix approach for the experimental design of the study of the combined effects of gas composition, total gas pressure, total mass flow and substrate temperature on the quality and growth rate of CVD diamond films, the following conclusions can be withdrawn:

- increasing substrate temperature and decreasing total pressure result in a noticeable augment in the grain size.

- the substrate temperature is the most important factor to achieve a good diamond structural quality factor, i.e. the highest relative intensity of the diamond peak.
- the residual stress (compressive) is mainly sensitive to the methane content increase.
- the main growth rate enhancing factors are total gas pressure and methane content.

Furthermore, it was proposed a new Figure-of-Merit (FOM) that gives a more accurate indication of film valuation. The best film is obtained at the highest total gas pressure and mass flow, average CH_4 content, and lowest substrate temperature, within the considered deposition condition ranges.

Acknowledgements

E. Salgueiredo, M. Amaral and M.A. Neto acknowledge FCT for the grants SFRH/BD/41757/2007, SFRH/BPD/26787/2006 and SFRH/BPD/45610/2008, respectively.

References

[1] Guo L, Chen G. Diam Relat Mater 2007;16:1530-40.

[2] Porro S, Musso S, Giorcelli M, Chiodoni A, Tagliaferro A. Physica E 2007;37:16-20.

[3] Leal-Cruz AL, Pech-Canul MI. Solid State Ionics 2007;177:3529-36.

[4] Almeida FA, Amaral M, Oliveira FJ, Silva RF. Diam Relat Mater 2006;15:2029-34.

[5] López-Ríos T, Sandré É, Leclercq S, Sauvain É. Phys Rev Lett 1996;76:4935-8.

[6] Ferrari AC, Robertson J. Phys Rev B. 2001;63:121405-4.

[7] Zhang HB, Lin GD, Zhou ZH, Dong X, Chen T. Carbon 2002;40:2429-36.

[8] Ferreira NG, Abramof E, Leite NF, Corat EJ, Trava-Airoldi VJ. J Appl Phys 2002;91:2466-2472.

[9] Ralchenko VG, Smolin AA, Pereverzev VG, Obraztsova ED, Korotoushenko KG, Konov VI, Lakhotkin YV, Loubnin EN. Diam Relat Mater 1995;4:754-8.

[10] Pal AK. Current Science 2002;83:225-36.

[11] May PW, Ashfold MNR, Mankelevich YA. J Appl Phys 2007;101:053115-9.

[12] Ye H, Sun CQ, Hing P. J Phys D: Appl. Phys 2000;33:L148-152.

[13] Kang M, Lee W, Baik Y. Thin Solid Films 2001;398-399:175-9.

[14] Wei J, Tzeng Y. Diam Films Tech 1995;5:79-86.

[15] Li X, Perkins J, Collazo R, Nemanich RJ, Sitar Z. Diam Relat Mater 2006;15: 1784-8.

[16] Gruen DM. Growth of nanocrystalline diamond films. In: Nazaré MH, Neves AJ, editors. Properties, Growth and Applications of Diamond, London: IEE; 2001, p. 299-302.

[17] Vila M, Amaral M, Oliveira FJ, Silva RF, Fernandes AJS, Soares MR. Appl Phys Lett 2006;89:093109-3.

II.3. Mechanical performance upgrading of CVD diamond using the multilayer strategy

E. Salgueiredo[1]; M. Amaral[2]; F.A. Almeida[1]; A.J.S. Fernandes[2]; F.J. Oliveira[1]; R.F. Silva[1]

[1]CICECO, Materials and Ceramic Eng. Dept., University of Aveiro, Campus de Santiago, P-3810-193 Aveiro, Portugal
[2]I3N, Physics Department, University of Aveiro, Campus de Santiago, P-3810-193 Aveiro, Portugal

Surface and Coatings Technology, 236 (2013) 380-387

DOI:10.1016/j.surf.coat.2013.10.017

Abstract

The present work is a comparative study of different combinations of microcrystalline (MCD) and nanocrystalline diamond (NCD) varieties (monolayers, bi-, tri- and fourfold layers) grown by hot filament CVD technique on silicon nitride ceramic substrates. The Hertzian stress states under static indentation are estimated and compared on the basis of the von Mises stress parameter. The diamond multilayer morphology and the structural quality were evaluated step-by-step by SEM, AFM and UV-Raman spectroscopy. By using the multilayer strategy, starting with a MCD adherent layer on Si_3N_4 ceramic substrates and finishing with a NCD smooth layer at the top, it was possible to keep the surface roughness at a lower RMS level, of around 90 nm. The fourfold multilayer configuration allowed obtaining 10 µm thick diamond coatings that endure an indentation load of 800 N with a Brale cone, before film spalling-off. This behaviour is determined by the high bonding strength of the initial MCD layer grown on the Si_3N_4 ceramic substrate, where the von Mises stress ($J_2^{1/2}$) is estimated as 27 GPa.

Keywords: CVD diamond, multilayers, hot filament, adhesion, Von Mises stress.

1. Introduction

Nanocrystalline diamond (NCD) coatings offer a suitable combination of high hardness and reduced surface roughness for mechanical applications [1-3]. However, the threshold load for delamination is somewhat restricted by the relatively poor NCD adhesion when comparing to that of the microcrystalline diamond (MCD) variety [1, 4, 5]. This is due to the NCD lower deposition temperature that hinders a strong chemical bonding to the substrate, and to the higher content of non-diamond species at the grain boundaries. However, comparing to NCD, the MCD variety presents a higher initial friction peak in tribological solicitations, due to the mechanical interlocking caused by the asperities of the micro-sized diamond crystals [6]. This may limit its direct application as a coating in tribological parts. To overcome the MCD high surface roughness, a post-polishing may be done, but this is time-consuming, expensive and impractical in the case of complex geometries. Therefore, an alternative solution is a CVD diamond multilayer combination, starting with MCD to assure a superior adhesion to the substrate, and ending with a smooth nanocrystalline diamond (NCD) top coating. Alternating MCD and NCD thin films in a simple bilayer or a more complex multilayer combination will also prevent MCD grains to grow excessively and may enhance the fracture toughness by the crack-arresting role of interfaces between layers [7].

Multilayer diamond coatings have been explored on WC-Co substrates [7-14]. Bias-on cycles allowed the formation of thin ball-like NCD layers which were intercalated between MCD layers grown in the absence of bias current; results have shown an enhancement in the bending strength by 30% compared to MCD monolayers [8]. A similar strategy was performed by Vojs *et al*. [9] to obtain diamond multilayers on cutting inserts, attaining a notable decrease in the surface roughness from 650 nm to 50 nm. Alternating layers of fine- and coarse-grained MCD on cemented carbide cutting inserts were reported by Schafer *et al*. [10], being said to result in increased mechanical impact resistance due to reduced crack propagation. Kadlečíková *et al*. [15] deposited a bilayered MCD/NCD coating by bias-assisted hot-filament CVD (HFCVD) similarly to Sun *et al*. [11]. The latter demonstrated remarkable improvements on the working lifetime of drawing dies by a factor of above 15 (compared to uncoated ones).

Shen and Sun [12] propose a method combining HFCVD deposition and polishing techniques, with which an ultrasmooth composite diamond film consisting of a first layer of MCD and multiple layers of NCD films is obtained. The friction properties were examined in both dry sliding and water-lubricating conditions against ball-bearing steel, copper and silicon nitride (Si_3N_4) balls, and the results show that the multilayer film presents much superior friction properties [13] than uncoated WC-Co or MCD samples, regardless lubricating condition. Dumpala *et al*. [14] proposed an integrated composite diamond consisting of NCD layer over MCD with a coating architecture of NCD/transition layer/MCD/WC–Co. The graded transition layer (~1 μm in thickness) was performed by controlling the process parameters such as methane concentration and chamber pressure in a HFCVD reactor in order to integrate the MCD and NCD layers.

The benefits of the multilayer strategy can be further assured if Si_3N_4 ceramics are used as substrate material. By itself, Si_3N_4 is a well-known wear resistant ceramic used in rolling contact applications in various industries such as turbomachinery, power and automotive industries, with significant advantages over steel and tungsten carbide due to its lower density, better corrosion resistance and excellent performance under extreme environmental conditions [16-22]. The tribological performance of this ceramic is enhanced by CVD diamond coatings, which reduce both friction and wear, even in unlubricated conditions [1]. This improvement can be particularly significant when components work in boundary lubrication regime or in the case of lubricant starvation, as it may happen at the start-up of engines. The superior performance of CVD diamond coatings over Si_3N_4 in severe mechanical/tribological solicitations is due to the excellent adhesion strength of the film to the substrate, given the good thermal expansion match and structural compatibility [23, 24]. Static Brale indentation evidenced that MCD coatings on Si_3N_4 ceramic supported a notable normal load of 1600 N without film spalling-off, while delamination of NCD took place under 400 N, for coatings of about 30-40 μm in thickness [5]. In self-mated tribological tests, film delamination happened for higher applied loads in the case of MCD (160 N [6]) than for NCD (85N [25]).

Multilayer diamond coatings on Si_3N_4 ceramic substrates were recently tested in erosive tests by hard particle impacts [26]. The “energy sink” action of the MCD/NCD

interfaces was demonstrated, as the first signal of severe damage is the adhesive failure between the diamond layers that delays the induction time to substrate exposure [26]. Self-mated tribological tests of these composite coatings in dry sliding condition showed that the NCD outer layer progressively wears out performing a sacrificial role, while the underneath harder MCD layer keeps the residual stresses at lower levels [27]. The result is a superior bearing capacity of the coatings, increasing the critical load before film detachment from 60-100 N for mono-layers to 130-200 N for the multilayer diamond [27]. Under biodiesel lubrication, the multilayered coatings rendered a more even performance of the ball and plate counterparts, denoting less fatigue sensitivity, and an almost constant variation with applied load [28]. Chen *et al*. [29] also coated Si_3N_4 ceramics with multilayer diamond films, the Al-Si alloy turning tests showed a superior performance of these coatings, which did not fail by film delamination as it happened for the monolayered ones.

In the present work, distinct multilayer combinations of MCD and NCD varieties (monolayers, bi-, tri- and fourfold layers), grown by HFCVD on silicon nitride ceramic substrates, are investigated. Morphological (SEM, AFM), structural (micro- Raman spectroscopy) and mechanical (static indentation) characterizations demonstrate the growing interest in the development of multilayer CVD diamond coatings for highload mechanical solicitations.

2. Experimental

Dense disc shaped Si_3N_4 ceramic substrates (∅10 mm x 3 mm thick) were fully densified by pressureless sintering at a dwelling temperature of 1750 °C for 2 h, in an atmosphere of 0.1 MPa N_2, using aluminium and yttrium oxides as densification additives. The weight percentages were: 89.3% α–Si_3N_4 (Starck grade M11), 7.0% Y_2O_3 (Starck grade C) and 3.7% Al_2O_3 (CT-3000SG, Alcoa). The substrates were then sequentially ground with a 46 µm diamond wheel, flat lapped with a 15 µm diamond slurry in an iron/polymer plate, followed by ultrasonic scratching during 1 h with a 15 µm diamond powder suspension in ethanol.

Diamond deposition was conducted in an in-house built 3 kW HFCVD reactor. Six tungsten wires (∅=0.25 mm, 75 mm length) were kept at a constant distance of ~7

mm from the substrate. The filament temperature was measured with a two-colour pyrometer (Raytek) and kept constant at about 2300 °C. The substrate temperature was assessed by a K-type thermocouple inserted into the substrate holder, placed on the back side of the substrate. The samples were heated at approximately 630 °C by thermal radiation. The additional heating of the substrate was achieved by graphite dissipating element fed by an AC external power supply, permitting full temperature control. A carburization step of the filaments was conducted at a gas flow rate of 200 sccm with 2% of CH_4 in H_2, and a pressure of 10 kPa for about 10 minutes.

The HFCVD system enabled the deposition of polycrystalline diamond coatings with different morphologies. Microcrystalline (MCD) and nanocrystalline diamond (NCD) were obtained by adjusting the optimized deposition parameters from gas mixtures of H_2 and CH_4, as given in Table 1. In the case of the NCD film, nanocrystals develop as a result of the higher methane (CH_4) concentration (carbon supersaturation) in the gas composition along with a decrease of the total pressure and substrate temperature. Besides the MCD and NCD monolayers, the step-by-step construction of the multi-layered systems permitted obtaining the following composite coatings: i) Bilayer: MCD/NCD; ii) Trilayer: MCD/NCD/MCD; iii) Fourfold layer: MCD/NCD/MCD/NCD.

Table 1: Hot filament deposition parameters of MCD and NCD layers**.**

Diamond varieties	CH_4/H_2 ratio	Gas flow (sccm)	Total pressure (kPa)	Substrate temperature (°C)
MCD	0.026	100	17.5	800
NCD	0.073	100	5.0	700

Field emission scanning electron microscopy (FE-SEM) was performed using a Hitachi SU-70 system for surface morphology characterization of the diamond coated ceramic substrates (top view and cross-section). UV µ-Raman spectroscopy (HORIBA JOBIN YVON HR800UV), using the line 325 nm from a He-Cd laser (KIMMON IK series) allowed the identification of the carbon phases. AFM 15 µm x 15 µm scans (Nanoscope IIIa, Digital Instruments) were accomplished to determine the surface roughness of the

diamond layers. The crystalline structure of the coatings was characterized by X-ray diffraction analysis (XRD) performed on a Philips X'Pert MPD equipment with CuKα λ=1.5406 Å (40 kV; 50 mA) as the primary source of radiation. Low incident beam angle X-ray diffraction (LIBAD) technique in combination with the Debye-Scherrer equation was applied for assessment of the average crystallites sizes, considering the broadening of the XRD diffraction peak at 2θ~44°, which corresponds to the diamond (111) plane. The equipment used a PW1711 (proportional) detector with 2θ varying from 42.5° to 45° in steps of 0.02° for 5 s at a fixed 2° incident angle.

The adhesion of the coatings was evaluated in the 100 to 1000 N normal load range using a diamond Brale indenter (tip radius of 0.2 mm and cone angle of 120°) coupled to a universal testing machine. At least three indentations per load were performed for each diamond grade. Circumferential (lateral) cracks of all the indentation imprints were measured using optical and scanning electron microscopy. For this comparative study, coatings with the same end thickness of 10-12 μm were produced by adjusting the deposition times of each layer.

3. Results and Discussion

3.1. Microstructure, phase composition and surface morphology

Top and cross-sectional views of monolayers of both diamond grades with similar thickness (3-4 μm), as well as the respective Raman spectra and AFM scans, are given in Figure 1. For the MCD monolayers, pyramidal micrometric diamond crystals are visible at the end surface (Figs. 1a, c). Figs. 1b and 1d reveal the distinctively nanocrystalline feature of the NCD films, presenting a finer grained, clustered morphology. The analysis of the LIBAD-XRD spectra with the Debye-Scherrer equation provides a crystallite size average value of 19 nm for the NCD film. The typical Raman spectrum of the MCD coating is given in Fig. 1e showing the conspicuous diamond signature at 1332 cm^{-1}. In the NCD film, this peak is still present (Fig. 1f) but it is much weaker and it appears combined with the disordered (D) and crystalline (G) graphite bands, respectively at ~1370 cm^{-1} and ~1580 cm^{-1} [30]. The noticeable graphite bands

reflect the incorporation of the sp^2 carbon phase at the grain boundaries, with extensive amount due to the very small diamond crystallite size of the NCD grades.

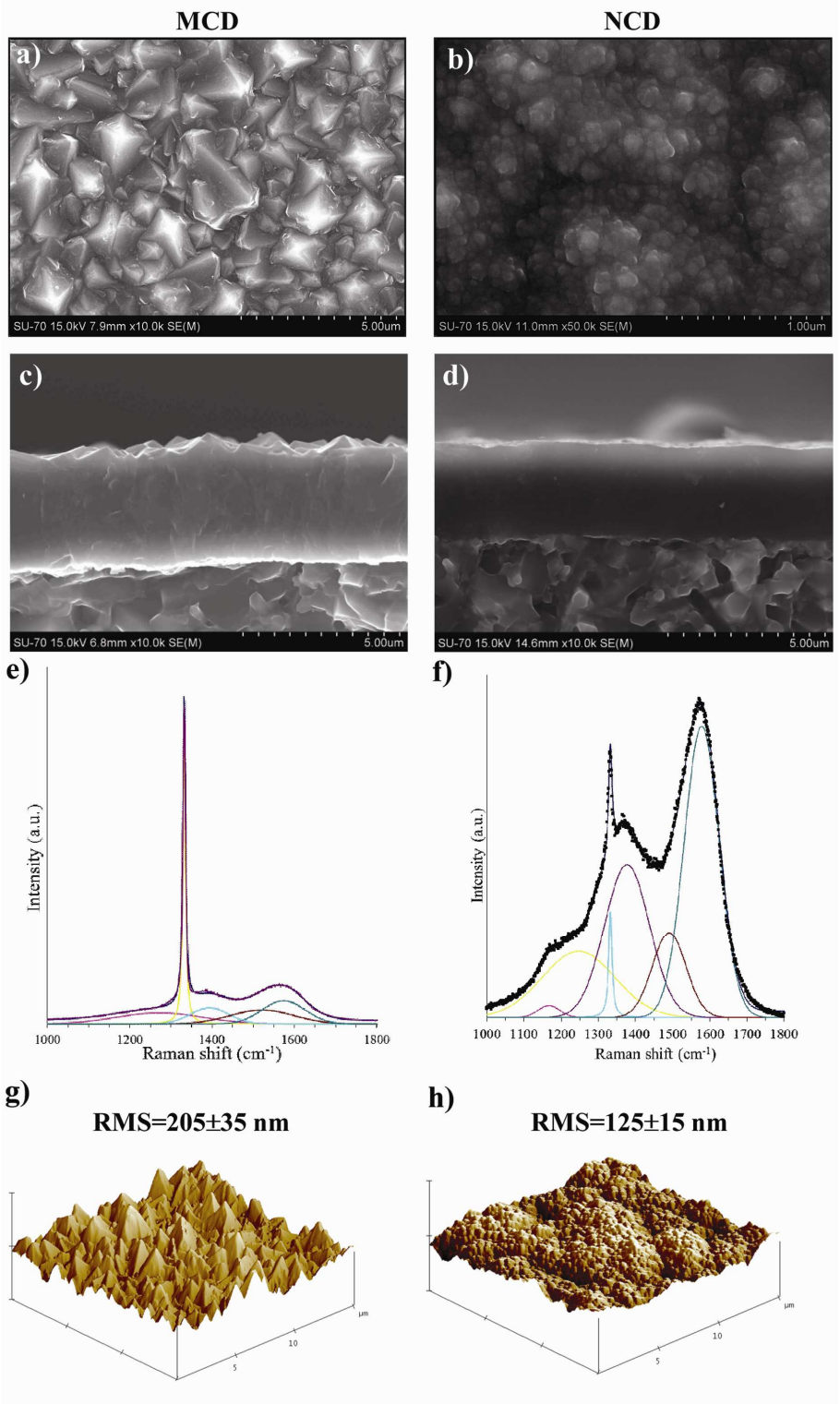

Figure 1 - SEM micrographs of the monolayered films: top view of a) MCD and b) NCD; (c-d) respective cross section; (e-f) correspondent UV-Raman spectra; (g-h) respective AFM scans.

The dispersive D band is shifted to higher wavenumbers from its common position (~1350 cm^{-1}) in visible Raman, as a result of 325nm UV excitation wavelength [31]. As commonly accepted, the bands located at 1170 cm^{-1} and 1500 cm^{-1}, attributed to intergranular trans-polyacetylene, are typical of NCD films [30, 32]. Another band is considered at ~1250 cm^{-1} that may be correlated with the bands usually assigned to other acetylene C-H chains [30, 32, 33].

All the uncoated Si_3N_4 substrates presented an average roughness value (RMS) of approximately 200 nm (image not presented). From the AFM scans of the films (Fig. 1g and h), the average RMS value for MCD is 205 nm, while it decreases for the nanocrystalline diamond films to an average value of 125 nm. The reduction of surface roughness is advantageous considering the tribological applications that are envisaged. It is worth to note that the RMS values for the nanocrystalline coatings are much higher than the crystallite size, revealing that the substrate surface finishing still has a significant influence on the surface roughness of the diamond coating, despite the smoothing effect of the NCD agglomerates.

In order to follow the morphological evolution and quality of the multilayer building, SEM, Raman and AFM techniques were performed step-by-step in bi-, tri- and fourfold CVD diamond multilayers (Figure 2).

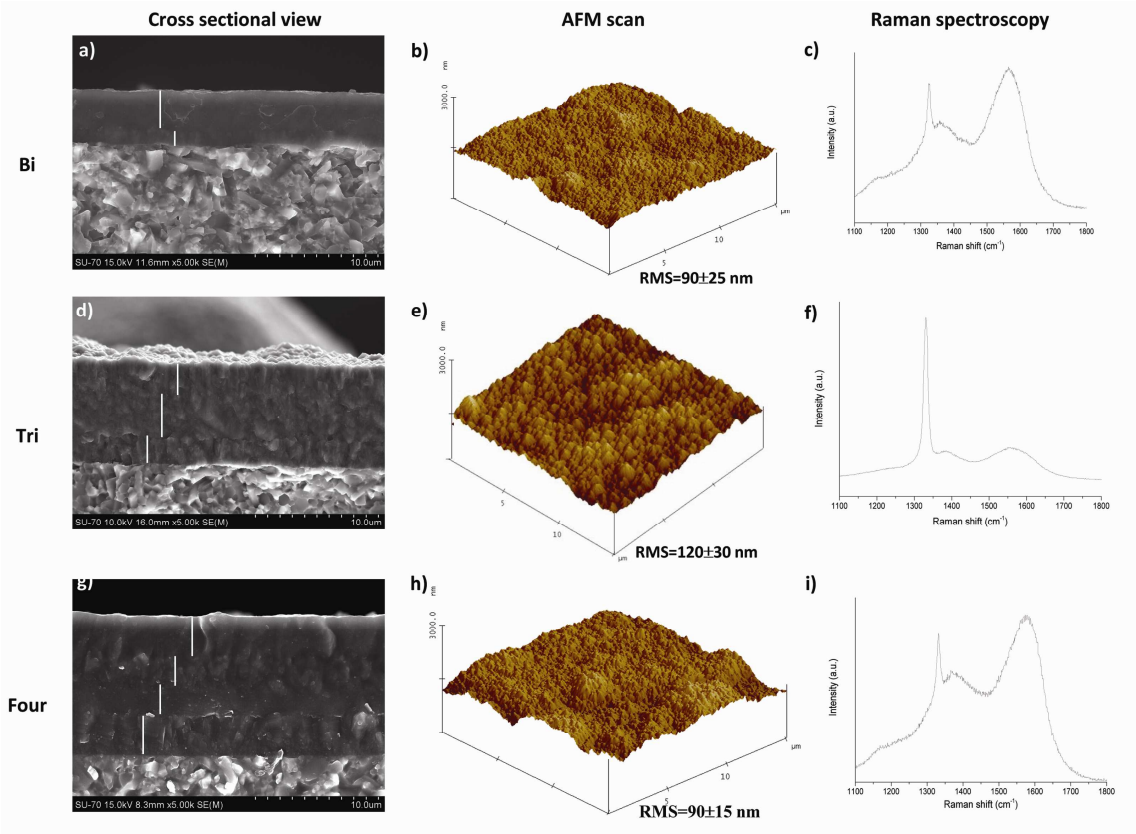

Figure 2 -. Representative SEM cross sectional view (a, d, g), AFM scans (b, e, h) and UV-Raman spectra (c, f, i) of the bi-, tri- and four-fold layer composite diamond films over Si_3N_4 substrates.

Bilayers correspond to the coating of the first MCD layer (deposition time 1 h; ap. 2 µm in thickness) by one NCD layer (3 h; 3 µm), resulting in a net surface smoothening action (see SEM view and AFM scan in Figs. 2a and 2b, respectively) when compared to the respective monolayers (Figure 1). The Raman spectrum of the bilayered coating in Fig. 2b is very similar to that in Fig. 1f as they mainly express the contribution of the top NCD layer. The addition of one layer of MCD over this film makes the trilayer coating, as shown in Figs. 2d and 2e, with the natural increase in the RMS surface roughness due to the columnar-like growth of the microcrystalline diamond crystals. The Raman spectra of the film reveals again the signatures of the top coating, in this case the one of the MCD, the same aspect as the one of the MCD monolayer in Fig. 1e. The fact that the Raman signal does not show an evident interference of the underlying layers is due to the shallow penetration depth of the 325 nm laser radiation used in the UV-Raman analysis [34].

Finally, the fourfold multilayered composite coating, with and ending layer of NCD, is clearly illustrated by the SEM cross-sectional micrograph of Fig. 2g, where well defined boundaries between MCD and NCD layers are depicted. Here, the smoother NCD top layer rendered again the lower levels of surface roughness (Fig. 2h) and its characteristic Raman spectrum (Fig. 2i), the same as the one of the bilayer coating (Fig. 2b), but now with twice the film thickness The evolution of the surface roughness with the thickness of the composite films is better visualized in Figure 3. The RMS value for the 4 µm thick MCD monolayer is the highest one (~200 nm), and decreases to values around 120 nm for the 3 µm thick NCD monolayer. The values of the surface roughness remain at lower levels as the stacked diamond structure is being built, and finishes with average values lower than 100 nm for an 11 µm thick multilayer diamond film.

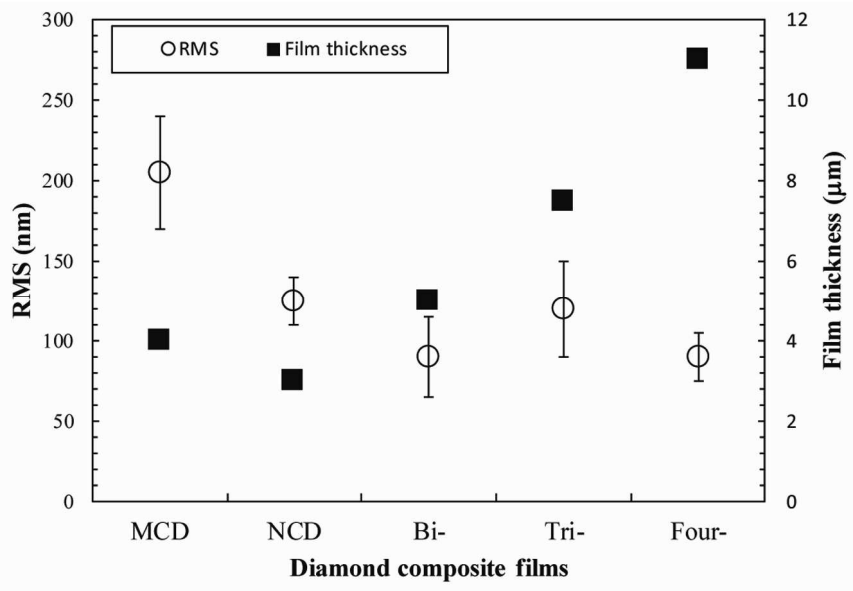

Figure 3 - Evolution of the surface roughness with thickness of the composite films.

3.2. Static indentation behaviour

The overall set of distinct diamond coatings was subjected to static indentation experiments in order to evaluate their adhesion to the Si_3N_4 ceramic substrate. Figure 4 displays the indented diamond surfaces observed under optical microscopy. In the left-hand column, crack patterns (radial and/or circumferential) that occur at loadings below film spallation are visible. In the right-hand column, the spalling-off loads are given and the delamination patterns are depicted.

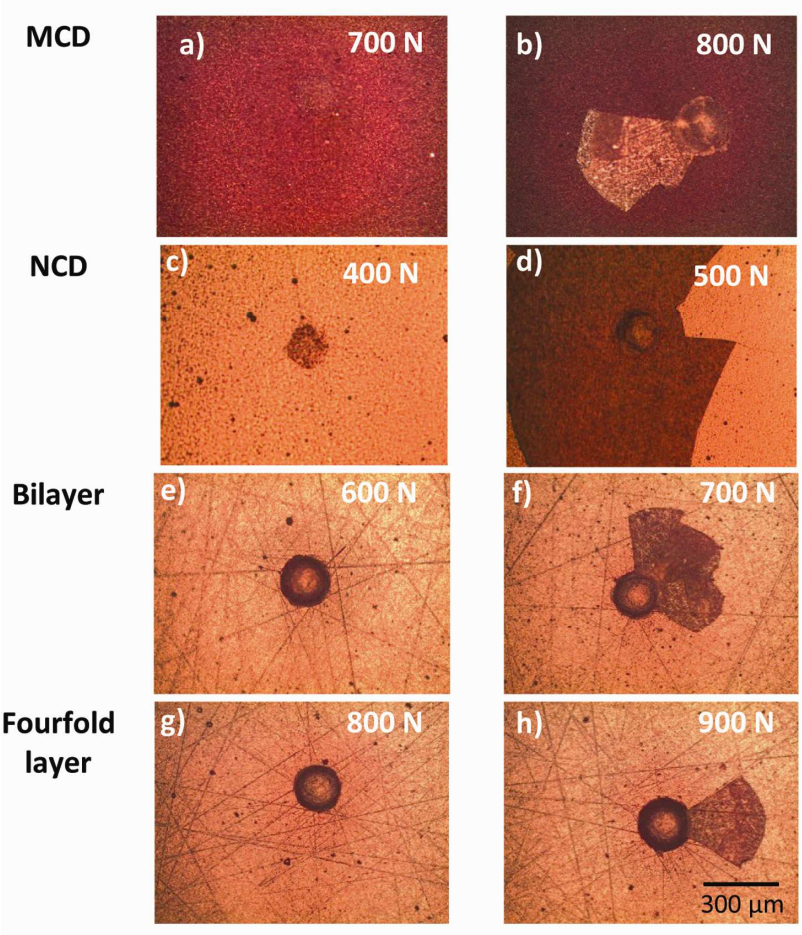

Figure 4 - Optical images of the Brale imprints at selected loads on the different diamond composite films; left column: crack pattern for loads just below films spalling-off; right side: the corresponding indent features at the spalling-off loads.

Adhesion evaluation by static indentation is founded in the well-known Marshall and Evans model [35] of propagation of radial and lateral (circumferential) cracks along the film/substrate interface due to the combination of a set of factors: residual stresses, mechanical properties of both the film and the substrate and interfacial fracture resistance. Due to the brittle nature of the silicon nitride substrate, these cracks initiate in the substrate bulk [36]. Film spalling-off occurs when radial and circumferential cracks meet, after emerging from the coating/substrate interface.

MCD diamond coating (Fig. 4a) showed the highest adhesion failure load (700N), when compared to NCD (400N, Fig. 4c) monolayered film. This behaviour is the result of the very high crystalline purity of the former, as illustrated by Raman spectroscopy (Fig. 1e), which promotes adhesion by two methods: i) direct bonding by grain-to-grain epitaxial growth on the substrate [24]; ii) the coating hardness is

increased and therefore the substrate plastic deformation is reduced [37]. The higher graphite content of NCD (Fig. 1f) results in a lower bonding strength to the substrate [38]. The finer grain size of NCD (Fig. 1c) increases the grain boundary volume where non-diamond phases are present [39].

Adhesion failure values of 600N were found for the Bilayer coating (Fig. 4e), close to that of the MCD monolayer (700 N, Fig. 4a). The indentation behavior of the bilayered film is thus dictated by the bonding strength of the initial layer of MCD to the substrate. In the case of the fourfold multilayer film, the threshold to film spalling-off (800 N, Fig. 4g) is slightly superior to the MCD value (700N, Fig. 4a).

Table 2 - Young's modulus (E) and Poison's coefficient (ν) of the different half-spaces.

Half-space	E_2 (GPa)[a]	ν_2 (GPa)[b]
MCD/Si_3N_4	480	0.18
NCD/Si_3N_4	430	0.21
Bi- and Fourfold layer/Si_3N_4	450	0.20

[a] calculated from the inverse law of mixtures, considering: E_{MCD} = 1140 GPa [42]; E_{NCD} = 740 GPa [43]; E_{Si3N4} = 300 GPa [44]

[b] calculated from the simple law of mixtures, considering: ν_{MCD} = 0.07 [42]; ν_{NCD} = 0.12 [43]; ν_{Si3N4} = 0.3 [44]

Stress distribution analysis was performed in an attempt to know the stress field in the coated material associated to a static indentation. This can be estimated considering the Hertzian equations [40] applied to the contact between the diamond indenter and the diamond coated Si_3N_4. All the equations used in this calculation are presented in Annex A, and the symbols presented in Annex B. For the calculations, the values for the physical constants E_1 and ν_1 (of the diamond indenter) are 1220 GPa and 0.2, respectively [41]. The physical constants of the half space (E_2, ν_2) were estimated considering the diamond coatings and the Si_3N_4 substrate as a laminated composite, in which 50% of this composite is the diamond film and 50% the Si_3N_4 substrate. This approximation was done taken into account that the depth of penetration (Eq. 1) of the indenter into the material was estimated to be between 17-20 µm for loads from 500 to 900 N, being roughly twice the thickness of the diamond coatings (around 10 µm). The values of E_2 and ν_2 for all the samples are given in Table 2. Profiles of the von

Mises stress parameter $J_2^{1/2}$ along the perpendicular z-axis estimated for all types of diamond coatings are given in Fig. 5.

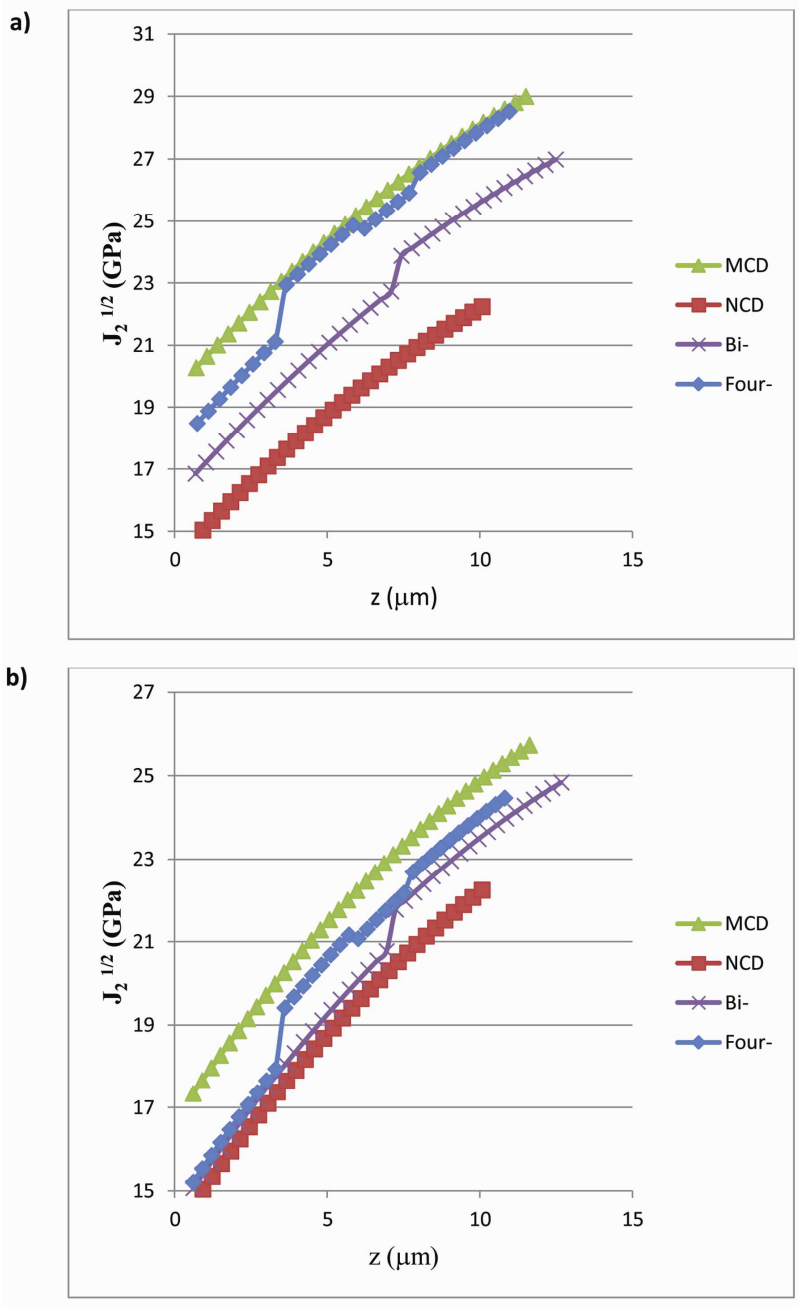

Figure 5 - Profile estimation of the von Mises parameter along z axis for the monolayered coatings (MCD and NCD), bilayer and fourfold multilayers: a) profiles of stress under the respective critical load for each film; b) profile at a 500N normal load for all films.

Fig 5a gives the evolution of the stress state under their respective critical loads before spalling-off (Fig. 4). The X-axis origin is the surface and $J_2^{1/2}$ stress values were represented until the respective diamond/substrate interface (the real total film

thickness). The following features are highlighted: 1- the higher stiffness of the MCD grade dictates the increasing of the stress state of the bi- and fourfold layer coatings, compared to the NCD monolayer, until the highest values of the MCD monolayer coating; 2- steps presented in the curves of the bilayer and fourfold layer coatings correspond to the diamond layer transitions; 3- under the critical load, at which all coatings delaminate at the diamond/substrate interface, the value of $J_2^{1/2}$ can be taken as a measure of the adhesion strength; hence, the NCD grade has a adhesion strength value of about 22 GPa, while the MCD/ Si_3N_4 interface supports 27 GPa (the value taken from the bilayer coating that starts by a MCD layer on the Si_3N_4 surface); 4 – stress values at the MCD /substrate interface for the fourfold multilayer and for the MCD monolayer are higher than 27 GPa, approx. 30 GPa, and so the coatings delaminate; in these cases the above critical value of 27 GPa is attained inside the coatings without fracture, denoting the higher cohesive resistance of diamond than the adhesive diamond/Si_3N_4 one.

Stress states at the same applied load of 500 N are showed in Fig. 5b. At this load only the NCD monolayer delaminates (as 500 N is the critical load) and in all the other grades, that start by a first MCD layer, the stresses at the interface are below the threshold value of 27 GPa, thus corroborating the absence of delamination.

4. Conclusions

Hot filament CVD demonstrated to be a very suitable technique for growing multilayer diamond films in a continuous process simply by adjusting the deposition parameters of microcrystalline (MCD) and nanocrystalline diamond (NCD) grades. HFCVD further allows coating of components with complex geometries.

A set of advantages for the MCD/NCD multilayer design for mechanical applications, is manifest: i) it provides a smooth end surface when the top coating is of the nanocrystalline diamond (NCD) type, which is particularly relevant for tribological applications that require high load bearing capacity and low frictional loss; ii) it ensures an high adhesion level as the initial layer is of the very adherent MCD grade.

A bilayered MCD/NCD structure was firstly designed. By using this approach, the RMS surface roughness of the diamond coatings decreased by half the value of the

MCD monolayered one. Fourfold multilayer diamond coatings were then produced by doubling the deposition procedure used for the bilayered coatings. Final coating thicknesses were of ~10 μm. Here again, it was possible to obtain diamond coatings with a RMS surface roughness kept at the lower level, of around 90 nm, even if the total thickness is increased. Cross sectional SEM micrographs reveal well adhered MCD layers to the Si_3N_4 substrate, and well defined planar boundaries between the diamond layers, with no evidence of interfacial fracture.

Calculations of the von Mises parameter ($J_2^{1/2}$) distribution along the film depth, estimated from Hertzian contact theory, give adhesion strength values of 27 GPa for the MCD/Si_3N_4 interface and 22 GPa for the NCD/Si_3N_4 one. In fact, diamond static indentation technique proved the high adhesion level of the MCD monolayered coatings, which attained a load of 700 N before film spalling-off, whereas NCD coatings undertook 400 N. Multilayered samples reached the highest load of 800 N, slightly higher than the MCD value as spalling-off is attained under a $J_2^{1/2}$ value of 30 GPa.

Acknowledgements

This work was conducted under the frame of the FCT project MULTIDIACOAT-PTDC/EME-TME/100689/2008. E. Salgueiredo, M. Amaral and F.A. Almeida gratefully acknowledge FCT for the grants SFRH/BD/41757/2007, SFRH/BPD/26787/2006 and SFRH/BPD/34869/2007, respectively.

References

[1] C.S. Abreu, M. Amaral, A.J.S. Fernandes, F.J. Oliveira, R.F. Silva, J.R. Gomes, Diamond Relat. Mater. 15 (2006) 739.

[2] Q. Wei, Z.M. Yu, M.N.R. Ashfold, J. Ye, L. Ma, Applied Surface Science 256 (2010) 4357.

[3] S.C. Tjong, H. Chen, Materials Science and Engineering R 45 (2004) 1.

[4] R. Ikeda, M. Hayashi, A. Yonezu, T. Ogawa, M. Takemoto, Diamond and Related Materials 13 (2004) 2024.

[5] F.A. Almeida, M. Amaral, F.J. Oliveira, A.J.S. Fernandes, R.F. Silva, Vacuum 81 (2007) 1443.

[6] C.S. Abreu, E. Salgueiredo, F.J. Oliveira, A.J.S. Fernandes, R.F. Silva, J.R. Gomes, Wear 265 (2008) 1023.

[7] S. Takeuchi, S. Oda, M. Murakawa, Thin Solid Films 398-399 (2001) 238.

[8] S. Takeuchi, M. Kojima, S. Takano, K. Kazutaka, M. Murakawa, Thin Solid Films 469-470 (2004) 190.

[9] M. Vojs, M. Veselý, R. Redhammer, J. Janík, M. Kadlečíková, T. Daniš, M. Marton, M. Michalka, P. Šutta, Diamond Relat. Mater. 14 (2005) 613.

[10] L. Schäfer, M. Höfer, R. Kröger, Thin Solid Films 515 (2006) 1017.

[11] F. Sun, Y. Ma, B. Shen, Z. Zhang, M. Chen, Diamond Relat. Mater. 18 (2009) 276.

[12] B. Shen, F. Sun, Diamond and Related Materials 18 (2009) 238.

[13] B. Shen, F. Sun, Z. Zhang, H. Shen, S. Guo, Transactions of Nonferrous Metals Society of China, 23 (2013) 161.

[14] R. Dumpala, M. Chandran, N. Kumar, S. Dash, B. Ramamoorthy, M.S. Ramachandra Rao, International Journal of Refractory Metals and Hard Materials 37 (2013) 127.

[15] M. Kadlečíková, M. Vojs, J. Breza, M. Veselý, Z. Frgala, M. Michalka, J. Matějková, A. Vojačková, T. Daniš, M. Marton, Microelectronics Journal 38 (2007) 20.

[16] J.M. Carrapichano, J.R. Gomes, F.J. Oliveira, R.F. Silva, Wear 255 (2003) 695.

[17] W. Wang, M. Hadfield, A. A. Wereszczak, Tribology International 43 (2010) 423.

[18] I. Khader, A. Kailer, J. Mater. Proc. Technol. 210 (2010) 1314.

[19] S.M. Wiederhorn, M.K. Ferber, Curr. Opin. Solid State Mater. Sci. 5 (2011) 311.

[20]Rolamentos Híbridos. Available from:

http://www.sferarolamentos.com.br/informacoes/Rolamentos%20Hibridos.pdf, (accessed in 26.04.2011)

[21] Silicon nitride (Si_3N_4) ceramic parts for automobiles – to make environmentally friendly automobiles. Available from: http://www.toshibatmat.co.jp/eng/list/ce_car.htm (accessed 26.04.13).

[22]Diesel fuel-injection components. Available from: http://global.kyocera.com/application/automotive/product/compo/pump.html (accessed 26.04.13).

[23] M.R. Soares, M. Belmonte, R.F. Silva, J. Appl. Phys. 94 (2003) 5633.

[24] F.A. Almeida, F.J. Oliveira, R.F. Silva, D.L. Baptista, S.B. Peripolli, C.A. Achete, Appl. Phys. Lett. 98 (2011) 171913.

[25] C.S. Abreu, M. Amaral, F.J. Oliveira, J.R. Gomes, R.F. Silva, Diamond Relat. Mater. 18 (2009) 271.

[26] E. Salgueiredo, F.A. Almeida, M. Amaral, M.A. Neto, F.J. Oliveira, R.F. Silva, Wear 297 (2013) 1064-1073.

[27] E.Salgueiredo, C.S. Abreu, M. Amaral, F.J. Oliveira, J.R. Gomes, R.F. Silva, Wear 303 (2013) 225.

[28] F.A. Almeida, M.M. Maru, M. Shabani, F.J. Oliveira, R.F. Silva, C.A. Achete, Wear 302 (2013) 1370.

[29] N. Chen, B. Shen, G. Yang, F. Sun, Appl. Surf. Sci. 265 (2013) 850-859.

[30] A.C. Ferrari, J. Robertson, Phys. Rev. B 63 (2001) 121405(R).

[31] H.B. Zhang,G. D. Lin, Z.H. Zhou, X. Dong, T. Chen, Carbon 40 (2002) 2429.

[32] M. Roy, V.C. George, A.K. Dua, P. Raj, S. Schulze, D.A. Tenne, G. Salvan, D.R.T. Zahn, Diamond Relat. Mater. 11 (2002) 1858.

[33] A.J.S. Fernandes, M.A. Neto, F.A. Almeida, R.F. Silva, F.M. Costa, Diamond Relat. Mater. 16 (2007) 757.

[34] S. Gupta, B.R. Weiner, W.H. Nelson, G. Morell, J. Raman Spectrosc. 34 (2003) 192.

[35] D.B Marshall, A.G. Evans, J. Appl. Phys. 56 (1984) 2632.

[36] M. Belmonte, A.J.S. Fernandes, F.M Costa, F.J. Oliveira, R.F. Silva, Diamond Relat. Mater. 12 (2003) 733.

[37] M. Nesládek, K. Vandierendonck, C. Quaeyhaegens, M. Kerkhofs, L.M. Stals. Thin Solid Films 270 (1995) 184.

[38] K. Mallika, R. Komanduri, Thin Solid Films 396 (2001) 145.

[39] D.M. Gruen, D.M. Annual Review of Materials Science 29 (1999) 211.

[40] V.L.Popov,ContactMechanicsandFriction,Springer-Verlag,Berlin,Heidelberg,

2010.

[41] J. Angus, in: Synthetic Diamond: Emerging CVD Science and Technology, K.E. Spear and J.P. Dismukes, John Wiley & Sons, Inc., New York, 1994.

[42] V.G. Ralchenko, A.A. Smolin, V.G. Pereverzev, E.D. Obraztsova, K.G. Korotoushenko, V.I. Konov, Y.V. Lakhotkin, E.N. Loubnin, Diamond Relat. Mater. 4 (1995) 754.

[43] S. Jeedigunta, Doctoral Thesis, University of South Florida, Department of Electrical Engineering, Tampa, FL, USA, 2008. Available from: http://scholarcommons.usf.edu/etd/316/ (accessed 26.04.13)

[44] B.S. Bal, M.N. Rahman, Acta Biomaterialia 8 (2012) 2889.

II.4. Interfaces in nano/microcrystalline multigrade CVD diamond coatings

Flávia A. Almeida[1*], Ermelinda Salgueiredo[1], Filipe J. Oliveira[1], Rui F. Silva[1], Daniel L. Baptista[2,3], Suzana B. Peripolli[4], Carlos A. Achete[2]

[1]*Department of Materials and Ceramic Engineering, CICECO, University of Aveiro, 3810-193 Aveiro, Portugal*
[2]*Inmetro - Divisão de Metrologia de Materiais - DIMAT, Av. Nossa Senhora das Graças 50, Xerém, Duque de Caxias, RJ - 25250-020, Brasil*
[3]*PPGMicro - Instituto de Física, Universidade Federal do Rio Grande do Sul, PortoAlegre, RS, 91501-970, Brasil*
[4]*Centro de Tecnologia SENAI Solda, Rua São Francisco Xavier, 601, Maracanã, Rio de Janeiro, 20550-011, Brasil*

ACS Appl. Mater. Interfaces 2013, 5, 11725−11729
DOI: dx.doi.org/10.1021/am403401s

Abstract

The interfaces of multilayered CVD diamond films grown by the hot-filament technique were characterized with high detail using HRTEM, STEM-EDX and EELS. The results show that at the transition from micro- (MCD) to nanocrystalline diamond (NCD), a thin precursor graphitic film is formed, irrespectively of the NCD gas chemistry used (with or without argon). On the contrary, the transition of the NCD to MCD grade is free of carbon structures other than diamond, the result of a higher substrate temperature and more abundant atomic H in the gas chemistry. At those transitions WC nanoparticles could be found due to contamination from the filament, being also present at the first interface of the MCD layer with the silicon nitride substrate.

Keywords: CVD diamond, multilayer, interface, high resolution transmission electron microscopy.

1. Introduction

Chemically vapor deposited (CVD) diamond coatings are used in wear resistant parts for demanding mechanical and tribological solicitations, due to properties such as high hardness and elastic modulus, chemical inertness and low self-friction coefficient. Microcrystalline diamond (MCD) grades ensure higher adhesion to suitable substrates, like silicon nitride (Si_3N_4) ceramics, when compared to nanocrystalline diamond (NCD) coatings.[1,2] Also, the hardness and Young's modulus values of NCD are slightly lower than those of MCD, which is attributed to the presence of sp^2 amorphous carbon phases incorporated at the grain boundaries.[3] However, the evolutionary crystal growth mechanism of MCD results in the increase of the crystal size with thickness, and thus of the surface roughness.[4] This has a negative effect in the behavior of cutting tools and components subjected to tribological contact, such as mechanical seals or drawing dies, by increasing the wear rates and the initial friction coefficients, compromising the efficiency and quality of the products.[5-7] Contrarily, the continuous renucleation process of the NCD film ensures an even crystallite size along the thickness, resulting in very smooth ending surfaces, ready for tribological applications.[8]

By combining the advantages of each type of diamond coating grade, while simultaneously minimizing their limitations, multilayered multigrade CVD diamond coatings are a promising solution to improve the tribological performance. In an earlier work,[9] high resolution transmission electron microscopy (HRTEM) and electron energy loss spectroscopy (EELS) characterization were crucial to fully understand the nature of the interface between monolayer MCD films and Si_3N_4 ceramic substrates. The formation of a diamond-like carbon interlayer was detected and, to a lesser extent, grain-to-grain direct transition of diamond to Si_3N_4 crystals with a 8.2° misorientation angle was demonstrated. So far, to our knowledge, the only study of interfaces using HRTEM within a multilayer coating, i.e. between diamond layers, is the work of Jiang and co-workers.[10] They characterized a bilayered MCD/NCD diamond coating on silicon substrates grown using a microwave plasma CVD reactor, assisted by a negative bias for NCD growth. At the MCD/NCD interface region, a local lattice distortion was observed within a range of several angstroms. They supposed that such feature was

induced by the negative bias application, by creating energetic ion bombardment to the diamond growing facets, which locally caused diamond lattice distortions. The subsequent insertion of C atoms did not follow the original crystallographic orientation, resulting in the secondary nucleation of NCD crystals.

In the present work, fourfold multilayered MCD/NCD multigrade diamond coatings were grown by hot filament chemical vapor deposition (HFCVD) technique. Very recently, it was shown that the interfaces between the two diamond types play an important role on the mechanical response of those multilayer structures.[11,12] The superior erosion behavior of the diamond multigrade coatings was attributed to the action of the MCD/NCD interfaces in deflecting cracks, thus acting as “energy sinks” to further propagation. Besides improved mechanical response, optical and electrical properties can also be influenced by the presence of impurities, porosity, non-diamond carbon content and other structural aspects at the MCD/NCD interfaces. The study of these features and their correlation with the deposition processes is the main subject of the present paper, and can be beneficial to tailor the properties for other applications, such as micro electrical mechanical systems, sensors and energy devices. It is thus imperative to carefully observe the diamond interfaces by high resolution electron microscopy and spectroscopic techniques. The knowledge of how the different layers and diamond grades connect to each other and the possible formation of graphitic interlayers are some of the questions to be answered. A detailed study of interfaces using high resolution transmission electron microscopy (HRTEM) and scanning TEM (STEM), coupled with electron energy-loss spectroscopy (EELS) is hereby presented.

2. Experimental

Fourfold multilayered MCD/NCD multigrade coatings were grown by hot filament chemical vapor deposition (HFCVD), starting with a first layer of adherent MCD onto the Si_3N_4 ceramic substrate and finishing with a smooth NCD top layer. Prior to diamond deposition all substrates were ultrasonically seeded during 1 h with a nanometric diamond (4–6 nm) powder suspension in ethanol, for diamond nucleation enhancement. One type of MCD and two types of NCD layers were involved. The

deposition conditions of each layer are given in Table 1 together with the filament carburization mode. The NCD diamond growth parameters differ from those of MCD firstly on the lower substrate temperature and, mainly, on the strategies used for enhancing diamond re-nucleation: i) in the case of the NCD-(CH_4) grade, it is achieved by carbon supersaturation coming from a high methane (CH_4) concentration; ii) for the NCD-(Ar) grade, besides a methane rich gas phase, the partial replacement of hydrogen (H_2) by argon (Ar) in the gas composition also contributes for the increased diamond re-nucleation.

Table 1 - Deposition conditions of the different diamond grades in HFCVD reactor.

	CH_4/H_2 ratio	Ar/H_2 ratio	Gas flow (sccm)	Total pressure (kPa)	Substrate temperature (°C)	Growth rate ($\mu m \cdot h^{-1}$)
Filament carburization	0.026	-	200	10.0	630	-
MCD	0.026	-	100	17.5	800	1.7
NCD-(Ar)	0.04	0.1	200	10.0	700	0.1-0.4**
NCD-(CH_4)	0.073	-	100	5.0	700	1.2

** depending whether it is a continuous or interrupted deposition procedure

Three types of diamond multilayers were designed: i) Multi-A, consisting on a fourfold MCD/NCD-(Ar)/MCD/NCD-(Ar) stacking performed in one single deposition step, by switching the deposition parameters without venting the reactor; ii) Multi-B, grown as Multi-A but with the NCD-(CH_4) grade replacing NCD-(Ar); iii) Multi-C, grown using the same deposition parameters of Multi-A but interrupting the process after each deposited layer to vent the reactor and to replace the tungsten filaments.

Diamond deposition was conducted in an in-house built 3 kW HFCVD reactor. Six tungsten wires (Ø=0.25 mm, 75 mm length) were placed at a constant distance of ~7 mm from the substrate. The filament temperature was measured with a two-color pyrometer (Raytek) and kept constant at about 2300 °C, while the substrate temperature was assessed by a K-type thermocouple inserted into the substrate holder, contacting the bottom face of the substrate. The samples were heated to

approximately 630 °C by thermal radiation, and additional heating was done by a graphite dissipating element for full temperature control.

The cross-sectional preparation of well-preserved interfaces for HRTEM/EELS characterization was only possible using the focused ion beam (FIB) technique (FEI Nova Nanolab 600), following an earlier optimized preparation protocol.[9] HRTEM and scanning TEM (STEM), coupled with EELS, were accomplished in a FEI Titan 80/300 apparatus equipped with a Gatan imaging filter Tridiem.

3. Results and discussion

A general cross section view of Multi-A coating is given in the conventional transmission electron microscopy (CTEM) micrograph of Fig.1a, in bright field mode, where the different layers are delimited by net interfaces, corresponding to the transitions between the diamond grades. The Si_3N_4 substrate is evident at the bottom, well defined by the faceted Si_3N_4 grains. Fig. 1b is an image of scanning transmission electron microscopy in high angle annular dark field (STEM-HAADF) of the same region of Fig. 1a and it highlights the larger, micrometric, diamond crystals in the case of MCD layer, in contrast to the nanometric crystals of the NCD–(Ar) layers. In the case of MCD, grains form perpendicularly to the substrate, while in NCD-(Ar) deposition equiaxed crystallites grow. These features are better visualized in the higher magnifications images of Figs 1c and 1d. Furthermore, the Z-contrast imaging given by the STEM-HAADF reveals that the NCD-(Ar)/MCD and MCD/NCD-(Ar) transitions are very distinct: an abrupt interface is revealed in the former (Fig. 1c), while an interphase transition appears in the latter (Fig. 1d). In the MCD/NCD-(Ar) transition, approximately 50 nm thick, dark contrast nodules are visible in all extension, corresponding to graphitic carbon.

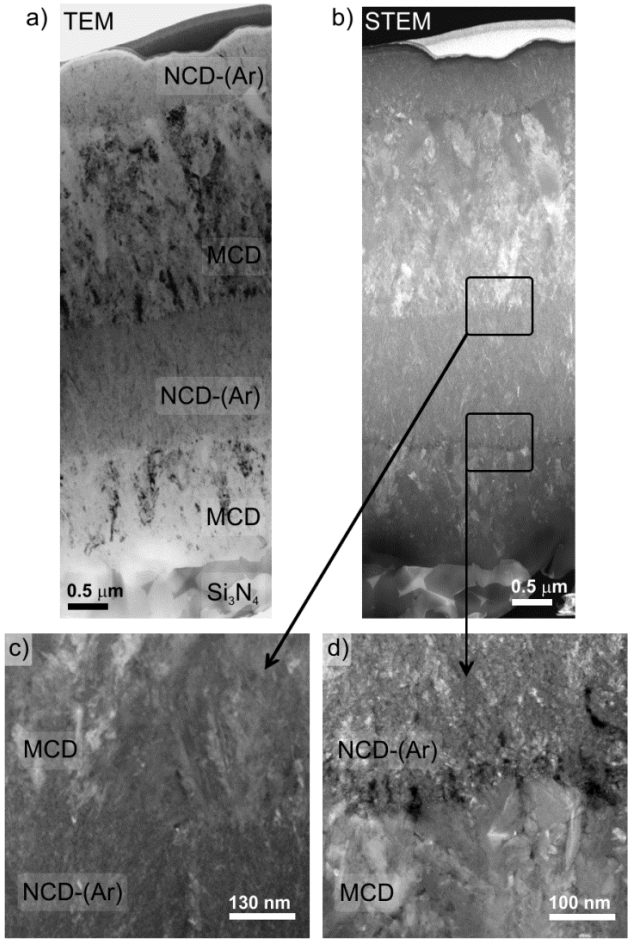

Figure 1 - Cross sectional view of Multi-A sample: a) bright field mode CTEM micrograph; b) same region in HAADF-STEM mode; c) and d) high magnifications of the NCD-(Ar)/MCD and MCD/NCD-(Ar) transitions, respectively.

A cross section view of sample Multi-B is presented in Fig.2a and by the superposition of Fig. 2b (after sample thinning). No significant differences could be found in the nature of the interfaces relatively to those of Multi-A coatings. The higher magnification HRTEM image in Fig. 2c emphasizes the structure of the dark contrast nodules that appear in the MCD/NCD transition zone of both types of coatings. Straight and wavy fringes of graphite-like structures are visible as well as some loop formation of graphite sheets, where there is no stacking order between adjacent graphene planes, typical of disordered turbostratic graphite.[13] Their graphitic character is confirmed by the interplanar measurement of the inverse fast Fourier transform (IFFT) filtered image (inset of Fig. 2c) and electron energy loss spectroscopy (EELS) (inset of Figs. 2a and 2b).

During the different diamond coating transitions, several time-dependent events take place: i) change of chamber pressure by a few seconds of purge, ii) introduction of the new gas mixture, iii) stabilization of new pressure value; iv) fluctuation of filament and substrate temperatures; and v) new gas composition under equilibrium. Some minutes are necessary for the stabilization of growth conditions, where graphite deposition may take place as shown above in Fig. 1d and Fig. 2. This graphitic phase appears only in the transition from MCD to NCD deposition conditions, most likely due to a combined effect of a lower deposition temperature of NCD and the lower amount of H_2 supplied in the gas mixture (Table 1). It is well known that there is a competition between the sp^2 and sp^3 carbon deposition during CVD diamond growth, where the atomic H plays a decisive etching role of the graphitic phases.[14] During that transition and before the NCD growth surface is established, the atomic H content decreases to a level that is not sufficient for total removal of the graphitic phases. A progressive transition from MCD to NCD growth conditions would prevent the formation and stabilization of graphite.

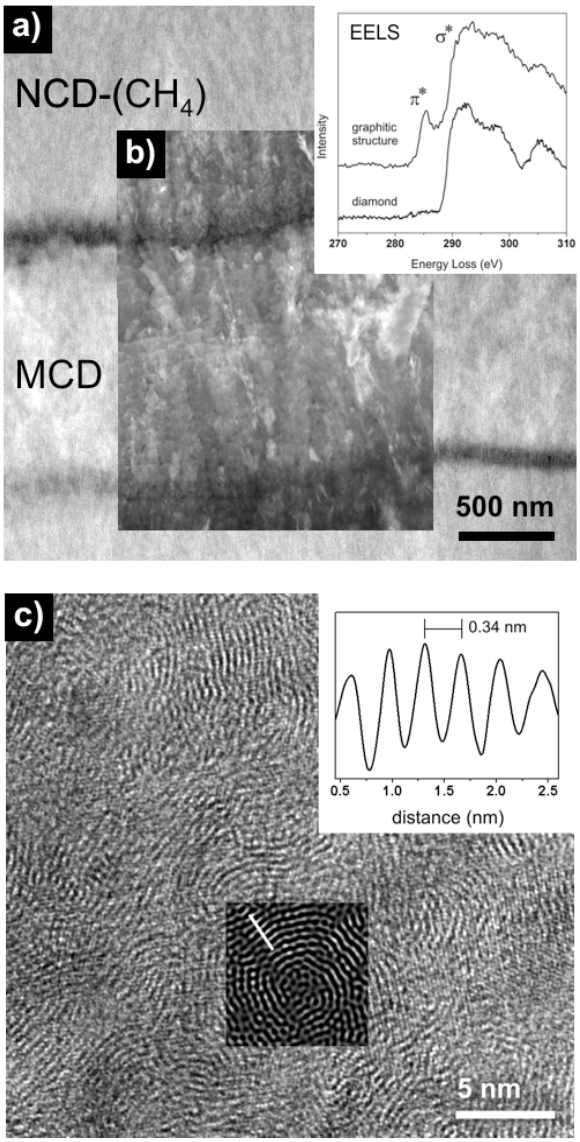

Figure 2 - a) cross sectional view of Multi-B sample; b) superposition after sample thinning; c) higher magnification of the black nodules in MCD/NCD transition. Inset in a) and b): electron energy loss spectroscopy (EELS) of the MCD/NCD-(CH_4) interface region Inset in c: inverse fast Fourier transform (IFFT) of the black nodules in that region, showing their graphitic character.

Spatially localized STEM-EELS spectra on the inset of Fig. 2a,b present both 1s → σ* and 1s → π* C electronic transitions, at around 289 and 285 eV, respectively. The spectrum of crystallites from the bulk NCD region shows only the typical diamond σ* peaks, indicating a good quality of the diamond nanocrystals. Hoffman *et al.*[15] observed the formation of a thin precursor graphitic film on silicon followed by the deposition of a film of diamond character as a function of substrate temperature in the

direct current glow discharge (DCGD) CVD method. They determined that at a certain temperature (of about 880 °C in that case), the evolution of local stresses reached a maximum value, suggesting that it is the relaxation of these stresses that leads to the transformation of the graphitic material into the nanodiamond phase. Thus, the stabilization of the diamond phase would be given by the hydrogen adsorption/desorption process in the nucleation and growth of the nanocrystalline diamond films in a narrow range of temperatures. It is worth noting that in the NCD-(Ar)/MCD transition (Figs. 1b and 1c), when MCD deposition conditions are imposed and graphitic phases form, the higher substrate temperature and more abundant atomic H do not allow these phases to survive the subsequent diamond growth.

Fig. 3a is a magnified STEM-HAADF micrograph of the MCD/NCD-(Ar) interface region, showing white contrast nanoparticles, also present between the Si_3N_4 substrate and the first MCD layer (Fig. 3b). Though, these particles were never found inside the diamond layers. Energy dispersive X-ray (STEM-EDX) analysis (Fig. 3c) of that region shows the characteristic L and M peaks of tungsten that can only be due to contamination from the filament.

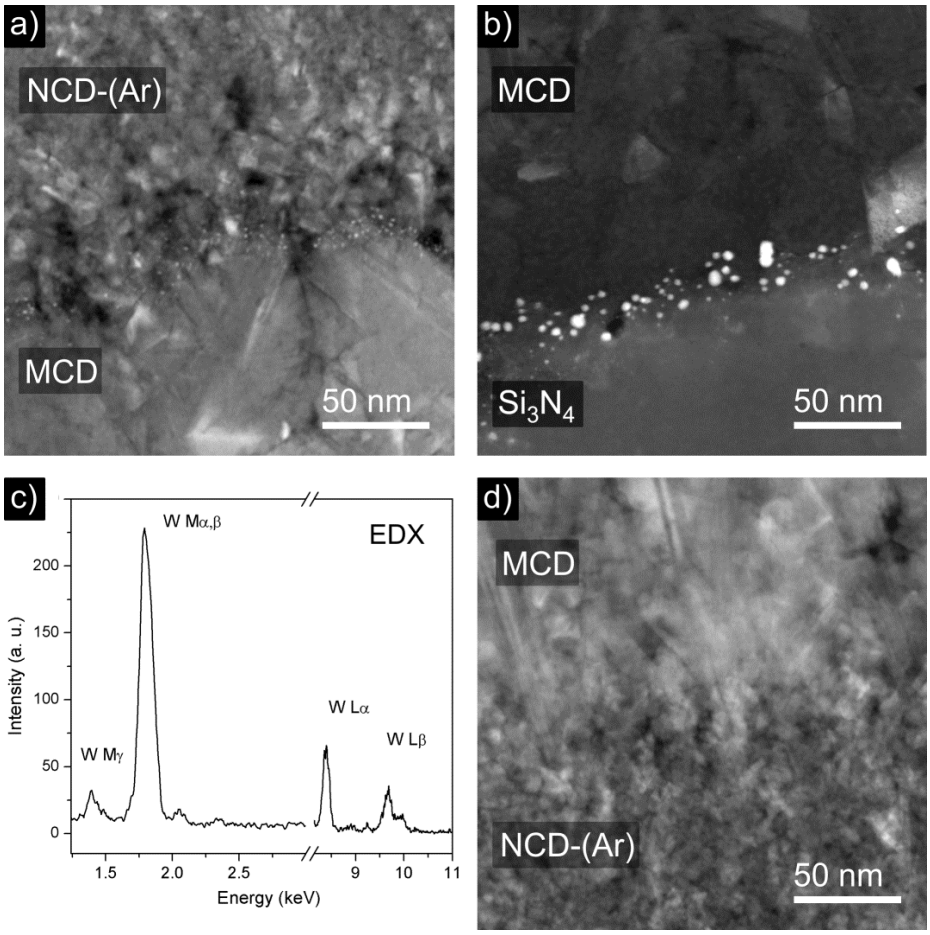

Figure 3 - Interfaces details of Multi-A sample: a) STEM-HAADF micrograph of the MCD/NCD-(Ar) interface region; b) of the Si_3N_4/MCD interface region; c) Energy dispersive X-ray (STEM-EDX) analysis showing the characteristic L and M peaks of tungsten; d) STEM-HAADF micrograph of the NCD-(Ar)/MCD interface region

It is well known that contamination of the coating by tungsten from filament vaporization can happen, even when the filaments are previously carburized for long periods of time.[16-18] Neto *et al*.[19] used this phenomenon to produce bilayered coatings of diamond/WC over Si in a hot filament reactor starting with a W film. In the present work, tungsten carbide nanoparticles at the MCD/NCD-(Ar) (Fig. 3a) and Si_3N_4/MCD (Fig. 3b) interfaces could only be visualized at high magnifications under TEM/STEM and for carefully prepared samples.

The filament carburization step before the growth of the first MCD layer is carried out with the Si_3N_4 substrates inside the reactor, so, W vaporization from the filament occurs before an outer layer of W_2C can be formed. This probably explains why larger nanoparticles (5-10 nm) are found at the Si_3N_4/MCD transition (Fig. 3b) than

at the MCD/NCD-(Ar) ones (~3 nm, Fig. 3a). The last diamond layer transition is from MCD to NCD grade, where the tungsten carbide nanoparticles are more easily found than in the case of NCD to MCD switching, as seen in the high magnification of Fig. 3d. This phenomenon happened irrespectively of the NCD growth condition, whether by Ar addition (Multi-A coating) or CH_4 supersaturation (Multi-B one). In the case of MCD to NCD transition, an abrupt increase of the filament temperature occurs (to ~2500 °C) when adding larger quantities of CH_4 and/or Ar to the reactor. This compels a rapid adjustment of the total current in order to maintain the temperature range of deposition (54 A in the case of MCD, 50 A for NCD-(CH_4) and 48 A for NCD-(Ar) depositions, for six filaments). This temperature increase probably causes WC dissociation, as reported in the work of Menon *et al*.,[17] leaving W vulnerable to vaporization before carburization restarts under moderate filament temperatures. Nevertheless, tungsten vaporization is likely to happen in a few instants, as no noticeable amount of WC nanoparticles is found throughout the cross section of the NCD films. Moreover, a "poisoning" or "sooting" effect of graphitic deposition at the filament surface occurs, especially in the case of Multi-A coating (with Ar addition). These graphitic depositions reduce the number of active sites available for the H_2 decomposition reactions,[20,21] accounting for the decrease of growth rate and re-nucleation effects of the NCD films with time. Inspection of the filaments after the deposition of Multi-A coatings showed the formation of a thick and stable carbon layer around them, with the same aspect as the one found in the work of May *et al*., [22] which is responsible by the stopping of the diamond film growth.

However, by venting the reactor and renewing the tungsten filaments after the deposition of each diamond layer, this drawback could be easily overcome in the growth of Multi-C samples. In the case of Multi-C films, large WC nanoparticles, as those seen at the Si_3N_4/MCD interface for the other samples, are visible in all the diamond transition regions (Fig. 4). Graphitic phases, especially at the MCD/NCD transition, also form as in the Multi-A and Multi-B samples. The micrograph of Fig. 4b presents the region between the first MCD and the subsequent first NCD film, where a transition layer is clearly marked by the WC nanoparticles. This transition layer, approximately 150 nm thick, develops during the 10 min of carburization. Although during this stage the filaments consume C from the reactive species, the previous MCD

layer continues to grow until the deposition condition changed fully to the NCD one. This feature also happens in the NCD/MCD interface, where a MCD transition layer (formed during carburization) is recognizable below the MCD coating, formed during the growth step (Fig. 4c).

The crystallographic analysis of the diamond layers is given in Fig. 4d, in the form of overlapping selected-area electron diffraction (SAED) projections of both diamond grades. Sharp Bragg reflection spots are visible at the left-hand side, in the case of MCD, and sharp ring patterns at the right-hand side of Fig. 4d, for the NCD-(Ar) layer; the latter being indicative of the randomness of the crystallite orientation. All the SAED patterns correspond to the diamond (111), (220), (311), (222), (400) and (331) planes, from inner to outer rings, respectively.

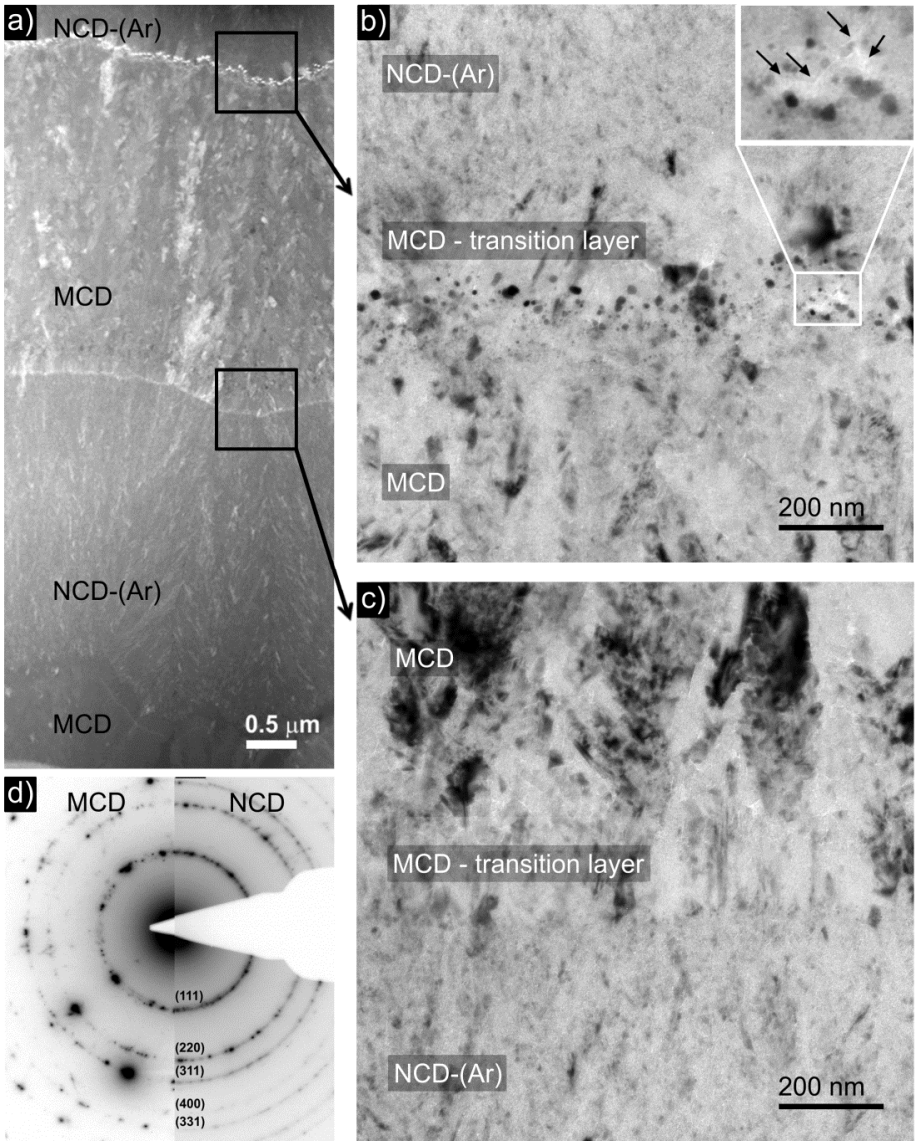

Figure 4 - a) Cross sectional view of Multi-C sample: a) general view of the different diamond interfaces in STEM mode; b) and c) CTEM micrograph of the MCD/NCD-(Ar) and NCD-(Ar)/MCD transitions, respectively; d) selected-area electron diffraction (SAED) overlap projections of both diamond grades.

This detailed characterization of the different types of interfaces helps reinforcing the conclusions of two recently published papers on the mechanical performance of these multilayer coatings under erosive wear[11] and in reciprocating dry contacts.[12] Particularly, in the first paper, interfacial failure is clearly revealed at the transition between MCD and the top NCD layer. The combined role of graphitic and WC nanoparticles contributed in fact to enhance the erosion resistance by acting as "energy sink" toughening mechanism to the further development of cracks into the

substrate/diamond interface region. As a result, the induction time to film delamination under SiC particles impact more than duplicates in the case of multilayer coatings compared to diamond monolayers. For the tribological tests, it was found that these composite coatings exhibit a critical load before delamination (130–200 N) much larger than mono- (60–100 N) or even bilayer coatings (110 N), for films of the same thickness (~10 μm). This was accompanied by a progressive wear of the NCD top layer that acted sacrificially, while the harder microcrystalline diamond layer kept the residual stresses at lower levels.

Conclusions

Multilayered MCD/NCD diamond coatings have been successfully grown by hot-filament CVD using continuous and discontinuous approaches. Three different multigrade diamond films were obtained, by changing the deposition parameters of the nanocrystalline diamond (with or without argon) and the transition mode between the diamond grades (continuously or venting the reactor after each layer deposition and changing the tungsten filaments). Cross-sectional samples, with well-preserved interfaces, were prepared by FIB and were successfully characterized by means of HRTEM, STEM-EDX and EELS techniques.

The interface between the diamond layers depends on the switching order: from MCD to NCD or from NCD to MCD. In the former, the transition is characterized by the formation of graphite-like structures, as confirmed by the more prominent π^* C peak at 285 eV in spatially resolved STEM-EELS. The higher carbon content (and lower H concentration) of both NCD growth parameters allowed the formation of those sp^2 structures. This occurs before stabilization of the hydrogen adsorption/desorption process allows the nucleation of the diamond phase. On the contrary, the transition from the NCD to MCD grade is free of carbon structures other than diamond. In this case, the more abundant atomic H of the MCD deposition conditions does not allow the sp^2 phases to survive etching.

Another common feature found in all the interfaces of MCD to NCD transitions, for both kinds of NCD, is the presence of nanometric round-shaped particles of tungsten carbide, which arise from filament contamination. At this transition, the parameters imposed to grow the NCD crystals (higher CH_4 concentration and/or argon

addition), increase considerably the filament temperature, probably dissociating the carburized layer around the filament and leaving W vulnerable to vaporize.

The addition of argon also changes the filament structure, creating a thick and stable carbon layer around it. This causes the loss of filament efficiency, decreasing the diamond film growth rate. So, when using argon to perform the NCD layer of a multilayered diamond film, aiming a well-controlled layer thickness, the discontinuous process of stopping the deposition and replacing the filaments showed to be a better solution for the NCD-Ar coatings.

Acknowledgements

Brazil/Portugal collaboration was undertaken under CNPq project no. 402251/2012-1 “Nanostructured carbon allotropes”. Flávia A. Almeida and Ermelinda Salgueiredo acknowledge FCT for the grants SFRH/BPD/34869/2007 and SFRH/BD/41757/2007, respectively. Authors acknowledge Foundation for Science and Technology (FCT, Portugal) for funding the projects MULTIDIACOAT PTDC/EME-TME/100689/2008 and PEst-C/CTM/LA0011/2013.

References

(1) Almeida, F. A.; Amaral, M.; Oliveira, F. J.; Fernandes, A. J. S.; Silva, R. F. *Vacuum* **2007**, *81*, 1443-1447.

(2) Abreu, C. S.; Amaral, M. S.; Fernandes, A. J. S.; Oliveira, F. J., Silva, R. F.; Gomes, J. R. *Diamond Relat. Mater.* **2006**, *15*, 739-744.

(3) Catledge, S. A.; Borham, J; Vohra, Y. K.; Lacefield, W. R.; Lemons, J. E. *J. Appl. Phys.* **2002**, *91*, 5347-5352.

(4) Kulisch, W.; Popov, C. *Phys. Status Solidi A* **2006**, *203*, 203-219.

(5) Almeida, F. A.; Amaral, M.; Oliveira, F. J.; Silva, R. F. *Diamond Relat. Mater.* **2006**, *15*, 2029-2034.

(6) Mubarok, F.; Carrapichano, J. M.; Almeida, F. A.; Fernandes, A. J. S.; Silva, R. F. *Diamond Relat. Mater.* **2008**, *17*, 1132-1136.

(7) Sun, F.; Ma, Y.; Shen, B.; Zhang, Z.; Chen, M. *Diamond Relat. Mater.* **2009**, *18*, 276-282.

(8) Gruen, D. M. *Annu. Rev. Mater. Sci.* **1999**, *29*, 211-259.

(9) Almeida, F. A.; Oliveira, F. J.; Silva, R. F.; Baptista, D. L.; Peripolli, S. B.; Achete, C. A. *Appl. Phys. Lett.* **2011**, *98*, 171913-1 - 171913-3.

(10) Jiang, N.; Sugimoto, K.; Nishimura, K.; Shintani, Y.; Hiraki, A. *J. Cryst. Growth* **2002**, *242*, 362-366.

(11) Salgueiredo, E.; Almeida, F. A.; Amaral, M.; Neto, M. A.; Oliveira F. J.; Silva, R. F. *Wear* **2013**, *297*, 1064-1073.

(12) Salgueiredo, E.; Abreu, C. S.; Amaral, M.; Oliveira, F. J.; Gomes, J. R.; Silva, R. F. *Wear* **2013**, *303*, 225-234.

(13) Pimenta M. A.; Dresselhaus, G.; Dresselhaus, M. S.; Cançado, L. G.; Jorio, A.; Saito, R. *Phys. Chem. Chem. Phys.* **2007**, *9*, 1276-1291.

(14) Frenklach, M. In *Diamond and diamond-like films and coatings*; Clausing, R. E.; Horton, L. L.; Angus, J. C.; Koidl, P., Eds.; Plenun Press: New York, 1991, p 499.

(15) Hoffman, A.; Heiman, A.; Strunk, H. P.; Christiansen, S. H. *J. Appl. Phys.* **2002**, *91*, 3336-3344.

(16) Zeiler, E.; Schwarz, S.; Rosiwal, S. M.; Singer, R. F. *Mater. Sci. Eng., A* **2002**, *335*, 236-245.

(17) Menon, P. M.; Edwards, A.; Feigerle, C. S.; Shaw, R. W.; Coffey, D. W.; Heatherly, L.; Clausing, R. E.; Robinson, L.; Glasgow, D. C. *Diamond Relat. Mater.* **1999**, *8*, 101-109.

(18) Contreras, O.; Hirata, G. A.; Avalos-Borja, M. *Appl. Surf. Sci.* **2000**, *158*, 236-245.

(19) Neto, M. A.; Silva, E. L.; Fernandes, A. J. S.; Oliveira, F. J.; Silva, R. F. *Surf. Coat. Technol.* **2012**, *206*, 3055-3063.

(20) Dandy, D.; Coltrin, M. E. *J. Appl. Phys.* **1994**, *76*, 3102-3113.

(21) Yehoda, J. E. In *Diamond Films Handbook*; Asmussen, J. and Reinhard, D. K., Eds.; Marcell Dekker: New York, 2001, p 119.

(22) May, P. W.; Smith, J. A.; Mankelevich, Y. A. *Diamond Relat. Mater.* **2006**, *15*, 345-352.

Chapter III

Wear behaviour of the diamond coatings

A description of the substrate preparation prior to diamond deposition is presented in the first part of this chapter (Chapter III.1). Polishing, plasma etching and ultrasonic scratching of the silicon nitride ceramics are addressed, highlighting the importance of surface preparation in the adhesion of the thin films. The apparatus used in the experimental part of the work, devoted to the erosive wear tests and the tribological sliding, both in dry and lubricated conditions is also presented (Chapter III.2).

The investigations done regarding the wear behaviour of the diamond coatings were reported on three SCI papers. This chapter is divided in three sections that correspond to the content of these publications in relevant journals of this research area:

- Chapter III.3 reports the erosion resistance to SiC particles of mono-, bi- and multilayer designed diamond coatings on Si_3N_4 ceramic substrates. An analytical model of the stress field distribution within the coatings, based on the von Mises criterion, was developed to elucidate the erosive mechanical behaviour of the different diamond composites.

- Chapter III.4. is focused on the self-mated tribological behaviour of monolayer, bilayer and multilayer micro- and nanocrystalline diamond coatings, both in high-load (max. 200 N) short-term tests (86 m) and endurance tests (60 N; 691 m).

- Chapter III.5 deals with the tribological behaviour of the mono-, bi- and multilayered diamond coatings on self-mated systems in lubricated sliding, using physiological fluids (HBSS and FBS).

III.1. Surface preparation of Si_3N_4 ceramic substrates

Of high importance regarding adhesion is the surface preparation of the Si_3N_4 substrates for CVD diamond deposition. In this work, the surfaces of the substrates were usually prepared, according to the following steps:

i. Grinding with a 15 μm diamond slurry (Diamit, Industrial Diamond), in an rotationary machine (Kemet 15) over a cast iron plate;
ii. polishing with a 15 μm diamond slurry in an automatic polishing machine (200 rpm) (Metaserv 200, Buehler) over a hard cloth (Struers, MD-Plan) with a 15 μm diamond suspension;
iii. polishing with colloidal silica, 0,25 μm (SBT, South Bay Technologies) over a hard cloth (MD-Nap);

After polishing, the Si_3N_4 based ceramics were chemically etched by a CF_4 plasma for 10 min in a RF generator (13.56 MHz, EMITECH K1050X, Ltd.). Several etching processes are known, using different mixtures of gases, types of reactors, pressures, and temperatures. Gas chemistries combinations include gases such as CF_4, H_2, O_2, Ar, N_2, SF_6, Kr, and Cl. The etching may be performed through plasma processing techniques, such as electron cyclotron resonance (ECR), inductively coupled plasma (ICP), or parallel plate reactive ion etching (RIE) [1, 2, 3]. Very low pressures (in the mTorr range) are used to remove material through the bombardment (as well as chemical reaction) rather than chemical surface reactions only (as it is the case for higher pressures).

Plasma etching (PE) techniques comprise two related mechanisms: chemical reactive etching and physical sputtering. Chemical reactive etching is the main mechanism involved in most dry etching techniques, but is isotropic and leads to pits. The sputtering mechanism is anisotropic but has a lower etch rate. Controlling the contributions of each of these mechanisms is the key to achieve a good etch morphology [4]. Pressure is a key factor to achieve the adequate ratio of these two mechanisms. In order to optimize the etching process, the coupled effects of RF power, reactor pressure and reactant flow rate must be regarded [5, 6].

The main advantages of PE include directional selectivity of the reactions that occur on the substrate surface, reduced processing time and elimination of wet chemicals that are used in the conventional etching processes [7]. The main drawbacks are the nonuniformity of the etching rate, and consequent irregular film thickness. The issue of surface chemistry associated with the plasma etching process was also addressed by Graves and Humbird [8].

A systematic study on the optimal etching parameters was conducted in the present work. Figure 1 depicts the SEM micrographs of the Si_3N_4 based ceramics after 5 (Figure 1a), 10 (Figure 1b), 15 (Figure 1c) and 20 min (Figure 1d) of CF_4 plasma attack. It is clear in all photos that the Si_3N_4 grains are preferentially etched, which causes the crystals to sink in, revealing the ceramic microstructure [9]. This is due to the atomic F generated from the CF_4 discharge plasma, which is responsible for the chemical attack of silicon and Si compounds. Figures 1c and 1d show a strong chemical modification of the surface by the Si fluorination, with a strong degradation of the surface and an abrupt increase in roughness. The vitreous layer formed on the surface is very fragile and compromises adhesion of the coatings. The optimal etching time was therefore set in 10 min, for all experiments, for it was later proven to provide the best compromise between roughness and adhesion.

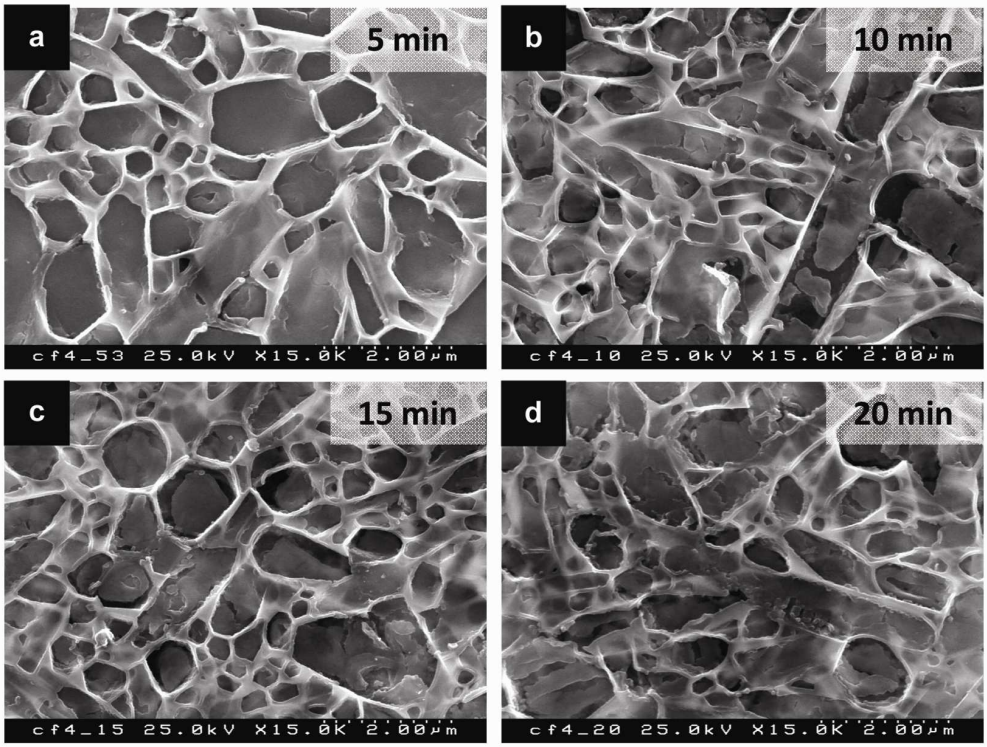

Figure 1 - SEM micrographs of the Si_3N_4 ceramic surface after PE for a) 5min; b) 10 min; c) 15 min and d) 20 min.

Finally the ceramic substrates were ultrasonically scratched during 1 h with a nanometric diamond powder suspension in ethanol, for diamond nucleation enhancement. Ultrasonical abrasion or mechanical scratching of the substrate with a diamond powder ate the most employed techniques for enhancing the nucleation density [10, 11]. Nucleation densities as high as 10^{11} cm^{-2} can be achieved with this method.

III.2. Tribological characterization and erosive wear experiments

The tribological behaviour of diamond self-mated pairs was evaluated in dry and lubricated conditions. For adhesion evaluation of the diamond coatings on the silicon nitride ceramics, erosive wear tests were conducted. A brief description of the equipment and experimental conditions used in this work are further presented.

Erosive wear

The apparatus presented in Figure 2 is a solid particle erosion equipment developed in our research group, to allow testing according to ASTM G76-95 [12].

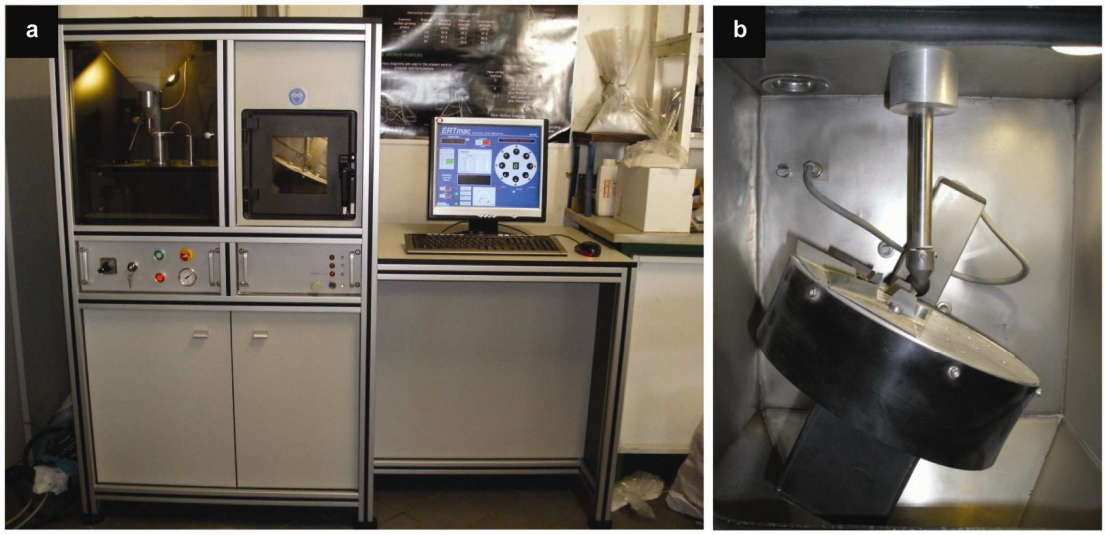

Figure 2 - Solid particle erosion equipment used in the experimental part of the work: a) general view, b) dust erosion chamber with the aluminium plate containing the sample holders

The erodent particles enter the gas stream directed to the samples. This system allows a wide range of particle sizes, shapes, and velocities. The erodent particles are accelerated into a small diameter jet by air pressure and blasted against a flat sample. The dust jet diameter is smaller than the sample area of the sample, so both sample holder and jet are articulated meaning that the sample can be moved to expose unworn areas to the dust jet. A small hole, appropriate to the size of the erodent particles, connects a reservoir where a large great amount of erodent can be stored. The erodent is fed into a rotating table that provides a very accurate and uniform dust flow, and is accelerated along a system to strike the specimens positioned around the perimeter of the enclosure. The amount of abrasive accelerated is controlled by the rotation imposed to the rotating table.

The particles are suctioned and sent to the acceleration system where they are mixed with air, accelerated to the target material causing erosive wear. The suction is guaranteed by the venturi positioned at the exit of the nozzle. The nozzle is a stainless

steel tube of ~3.8 mm inner diameter and 35 mm long. Pressure can vary from 0.5 to 5 bar, generating a wide range of particle velocities. Dust velocity is determined as a function of the nozzle inlet pressure and the particle size by prior calibration. The samples are motionless and mounted on an aluminium plate. Impact angles can vary from 30 to 90°. Flow rate, velocity and impact angle are controlled independently, providing an excellent capability to parametrically evaluate the response of materials to solid particle impact effects. A similar design for a gas-blast erosion test in which particles are accelerated along a parallel cylindrical nozzle and strike a plane coated specimen was reported by Hutchings [13].

Tribological testing

Laboratory tests are used in the study of friction and wear phenomena due to the much lower costs, when compared to field tests. Also, they give the possibility to adjust, sustain and change the operating parameters, i.e. to analyse their influence on the tribological behaviour. Furthermore, model tests can be used for screening and selection of materials, and allow the simulation of otherwise complex systems using relatively simple arrangements, which is of particular relevance in the study of basic mechanisms of friction, wear and lubrication [14].

To study the wear mechanisms and perform wear measurements, namely in total replacement hip joints, different types of equipment are commonly used: pin-on-disk machines, pin-on-plate machines and joint simulators. Pin-on-disc is particularly useful for the evaluation of the nature of wear and friction under steady-state conditions of load, sliding speed and environment. Although sacrificing the steady sliding between specimens, the pin-on-plate machines partially simulate the reciprocating action usually associated with the hip joint. However, for a comparative performance of different materials, joint simulators should be used [15].

Ball-on-Flat (BOF) counterformal asymmetrical design are particularly adequate for tribotests because of its overall combination of suitable features, namely the reciprocating motion, i.e. having the type of motion similar to the ones generally found in biotribological assessment using simple low cost designs [16]. It also has the advantage that relatively low loads provide high surface pressures, useful in tribo-

testing aimed at highly demanding tribological applications (like cutting tools or prosthetic joints).

In the present work, self-mated diamond systems (discs and balls/pins) were tested in a ball-on-flat (pin-on-plate) adapted tribometer (PLINT TE67/R), shown in Figure 3a. The upper ball diamond-coated specimen is fixed on the sample holder arm, which is in contact with a load cell that is used to measure the tangential force (Figure 3b. The flat diamond-coated specimen is fixed on the lower oscillating table, to reproduce the reciprocating motion. An unlubricated reciprocating sliding arrangement was used for the dry sliding experiments, while in lubricated sliding two physiological fluids were used (Hanks' balanced salt solution, HBSS, and Fetal Bovine Serum, FBS). Lubricants were supplied to the contact region in a pool type configuration (Figure 3c). All tests were performed in ambient air (R. H.∼50%–60%) at room temperature, with constant frequency (1 Hz) and stroke length (6 mm). The tests were carried out using two different length scales: the standard ones with duration of 2 h, representing a sliding distance of ∼86 m, and the endurance tests, corresponding to a sliding distance of ∼691 m.

The shorter tests (2h) were used to study the running-in regime, using higher acquisition rates to more accurately record variations on the friction signal, and also for screening the different diamond films regarding their threshold loads for the different sliding conditions and applied loads. The endurance tests allowed the study of the steady-state regime, fatigue effects, possible occurrence of coating failure due to progressive wear to the substrate, measure the steady-state friction coefficient and assess with higher accuracy the wear rates of the diamond coatings (reducing the contribution of the running-in more intense surface interactions). After the experiments, the samples are removed from the tribometer and cleaned in an ultrasonic bath prior to wear assessment, to remove non-adherent wear debris particles.

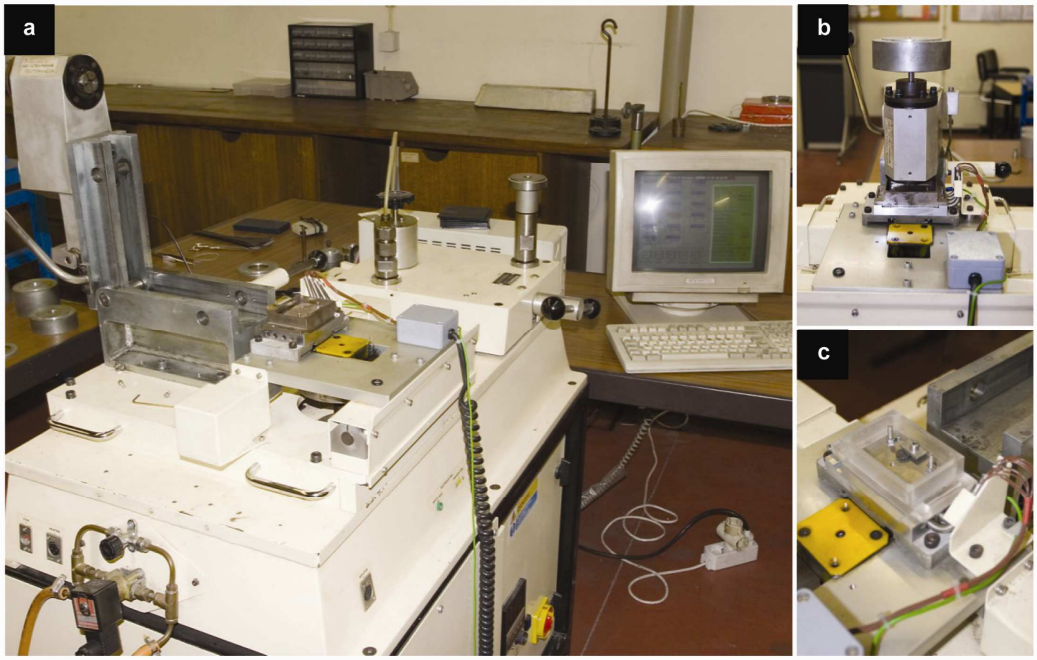

Figure 3 - Ball-on-flat adapted tribometer (PLINT TE67/R) used for tribo-testing; a) general view of the equipment and data acquisition unit; b) tribometer's upper arm and static applied loads and c) sample holder for lubricated tests, showing the diamond coated Si_3N_4 flat specimen.

References

[1] I. Friel, S.L. Clewes, H.K. Dhillon, N. Perkins, D.J. Twitchen, G.A. Scarsbrook, Diamond Relat. Mater. 18 (2009) 808.

[2] C.L. Lee, E. Gu, M.D. Dawson, I. Friel, G. A. Scarsbrook, Diamond Relat. Mater. 17 (2008) 1292.

[3] D.T. Tran, T.A. Grotjohn, D.K. Reinhard, J. Asmussen, Diamond Relat. Mater. 17 (2008) 717.

[4] G.F. Ding, H.P. Mao, Y.L. Cai, Y.H. Zhang, X. Yao, X.L. Zhao, Diamond Relat. Mater. 14 (2005) 1543.

[5] E. Drift, R. Cheung, T. ZijIstra, Microelectron. Eng. 32 (1996) 241.

[6] T. Ižák, A. Kromka, O. Babchenko, M. Ledinský, K. Hruška, E. Verveniotis, Vacuum 86 (2012) 799.

[7] A. Armaou, J. Baker, P.D. Christofides, Chem. Eng. Sci. 56 (2001) 1467.

[8] D.B. Graves, D. Humbird, Appl. Surf. Sci. 192 (2002) 72.

[9] M. Belmonte, V.A. Silva, A.J.S. Fernandes, F.M. Costa, R.F. Silva, J. Am. Ceram. Soc. 86 (2003) 74.

[10] S. Iijima, Y. Aikawa, K. Baba, Appl. Phys. Lett. 57 (1990) 2646

[11] W. Zhu, R.C. McCune, J.E. deVries, M.A. Tamor, K.Y.S. Ng, Diamond Relat. Mater. 4 (1995) 220.

[12] ASTM, Standard test method for conducting erosion tests by solid particle impingement using gas jets, Editor (1995) 308 .

[13] I.M. Hutchings, Tribol. Inter. 31 (1998) 5.

[14] K.H. Zum Gahr, Microstructure and Wear of Materials, Number 10 *in* Tribology Series, Elsevier Science Publishers, Amsterdam, The Netherlands, (1987) 118.

[15] Z.M. Jin, M. Stone, E. Ingham, J. Fisher, Current Orthopedics 20 (2006) 32.

[16] J.H. Dumbleton, Tribology of natural and artificial joints, Number 3, *in* Tribology Series, Elsevier Scientific Publishing Company, Amsterdam, The Netherlands (1981).

III.3. A multilayer approach for enhancing the erosive wear resistance of CVD diamond coatings

E. Salgueiredo[a]; F.A. Almeida[a,*]; M. Amaral[a,b]; M.A. Neto[a]; F.J. Oliveira[a]; R.F. Silva[a]

[a]*CICECO, Materials and Ceramic Engineering Dept., University of Aveiro, Campus de Santiago, P-3810-193 Aveiro, Portugal*

[b]*I3N, Physics Dept., University of Aveiro, Campus de Santiago, P-3810-193 Aveiro, Portugal*

Wear 297 (2013) 1064–1073

DOI: 101016/jwear.2012.11.051

Abstract

The erosive wear behavior of mono-, bi- and multilayered diamond composite coatings grown by hot filament chemical vapor deposition (HFCVD) is investigated. The effect of the surface pre-treatment on the silicon nitride substrates was firstly evaluated revealing that flat lapping mechanical treatment combined with chemical CF_4 plasma etching is the best surface preparation to achieve high adhesion levels. Multilayers were designed to combine the excellent adhesion of microcrystalline diamond (MCD) with a top nanocrystalline diamond (NCD) layer of reduced surface roughness. Indeed, the multilayered diamond coatings revealed the best erosive resistance, whose damage occurred by gradual loosening of material from the outer layer after longer testing time. The absence of areas with film spallation or substrate exposure is given by the action of the MCD/NCD interfaces in deflecting cracks, thus acting as "energy sinks" to further propagation. An analytical model of the stress field distribution within the coatings based on the von Mises criterion was developed to elucidate the erosive mechanical behavior of the different diamond composites.

Keywords: CVD diamond multilayers; Erosive wear; Adhesion; Stress field; von Mises criterion.

1. Introduction

CVD diamond possesses an attractive set of properties, such as hardness, thermal conductivity and chemical inertness making this material a widely accepted wear resistant coating. Among several wear modes, erosion appears in components subjected to solid particles impact and/or fluids impingement. This is the case of systems for fluids transport, like choke valves used in the offshore oil industry [1, 2], or barriers to rain erosion, like IR transparent radome materials for missiles and aircrafts [3, 4]. It was found that diamond films are superior in the resistance to erosion damage by 4 to 5 orders of magnitude relatively to commonly IR window materials such as Ge, ZnS, $MgAl_2O_4$, MgF_2 and quartz glass [4]. For solid particle impact, the use of CVD diamond coatings increases the resistance to wear due to the reduction of damage caused by the successive impact of erosive particles, reducing or even inhibiting the formation of cracks into the substrate [5].

The very good thermal expansion match and structural compatibility between CVD diamond and silicon nitride (Si_3N_4) assures low levels of residual stresses and excellent film adhesion [6-9], making this ceramic an optimal choice as substrate. In the literature, few reports are available on the testing of CVD diamond coated Si_3N_4-based ceramics by solid particle impact [10, 11]. In an early work, experiments were performed at an impact velocity of 59 $m.s^{-1}$ showing that film removal took place after an exposure time of 70 s [10]. Almeida *et al*. [11] studied the effect of the application of pulsed microwave (PW) discharges to grow nanocrystalline diamond (NCD) on Si_3N_4 substrates, aiming the best erosive wear resistance: PW at 50 Hz lead to a six times lower erosion rate comparing to the continuous wave (CW) grown ones. Other substrates with diamond coatings submitted to particle erosion tests include silicon [10, 12], tungsten [12, 13], tungsten carbide [2, 14, 15], titanium-aluminium alloys [12, 16], and steel [17].

Field *et al*. [3, 10] showed that the erosive wear mechanism of diamond films is thought to happen in three steps: i) formation of ring/cone cracks due to Hertzian stress fields, ii) chipping of small particles after intersection of adjacent cracks and (iii) delamination of the film when cracking progresses along the film/substrate interface.

For low impact velocities (34 $m \cdot s^{-1}$ [3,10]), only step i) takes place. By estimating the Hertzian stress field associated to the impact of particles, it was stated that a fast reduction in the coating life is predictable under conditions where the depth of maximum shear stress approaches the coating thickness, inducing interfacial crack growth that leads to the spallation of the film [2]. The influence of the diamond coating adhesion to the substrate in the erosion behaviour is determinant because failure is mainly caused by the premature delamination of the film and diamond is itself very resistant to erosion damage. Once adhesion is assured, the most important parameter to control the erosion resistance is the diamond coating thickness [2, 11, 14]. It is considered that a ratio of above 0.4, between the film thickness and the particle contact radius, assures a good performance of the coating [1].

In the present work, multilayered CVD diamond coatings were designed as a new approach to enhance the erosive wear resistance of mechanical components. By combining the advantages of MCD and NCD grades of diamond films, while simultaneously minimizing their limitations, multilayered composites were developed by alternating MCD and NCD layers grown on a hot filament chemical vapour deposition (HFCVD) reactor. As stated above, adhesion to the substrate is a key issue for the success of systems subjected to erosion. Here, the MCD grade demonstrated to withstand the highest spalling-off loads (1600 N) in static indentation, while NCD films suffered delamination at 400 N [8]. This behaviour is consistent with results obtained in tribological testing in dry and water lubricated conditions [18, 19]. However, the evolutionary crystal growth mechanism of MCD leads to the increase of the crystallite size with thickness, and thus of the surface roughness [20]. The opposite is true for NCD films where the continuous renucleation process of NCD assures an even crystallite size along the thickness, resulting in very smooth ending surfaces [21]. Thus, multilayers should always start by an adherent MCD layer on the Si_3N_4 ceramic substrate and finish with a smooth NCD top layer. The change between grades, with controlled thicknesses, is done by alternating the deposition parameters, as gas composition, total pressure and substrate temperature. The multilayer approach has a combination of objectives in mind: i) to prevent MCD grains to grow excessively; ii) to enhance the fracture toughness by the crack-arresting role of interfaces between layers [22-24]; iii) to reduce the overall stress field within the coating, due to the lower

Young's modulus of NCD that contains sp^2 amorphous carbon at the grain boundaries [25].

2. Experimental

Silicon nitride (Si_3N_4) ceramic substrates (∅ 10 mm x 3 mm thickness) for CVD diamond deposition were produced via powder technology, ground with a 46 µm diamond wheel and flat lapped (FL) with a 15 µm diamond slurry in an iron/polymer plate. A study about the substrate surface finishing was then conducted aiming a high adhesion of the diamond film. This is an important issue, since the main failure of such coatings in protecting the substrate materials against wear is related to their detachment, as previously mentioned. So, three different surface finishing procedures were performed for the deposition of the diamond coatings: (i) FL only; (ii) FL followed by pre-polishing in a hard cloth with 15 µm diamond suspension (PP); and (iii) FL plus PP and final polishing with a colloidal silica suspension (P) to guarantee a mirror-like surface. Some samples were further dry etched with CF_4 plasma for 10 minutes using a rf generator (13.56 MHz, EMITECH K1050X). A final common step to all samples was ultrasonic seeding in a nanodiamond (4-6 nm) powder suspension in ethanol for 1 hour.

The deposition of the diamond films was conducted in an in-house built 3 kW HFCVD reactor. Six tungsten wires (∅=0.25 mm, 75 mm length) were placed at a distance of ~7 mm from the substrate. The filament temperature was measured with a two-colour pyrometer, kept constant at about 2300 °C, while the substrate temperature was assessed by a K-type thermocouple inserted into the substrate holder, placed on the back side of the substrate. A carburization step of the filaments was conducted before each diamond deposition, at a gas flow rate of 200 sccm with 2% of CH_4 in H_2, and a pressure of 10 kPa for about 10 minutes. During the deposition cycles, the samples were heated to approximately 630 °C by thermal radiation, and the additional heating of the substrate was achieved by graphite dissipating element fed by a DC external power supply, permitting full temperature control.

Firstly, the influence of the surface finishing on the erosion behaviour was evaluated. Microcrystalline diamond (MCD) monolayer coatings were used for this study. In the second part of the work, diamond films were then grown on the selected

surface finishing in the form of monolayers of MCD or nanocrystalline diamond (NCD), and as composite coatings: i) Bilayer-1: MCD+NCD-1; ii) Bilayer-2: MCD+NCD-2; iii) Multilayer-1: MCD+NCD-1+MCD+NCD-1; iv) Multilayer-2: MCD+NCD-2+MCD+NCD-2. The deposition parameters of each diamond grade are presented in Table 1.

Table 1 – Filament deposition parameters for MCD, NCD-1 and NCD-2.

Sample	CH_4/H_2 ratio	Ar/H_2 ratio	Gas flow (sccm)	Total pressure (kPa)	Substrate temperature (°C)
MCD	0.026	-	100	17.5	800
NCD-1	0.073	-	100	5.0	700
NCD-2	0.040	0.1	200	10.0	700

In the case of the NCD-1 film, nanocrystals develop as a result of the high methane (CH_4) concentration (carbon supersaturation) while in the NCD-2 films renucleation is promoted by the partial replacement of hydrogen (H_2) with argon (Ar) in the gas composition. For erosion behaviour comparison purposes, the total film thickness of all diamond coatings was nearly the same, within the 10-12 µm range. SEM images of cross-sections and top views of the as-coated samples are given in Fig. 1.

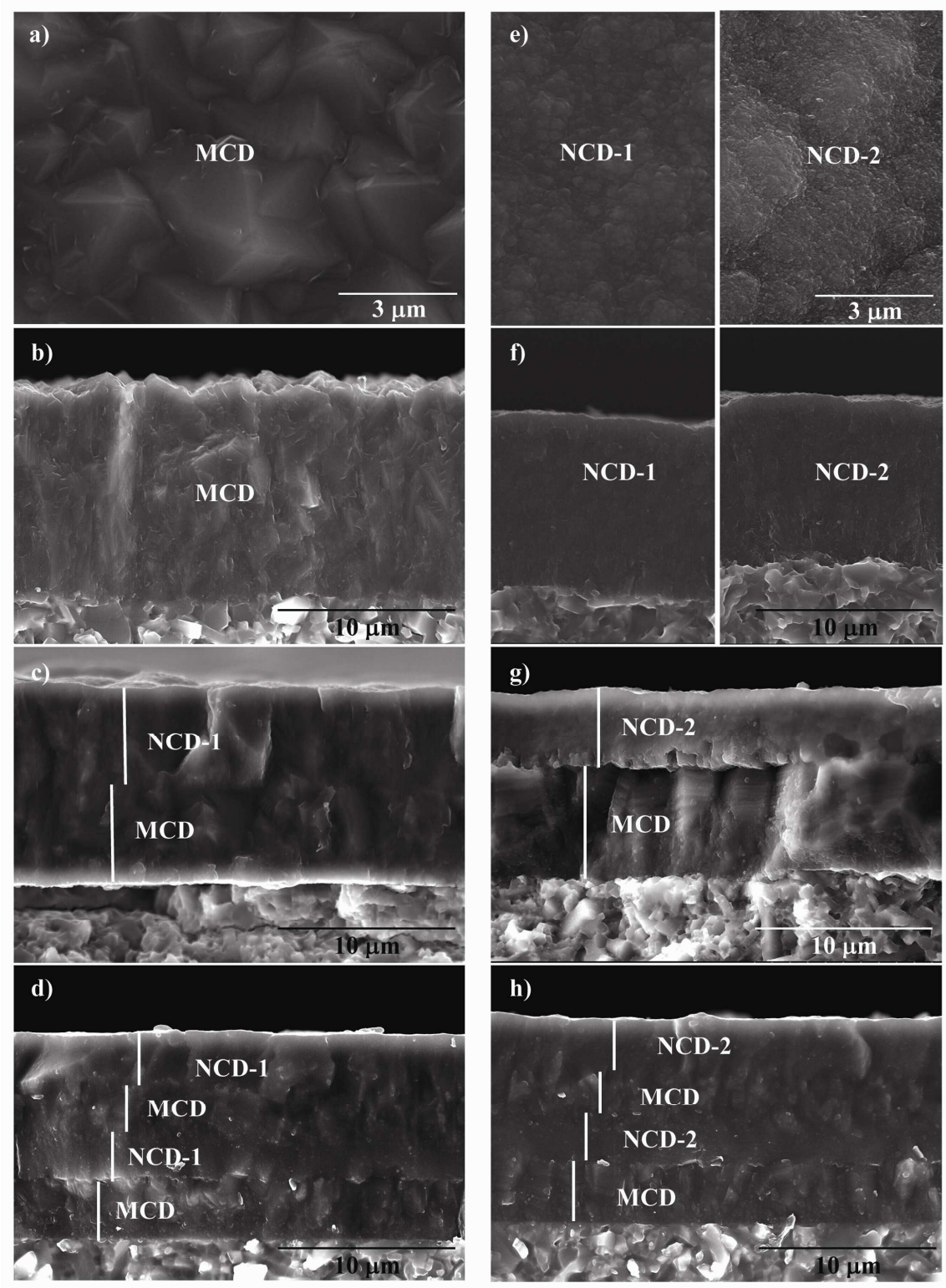

Figure 1 – SEM images of monolayer MCD, NCD-1 and NCD-2 in top-view (a, e) and cross section (b, f). Cross sectional images of (c) bilayer-1, (g) bilayer-2, (d) multi-1 and (h) multi-2 are also presented.

The erosive wear behaviour was studied by solid particle impact of SiC grains. Fig. 2 shows a micrograph of the SiC particles, while their physical characteristics and

test conditions are given in Table 2. It can be seen that the particles have an irregular blocky shape, with a mean roundness factor (RF) of 0.57, as measured by image analysis from SEM micrographs, following the procedure described in the work of Horovistiz *et al*. [26].

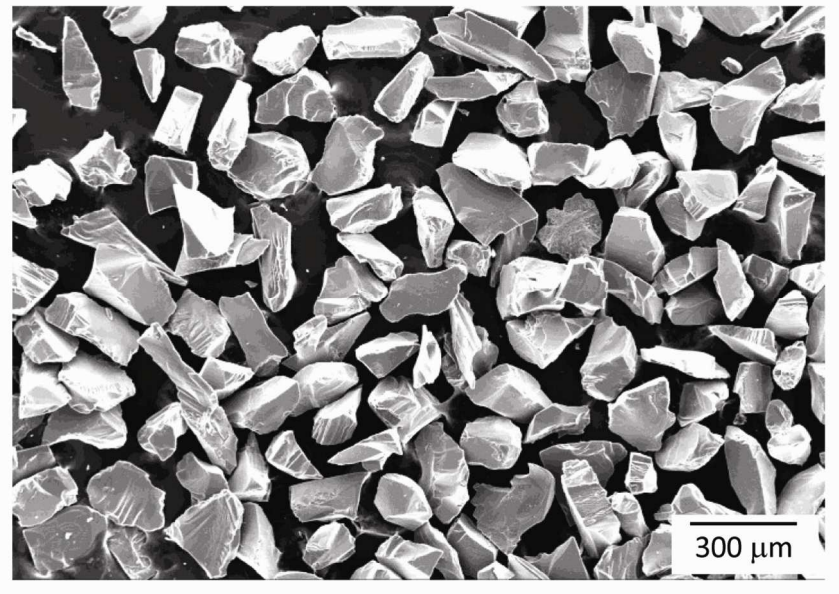

Figure 2 – SEM micrographs of the SiC erodent particles.

Table 2 – Erosion testing parameters and characteristics of the SiC particles.

Erodent	SiC particles
Particle radius - R	75 µm
Density – ρ_2	3200 $Kg.m^{-3}$
Young's modulus – E_2	700 GPa
Poisson – ν_2	0.14
Velocity - V	38 $m.s^{-1}$ ± 6 $m.s^{-1}$
Flux	5.2 $kg.m^{-2}.s^{-1}$ (5.0 $g.min^{-1}$)
Nozzle diameter	4.5 mm
Nozzle – surface distance	2.5 mm
Eroded surface diameter	~4.5 mm
Angle of incidence	90°

The erodent particles were driven by compressed air through a steel nozzle, where the velocity of the particles is assumed to be that of the air stream. The air velocity evaluation was done by using a portable anemometer placed at a distance of

2.5 mm, the same distance used to place the samples surfaces when doing the erosion tests.

A calibration curve was done, correlating the air pressure with the measured air velocity, with a set of ten consecutive measurements for each pressure. The angle of attack was set at 90°, as the erosion of brittle materials is at its maximum at normal impingement [2]. The erosive wear resistance criterion was the induction time (IT) for substrate exposure by eye-inspection during the test. To help in this inspection, the erosion chamber was equipped with a lamp that illuminates the sample while being eroded, and a mirror was placed at an angle of approximately 30° of the specimen and turned to the chamber window to make possible the observation by the operator. As the diamond coatings are darker than the ceramic substrate, it is easily recognizable the coating delamination from the substrate. The tests were stopped as soon as the substrate starts to be exposed, disregarding the size of the pits, and that time taken as the IT criterion. Scanning electron microscopy (SEM) was performed using Hitachi SU-70 and Hitachi S4100 microscopes for characterization of the pristine and eroded diamond films. Atomic force microscopy (AFM – Nanoscope IIIa, Digital Instruments) using 50 µm x 50 µm scans, allowed the determination of the surface roughness of the Si_3N_4 ceramic substrates and the diamond films.

3. Results and Discussion

3.1. Effect of the surface finishing in the erosive wear resistance

When considering these highly demanding applications, adhesion of the film to the substrate determines the success of the component in service. In order to improve the adhesion strength, the mechanical surface preparation of the substrate is a critical step to enhance the physical interlocking on the interface and to increase the specific surface area available for diamond nucleation. Further chemical etching of the substrate surface may promote adequate activation for chemical bonding to diamond. Thus, in a first set of experiments, the erosion tests were performed on the MCD diamond films deposited on Si_3N_4 surfaces subjected to distinct pre-treatments: FL-, PP- and P-polished; and also on the CF_4 plasma etched FL-, PP- and P- ones. AFM

topographic images and the respective root-mean square (RMS) surface roughness values are shown in Fig. 3.

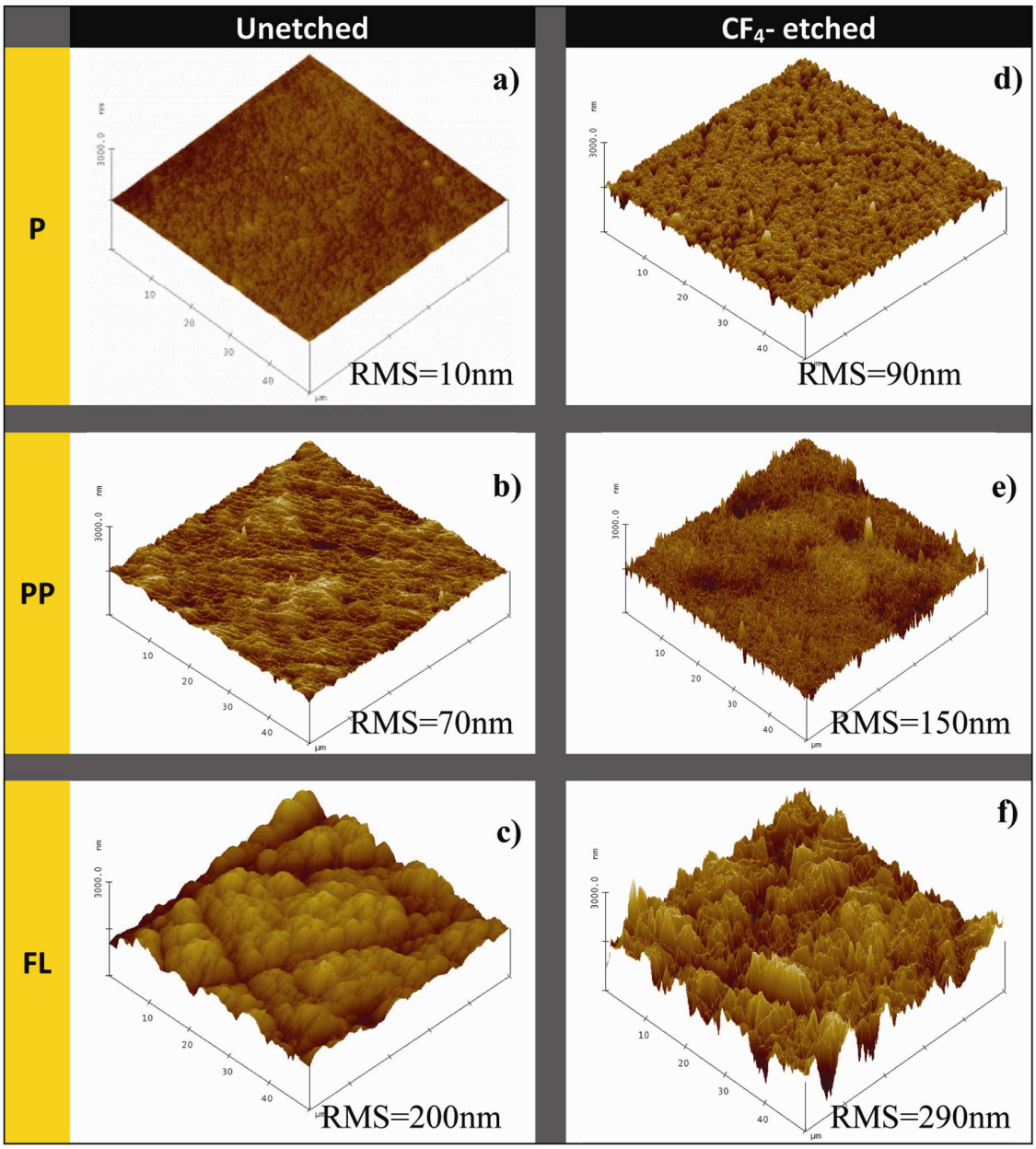

Figure 3 – AFM scans with respective root-mean square roughness values of the Si_3N_4 surfaces submitted to different mechanical pre-treatments: a) P- final polishing with colloidal silica; b) PP-final polishing with 15 µm diamond; c) FL- flat lapped. D-f) the same followed by CF_4 etching.

General SEM views of the impinged areas after the tests are given in Fig. 4. The left-hand side column refers to the eroded MCD films grown onto P-, PP-, and FL-polished surfaces, while the eroded MCD films grown on the CF_4 plasma treated substrates are presented in the second column.

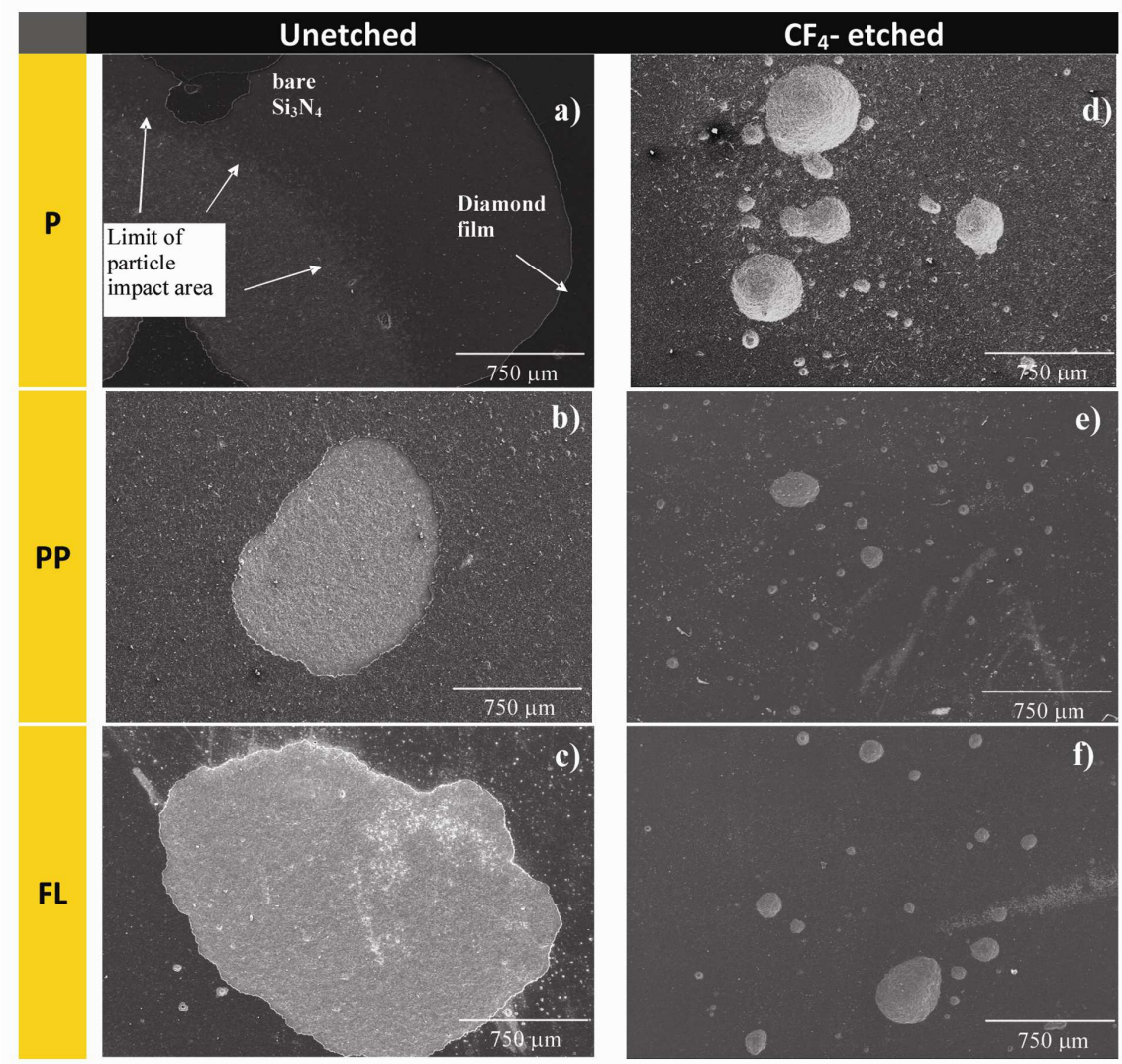

Figure 4 – SEM views of the MCD films after the erosive wear tests on the unetched (a-c) and CF4 plasma etched (d-f) P, PP and FL pre-treated surfaces. The state of the samples surfaces correspond to test durations of: a) 1 min 40 s; b) 35 min; c) 68 min; d) 65 min; e) 72 min; f) 80 min.

The erosive wear resistance values, in terms of induction time (IT) to diamond film detachment, are given in Fig. 5. It can be seen that the IT increases considerably from the P-polished surfaces to PP- and then to the FL finished surfaces, by approximately 8 and 14 times, respectively. When surfaces are submitted to the additional chemical dry etching with CF_4, the IT always increases with respect to the unetched surfaces, being notable in the MCD P+CF_4 samples (almost 14 times higher than for MCD P).

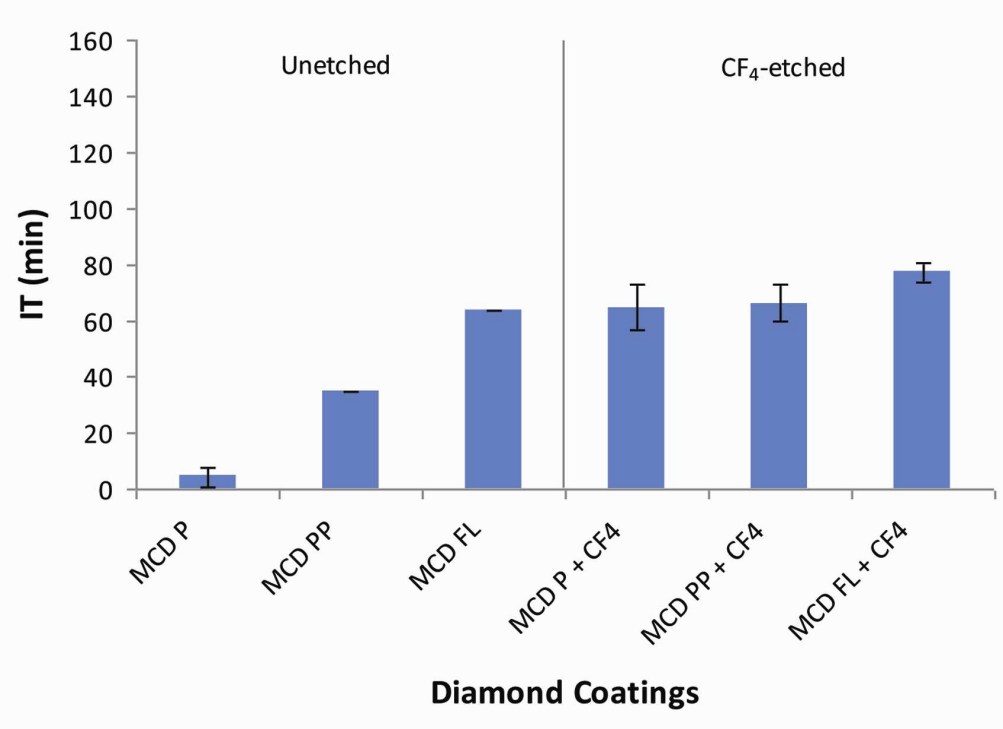

Figure 5 – Induction time (IT) for erosion of the MCD coatings grown on the unetched surfaces (P, PP, FL) and on the respective CF4-etched surfaces.

The surface of the coated mirror-polished P substrate, that suffered fast erosion (few minutes, as seen in Fig. 4a), is characterized by an extensive, catastrophic delamination of the film that extends beyond the area of the particle impingement. This is clearly seen by the differential erosion of the bare Si_3N_4 surface where the light greyish circular pattern corresponds to the area of particle impact. It is then evident that catastrophic failure was caused by crack spreading along the interface between the diamond film and the substrate, denoting a lack of film adhesion in the mirror-polished surface. The PP- and FL- samples without CF_4 plasma treatment (Figs. 4b and 4c, respectively) also present large areas of film delamination, but only inside the zone of particle impingement.

The increasing IT values for the unetched samples correlate well with the increasing RMS surface roughness values of the substrate (Fig. 6).

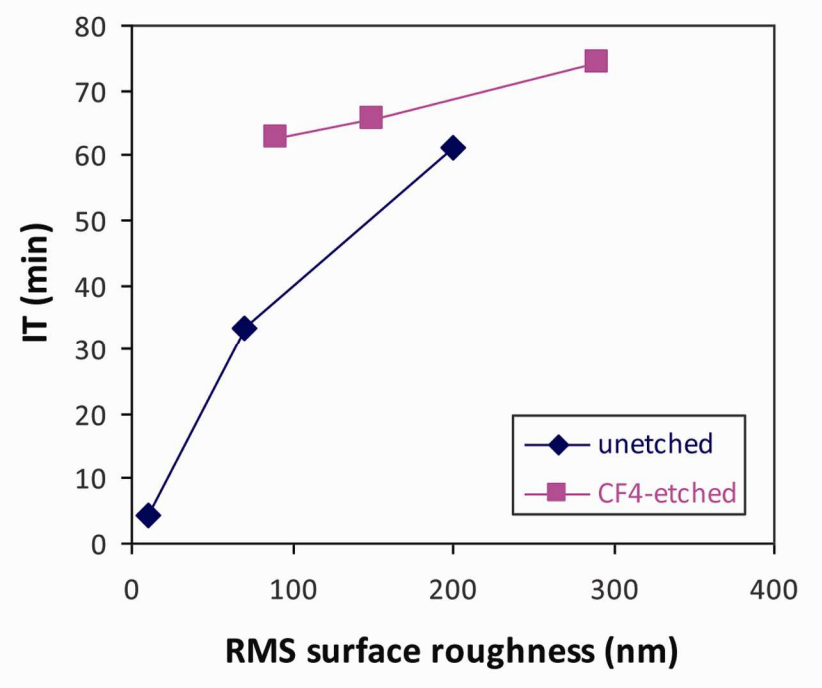

Figure 6 – Relationship between the IT for erosion of the MCD coatings and the RMS surface roughness of the respective unetched and CF_4-etched substrates.

Diamond is an erosion wear-resistant material itself [1-3], the difference in the wear behaviour is then related to the adhesion strength of diamond to the ceramic substrate, promoted by surface roughening that result in enhanced physical interlocking.

In the case of CVD diamond films, the life of the coatings is dependent on the progression of sub-surface damage provoked by sub-surface shear stresses induced by the successive particle impacts. Once the cracks develop along the substrate/coating interface, premature removal of the film by delamination takes place instead of material loss by gradual erosion wear [10].

With respect to the CF_4 plasma treated substrates, right-hand column of Fig. 4, a major difference is the much smaller delaminated area comparing to the behaviour of the unetched substrates. Furthermore, a very distinct wear pattern is observed for the CF_4 etched samples, where small spots of diamond delamination arise in the central part of the eroded area. Combining the polishing of the surface with a CF_4 plasma treatment also proved to be decisive for the improvement in the IT, being more evident for the P- samples (Fig. 5).

The chemical attack of the surface with CF_4 plasma aims at the removal of oxides from the surface by the action of F atomic species [27, 8], selectively etching the

Si_3N_4 grains that are structurally compatible to diamond and thus assure chemical bonding [9]. The CF_4 attack further increases the surface area by setting up the substrate surface roughness at the Si_3N_4 grain size level [28]. Microstructuring of the substrate surface also leads to stress relaxation in the diamond film [15, 17]. It is stated that superior results concerning higher nucleation density of diamond and film uniformity can be reached by an adequate design of the surface pretreatment of Si_3N_4 before the diamond deposition [29]. This leads to better grain coalescence, and then, less voids between the grains, whose presence would cause the reduction of the mechanical resistance at the interface [2]. These cumulative effects contribute to the high bonding strength of the film to the substrate, thus localizing delamination in a few small spots (Fig 4d-f), instead of large catastrophic spalling of the coating (Fig 4a-c). The "plus" effect of CF_4 with respect to the increment of surface roughness is very evident in Fig. 6, where the IT is much larger for a given RMS value.

Taking into account the maximum value of IT obtained in this first study, the combination of FL- surface polishing with dry etching with CF_4 plasma was the chosen surface pre-treatment for the subsequent deposition of the NCD grade and of the composite diamond films to be subjected to the erosion tests.

3.2. Effect of SiC particle impact on NCD, bilayered and multilayered diamond coatings

From the data in Fig. 7 it is clear that the nanocrystalline diamond grades NCD-1 and NCD-2 present a much lower erosive wear resistance when compared to the MCD FL+CF_4 sample. The IT decreases by about 9 times, being nearly the same for both kinds of NCD coatings, even though they were deposited in the optimized substrate surface pre-treatment.

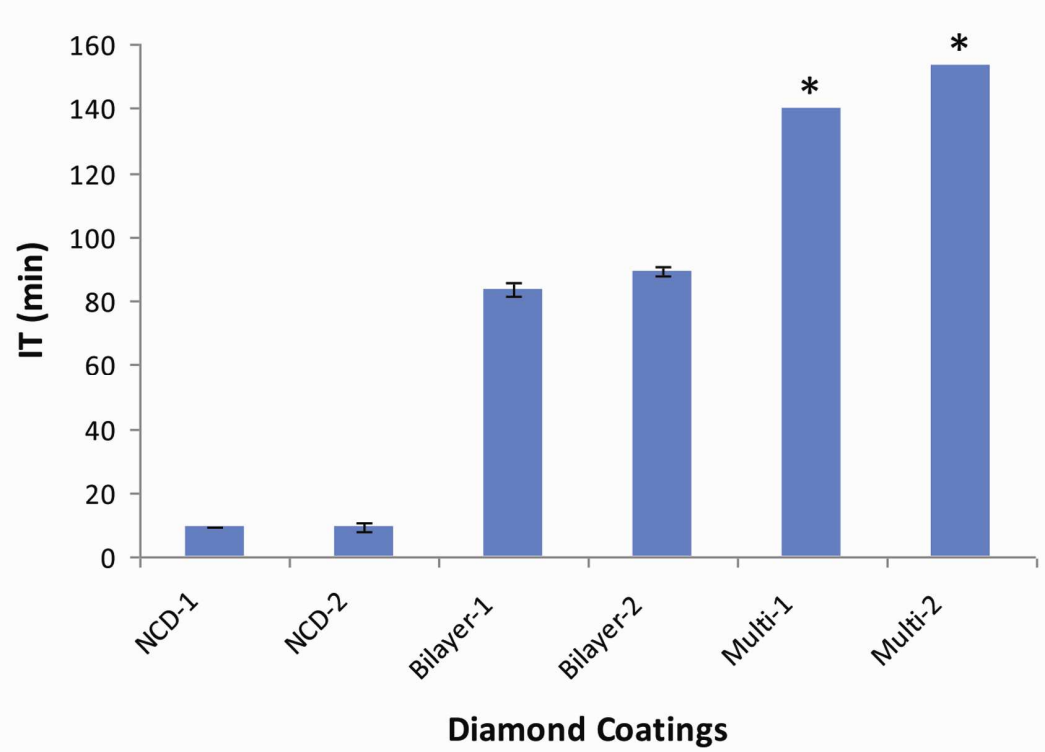

Figure 7 – Induction time (IT) for erosion of the nanocrystalline monolayers (NCD-1 and NCD-2), of the bilayered coatings (bilayer-1 and bilayer-2), and of the multilayers (Multi-1 and Multi-2). The stacking structures of the bi- and multilayered composites are detailed in the text.

The wear pattern is also similar for both NCD coatings, starting by showing the formation of small pits where the substrate is exposed, as for the MCD film, but at much lower IT values (Fig. 8a and Fig. 4f, respectively). In the case of the NCD films, the spots develop rapidly to a larger area with the undermining of the surrounding diamond film, as can be seen in the inset of Fig. 8a. It is believed that the higher grain boundary area of either NCD grades and their more graphitic/amorphous carbon nature results in weaker boundary cohesion than in MCD coatings [16,30]. The nanocrystalline character of the NCD films, the quantity of lower strength grain boundary area is increased relatively to the MCD, which lowers the in-plane strength of the coatings [16]. Intergranular crack propagation within the NCD coatings is depicted in Fig. 8b.

The film surface adjacent to a delaminated area is shown in Fig. 8c. The white arrows indicate the formation of cone cracks (orange colored lines) at the film depth, one of them presenting a well preserved ring fracture pattern at the surface (delimitated by dotted orange circle). A rough estimation of the ring crack radius, of

around 12 µm, is in a good agreement with the estimated radius of contact of the impacting sphere following hertzian theory of 10 µm, where the cracks form at, or just outside the contact radius [5].

Another crack pattern can be seen on the higher SEM magnifications in Fig. 8d where radial and lateral cracks emanate from underlying regions [12, 13]. The confluence of both cracking systems facilitates chipping from the surface by successive erodent particle impacts, eventually evolving to final delamination of the NCD coatings.

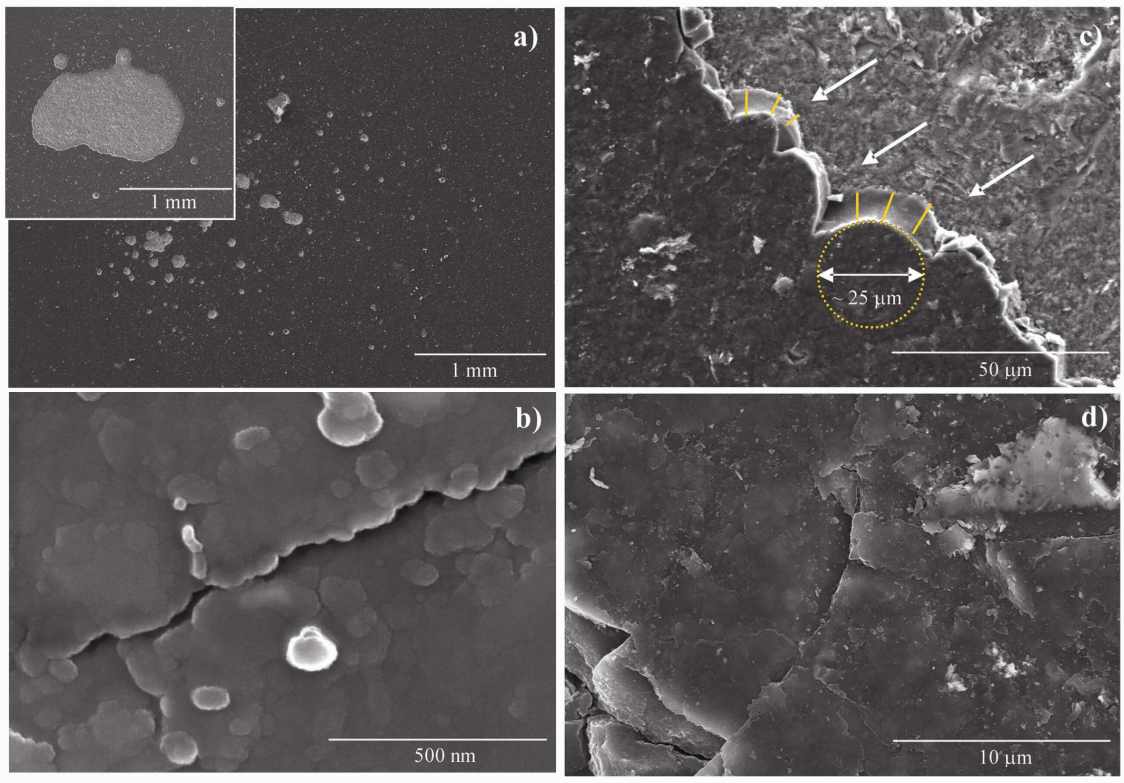

Figure 8 – Micrographs of the eroded NCD films: a) small pits with exposed substrate. The inset depicts the enlargement of the substrate exposure with increased test time; b) intergranular crack propagation; c) film surface adjacent to delaminated area; d) fracture pattern with radial and lateral cracks.

By combining MCD and NCD grades, as bilayers, much higher IT values are achieved relatively to the monolayered NCD coatings, being even superior to the MCD one (Figs. 5 and 7). A first advantage of using the bilayer approach is evident in the remarkable increase of NCD performance by adding a highly adherent underlayer of MCD. In addition, the surface roughness of the bilayers decreases with respect to the

MCD monolayers while slightly improving its erosion resistance. In most cases, the damage accumulation in these films causes adhesive failure between the two diamond layers, where the interface may act as “energy sinker” toughening mechanism to the further development of cracks into the substrate interface region. This evidence is shown in Fig. 9a, where a large circular area can be distinguished exposing the MCD underlayer (Fig. 9b). Furthermore, this feature works also as a visual predictive signal of the subsequent substrate exposure as the particle impingement continues in that weakened area, as shown in Fig. 9c.

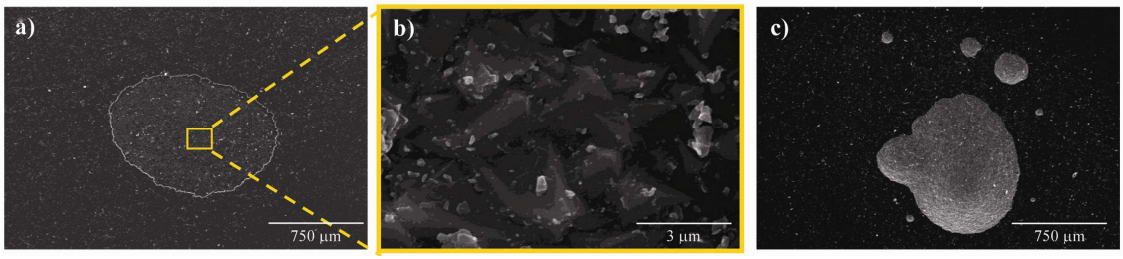

Figure 9 – SEM micrographs of the impinged bilayered diamond coatings: a) eroded surface showing the adhesive failure between the two diamond layers; b) exposed MCD underlayer; c) substrate exposure with increasing particle impingement.

The improvement on the erosion behavior by using a layered composite of diamond films is markedly evident in the case of both types of multilayered samples, whose erosion tests lasted for more than two hours without reaching the Si_3N_4 substrate. In Fig. 7, the asterisks above the bars of the multilayered samples indicate that the tests were stopped and so the IT to evident substrate exposure is higher than the value reported on the bar plot. A low magnification SEM micrograph representative of the eroded area of such composite diamond films is presented in Fig. 10a. Here, no detachment of layers or formation of pits can be seen, but erosive wear proceeds by gradual loosening of material from the surface, as is better visualized in Figs 10b and 10c. A region with well defined crack patterns is shown in Fig. 10b, showing the ring/cone cracks (the dotted region), lateral cracks (dashed arc) and the median/radial cracking system (dashed lines). The absence of areas with film spallation or substrate exposure, even after very long erosion times, suggests that the energy associated with the particles impacts must have been dissipated by the interfaces, thus increasing the work necessary for catastrophic fracture.

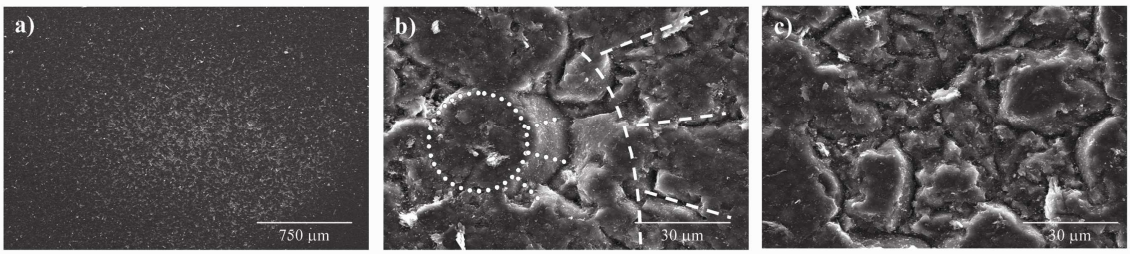

Figure 10 – SEM micrographs of the multilayered composite films: a) low magnification of the eroded area; b) crack patterns evidencing the ring/cone cracks (dotted region), lateral cracks (dashed arc) and radial cracking (dashed lines); c) loosening of material from the surface by the intersection of cracks.

3.3. Stress distribution analysis in multilayered diamond composite coatings

The resultant stress field in the coated material can be estimated considering an Hertzian contact between the SiC particle, assuming as a sphere, and the diamond film, taken as a half-space. Annexes A and B resume the equations used in this calculation. The values of the SiC particle constants (ρ_2, ν_2, E_2, R, V) are given in Table 2 [31]. For the calculations, the following values were considered for the physical constants E_1 and ν_1, in the case of the MCD and NCD monolayers: E_{MCD} = 1063 GPa, ν_{MCD} = 0.07, E_{NCD} = 740 GPa, ν_{NCD} = 0.12 [1, 32, 33]. In this estimation, no distinction is made between NCD-1 and NCD-2 coatings. For the multilayered diamond composites, the E_1 and ν_1 values were calculated from the inverse mixture law using above Young's moduli, in the first case, and the simple mixture law using the above Poisson´s coefficients, in the later, considering the relative layers thicknesses. According to Eq. 1, the estimated maximum load F_m at the particle impact lies in the range 7.2-7.6 N, and the mean contact pressure P_m (Eq. 4) varies between 21.4 and 24.2 GPa, for all the seven tested types of coatings. The contact radius estimated with Eq. 5 is approximately 10 microns for all diamond coatings. The ratio between the coating thickness (ap. 10 micron) and the contact radius (a) is thus around the unity, much higher than 0.5, a limit above which the substrate can be ignored in the stress field calculation [34].

An in-depth calculation (along the perpendicular *z*-axis) of the stress field within the coating was performed from analytical solutions for the components of the stress tensor, Eqs. 6 and 7. The von Mises parameter $J_2^{1/2}$ is a very convenient way to represent such stress field and it can be estimated by Eq. 8. Knowing that under a

Hertzian contact the principal axes coincide with the coordinate axes [35], Eq. 8 is simplified to Eq. 9. The profile of $J_2^{1/2}$ along the coating thickness for all diamond coatings is plotted in Fig. 11. A first common feature among the distinct diamond coatings is that the region of maximum stresses lies at about 4 to 5 µm beneath the surface, at half the coating thickness. This means that the coatings are supporting the most critical stresses generated by the particle impact, an important issue to be considered when designing coatings for components protection.

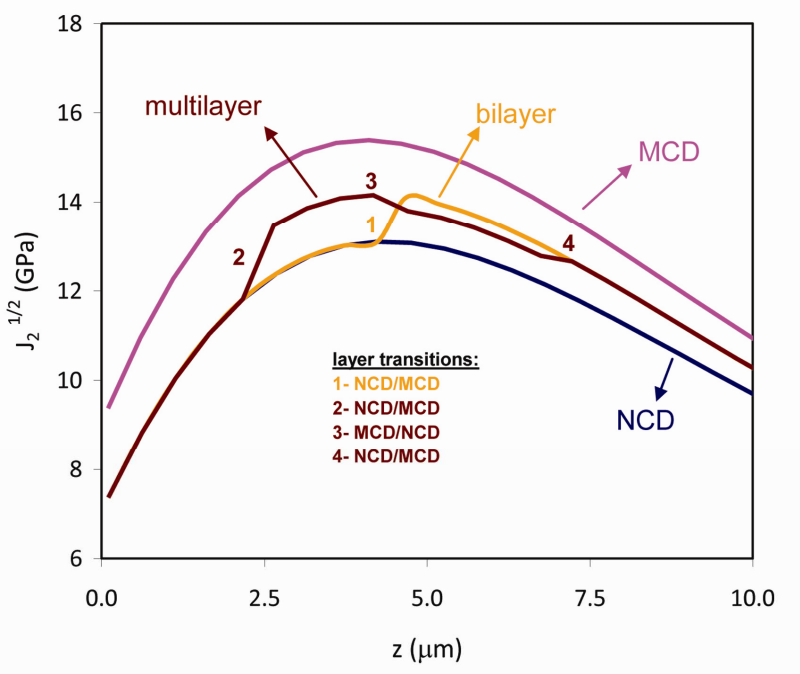

Figure 11 – Profile estimation of the von Mises parameter along the coating thickness for the monolayered coatings (MCD and NCD), bilayers (MCD+NCD) and multilayers (MCD+NCD+ MCD+NCD). In these calculations, the physical properties are representative values of the microcrystalline (MCD) and nanocrystalline (NCD) diamond took from the literature.

Fig. 11 also evidences that the use of the MCD coating leads to the highest stress level, while the NCD presents the lowest. However, for the single layer coatings, only the nanocrystalline grades present an outer crack pattern due to its lower cohesion resistance, as pointed out in subsection 3.2 with respect to Fig. 8d. In the MCD and NCD monolayered coatings, the predominant failure mode is delamination, which reveals that the magnitude of the stresses at the coating/substrate interface (z ~10 micron) is enough to assist on the propagation of the cracks through the interface.

The interfacial crack resistance is higher for MCD (12.0 N.μm^{-1}) than for NCD (6.8 N.μm^{-1}) [8], which explains the higher IT value in the former case (Fig. 5).

Comparing to the monolayered MCD, the von Mises parameter is reduced by the introduction of NCD layers, as is the case of the bilayers and fourfold layers (Fig. 11). In the bilayered coatings, a transition on the stress field takes place at the MCD/NCD interface situated at half the thickness (Fig. 11), which coincides to the maximum value of $J_2^{1/2}$. Thus, cracks tend to propagate along the MCD/NCD interface, as depicted in Fig. 9a, which acts as an "energy sink". This delays the film spallation from the ceramic substrate (Fig. 9c). This toughening, crack deflection, mechanism must be more effective in the case of the multilayers that show three stress field transitions (Fig. 11). The SEM micrograph in Fig. 10c shows that the interfaces between layers emerge in a dispersed mode, revealing the underneath microcrystalline faceted grains, but not in a wide extension as for the bilayers, Fig. 9a. Another important feature of multilayers is that the most loaded interface is of the NCD/MCD type, i.e. the transition from NCD to MCD growth. The NCD/MCD interface is more mechanically resistant because it is less graphitic than the MCD/NCD ones, due to the cleaning role of non-diamond phases by hydrogen when switching to MCD growth conditions [20]. As a consequence, the IT values for the multilayers are the highest ones (Fig. 7).

4. Conclusions

The mechanical resistance of CVD diamond in the form of mono-, bi- and multilayer designed diamond coatings on Si_3N_4 ceramic substrates was evaluated by solid particle erosion of SiC particles. It was shown that a decisive first step for the improvement of the coating life is the accomplishment of an adequate substrate preparation by a combination of mechanical treatment (grinding plus flat lapping with 15 μm diamond suspension) followed by chemical activation with CF_4 plasma etching. By mechanical tailoring the substrate surface roughness, coatings do not fail by catastrophic extensive delamination but by film detachment in more localized and smaller areas, after longer test times. The extra improvement provided by the CF_4 etching resulted in values of induction time (IT) to substrate exposure of more than 1 hour, up to 14 times relatively to the unetched surfaces.

The typical fracture mode of CVD diamond coatings when subjected to particle impacts was found to be a combination of Hertzian ring/cone and radial/median cracking systems, which propagate along the diamond grain boundaries as well as along the film/substrate interface. However, a very distinct behavior of the erosion response of microcrystalline (MCD) and both types of nanocrystalline (NCD) diamond coatings was observed, the NCD presenting much lower IT values. This is due to the higher grain boundary area of the NCD grade, concurrently richer in graphitic or amorphous carbon, leading to weaker boundary cohesion than in MCD coatings. Also, the adhesion strength of NCD to Si_3N_4 is lower than that of MCD.

By designing composite multilayered coatings consisting of a first adherent MCD layer and a top smoother NCD one, bilayers and fourfold layer films were developed. The bilayer combinations resulted in a slightly higher IT value than for MCD and one order of magnitude superior to those of the NCD monolayers. But, most of all, the first signal of damage is the adhesive failure between the two diamond layers, which acts as “energy sink” delaying the further development of cracks into the substrate interface region. This mechanism helps explaining the excellent erosion behavior of the multilayered diamond composites. Here, tests were stopped after more than two hours of SiC particle impingement without any signal of extensive delamination, with damage occurring by gradual loosening of material from the surface.

An analytical model on the stress field distribution within the coatings was developed to elucidate the erosive mechanical behavior of the different diamond composites. It was demonstrated that the region of maximum stresses lies at about half of the coating thickness, meaning that the coatings are supporting the most critical stresses generated by the particle impact. In MCD and NCD monolayers, the magnitude of the estimated stresses at the coating/substrate interface results in film delamination. The model allowed explaining the different behaviour of the multilayered diamond composites where the maximum value of the von Mises parameter $J_2^{1/2}$ is reached at the MCD/NCD transitions. Cracks tend to propagate along it working as a toughening mechanism, absorbing the energy of the particles impact and delaying the coating delamination.

Acknowledgements

E. Salgueiredo, M. Amaral, F.A. Almeida and M.A. Neto acknowledge FCT for the grants SFRH/BD/41757/2007, SFRH/BPD/26787/2006, SFRH/BPD/34869/2007 and SFRH/BPD/45610/2008, respectively. Project MULTIDIACOAT – PTDC/EME-TME/100689/2008 is also gratefully acknowledged.

References

[1] D.W. Wheeler, R.J.K. Wood, Wear 233-235 (1999) 306-318.

[2] S. Amirhaghi, H.S. Reehal, R.J.K. Wood, D.W. Wheeler, Surface and Coatings Technology 135 (2001) 126-138.

[3] J.E. Field, Q. Sun, H. Gao, G.H. Jilbert, Wear 186-187 (1995) 195-202.

[4] F.X. Lu, Q. He, S.B. Guo, F.L. Zhang, Y.M. Tong. Diamond and Related Materials 19 (2010) 936-941.

[5] I.P. Hayard , J.E. Field. Journal of Hard Materials 1 (1990) 53-64.

[6] M.R. Soares, M. Belmonte, R.F. Silva, Journal of Applied Physics 94 (2003) 5633-5638.

[7] M. Amaral, F.J. Oliveira, M. Belmonte, A.J.S. Fernandes, F.M. Costa, R.F. Silva, Surface Engineering 19 (2003) 410-416.

[8] F.A. Almeida, M. Amaral, F.J. Oliveira, A.J.S. Fernandes, R.F. Silva, Vacuum 81 (2007) 1443-1447.

[9] F.A. Almeida, F.J. Oliveira, R.F. Silva, D.L. Baptista, S.B. Peripolli, C.A. Achete, Applied Physics Letters 98 (2011) 171913-1 – 171913-3.

[10] Z. Feng, Y. Tzeng, J.E. Field, Thin Solid Films 212 (1992) 35-42.

[11] F.A. Almeida, N. Derkaoui, F.J. Oliveira, F. Bénédic, R.F. Silva, A. Gicquel, Diamond and Related Materials 19 (2010) 484-488.

[12] M.V. Kral, J.L. Davidson, J.J. Wert, Wear 166 (1993) 7-16.

[13] K. Bose, R.J.K. Wood, D.W. Wheeler, Wear 259 (2005) 135-144.

[14] A. Alahelisten, P. Hoolman, S. Hogmark, Wear 177 (1994) 159-165.

[15] S. Amirhaghi, H.S. Reehal, E. Plappert, Z. Bajic, R.J.K. Wood, D.W. Wheeler, Diamond and Related Materials 8 (1999) 845-849.

[16] G. Heinrich, T. Grögler, S.M. Rosiwal, R.F. Singer. Surface and Coatings Technology, 94-95 (1997) 514-520.

[17] J.C. Bareiβ, G. Hackl, N. Popovska, S.M. Rosiwal, R.F. Singer, Surface and Coatings Technology 201 (2006) 718-723.

[18] C.S. Abreu, M. Amaral, A.J.S. Fernandes, F.J. Oliveira, R.F. Silva, J.R. Gomes Diamond and Related Materials 15 (2006) 739-744.

[19] C.S. Abreu, M. Amaral, F.J. Oliveira, J.R. Gomes, R.F. Silva, Diamond and Related Materials 18 (2009) 271-275.

[20] W. Kulisch, C. Popov, Physica Status Solidi (a) 203 (2006) 203-219.

[21] D.M. Gruen, Annual Review of Materials Science 29 (1999) 211-259.

[22] L. Schafer, M. Höfer, R. Kröger, Thin Solid Films 515 (2006) 1017-1024.

[23] S. Takeuchi, S. Oda, M. Murakawa, Thin Solid Films 398 – 399 (2001) 238-243.

[24] N. Jiang, K Sugimoto, K. Nishimura, Y. Shintani, A. Hiraki, Journal of Crystal Growth 242 (2002) 362-366.

[25] S.A. Catledge, J. Borham Y.K. Vohra, W.R. Lacefield, J.E. Lemons, Journal of Applied Physics 91 (2002) 5347-5352.

[26] A.L. Horovistiz, E.N.S. Muccillo, Journal of the European Ceramic Society 31 (2011) 1431-1438.

[27] H. Mader, I. Syniawa, W. Durner, Proceedings of the International Symposium on Plasma Chemistry ISPC-5, Edingburgh (Scotland), August 10 – 14, 1981, p. 301.

[28] M. Amaral, F. Almeida, A.J.S. Fernandes, F.M. Costa, F.J. Oliveira, R.F. Silva, Surface and Coatings Technology 204 (2010) 3585 – 3591.

[29] M. Belmonte, V.A. Silva, A.J. Fernandes, F. Costa, R. Silva, Journal of American Ceramic Society 86 (2003) 749 – 54.

[30] R. Ikeda, M. Hayashi, A. Yonezu, T. Ogawa, M. Takemoto, Diamond and Related Materials 13 (2004) 2024 – 2030.

[31] K.E. Petersen, Proceedings of the IEEE, v. 70 (1982) p. 421.

[32] S. Jeedigunta. Growth and characterization of nanocrystalline diamond films for microelectronics and microelectromechanical systems. Doctoral Thesis. University of South Florida. Department of Electrical Engineering. Tampa, Florida, USA, 2008. Available on-line at: http://scholarcommons.usf.edu/etd/316/

[33] J. Philip, P. Hess, T. Feygelson, J.E. Butler, S. Chattopadhyay, K.H. Chen, L.C. Chen, Journal of Applied Physics 93 (2003) 2164 – 2171.

[34] M.G.D. E-Sherbiney, J. Hallin, Wear 40 (1976) 325-337.

[35] V.L. Popov. Contact Mechanics and Friction. Springer-Verlag Berlin Heidelberg, 2010.

Appendix A – Equations used for the calculation of von Mises stresses according to Hertzian response to particle impact solicitation [10, 34].

- Maximum load, F_m, at the particle impact:

$$F_m = \left(\frac{5\pi\rho_2}{3}\right)^{3/5}\left(\frac{4k}{3E_1}\right)^{-3/5} R^2 V^{6/5} \quad \text{Eq. 1}$$

where:

$$k = \frac{9}{16}\left[\left(1-\nu_1{}^2\right)+\left\{\left(1-\nu_2{}^2\right)\left(\frac{E_1}{E_2}\right)\right\}\right] \quad \text{Eq. 2}$$

- Mean contact pressure P_m:

$$P_m = \frac{1}{\pi}\left(\frac{5\pi\rho_2}{3}\right)^{1/5}\left(\frac{4k}{3E_1}\right)^{-4/5} V^{2/5} \quad \text{Eq. 3}$$

- Maximum contact pressure, P_0:

$$P_0 = \frac{3}{2}P_m \quad \text{Eq. 4}$$

- Contact radius, a:

$$a = \sqrt{\frac{F_m}{\pi P_m}} \quad \text{Eq. 5}$$

- Components of the stress tensor:

$$\sigma_{zz} = -P_0\left(1+\frac{z^2}{a^2}\right)^{-1} \quad \text{Eq. 6}$$

$$\sigma_{xx} = \sigma_{yy} = -P_0\left[(1+\nu)\left(1-\frac{z}{a}\arctan\frac{a}{z}\right)-\frac{1}{2}\left(1+\frac{z^2}{a^2}\right)^{-1}\right] \quad \text{Eq. 7}$$

- von Mises parameter $J_2{}^{1/2}$:

$$\sqrt{J_2} = \frac{1}{6}\left[\left(\sigma_{xx}-\sigma_{yy}\right)^2+\left(\sigma_{yy}-\sigma_{zz}\right)^2+\left(\sigma_{zz}-\sigma_{xx}\right)^2\right]+\tau_{xy}^2+\tau_{yz}^2+\tau_{zx}^2 \quad \text{Eq.8}$$

$$\sqrt{J_2} = \frac{1}{6}\left[\left(\sigma_1-\sigma_2\right)^2+\left(\sigma_2-\sigma_3\right)^2+\left(\sigma_3-\sigma_1\right)^2\right] \quad \text{Eq. 9}$$

Appendix B – Symbols list:

F_m	maximum load (N)
P_m	mean contact pressure (Pa)
P_0	maximum contact pressure (Pa)
a	Hertzian contact radius (m)
σ_{xx}; σ_{yy}; σ_{zz}	principal stresses in the half-space (Pa)
τ_{xy}; τ_{yz}; τ_{zx}	shear stresses (Pa)
$J_2^{1/2}$	von mises parameter (Pa)
ρ_2	density of the impact particle material ($kg \cdot m^{-3}$)
E_1	Young's modulus of the half-space material (Pa)
E_2	Young's modulus of the impact particle material (Pa)
v_1	Poisson coefficient of the half-space material
v_2	Poisson coefficient of the impact particle material
R	impact particle radius (m)
V	particle velocity ($m^{-1} \cdot s^{-1}$)
z	distance to the surface (depth)

III.4. Self-mated tribological systems based on multilayer micro/nanocrystalline CVD diamond coatings

E. Salgueiredo[1]; C.S. Abreu[2,3]; M. Amaral[1,4]; F.J. Oliveira[1]; J.R. Gomes[3,5]; R.F. Silva[1]

[1]*CICECO, Materials & Ceramic Engineering Dept., University of Aveiro, Campus de Santiago, 3810-193 Aveiro, Portugal*
[2]*Physics Dep., School of Engineering (ISEP), Polytechnic of Porto, Portugal*
[3]*Centre for Mechanical and Materials Technologies (CT2M), Portugal*
[4]*I3N, Physics Dept., University of Aveiro, Campus de Santiago, 3810-193 Aveiro, Portugal*
[5]*Mechanical Engineering Department, CIICS, University of Minho, 4800-058 Guimarães, Portugal*

Wear 303 (2013) 225–234

DOI: 10.1016/j.wear.2013.03.049

Abstract

The tribological response of multilayer micro/nanocrystalline diamond coatings grown by the hot filament CVD technique is investigated. These multigrade systems were tailored to comprise a starting microcrystalline diamond (MCD) layer with high adhesion to a silicon nitride (Si_3N_4) ceramic substrate, and a top nanocrystalline diamond (NCD) layer with reduced surface roughness. Tribological tests were carried out with a reciprocating sliding configuration without lubrication. Such composite coatings exhibit a superior critical load before delamination (130-200 N), when compared to the mono- (60-100 N) and bilayer coatings (110 N), considering ~10 μm thick films. Regarding the friction behaviour, a short-lived initial high friction coefficient was followed by low friction regimes (friction coefficients between 0.02 and 0.09) as a result of the micropolished surfaces tailored by the tribological solicitation. Very-mild to mild wear regimes (wear coefficient values between 4.1×10^{-8} and 7.7×10^{-7} $mm^3.N^{-1}.m^{-1}$) governed the wear performance of the self-mated multilayer coatings when subjected to high-load short-term tests (60 – 200 N; 2h; 86 m) and medium-load endurance tests (60 N; 16h; 691 m).

Keywords: Diamond multilayers; nanocrystalline diamond; hot filament CVD; friction; wear.

1. Introduction

The intrinsic relatively high surface roughness of microcrystalline diamond (MCD) coatings, when compared to other related films such as the nanocrystalline diamond (NCD) variety or the diamond-like carbon material may hinder its use in several mechanical and tribological potential applications. Such surface characteristic of MCD implies a prevailing mechanical component to the friction phenomenon, resulting from the mechanical interlocking between the micro-sized pyramidal asperities of diamond crystals, which leads to high initial friction values in sliding contacts. This drawback could normally be overcome using NCD films instead, which combine a low surface roughness with the outstanding properties of diamond, namely high hardness, thermal conductivity and chemical inertness [1]. Hence, some of the lowest friction coefficient (μ) values involving self-mated hard coatings under ambient conditions, without lubrication, were found for NCD (μ≈ 0.01 to 0.04), also offering high wear resistance (wear coefficient k ~ 10^{-8} to 10^{-7} $mm^3.N^{-1}.m^{-1}$) [2-4]. Nonetheless, these coatings suffered delamination under tribological stress at lower loads (60 N) compared to those of the MCD system (80 N) [5,6], due to the higher content of non-diamond species at the grain boundaries and poorer adhesion to the substrate [7].

Thus, multigrade multilayer coatings are here proposed for tribological applications that would combine the higher adhesion of the MCD variety, as the starting layer, with the very low surface roughness of NCD, as the top layer. Particularly, the MCD coatings provide excellent adhesion levels to Si_3N_4 ceramic substrates due to a good thermal expansion match and structural compatibility with diamond [8].

The multilayer coating approach is not unfamiliar in literature, as it is well known to improve the tribological behaviour of conventional [9-11], by increasing the adhesion between the coating and the substrate, allowing higher applied loads, surface stress reduction and improving crack propagation resistance [12]. Diamond multilayers were already grown on cemented carbide substrates aiming improvements in the cutting tools performance [13-17]. Sun *et al*. achieved an upgrade on the working lifetime of drawing dies by a factor of above 15, compared to uncoated ones

[16]. Takeuchi and co-workers reported a 30% increase in the bending strength of the multilayer system, compared to MCD monolayers [13].

Diamond films were also combined in multilayer coatings with other structures, such as nanocubic boron nitride [18], amorphous carbon [19] or tetrahedral amorphous carbon (ta-C) [20]. In all cases, the composite structure shows improved properties, when compared to the individual coatings.

The present work compares the tribological behaviour of monolayers, bi- and fourfold multilayers of micro- and nanocrystalline CVD diamond varieties. In all cases, self-mated ball-on-flat systems in dry sliding conditions were tested. To our knowledge, the applied loads used (up to 200 N) are considerably higher than those reported in literature.

2. Experimental

Dense disc shaped Si_3N_4 ceramic substrates (Ø 10mm x 3mm thickness) were pressureless sintered at 1750 °C for 2h, in a nitrogen atmosphere. The substrates were then sequentially ground with a 46 µm diamond wheel, flat lapped with a 15 µm diamond slurry in an iron/polymer plate. Si_3N_4 commercial balls (Kema Nord) with a 5 mm diameter were used as counter bodies in the tribological tests. Prior to diamond deposition, both discs and balls were dry etched for 10 minutes with CF_4 in an rf generator (13.56 MHz, EMITECH K1050X) and ultrasonically scratched during 1h with a nanometric diamond powder suspension in ethanol, for diamond nucleation enhancement.

An in-house built 3kW hot filament reactor was used for chemical vapour deposition of diamond, comprising six tungsten wires (Ø = 0.25 mm, 7.5 mm length). The filaments to substrate distance and the filament temperature were kept constant at about 7 mm and ~2300 °C, respectively. A two-colour pyrometer was used to measure the filament temperature. This way, samples were heated at approximately 630 °C by thermal radiation, as measured a K-type thermocouple inserted into the substrate holder, placed on the back side of the substrate. Additional heating of the

substrate was achieved by graphite dissipating element fed by a DC external power supply, permitting full temperature control.

Prior to the deposition of the bilayer and multilayer coatings, monolayers of MCD and of two varieties of NCD were deposited using the conditions expressed in Table 1. In the case of the NCD-1 film, nanocrystals develop as a result of the high methane (CH_4) concentration (carbon supersaturation) while in the NCD-2 films renucleation is promoted by the partial replacement of hydrogen (H_2) with argon (Ar) in the gas composition. Then, bilayer and multilayer composites were designed as follows: i) Bilayer-1: MCD+NCD-1; ii) Bilayer-2: MCD+NCD-2; iii) Multilayer-1: MCD+NCD-1+MCD+NCD-1; iv) Multilayer-2: MCD+NCD-2+MCD+NCD-2. All coatings present a total film thickness in the 10-12 μm range, for comparison purposes.

Table 1 - Hot filament deposition parameters for MCD, NCD-1 and NCD-2.

Sample	Deposition time (h)	CH_4/H_2 ratio	Ar/H_2 ratio	Gas flow (sccm)	Total pressure (kPa)	Substrate temperature (°C)
MCD	2	0.026	-	100	17.5	800
NCD-1	3	0.073	-	100	5.0	700
NCD-2	6	0.04	0.1	200	10.0	700

Tribological tests of self-mated systems based on diamond coated discs and balls were performed in a ball-on-flat adapted tribometer (PLINT TE67/R) using an unlubricated reciprocating sliding arrangement. All tests were performed in ambient air (R.H. ~50-60%) at room temperature, with constant frequency (1 Hz) and stroke length (6 mm). Normal applied loads varied in the 60-200 N range. Sliding distances ranged from 86 m (2h) to ~691 m (16h, endurance tests) in order to evaluate the short and long term evolution of the tribological response of the monolayers and of the bi- and fourfold diamond multilayers.

Field Emission Scanning Electron Microscopy (FE-SEM) was performed using a Hitachi SU-70 system for surface morphology characterization of the diamond coatings, before and after the tribological tests. UV μ-Raman spectroscopy (HORIBA JOBIN YVON HR800UV), using the line 325 nm from a He-Cd laser (KIMMON IK series) allowed the identification of the carbon phases. AFM (Nanoscope IIIa, Digital

Instruments) using 50 µm x 50 µm scans, allowed the determination of the surface roughness of the diamond layers and also of the wear coefficient, using the AFM bearing function for volume loss quantification data [21]. The wear coefficient (k) of the ball specimen was estimated from the near circular wear scar dimension, according to the following expression that combines the Zeiler equation and the Archard law [22, 23]:

$$k = \frac{\pi \times d^4}{64 \times r \times W \times x} \quad \text{(Eq. 1)}$$

where *d* is the diameter of the near-circular wear scar, *r* the ball radius, *W* the normal applied load and *x* is the sliding distance.

3. Results and Discussion

3.1. As-deposited diamond coatings

Typical initial RMS surface roughness values for the MCD, NCD-1 and NCD-2 monolayer coatings were 485±50, 350±1 and 295±15 nm, respectively. These AFM measured values are somewhat high, but easily explained by the initial surface roughness of the substrate. The flat lapped surface finishing of the Si_3N_4 substrates presented a RMS value of ~200 nm. Moreover, the 10 min plasma etching with CF_4 induced a further increase in surface roughness to ~308 nm. However, plasma etching allows a more effective diamond seeding, and consequently higher adhesion levels of the diamond coating to the substrate [24]. The use of an appropriate surface pre-treatment becomes important to overcome the poor intrinsic adhesion of diamond to most substrates, as a result of its chemical inertness. Another proven advantage of Si_3N_4 ceramics is the similar thermal expansion coefficient to that of diamond, thus diminishing the thermal stress and, therefore, enhancing the coating adhesion [25, 26].

Fig. 1 displays cross-sectional SEM images of the as-deposited bilayers ((a), (b)) and multilayers ((c), (d)). As shown in the micrographs, all structures begin with a rough MCD microstructure and end in a smooth top NCD layer. The multilayers present a fourfold configuration, being that Multi-1 and Multi-2 were obtained after doubling

Bilayer-1 and Bilayer-2 layers, respectively. The RMS values are 275±10, 260±8, 310±11 and 280±34 nm for Bilayer-1, Bilayer-2, Multi-1 and Multi-2, respectively.

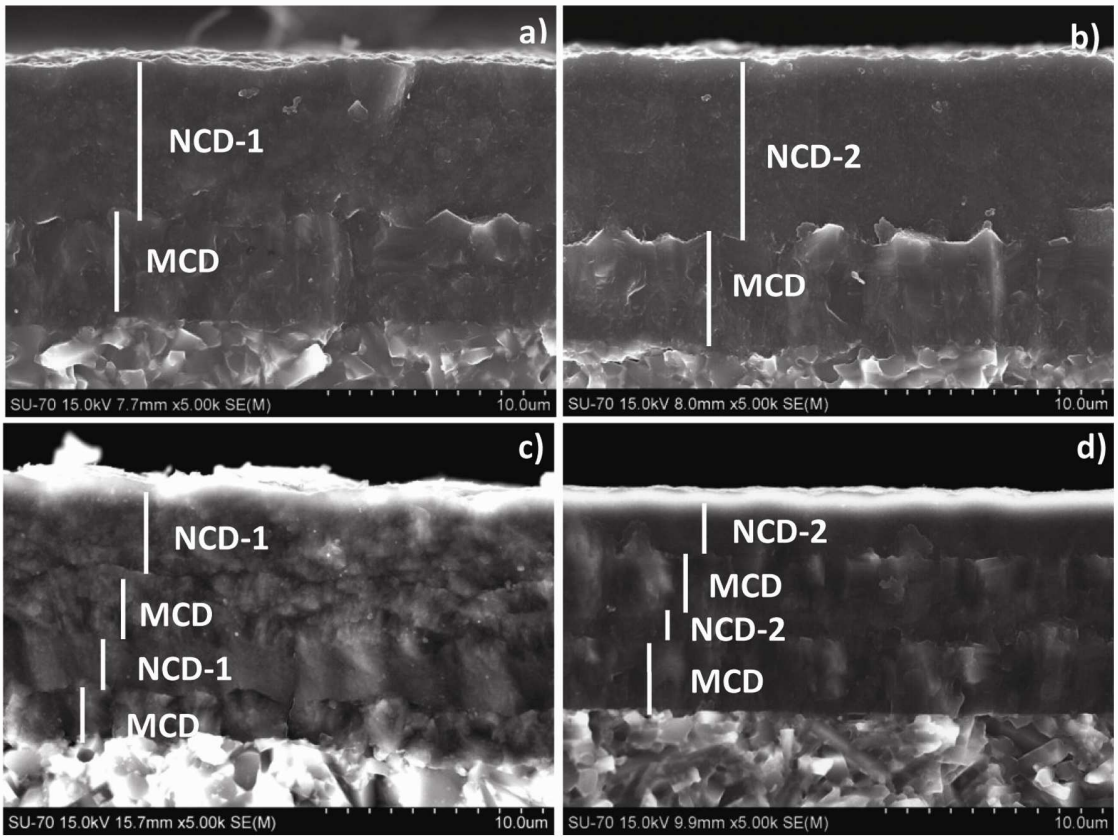

Fig. 1 – Cross sectional SEM micrographs of Bilayer-1 and 2 (a,b) and Multi-1 and 2 (c,d) diamond coatings, exhibiting the two-fold and four-fold configuration, respectively.

3.2 Worn diamond coatings

The long term evolution of the tribological response of the diamond coatings was assessed by performing endurance tests with ~691 m of sliding distance, and a constant applied load of 60 N. This value was chosen based on the lower limit obtained for the critical load tests that were carried out to determine the maximum load prior to film delamination, which are detailed later on.

The worn surfaces of both flat and ball specimens are depicted in Fig 2. Micrographs in the left column are low magnification views of the wear track regions of Bilayer-1 (a), Multi-1 (c), Bilayer-2 (e) and Multi-2 (g) samples, respectively. Insets depict the corresponding counterpart ball worn surfaces, which were also used to estimate the wear coefficient value according to Eq. 1.

The column in the right side of Fig. 2 shows higher magnification micrographs taken inside the wear track regions. As can be seen, Bilayer-1 and Multi-1 exhibit smooth polished surfaces (RMS 55±38 nm and 75±6 nm, respectively) inside the wear track region, characteristic of a fine-scale abrasive wear mechanism. These endurance tribotests also produced some interspersed cracking leading to some grain pullout. Although the relatively high contact loads considered (3.5 GPa), the scratch patterns from the substrate polishing were kept inside the wear tracks (Fig. 2(a) and (c)), which evidences the high adhesion level of the diamond coatings. On the other hand, the Bilayer-2 sample shows the presence of several shallow wear grooves (Fig. 2f), resulting in higher surface roughness values (RMS 245±54 nm) than those found on the NCD-1 grade systems. This result can be explained from the higher content of sp^2 softer phase present on NCD-2 grade samples, making these systems more prone to abrasion wear damage. In the Multi-2 film, a striking feature is the existence of an angular crack pattern bordering a smooth wear track (RMS 75±7 nm), superimposed on the aforementioned worn surface characteristics of Bilayer-2. The film cracking could be explained by the collapse of the top NCD-2 layer, where high Hertzian contact stresses, resulting from the non-conformal sphere-on-plane configuration, give rise to their arching. Because the NCD-2 grade systems have similar total thickness, the individual layers on Multi-2 will be thinner than those of Bilayer-2, and as such the top layer of the former will become less resilient to accommodate a similar applied stress, bulging toward the edges of the wear track. It is noteworthy, that the applied load of 60 N corresponds also to the critical load prior to film detachment assessed for the NCD-2 diamond grade, as reported later on.

In relation to the ball specimens, they are characterised by near-circular wear scars with a smooth polished appearance and the presence of a few pullouts, originating from the brittle fracture of the diamond structures. Moreover, the ball corresponding to the Bilayer-2 sample evidences the existence of shallow abrasive grooves, like those found on the counterpart plate.

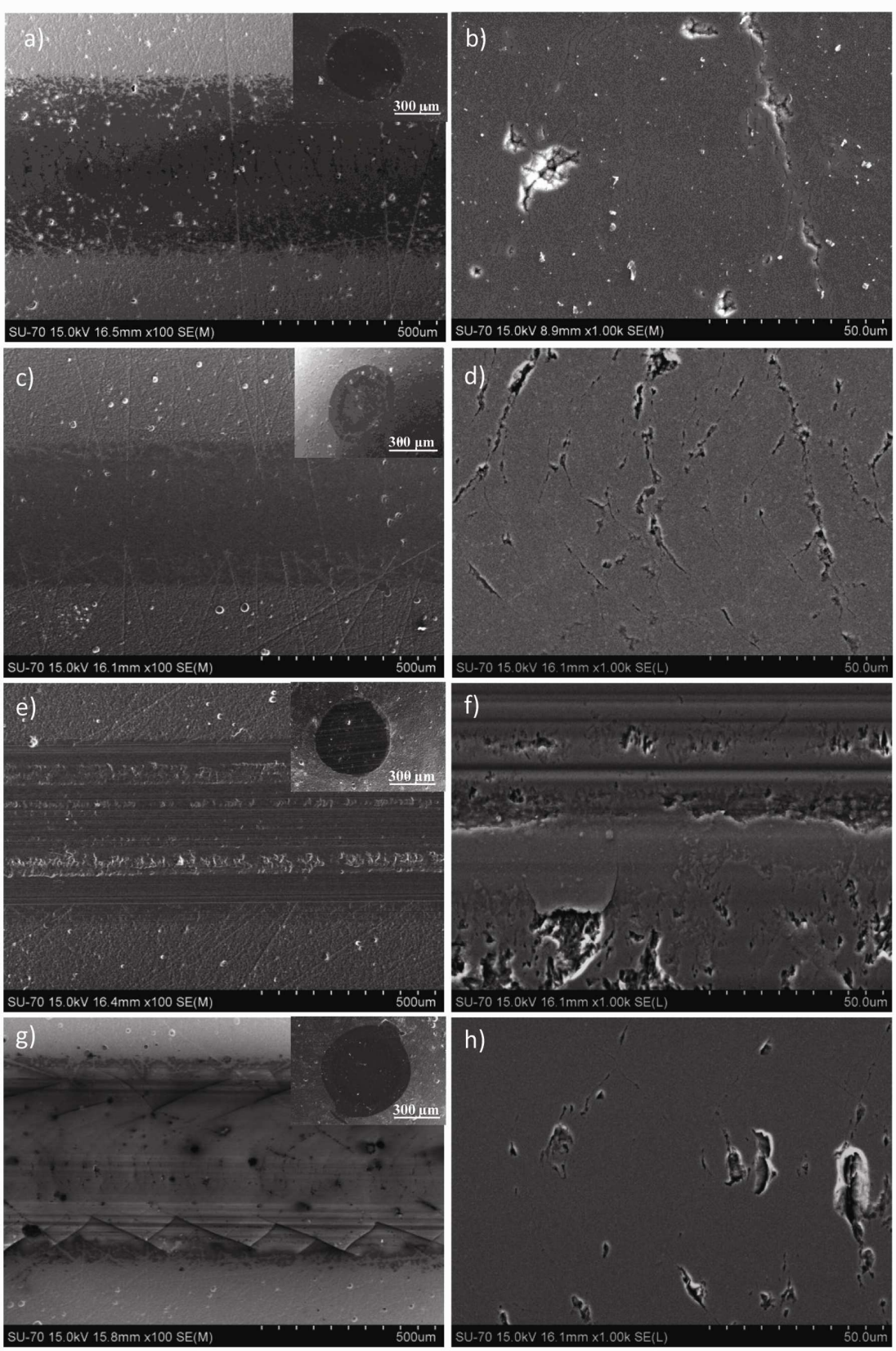

Fig. 2 – Morphology of the worn specimens (plate and ball) for Bi-1 (a), Multi-1 (c), Bi-2 (e) and Multi-2 (g) after the endurance tests (~691 m) at a constant 60 N load; magnifications inside the wear track for Bi-1, Multi-1, Bi-2 and Multi-2 are presented in images (b), (d), (f) and (h), respectively.

3.3 Critical load of diamond coatings

The tribotests were also used to determine the critical load (W_C) of the diamond coatings prior to film delamination under sliding, which are given in Table 2.

Table 2 – Critical load values, friction coefficient (maximum and average) for the 2h at the critical load, and 16h at a constant 60 N load sliding tests of the mono-, bi- and multilayer coatings.

Film	16h@60N			2h@W_C	
	W_C	μ_{max}	μ	μ_{max}	μ
MCD	100	0.8	0.09	0.77	0.05
NCD-1	80	0.75	0.06	0.78	0.03
NCD-2	60	0.72	0.02	0.79	0.02
Bilayer-1	110	0.89	0.10	0.67	0.06
Bilayer-2	110	0.63	0.08	0.78	0.05
Multi-1	130	0.79	0.05	0.71	0.06
Multi-2	200	0.75	0.09	0.87	0.06

Fig. 3 exhibits SEM micrographs of the wear track regions under the estimated critical loads. From top to bottom, the monolayer, bilayer and multilayer films are presented in sequence. Under the drastic loading conditions, a common feature consists in the presence of a mixed pattern of angular and transverse semi-circular cracks typical of an abrasive action from a hard component on a hard surface [27], revealing a micro-cracking abrasive mechanism. As readily seen, the density of micro-cracking on coatings NCD-1 (Fig. 3 (a)) and Bilayer-1 (Fig. 3 (c)) is significantly higher than the ones found on the corresponding NCD-2 and Bilayer-2 coatings, as a result of the higher brittleness of NCD-1 coming from their higher content of sp^3 phase [28]. Comparatively, the NCD-2 ended coatings (Figs. 3 (b,d)) are more prone to grain pullout due to a higher content of sp^2 phase. A lower critical load of 60 N was found for the NCD-2 monolayer when compared to the obtained value for the NCD-1 system (W_C= 80 N). The high sp^2 content at the interface diminishes grain cohesion and bonding strength to the substrate [7], which corroborates the observed behaviour. Bilayer-2 (Fig. 3 (d)), being relatively soft, also evidences abrasion grooves at the wear track border, along the sliding direction.

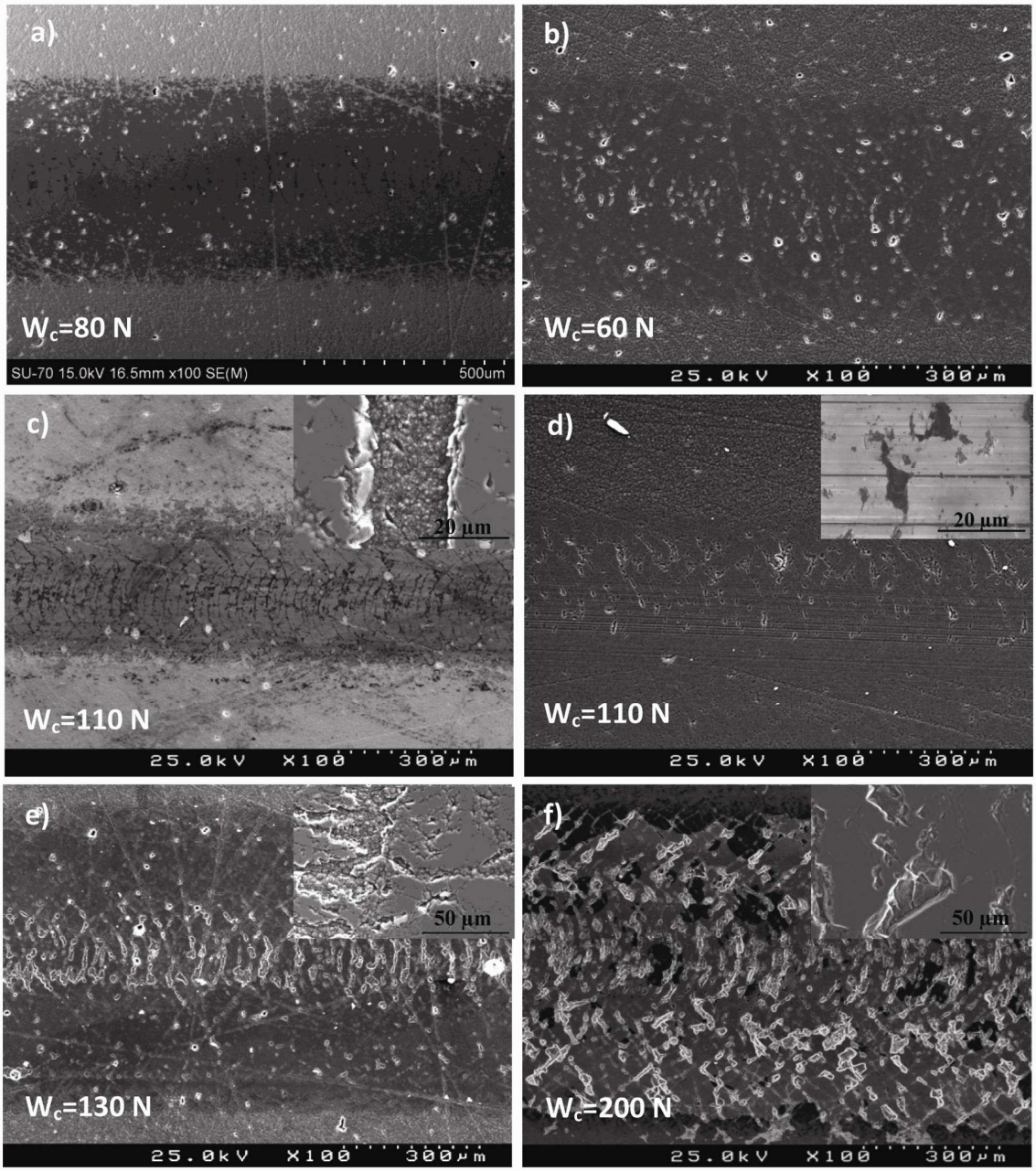

Figure 3 – Worn surfaces after self-mated testing under the critical load (W_C) for NCD-1 (a), NCD-2 (b), Bilayer-1 (c), Bilayer-2 (d), Multi-1 (e) and Multi-2 (f). The insets depict a magnification inside the correspondent wear track.

Higher magnification images are presented on the insets of Fig. 3 to highlight features regarding the tribological behaviour of bilayer and multilayer coatings. The inset in Fig. 3 (c), corresponding to Bilayer-1 coating, shows the presence of tribolayers in the lateral regions of the image, resulting from the agglomeration of wear debris particles and their subsequent plastic deformation into adhered layers. In addition, the

typical surface morphology of NCD-1 grade can be seen on the tribolayer-free central region of the inset. Showing a distinct behaviour, the Bilayer-2 film magnification (Fig. 3 (d) inset) reveals abraded surface asperities, amid grain pullouts features, without the evidence of tribolayers formation, and parallel grooves typical of abrasion (two-body) by micro-cutting.

Regarding the multilayer systems, both coatings present tribological surfaces with similar features like the presence of grain pullouts, covering the full extent of the wear track. It is noteworthy, that the Multi-2 system sustained a critical load of 200 N, which represents an almost two fold increase when compared to the Multi-1 system (130 N), although having similar wear mechanisms involved. Also, there is a substantial difference in the critical load values of monolayered NCD-2 (60 N) and its multilayer composite (Multi-2).

Raman spectra of the NCD-2 and Multi-2 films are depicted in Fig. 4 (a) and (b), respectively. The shallow penetration depth of the laser radiation used in UV-Raman analysis (λ = 325 nm) [29] gives a picture of the exposed top layer. In both coatings a sharp diamond peak localized at ~1331 cm^{-1}, combined with the disordered (D) and crystalline (G) graphite bands, at ~1370 cm^{-1} and ~1580 cm^{-1}, respectively, is visible. The bands located at ~1150 cm^{-1} and ~1540 cm^{-1}, attributed to intragranular trans-polyacetylene (TPA), are commonly accepted as typical of NCD films [30]. In the wear track spectra, the shift of the diamond peak outcomes from intrinsic residual stresses associated with the presence of non-diamond material, as well as structural defects, like microtwins, dislocations or impurities [31], created during the sliding action. As can be seen in Fig. 4 (a), a positive shift $\Delta\nu$ = 7 cm^{-1} relative to the value of natural bulk diamond was obtained inside the wear track region of the monolayered NCD-2, which indicates a compressive biaxial stress state of ~ -4.0 GPa, according to Ralchenko's equation [32]. On the other hand, the Multi-2 track reveals a lower compressive biaxial stress of ~ -2.3 GPa ($\Delta\nu$ = 4 cm^{-1}). Moreover, the Raman spectra acquired inside the same Multi-2 worn track does not present the TPA bands and shows a much less pronounced G band. This indicates that the NCD top layer was almost completely worn out, exposing the underlying MCD layer. The MCD grade is harder and less susceptible to defects creation than NCD, keeping the residual stresses at lower levels. In resume,

in the NCD-2 monolayer the tribological solicitation is transposed throughout the coating giving rise to the above mentioned high stress state and consequent film delamination under low applied loads. A great benefit is obtained by the use of the Multi-2 coating where the sacrificial role of the top NCD-2 layer hinders the rise in the residual stress state, allowing its tribological application under much higher loads.

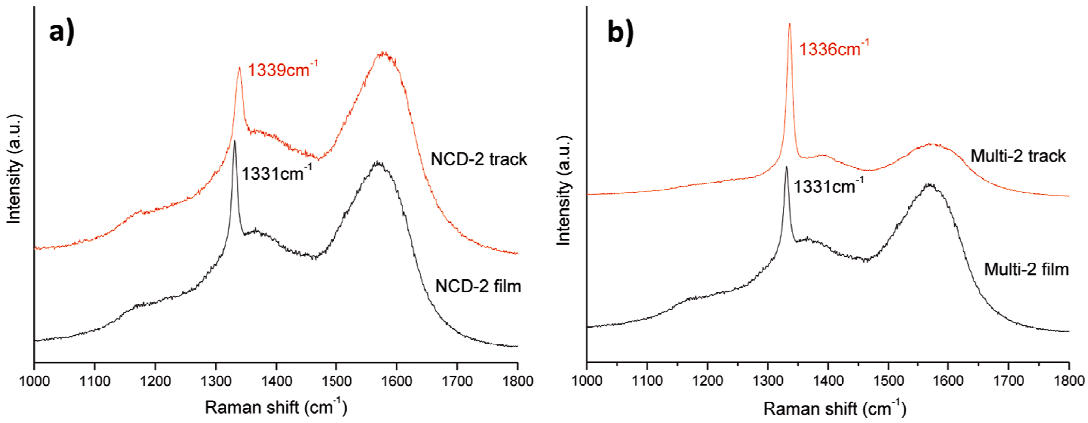

Figure 4 – Raman spectra of the NCD-2 (a) and Multi-2 (b) coatings: un-worn film and inside the wear track.

3.4. Topography of diamond coatings

A thorough study of the surface topography of the coatings, measured by AFM, was conducted in order to assess the evolution of worn surfaces under sliding and correlate it with prevailing wear damage mechanisms observed by SEM analysis. Depicted in Fig. 5 are AFM scans of the monolayered systems, for as-deposited, endurance tests and worn surfaces under critical load. The as–grown films exhibit topographies which are typical of the involved systems, namely the jagged topography of micropyramidal MCD (RMS 485±50 nm), a cauliflower shape-like topography of diamond nanoclusters for NCD-2 (RMS 295±15 nm) and an in between structure for NCD-1, characterized by faceted nanocrystallites (RMS 350±1 nm). As can be seen, the endurance tests (16 h) are characterized by a complete removal of the aforementioned topography features resulting in very smooth surfaces varying in the range 25-120 nm. These values represent more than a ten-fold decrease in surface roughness for MCD (RMS 40±2 nm) and NCD-1 (RMS 25±2 nm), typical of polished surfaces, namely as a result of a micro-cracking abrasive wear mechanism, as above discussed. The NCD-2

coating shows, however, evidences of shallow wear grooves, from micro-cutting abrasive action, leading to the highest surface roughness value (RMS 120±5 nm).

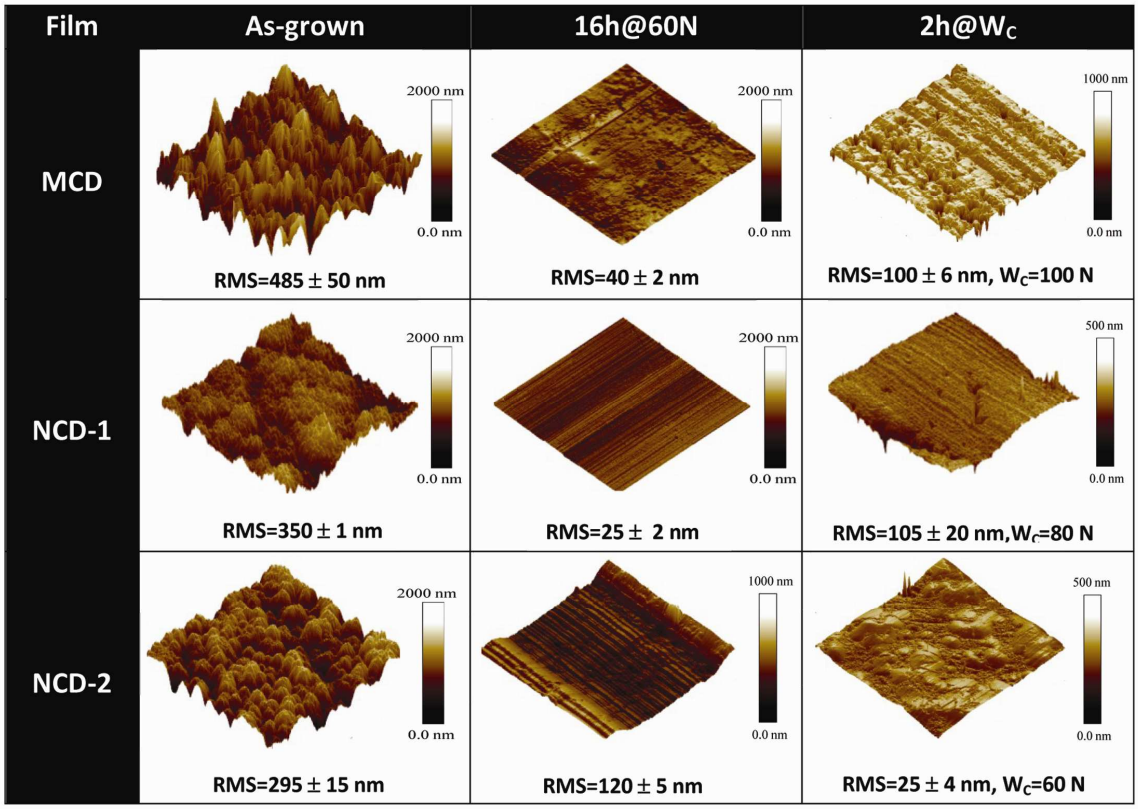

Figure 5 – AFM scans depict the MCD,NCD-1 and NCD-2 surfaces: unworn (leftcolumn), after the endurance tests at 60N (centre column) and at the critical load (right column), with respective root mean square roughness values.

Although the much higher applied loads, thus the higher severity of contact during the 2 h critical load tests, the surfaces of MCD and NCD-1 monolayers also present similar abrasive wear mechanisms to those above mentioned. After the initial truncating and progressive blunting of protruding surface asperities, the resulting worn surfaces exhibit some hints of the intrinsic deep valleys of MCD and the depressions of NCD-2 nanometer-scale roughness.

For the later, the initial topography is modified to a lesser extent, as a result of a shorter test under the same applied load (60 N) as that of the endurance tests. In the case of NCD-1, the initial topography is almost totally abraded as a result of the higher contact load involved (80 N), comparing to the NCD-2 coating (60 N).

Regarding the composite coatings, the evolution of their topography under tribological assessment is depicted in Fig.6.

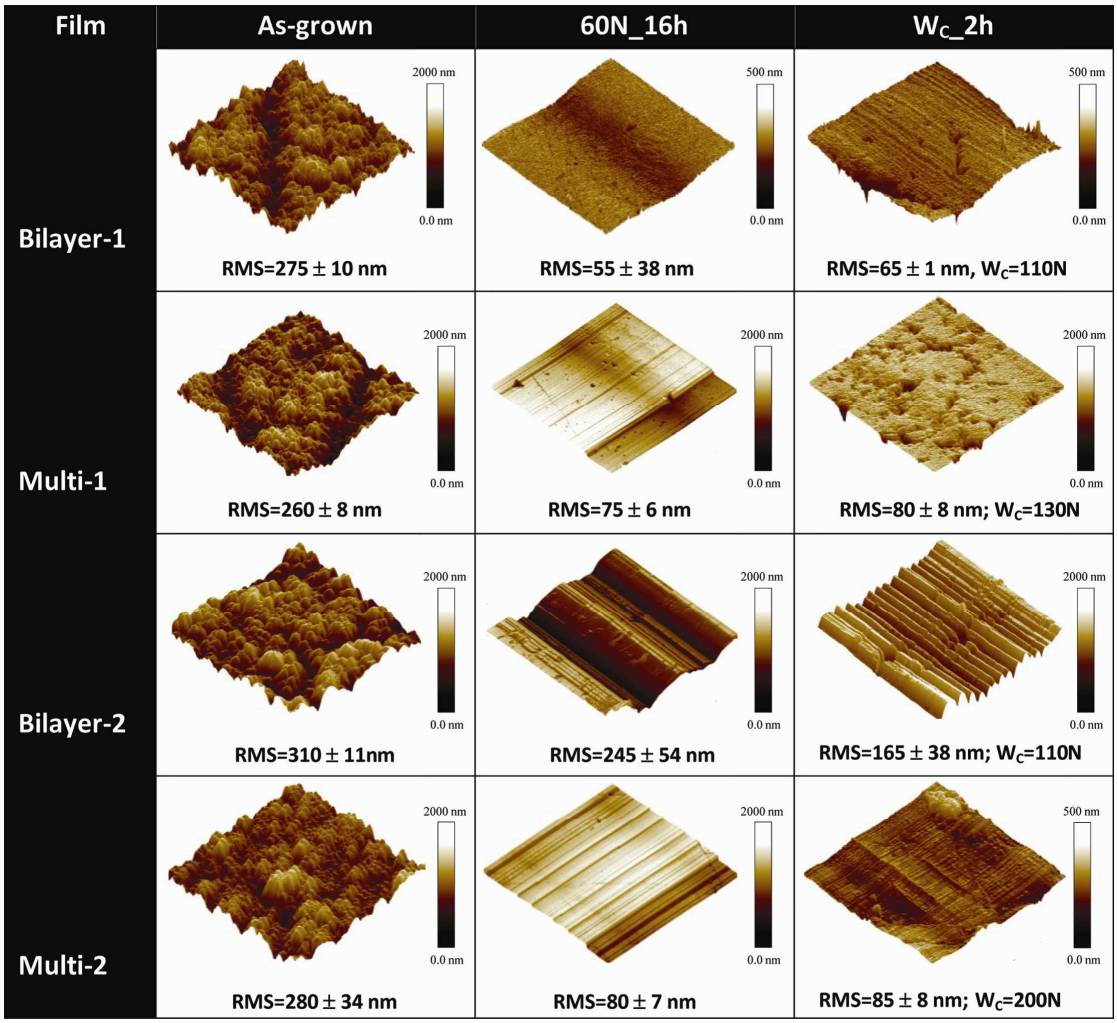

Figure 6 – AFM scans of the as-grown (left column) and worn surfaces after the endurance tests (center column) and under high loading conditions (right column) for the bilayer and multilayer coatings, with respective root-mean square roughness values.

All as-deposited coatings are characterized by the prevalence of elemental structural units spatially organized as diamond nanoclusters, resulting from the nanodiamond top layer. As readily seen, NCD-1 graded systems show a smoother appearance for the worn surfaces subjected to the endurance tribotests. On the other hand, the coatings having a NCD-2 top layer reveal the presence of abrasion grooves, more emphasized on the Bilayer-2 system. The surface finishing condition of NCD-1 systems is coherent with a self-polishing wear mechanisms, as previously reported in the corresponding SEM images (Fig. 2). This characteristic is also supported by the reduction in the surface roughness values of the worn coatings, namely a fivefold decrease for Bilayer-1 (RMS 55±38 nm) and an almost four fold reduction for Multi-1

(RMS 75±6 nm) and Multi-2 (RMS 80±7 nm). As for the Bilayer-2 coating with a starting roughness of RMS 310±11 nm, the decrease in surface roughness is considerably smaller as a result of the formation of deep wear grooves, leading to a final roughness of RMS 245±54 nm. Regarding the worn surfaces obtained under the critical load a similar trend is observed. Once more, the Bilayer-2 coating presents a higher surface degradation with a corresponding roughness value of RMS 165±38 nm due to the existence of a dense field of microabrasion wear grooves. Moreover, the topography of the Multi-1 coating reveals a widespread distribution of grain pullouts as a consequence of the high stresses imposed under the critical load (130 N). Subjected to the highest measured critical load value (200 N), the Multi-2 coating is characterized by a smooth topography superimposed on a surface exhibiting some waviness, as a result of the incomplete flattening of wear grooves.

3.5. Friction and wear coefficients of diamond coatings

Examples of the friction coefficient evolution of the diamond coatings are depicted in Fig. 7. As can be seen, all curves exhibit a similar trend whereby an initial intense peak, corresponding to static friction values as high as approx. 0.90, is followed by a short running-in regime not exceeding a sliding distance of 10 m. The initial short-lived friction peak results from the intense initial mechanical interlocking between antagonistic hard surface asperities. On the other hand, the subsequently running-in period corresponds to the truncating and subsequent blunting of diamond nanoclusters. Following these two features, a regime of low friction sets in for the remaining length of the tribotests. A summary of representative values for the the static friction (μ_{max}) and steady-state friction (μ) after running-in is presented in Table 2. As expected, based on previous work of this group, the MCD coating is generally characterised by the largest occurring values for the static friction (μ_{max}) and average values for the friction after running-in (μ). This can be explained due to the intrinsic rough starting topography of MCD, which gives rise to a high initial friction response resulting from a more important deformation component in the overall friction phenomenon. The friction behaviour of MCD will serve as a reference material for the other systems, since it constitutes the bottom layer for all composite coatings. The static friction coefficient values are strongly influenced by the surface roughness of all

the diamond coatings and, as such, all the studied systems present somewhat similar values for this feature, exhibiting high μ_{max} because of the substrate pre-treatment with CF_4 plasma. Among, the monolayer coatings, the MCD is characterised by the largest occurring values for μ. This can be explained due to the intrinsic rough topography of MCD that is partially kept during the runs. Regarding the monolayered nanocrystalline films, the endurance tribotests (16h, *W*=60 N) were characterised by very low steadystate friction coefficient values, with the NCD-1 coating showing a relatively higher coefficient as a result of the rougher faceted microstructure. On the other hand, the difference in μ for NCD-1 and NCD-2 when subjected to the critical load is decreased, due to the higher contact stress undergone by the NCD-1 coating. The initial topography is rapidly destroyed leading to a smoothed sliding surface with similar surface features as that of NCD-2, and, therefore, a similar friction interaction.

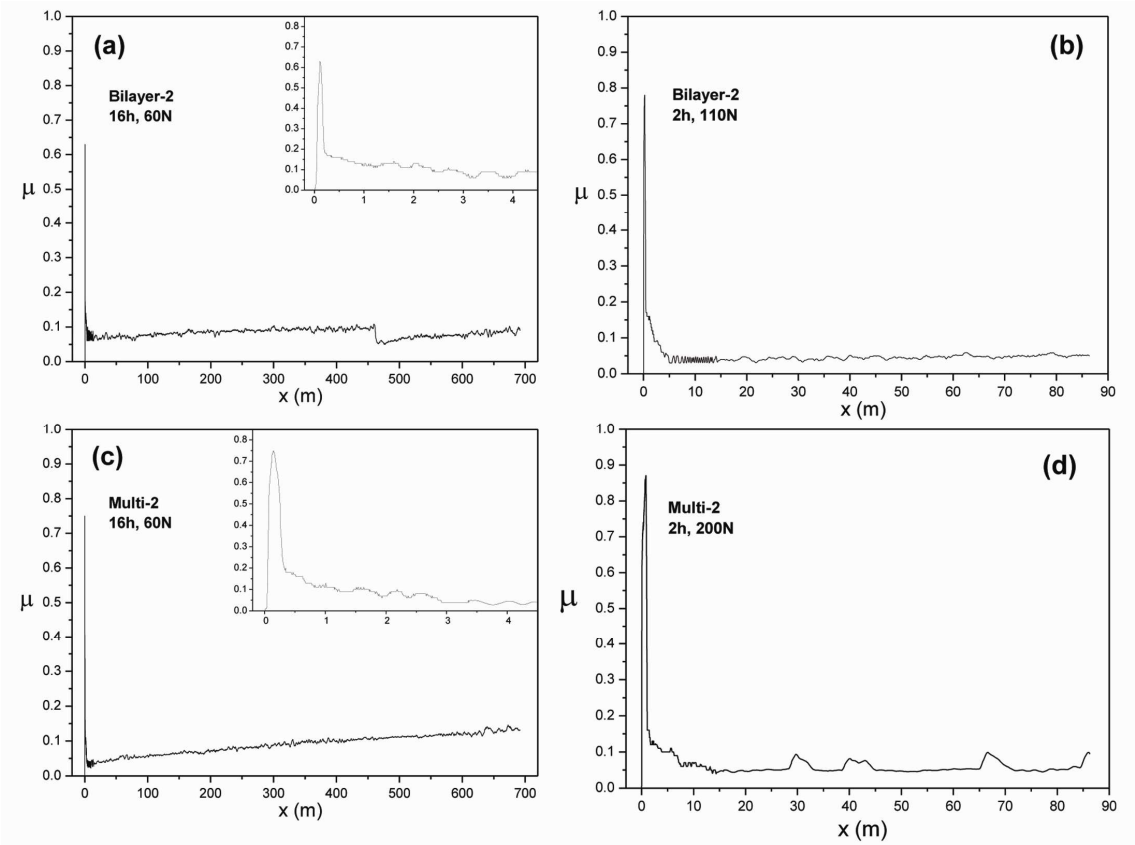

Figure 7 – Friction curve evolution as a function of sliding distance of Bilayer-2 and Multi-2 for the endurance tests ((a), (c)) and critical load tests ((b), (d)). Insets present a detailed view of the narrow peak and running-in period of the endurance tests friction curves.

In Fig. 7, the friction curves of Bilayer-2 and Multi-2 for the endurance tests ((a), (c)) and critical load tests ((b), (d)) are presented side-by-side. A detailed view of the narrow peak and running-in period is depicted on the insets of the endurance tests friction curves. The gradual decrease in friction response corresponds to the accommodation of opposing surfaces and the presence of oscillations to the progressive blunting of nanocluster asperities and wear debris production. Fig. 7 (b) shows the friction coefficient of Bilayer-2 subjected to its critical load (110 N). As readily seen, the initial friction μ_{max} is higher than for the endurance test as a result of the almost two fold increase in contact load, which implies a more intense energy dissipation to initiate the relative motion between surfaces. On the other hand, the low friction regime is characterised by slightly lower average values (0.05) under the critical load, which can be explained once more by the contact pressure increase. In this case, a higher applied load plays a beneficial role by producing smoother surfaces by accelerated blunting of nanodiamond asperities, which can be corroborated by the

SEM and AFM data (see Figs. 2, 3 and 6). A similar behaviour is found for the Multi-2 coating. Nonetheless, the endurance curve shows a monotonic increase in μ with the sliding distance. This is due to the progressive wear of the top NCD-2 layer as discussed in section 2.3. Ultimately, this leads to the influence of the exposed rougher MCD layer and increased friction response. Such phenomenon was also observed for the friction evolution of the Multi-1 coating, to a lesser degree due to the harder and thicker NCD-1 top layer, thus mitigating the influence of the underlying MCD.

Regarding to the wear resistance, all coatings were characterised by mild to very mild wear regimes, the wear coefficients varying in the range of 4.1×10^{-8} to 7.7×10^{-7} $mm^3.N^{-1}.m^{-1}$. The counterpart ball specimens were characterised by wear coefficient values in the leeway $2.5\times10^{-8} – 4.4\times10^{-7}$ $mm^3.N^{-1}.m^{-1}$, which were estimated from the wear scars dimensions. As can be seen in Fig. 8 (a), corresponding to the endurance experiments (W= 60 N), all plate specimens were characterised by a lower wear resistance compared to the ball samples, as a result of fatigue effects induced by the intermittent contact during the reciprocating sliding. The Bilayer-2 plate shows the lowest wear resistance (7.7×10^{-7} $mm^3N^{-1}m^{-1}$) due to the softer nature of the NCD-2 top layer, while the Multi-1 ball exhibited the highest wear resistance (2.5×10^{-8} $mm^3.N^{-1}.m^{-1}$). The later behaviour can be explained by the harder NCD-1 grade top layer combined with the lack of cyclic fatigue effects for the ball specimens.

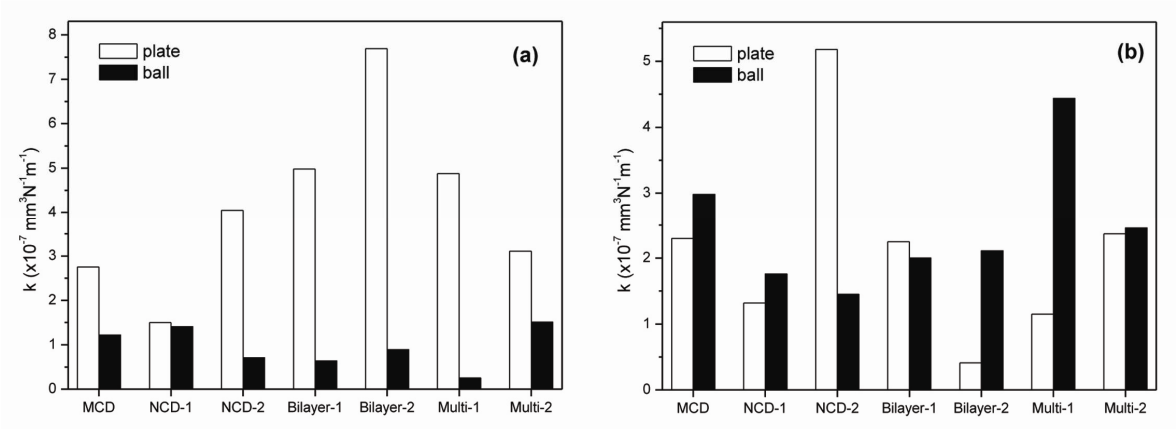

Fig.8 – Wear coefficient values for ball and plate specimens after the endurance experiments (a) and under the critical load, W_C (b), for all diamond systems.

As depicted in Fig. 8 (b), the tribotests under the critical load show a distinct general trend from the endurance experiments. As a rule, the ball specimens show a

lower resistance compared to the flat samples. The fatigue phenomenon is still present but the number of cycles is much less than for the endurance tests. Also, the very high contact pressures reached under critical loading will limit the wear life of the ball specimens, since they usually present lower adhesion levels to the substrate when compared to the flat ones [33]. As readily seen, the monolayered NCD-2 plate exhibit the highest wear coefficient due to the increased sp^2 content and, as a result, lower shear strength. Nonetheless, NCD-2 graded top-layer composites show an increased wear resistance. This can be explained by the accelerated wearing off of the thin sacrificial NCD-2 top layer, which will expose the underlying MCD coating less prone to subsequent wear damage. Such behaviour can be further corroborated by the similar wear resistances observed in Multi-2 and monolayered MCD systems. It is noteworthy to mention that the plate specimens of Multi-2 were able to perform even under higher applied loads (up to 235 N), although without a corresponding wear performance of the ball counterpart due to substrate adhesion limitations. Nevertheless, the coating integrity preservation in both elements of the tribosystem was established as a criterion to validate the critical load of the diamond coatings. Accordingly, of all studied systems the Multi-2 composite exhibited an outstanding threshold load of 200 N prior to gross film detachment, which highlights the enhanced wear performance under high loads of micro/nanocrystalline diamond multilayer coatings.

4. Conclusions

Self-mated tribological systems of monolayer, bilayer (or mono-, bi-.and multilayer) and multilayer micro- and nanocrystalline diamond coatings successfully perform both in high-load (max. 200 N)) short-term tests (86 m) and endurance tests (60N; 691 m). Experiments were performed without lubrication, showing very low values of the friction coefficient that varied between 0.02 and 0.09. Also, very-mild to mild wear regimes (wear coefficient values between 4.1×10^{-8} and 7.7×10^{-7} $mm^3.N^{-1}.m^{-1}$) were attained.

The fourfold diamond multilayers, characterised by a top most nanocrystalline diamond layer containing a higher amount of sp^2 carbon, outperform the other varieties of diamond coatings by withstanding an applied load value of 200 N without delamination, combined with a high wear resistance (~2.4×10^{-7} $mm^3N^{-1}m^{-1}$) and a low friction coefficient (0.06). In this composite coating, the top nanocrystalline diamond layer progressively wears out performing a sacrificial role, while the underneath harder microcrystalline diamond layer keeps the residual stresses at lower levels. Such superior performance validates the great potential offered by these systems in highly demanding tribological applications subjected to high contact pressures where lubrication is not practical, or in applications needing low friction coefficients combined with high wear resistance.

Acknowledgements

This work was funded by projects MULTIDIACOAT – PTDC/EME-TME/100689/2008 and Pest-C/CTM/LA0011/2011 from Fundação para a Ciência e Tecnologia (FCT, Portugal). E. Salgueiredo and M. Amaral also acknowledge FCT for the grants SFRH/BD/41757/2007 and SFRH/BPD/26787/2006, respectively. A.J.S. Fernandes from Physics Department of Aveiro University is gratefully acknowledged for the Raman spectroscopy analysis.

References

[1] O.A. Williams, Diamond Relat. Mater. 20 (2011) 621-640.

[2] C.S. Abreu, M. Amaral, A.J.S. Fernandes, F.J. Oliveira, R.F. Silva, J.R. Gomes, Diamond Relat. Mater. 15 (2006) 739-744.

[3] C.S. Abreu, M. Amaral, A.J.S. Fernandes, F.J. Oliveira, J.R. Gomes, R.F. Silva, Diamond Relat. Mater. 15 (2006) 2024-2028.

[4] C.S. Abreu, M. Amaral, F.J. Oliveira, A. Tallaire, F. Bénédic, O. Syll, G. Cicala, J.R. Gomes, R.F. Silva, Surf. Coat. Technol. 200 (2006) 6235-6239.

[5] C.S. Abreu, F.J. Oliveira, M. Belmonte, A.J.S. Fernandes, J.R. Gomes, R.F. Silva, Tribology Lett. 21 (2006) 141-151.

[6] C.S. Abreu, F.J. Oliveira, M. Belmonte, A.J.S. Fernandes, R.F. Silva, J.R. Gomes, Wear 259 (2005) 771-778.

[7] K. Mallika, R. Komanduri, Thin Solid Films 396 (2001) 146-166.

[8] M.R. Soares, M. Belmonte, R.F. Silva, J. Appl. Phys. 94 (2003) 5633-5638.

[9] A.A. Voevodin, J.S. Zabinski, C. Muratore, Tsinghua Sci. Technol.10 (2005) 665-679.

[10] J. Romero, A. Lousa, E. Martínez, J. Esteve, Surf. Coat. Technol. 163 –164 (2003) 392–397.

[11] Y.M. Zhou, R. Asaki, K. Higashi, W.H. Soe, R. Yamamoto, Surf. Coat. Technol. 130 (2000) 9-14.

[12] K. Holmberg, H. Ronkainen, A. Matthews, Ceram. Int. 26 (2000) 787-795.

[13] S. Takeuchi, M. Kojima, S. Takano, K. Kazutaka, M. Murakawa, Thin Solid Films 469-470 (2004) 190-193.

[14] L. Schafer, M. Höfer, R. Kröger, Thin Solid Films 515 (2006) 1017-1024.

[15] M. Vojs, M. Veselý, R. Redhammer, J. Janík, M. Kadlečíková, T. Daniš, M. Marton, M. Michalka, P. Šutta, Diamond Relat. Mater. 14 (2005) 613-616.

[16] F. Sun, Y. Ma, B. Shen, Z. Zhang, M. Chen, Diamond Relat. Mater. 18 (2009) 276-282.

[17] M. Kadlečíková, M. Vojs, J. Breza, M. Veselý, Z. Frgala, M. Michalka, J. Matějková, A. Vojačková, T. Daniš, M. Marton, Microelectronics Journal 38 (2007) 20-23.

[18] H.Q. Li, K.M. Leung, K.L. Ma, Q. Ye, Y.M. Chong, Y.S. Zou, W.J. Zhang, S.T. Lee, I. Bello, Appl. Phys. Lett. 91 (2007) 201918(3).

[19] C. Popov, W. Kulisch, M. Jelinek, A. Bock, J. Strnad, Thin Solid Films 494 (2006) 92-97.

[20] X. Chen, Z. Peng, X. Yu, Z. Fu, W. Yue, C. Wang, Appl. Surf. Sci. 257 (2011) 3180–3186.

[21] M. Amaral, C.S. Abreu, F.J. Oliveira, J.R. Gomes, R.F. Silva, Diamond Relat. Mater. 16 (2007) 790–795.

[22] E. Zeiler, D. Klaffke, K. Hiltner, T. Grögler, S.M. Rosiwal, R.F. Singer, Surf. Coat. Technol. 116-119 (1999) 599-608.

[23] I.M. Hutchings, Tribology-Friction and Wear of Engineering Materials, Ed. Butterworth-Heinmann, UK (2003).

[24] M. Belmonte, V.A. Silva, A.J.S. Fernandes, F. Costa, R.F. Silva, J. Am. Ceram. Soc. 86 [5] (2003) 749-754.

[25] S.J. Bull, Diamond Relat. Mater. 4 (1995) 827-836.

[26] M. Belmonte, A.J.S. Fernandes, F.M. Costa, F.J. Oliveira, R.F. Silva, Diamond Relat. Mater. 12 (2003) 733-737.

[27] K. Holmberg, A. Laukkanen, H. Ronkainen, K. Wallin, S. Varjus, Wear 254 (2003) 278–291.

[28] F.A. Almeida, M. Amaral, F.J. Oliveira, A.J.S. Fernandes, R.F. Silva, Vacuum 81 (2007) 1443-1447.

[29] S. Gupta, B.R. Weiner, W.H. Nelson, G. Morell, J. Raman Spectrosc. 34 (2003) 192-198.

[30] A.C. Ferrari, J. Robertson, Phys. Rev. B 63 (2001) 121405-4.

[31] N.G. Ferreira, E. Abramof, N.F. Leite, E.J. Corat, V.J. Trava-Airoldi, J. Appl. Phys. 91 (2002) 2466-2472.

[32] V.G. Ralchenko, A.A. Smolin, V.G. Pereverzev, E.D. Obraztsova, K.G. Korotoushenko, V.I. Konov, Y.V. Lakhotkin, E.N. Loubnin, Diamond Relat. Mater. 4 (1995) 754-758.

[33] M.J. Papo, S.A. Catledge, C. Machado, S. Kashef, A.E. Eberhardt, Y.K. Vohra, Materials Research Society Symposium Proceedings 791 (2004) 271-276.

III.5. Tribological assessment of multilayer micro/nanocrystalline CVD diamond coatings under physiological fluids

E. Salgueiredo[1]; F.J. Oliveira[1]; J.M. Carrapichano[2], C.S. Abreu[3,4]; J.R. Gomes[4,5]; R.F. Silva[1,*]

[1]*CICECO, Ceramics and Glass Eng. Dep., University of Aveiro, Campus de Santiago, P-3810-193 Aveiro, Portugal*
[2] *Mechanical Eng. Dept., Coimbra Superior Eng. Inst., 3040-228 Coimbra, Portugal*
[4]*Centre for Mechanical and Materials Technologies (CT2M), Portugal*
[5]*Mechanical Eng. Department, CIICS, University of Minho, 4800-058, Guimarães, Portugal*

(To be submitted)

Abstract

Biotribological tests with FBS and HBSS fluids were conducted using seven different types of diamond coating architectures: monolayers of MCD and NCD and four types of two and four layer coatings. Reciprocating, flat pin-on-flat plate, sliding tests were conducted under 11 N and 98 N loads at 12 $mm.s^{-1}$ and 24 $mm.s^{-1}$, respectively, for a maximum length of 6000 m. Apparent contact stresses are in the range of those found in micro-separation experiments, from 30 MPa to 750 MPa. Wear occurs initially by truncation of microcrystalline pyramids or blunting of nanocrystalline agglomerates and then by a fine scale abrasive wear mechanism that ends in surfaces becoming fully polished for the 98 N loads. AFM derived wear volumes confirmed that, for the 11 N loads, wear coefficient values, *k*, are from one to two orders of magnitude smaller than for similar dry experiments and are in the range 10^{-9} to 10^{-8} $mm^3.N^{-1}.m^{-1}$, corresponding to a very mild wear regime. These values increase by about one order of magnitude for the 98 N test, due to enhanced fatigue effects, with Bi- and Multi-layer films being less sensitive to the speed and load increment than the monolayers. For the 11 N tests, to larger steady state friction coefficient values correspond larger wear rates, for both fluids, although without a clear effect of the physiological liquids on the total wear rates. In these tests, μ_{ss} values vary from 0.015 to 0.081, with the larger values being obtained for the FBS lubrication, but still inside the range of values found for common hip-joint replacement materials.

Keywords: diamond multilayers, physiological fluids, tribology, wear.

1. Introduction

Fatigue and corrosion in the physiological environment are a major issue when using biomedical metallic alloys for these processes ultimately lead to the failure of the implant [1]. This is a particularly relevant issue in biotribological systems such as in prosthetic hip joints where the amount of wear debris generated from the acetabular cup/femoral head contact is still one of the most common causes for their long term failure. They may induce the three-body wear mechanism or get deposited on the femoral surface [2]. Carbon-based hard coatings may be crucial on the development of more reliable non-metallic tribosystems, namely for use in biomedicine [3]. Diamond-Like Carbon (DLC) coatings have drawn considerable attention in recent years for biomedical applications, but with a significant variance in the results [4] as several loading conditions, environments and materials combinations are reported. In tests conducted in a hip joint simulator, Liu *et al.* concluded that the DLC coated CoCrMo joint heads cannot improve the wear resistance of the CoCrMo/UHMWPE artificial hip joint, unless a UHMWPE modification for strengthening is performed [5]. Hauert *et al.* reported failed hip joints explants due to the poor adhesion strength of the DLC coating to Ti-6Al-4V [6]. Moreover, Si or Si-rich interlayers used to improve adhesion are prone to crevice corrosion in some lubricant media, promoting the delamination of the coating [7]. A similar behaviour was also reported by Hauert *et al*. for a DLC coated CoCrMo metatarsophalangeal (MTP) prosthesis where both articulating surfaces were coated and explanted after approximately 4 years [8]. Manhabosco *et al*. reported the catastrophic delamination of DLC coated Ti6Al4V alloys submitted to wear-corrosion tests in simulated physiological solution [9]. TiN- and DLC-coated SS316L presented a major improvement in corrosion, compared to the uncoated steel, in tribological testing in Simulated Body Fluid against HDPE (High Density Polyethylene) [10]. Nevertheless, the DLC coatings did not prove adequate to use in sliding with polymeric materials as a counterface. However, a different trend was observed in self-mated diamond-like coated articulating surfaces that showed improved wear resistance, with reduction in the number and size of the generated debris, when compared to the conventional hip tribosystems (UHMWPE against metal) [11].

CVD diamond may constitute a better option as a bio-tribo-coating. The tribological characterization of silicon nitride (Si_3N_4) ceramic parts coated with nanocrystalline diamond (NCD) was performed on Hank's balanced salt solution (HBSS) and diluted fetal bovine serum (FBS), revealing wear rates in the range of ~10^{-9} – 10^{-8} $mm^3.N^{-1}.m^{-1}$, and friction coefficients of 0.06 and 0.10 for HBSS and FBS experiments, respectively [12]. Thomas *et al.* studied the effect of the size of nanodiamond wear particles on macrophage proliferation, apoptosis, metabolic activity and inflammatory cytokine production evidencing no potential inflammations due to a size-effect (in the range 6-500 nm) of diamond wear particles at low concentrations (≤50 $\mu g.ml^{-1}$) [13]. Si_3N_4 ceramics, due to their high hardness and fracture toughness, are by themselves suitable candidates for ceramic-on-ceramic Total Joint Replacements (TJR) [14], presenting mechanical properties and suitability for in vivo implantation as reported by Bal *et al.*[15]. Over the past few years, our approach has been to try developing an excel tribosystem based on the well-known chemical and physical compatibility of this ceramic with CVD diamond coatings. The promising results obtained so far opened a window of opportunity for the use of multilayered diamond coatings that recently proved to have a superior mechanical behaviour [16], due to the combination of an initial highly adherent microcrystalline diamond (MCD) layer with the very low surface roughness of the NCD top layer and the presence of discontinuous interfaces [17]. Erosive wear tests showed that the induction time for delamination more than doubled and in the dry sliding characterization, the critical load for delamination more than tripled, when comparing with the best monolayer with the same thickness [18].

Laboratory bench tests are necessary to understand the wear mechanisms and the potential behaviour of these new multilayered CVD diamond coated materials for hip joints, before moving on to testing in simulators and, lastly, to *in vivo* environments [19, 20]. In this work, different types of monolithic MCD and NCD coatings and their combinations in two and four layer configurations were tribologically tested in a pin-on-plate configuration in lubricated sliding with simulated HBSS and FBS physiological fluids, to replicate the conditions of the hip tribosystem [21].

2. Experimental

The conditions for the CVD growth of microcrystalline diamond (MCD) and two grades of nanocrystalline diamond (NCD) are given in Table 1. The substrate material is an yttria and alumina doped Si_3N_4 ceramic. Besides the three monolithic diamond varieties, four other types of diamond coatings were obtained by combining MCD with NCD-1 or NCD-2 in two and four layers coatings that are termed as: Bilayer-1, Bilayer-2, Multilayer-1 and Multilayer-2, were the suffixes 1 and 2 refer to the type of NCD coating used. NCD-1 corresponds to nanocrystalline diamond grown in a hydrogen and methane atmosphere, and NCD-2 to nanocrystalline diamond grown in the presence of a third gas, argon. The deposition time of each layer was adjusted to give a total coating thickness of 10-12 µm. Detailed information on the production of the substrates, their surface preparation and development of the multilayered composite CVD diamond coatings can be found elsewhere [16].

Table 1 - Deposition parameters of MCD, and two NCD grades in a hot filament CVD reactor.

	CH_4/H_2 ratio	Ar/H_2 ratio	Gas flow (sccm)	Total pressure (kPa)	Substrate temperature (°C)
Filament carburization	0.026	-	200	10.0	630
MCD	0.026	-	100	17.5	800
NCD-1 (CH_4)	0.073	-	100	5.0	700
NCD-2 (Ar)	0.04	0.1	200	10.0	700

The bio-tribological characterization of the seven different coatings was carried out at different load regimes in two pin-on-flat adapted tribometers using reciprocating sliding arrangements: i) at 11 N, in a PLINT TE67/R tribometer with constant frequency (1 Hz) and stroke length (6 mm), a sliding distance of 6000 m, using flat ended (Ø ~2 mm) pins and ceramic plates (Ø10 mm x 3 mm); ii) at 98 N, in a TE92 PLINT machine, using the same frequency but a stroke length of 12 mm, using larger diameter pins (Ø ~5 mm) and plates (20x10x3 mm). The tests were performed in ambient air (R.H. ~50-60%) at room temperature. The 11 N tribological tests were

conducted under lubricated conditions with two types of physiological fluids: a) Hank's balanced salt solution (HBSS, Cambrex, Belgium) containing 8 $g \cdot L^{-1}$ NaCl, 1 $g \cdot L^{-1}$ glucose, 0.4 $g \cdot L^{-1}$ KCl, 0.35 $g \cdot L^{-1}$ $NaHCO_3$, 0.09 $g \cdot L^{-1}$ $Na_2HPO_4.7H_2O$ and 0.06 $g \cdot L^{-1}$ KH_2PO_4 as main components; and b) fetal bovine serum (FBS, Cambrex, Belgium) diluted to 50% to contain 18.5 $mg \cdot ml^{-1}$ protein, complying with synovial fluid plus 0.2 wt.% of a biocide (NaN_3, Merck, Germany). The 98 N tests were carried out using only HBSS. The objective of using loads with one order of magnitude difference and a longer stroke is related to the more stringent load regimes that are being considered for testing hip-joint replacement materials, having in mind daily life activities. Also, independently of the nominal value of the applied stresses, larger loads do induce stronger fatigue effects on the plate surfaces and this has to be factored in the biotribological behavior of these hard coatings based on CVD diamond.

A Field Emission Scanning Electron Microscopy (FE-SEM) Hitachi SU-70 was used for surface morphology characterization of the diamond coatings, before and after lubricated testing. The surface roughness of the diamond layers was determined by Atomic Force Microscopy (AFM) using 100 μm x 100 μm scans.

3. Results and discussion

In flat pin-on-plate tests, a common drawback is related to the misalignment of the pin with the plate that does not allow a fully flat contact during sliding [12]. As a result, the apparent contact area is reduced with respect to the nominal value corresponding to the area of the pins and this leads to larger apparent stresses. Figure 1a portrays this effect in the surface of a pin and Figure 1b is a general view of the respective wear track in the counterface, the plate. After testing, the apparent contact area of each pin, the wear scars, was then measured using optical microscopy. The apparent contact stresses are scattered in the range 30-750 MPa without a clear correlation with the applied load or the physiological fluid. This range of values corresponds to the stresses encountered in daily life activities and that are being considered for incorporation in the new ISO standard for the testing of artificial hip-joints for total hip replacements, by the use of micro-separation technique during testing [22]. The higher loads can serve as a reliability analysis of the adhesion of the

coatings and of their mechanical integrity, since they start approaching apparent stresses measured in dry-sliding tests.

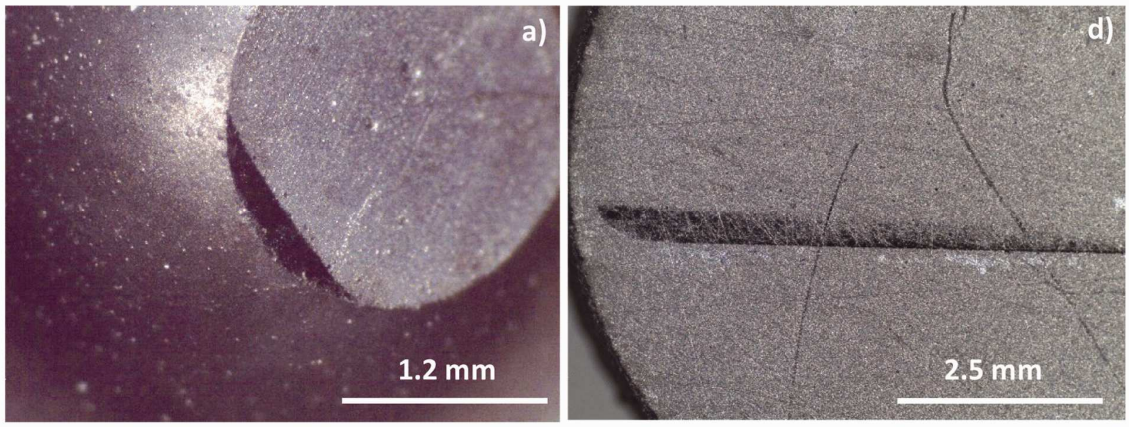

Figure 1 - Optical micrographs of a) worn pin and b) plate of NCD-2 monolayer coating after testing under HBSS lubrication with a 11 N load.

The as-deposited and worn surfaces of the plates were characterized by atomic force microscopy (AFM) with the purpose of estimating the wear volumes and thus the wear coefficient, *k*. Before analysis, all samples were cleaned in acetone and ethanol for removal of surface debris. The extremely low wear rate of CVD diamond renders impossible the measurement of material loss by the usual precision weighing, so the adopted method for *k* evaluation involves using the AFM bearing function and a procedure detailed elsewhere for volume loss quantification data [23]. Briefly, the bearing volume, the volume of material above the deepest valley, is measured in both the pristine and the worn coatings using AFM topographic tapping mode. In the worn surfaces this method is only valid if the wear track is not deeper than the deepest valley of the original surface. Data in Figure 2 show that there is a trend between these bearing volumes and the respective RMS values. In this plot an individual point corresponds to a value taken for a single tested coating, irrespectively of type of diamond (monolayer, bilayer, multilayer), load and lubricating fluid. The observed proportionality is a measure of the appropriateness of using the present approach, based on the bearing volume, as a means of obtaining the wear volumes.

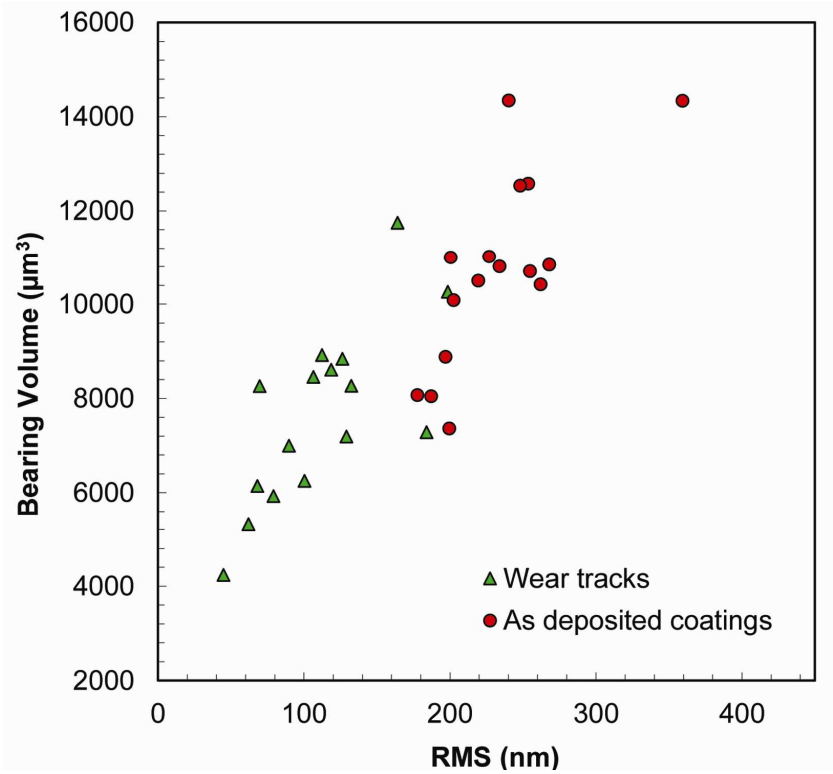

Figure 2 - Bearing volumes and surface roughness (RMS) values obtained by AFM on the worn tracks and pristine diamond surfaces for all tested samples.

The RMS values of the as-deposited coatings in Figure 2 correspond to the single value of each tested surface, while the average values given in Figure 3 are grouped by type of coating. The reduction in surface roughness of NCD coatings relatively to MCD ones is obvious, but data in this figure also shows that when using alternating layers, the RMS values of the coating approach those of the NCD, an effect that is enhanced for a larger number of layers. The somewhat large RMS values obtained in the present work for mono-layered NCD films are a result of a compromise between obtaining smooth surfaces and maximizing the mechanical anchoring by chemical etching of the substrate surface. This strongly increases RMS values of the coatings from about 70 nm for polished surfaces to the range 200-400 nm for the flat lapped and plasma etched substrates [12].

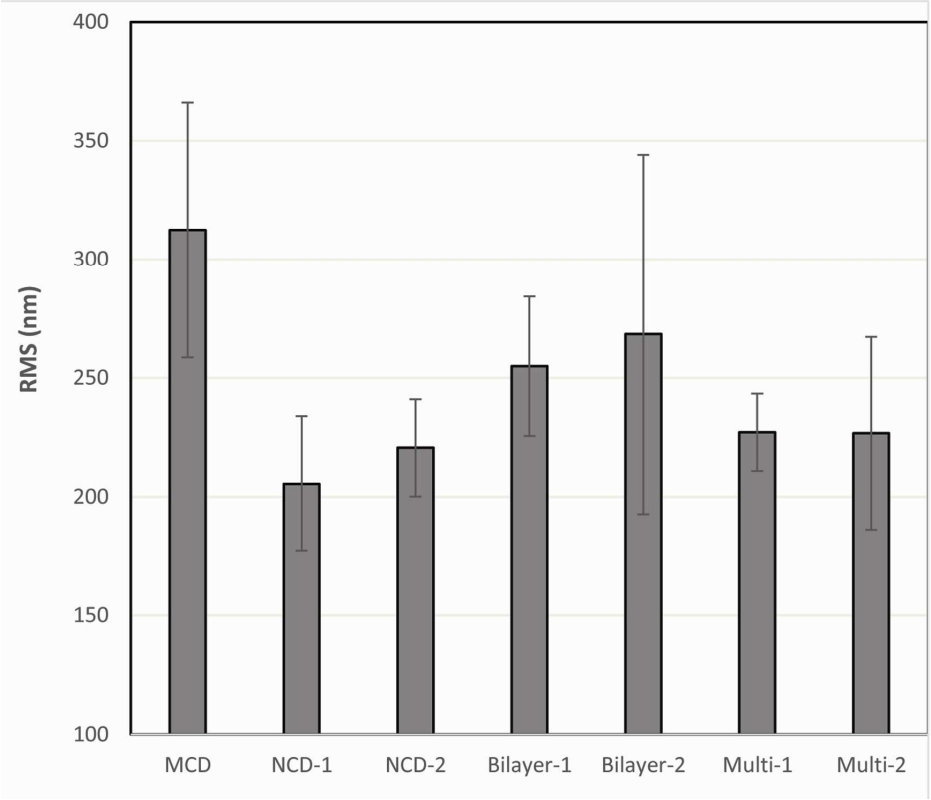

Figure 3 - Average and standard deviations of the RMS values for the MCD, NCD-1, NCD-2 monolayers and of the two- and four- layered coatings.

The bearing volumes given in Figure 4 were used to evaluate the total track wear volume for each type of diamond coating. The wear coefficient, *k*, is the ratio between this volume (mm^3) and the product of sliding distance (m) with the load (N). Figure 4 compiles *k* values obtained with 11 N of applied load, under HBSS and FBS lubrication. The main evidences from this set of values are the following:

i) *k* values are from one to two orders of magnitude smaller than for dry experiments done with similar pairs in a previous work [18]. This stems from the load bearing capacity brought by the lubricant and the effect of separation of opposing asperities. The magnitude of *k*, 10^{-9} to 10^{-8} $mm^3.N^{-1}.m^{-1}$, classified in the very mild wear regime, is remarkable, especially when considering biotribological applications, as are those envisaged for the present tribopairs;

ii) there is not a clear distinction between the behavior of different coatings. This lack of an obvious trend has been already observed for dry self-mated pairs when tested under loads smaller than the critical value for film delamination [18]. The major advantage of using multilayered coatings, the increase of critical load by a factor of two both in static [16] and in dry sliding tests [18], is here concealed due to the use of

a sub-critical load regime. Nevertheless, the smallest wear was measured for the single layer coatings NCD-1 and NCD-2 coatings under HBSS lubrication, both having the lower values of surface roughness, Figure 3.

iii) it is not possible to distinguish a clear effect of the physiological liquids on the total wear rates.

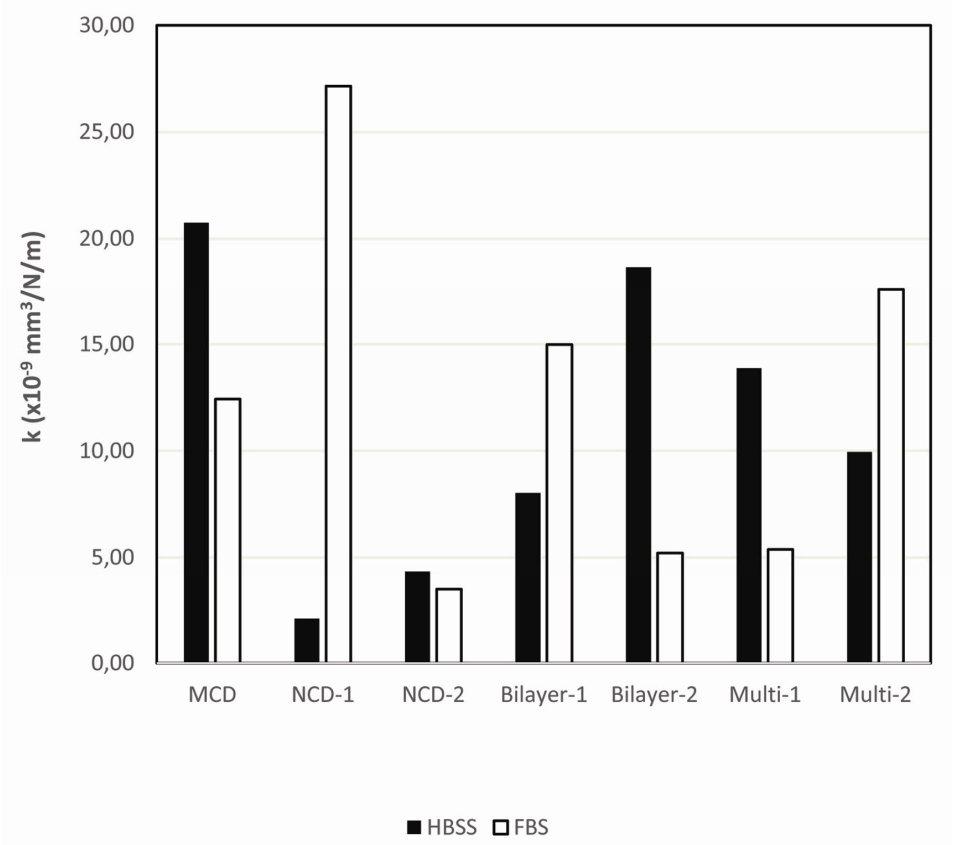

Figure 4 - Wear coefficient values obtained from the wear tracks on the diamond coated plates under HBSS and FBS lubrication and 11 N load.

Usually, in these hard coating systems, wear occurs by the same processes, independently of number of layers or type of diamond at the surface, because only the top asperities are worn out. In the case of MCD, the apexes of the micropyramidal crystals are truncated, as is illustrated in the 11 N wear tests under FBS and HBSS lubrication, Figure 5.

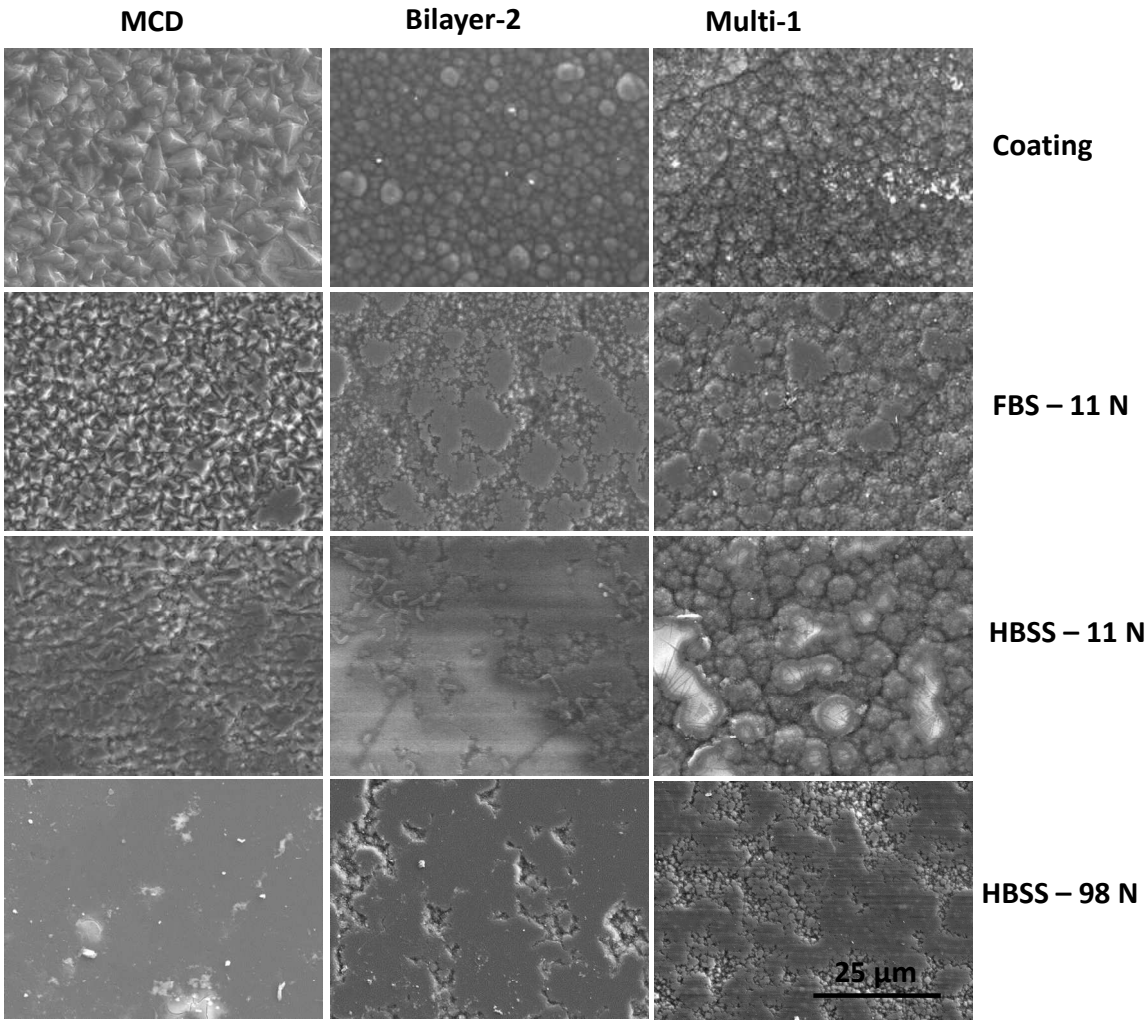

Figure 5 - SEM micrographs of selected examples of surface morphologies of the pristine and worn diamond coated plates of the following types: a monolayer (MCD); a bilayer (Bilayer-2) and a multilayer (Multi-1).

This fine scale abrasive wear mechanism may result in surfaces becoming fully polished for higher loads, as is the case of MCD coatings for the 98 N tests under HBSS lubrication. When there is a single NCD layer or the top layer of bi- and multi-layer coatings is of the nanocrystalline type, the pristine surface has agglomerates of nanometric diamond particles. They suffer the same wear mechanism and the result are near circular flattened plateaus, as depicted in Figure 5 for the 11 N tests under HBSS and FBS lubrication. The surfaces become increasingly flat with time and load, the latter being illustrated in Figure 5, for the 98 N tests, although unlike the MCD coating, the deepest valleys of the top diamond layers were not reached by wear. This truncation of diamond microcrystals and blunting of protruding nanocrystalline diamond agglomerates is quantitatively illustrated in Figure 1, where all RMS and

bearing volume values are shifted toward smaller values when comparing with the as-deposited coatings.

The bar graph shown in Figure 6 compares the wear coefficients of all types of coatings, under HBSS lubrication, for the 11 N ad 98 N tests. It should be noted that the average velocity of the pin is 12 mm.s^{-1} for the former tests while it is 24 mm.s^{-1} for the latter. The much larger severity of the 98 N tests is clearly illustrated by the one order of magnitude larger *k* values.

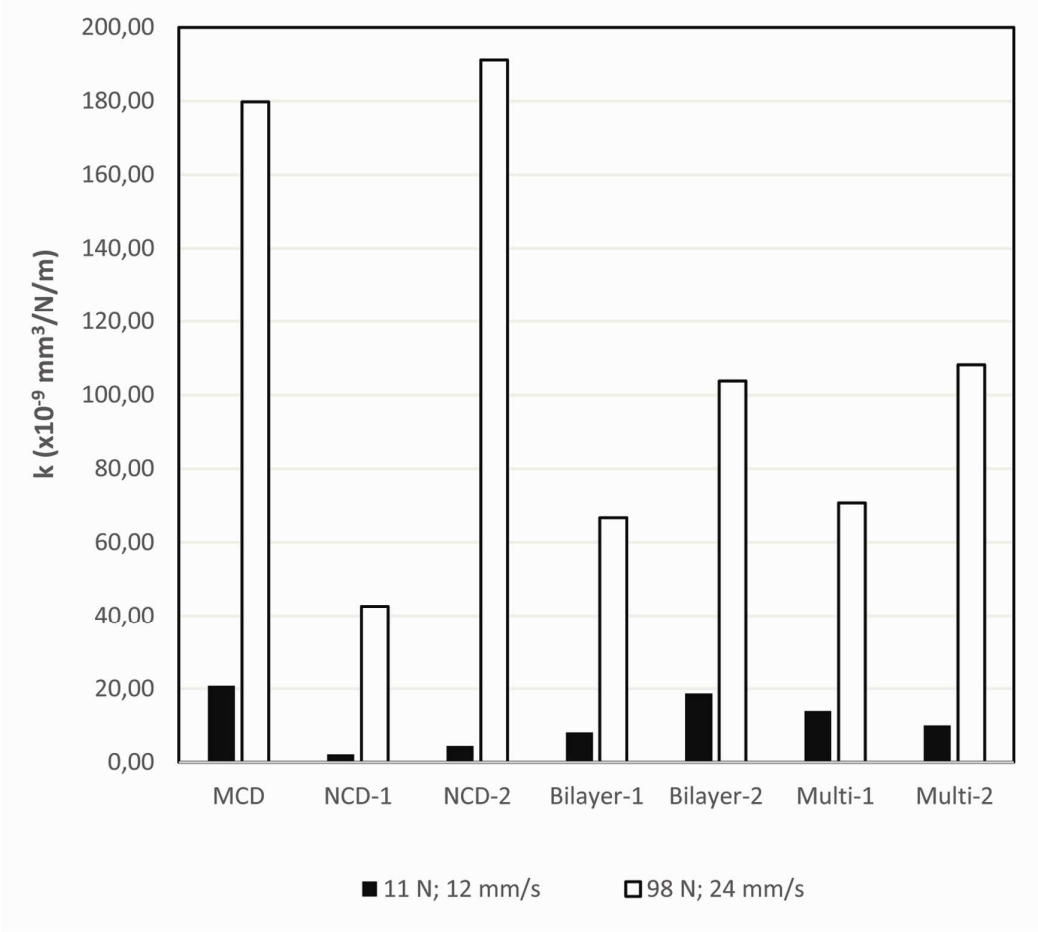

Figure 6 - Wear coefficient values obtained from the wear tracks on the diamond coated plates under HBSS lubrication for the 11 N and 98 N loads.

Data in Figure 6 further embodies the notions of increased fatigue effects with sliding speed and particularly load and of the independence of apparent contact stresses, calculated from the wear scar of the pins, on the wear coefficient. These quantitative results confirm the net polished appearance of the respective surfaces, observed in the SEM analysis, Figure 5. Another distinctive feature of the data on

Figure 6 is that, generally, Bi- and Multi-layer films are less sensitive to the speed and load increment than the monolayers, since *k* increases more for the latter than for the former, when increasing the load from 11 N to 98 N.

Self-mated systems of hard-coatings always have a starting friction peak that is a function of the starting RMS values, of the applied load and of the type, if any, of lubrication. It was demonstrated that the critical load for film delamination could be substantially increased by minimizing those values [24], this also being a measure of the importance of minimizing the starting surface roughness. In the present work, and for both 11 N and 98 N tests there was never evidence of film delamination from the plates. This means that the characterization of these systems was run mostly under sub-critical conditions, irrespectively of the apparent contact stresses calculated. The maximum friction coefficient, the starting peaks, recorded only for the 11 N load, are in the range 0.2 to 0.5, without a clear separation between type of coating or lubricating fluid. Nevertheless, these values are smaller than the maximum values recorded in dry-sliding tests [18] with this type of coatings which indicates a lubricating effect of both fluids. Despite the large scatter of data there is a mild indication that the starting friction peak increases with the surface roughness of the coatings, as expected. For the 11 N tests, after this initial peak and a relatively short transient period, all pairs entered a steady state regime with low measured friction coefficient values (μ) in the range 0.015 to 0.081, Figure 7, with the larger values being obtained for the FBS lubrication. The friction coefficient values do correlate fairly well, at least qualitatively, with the wear coefficients recorded in Figure 4. These values are within the range of values found for ceramic-on-ceramic and ceramic-on-metal bearings for artificial hip-joints in the presence of bovine serum (0.002-0.07) [25].

The larger values of μ_{ss} recorded for some of the coatings under FBS lubrication were not due to delamination of pin or plate, and neither correlate with the larger values of nominal contact stress mentioned above. This effect of increased friction values was also seen for NCD terminated surfaces in a previous work with monolithic diamond coatings [12]. Salt deposition and protein attachment was thought to be responsible for that increase, more pronounced for the smoother surfaces. As to the 98 N tests, conducted in a different machine, the friction coefficient values recorded are about one order of magnitude lower than the ones obtained for the 11 N tests and

in some cases it was even below the detection limit of the load cell. Despite the differences in the calibration of the load cells of both pieces of equipment it is clear that all systems behave in conditions of very low friction under HBSS lubrication.

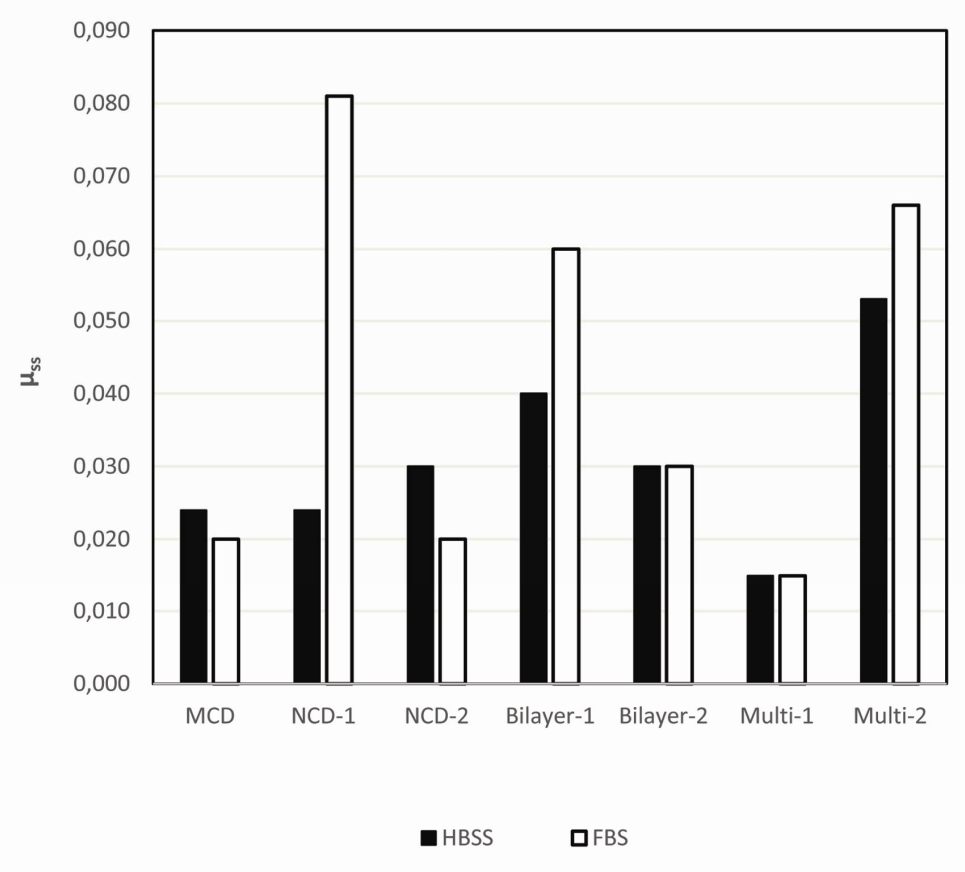

Figure 7 - Steady state friction coefficients of all coatings under a load of 11 N for HBSS and FBS lubrication.

4. Conclusions

Reciprocating, flat pin-on-flat plate, sliding tribological tests were conducted under 11 N and 98 N loads regimes and with FBS or HBSS lubrication. The apparent contact stresses are in the range of those found in micro-separation experiments and are much larger than the typical average contact stress values of standard hip-joint tests. Wear occurs initially by truncation of microcrystalline pyramids or blunting of nanocrystalline agglomerates and then by a fine scale abrasive wear mechanism that ends in surfaces becoming fully polished for high enough loads. Wear volumes were obtained from the difference in the volumes corresponding to AFM bearing areas of

the coatings before and after wear. For the 11 N loads, wear coefficient values, *k*, are from one to two orders of magnitude smaller than for similar dry experiments and are in the range 10^{-9} to 10^{-8} $mm^3.N^{-1}.m^{-1}$, corresponding to very mild wear regime. These values increase by about one order of magnitude for the 98 N test, due to enhanced fatigue effects, with Bi- and Multi-layer films being less sensitive to the speed and load increment than the monolayers. The sub-critical load regime of the tests concealed any trends attributable to differences in coating architecture, although the smallest wear was measured for the smoother single layer coatings NCD-1 and NCD-2 coatings under HBSS lubrication. For the 11 N tests, larger steady state friction coefficient values correspond to larger wear rates, for both fluids, although without a clear effect of the physiological liquids on the total wear rates. In these tests, μ_{ss} values vary from 0.015 to 0.081, with the larger values being obtained for the FBS lubrication, but still inside the range of values found for common hip-joint replacement materials.

Acknowledgements

This work was conducted under the framework of FCT project HipCerDiam-PTDC/EME-PME/112910/2009. E. Salgueiredo also acknowledges FCT for the grant SFRH/BD/41757/2007.

References

[1] R. A. Antunes, M. C. L. de Oliveira, Corrosion fatigue of biomedical metallic alloys: Mechanisms and mitigation, Acta Biomater. 8 (2012) 937-962.

[2] A. Borruto, L. Marrelli, F. Palma, The difference of material wettability as critical factor in the choice of a tribological prosthetic coupling without debris release, Tribol. Lett. 20 (2005) 1-10.

[3] B. Ben-Nissan, A. H. Choi, A. Bendavid,Mechanical properties of inorganic biomedical thin films and their corresponding testing methods, Surf. Coat. Tech. 233 (2013) 39-48.

[4] C. A. Love, R. B. Cook, T.J. Harvey, P. A. Dearnley, R. J. K. Wood, Diamond like carbon coatings for potential application in biological implants – a review, Tribol. Int. 63 (2013) 141-150.

[5] H. Liu *et al*., Tribological performance of ultra-high-molecular-weight polyethylene sliding against DLC-coated and nitrogen ion implanted CoCrMo alloy measured in a hip joint simulator, Surf. Coat. Tech. 206 (2012) 4907-4914.

[6]R. Hauert *et al.*, Retrospective lifetime estimation of failed and explanted diamond-like carbon coated hip joint balls, Acta Biomater. 8 (2012) 3170-3176.

[7] R. Hauert, K. Thorwarth, G. Thorwarth, An overview on diamond-like carbon coatings in medical applications, Surf. Coat. Tech. 233 (2013) 119–130.

[8] R. Hauert *et al*., Retrospective lifetime estimation of failed and explanted diamond-like carbon coated hip joint balls, Acta Biomater. 8 (2012) 3170–3176.

[9] T. M. Manhabosco, A. P. M. Barboza, R. J. C. Batista, B. R. A. Neves, I. L. Müller, Corrosion, wear and wear-corrosion behaviour of grafite-like a-C:H films deposited on bare and nitrided titanium alloy, Diam. Relat. Mater. 31 (2013) 58-64.

[10] L. Wang, J. F. Su, X. Nie, Corrosion and tribological properties and impact fatigue behaviors of TiN- and DLC-coated stainless steels in a simulated body fluid environment, Surf. Coat. Tech. 205 (2010) 1599–1605.

[11] R. Lappalainen, M. Selenius, A. Anttila, Y. T. Konttinen, S. S. Santavirta, Reduction of wear in total hip replacement prostheses by amorphous diamond coatings, J. Biomed. Mater. Res. B: Appl. Biomater. 66 (2003) 410–3.

[12] M. Amaral, C. S. Abreu, F. J. Oliveira, J. R. Gomes, R. F. Silva, Tribological characterization of NCD in physiological fluids, Diam. Relat. Mat. 17 (2008) 848-852.

[13] V. Thomas, B. A. Halloran, N. Ambalavanan, S. A. Catledge, Y. K. Vohra, In vitro studies on the effect of particle size on macrophage responses to nanodiamond wear debris, Acta Biomater. 8 (2012) 1939–1947.

[14] R. Sonntag, J. Reinders, J. P. Kretzer, What's next? Alternative materials for articulation in total joint replacement, Acta Biomater. 8 (2012) 2434–2441.

[15] B. S. Bal, M. N. Rahaman, Orthopedic applications of silicon nitride ceramics, Acta Biomater. 8 (2012) 2889–2898.

[16] E. Salgueiredo, M. Amaral, F. A. Almeida, A. J. S. Fernandes, F. J. Oliveira, R. F. Silva, Mechanical performance upgrading of CVD Diamond using the multilayer strategy, Surf. Coat. Tech. 236 (2013) 380–387.

[17] F. A. Almeida *et al*., Interfaces in nano-/microcrystalline multigrade CVD Diamond coatings, ACS Appl. Mater. Interfaces 5 (2013) 11725−11729.

[18] E. Salgueiredo, C. S. Abreu, M. Amaral, F. J. Oliveira, J. R. Gomes, R. F. Silva, Self-mated tribological systems based on multilayer micro/nanocrystalline CVD Diamond coatings, Wear 303 (2013) 225–234.

[19] T. M. Wright, S. B. Goodman (Eds.), Implant Wear in Total Joint Replacement: Clinical and Biological Issues, Materials and Design Considerations, American Academy of Orthopaedic Surgeons, 2001, Chapter 19.

[20] L. Mattei, F. Di Puccio, B. Piccigallo, E. Ciulli, Lubrication and wear modeling of artificial hip joints: A review, Tribol. Int. 44 (2011) 532–549.

[21] M. P. Gispert , A. P. Serro, R. Colaço, B. Saramago, Friction and wear mechanisms in hip prosthesis: Comparison of joint materials behavior in several lubricants, Wear 260 (2006) 149–158.

[22] M. Mak, Z. Jin, J. Fisher, T. D. Stewart, Influence of acetabular cup rim design on the contact stress during edge loading in ceramic-on-ceramic hi prostheses, J. Arthroplasty 26 (2011) 131-136.

[23] M. Amaral, C. S. Abreu, F. J. Oliveira, J. R. Gomes, R. F. Silva, Biotribological performance of NCD coated Si_3N_4-bioglass composites 16 (2007) 790-795.

[24] M. Amaral *et al*., A DLC/Diamond bilayer approach for reducing the initial friction towards a high bearing capacity, Wear 290–291 (2012) 18–24.

[25] Z. M. Jin, M. Stone, E. Ingham, J. Fisher, Biotribology, Curr. Orthop. 20 (2006) 32-40.

Chapter IV

In this chapter are summarized the main conclusions of the thesis and prospects on future work are outlined.

Hot filament CVD was demonstrated to be a very suitable technique for multilayered diamond coating of silicon nitride (Si_3N_4) ceramic substrates in a continuous process. Deposition parameters for monolayered films of microcrystalline diamond (MCD) were firstly optimized using a Taguchi matrix approach. The experimental design of nanocrystalline diamond (NCD) was further exploited. Very small crystallite sizes of 19 and 11 nm were obtained for NCD grown in a CH_4/H_2 atmosphere without and with Ar addition, respectively, while the MCD average grain size was 2 μm. Aiming at combining the excellent adherence of the MCD films to the ceramic substrates with the low intrinsic surface roughness of NCD, a bilayered structure was afterwards designed. Ultimately, fourfold multilayered diamond coatings were obtained by repeating the deposition procedure used for the bilayered coatings. Final coating thicknesses were of ~10-12 μm, which endured an indentation load of 800 N with a Brale cone, before film spalling-off.

Cross-sectional samples of the diamond multilayer structures, with well-preserved interfaces, were prepared by FIB and thoroughly characterized by HRTEM, STEM-EDX and EELS. In the MCD/NCD transition, graphite-like structures are formed due to the high carbon content (and low H concentration) used for NCD growth, when compared to MCD. In the NCD to MCD transition, no carbon structures other than diamond were found, due to the abundance of atomic H in the gas mixture used for MCD deposition. The analysis of the interfaces by the aforementioned techniques also showed the presence, in all the interfaces of MCD to NCD transitions, of nanometric round-shaped particles of tungsten carbide due to filament contamination. At this type of transition, the NCD growth parameters (higher CH_4 concentration and/or argon addition), considerably increase the filament temperature, probably dissociating the carburized layer around the filament and vaporizing the tungsten. Adding argon to the gas mixture causes the degradation of the filament and consequently decreases the film growth rate, limiting the layer thickness when a continuous deposition is used.

The wear resistance of CVD diamond in the form of mono-, bi- and multilayer coatings on Si_3N_4 ceramic substrates was then evaluated by solid particle erosion of SiC particles. It was shown that a decisive first step for the improvement of the coating life is the accomplishment of an adequate substrate preparation by a combination of mechanical treatment (grinding plus flat lapping with 15 μm diamond suspension)

followed by chemical activation with CF_4 plasma etching. By mechanical tailoring the substrate surface roughness, coatings do not fail by catastrophic extensive delamination but by film detachment in more localized and smaller areas, after longer test times. The extra improvement provided by the CF_4 etching resulted in values of induction time to substrate exposure of more than 1 hour, up to 14 times relatively to the unetched surfaces. An analytical model on the stress field distribution within the coatings was developed to elucidate the erosive mechanical behaviour of the different diamond composites. It was demonstrated that the region of maximum stresses lies at half of the coating thickness, meaning that the coatings are supporting the most critical stresses generated by the particle impact. In bilayers, the MCD/NCD transition is located at this level and cracks tend to propagate along it. This toughening mechanism is more effective in multilayers that have three interlayer transitions.

For dry sliding tribological experiments, the multilayered systems exhibited superior critical delamination thresholds when compared to the mono (80N for NCD and 100N for MCD) and bilayered coatings (110N), for ~10-12μm thick coatings. Fourfold multilayers showed an outstanding performance, with a critical load of 200N, without film delamination. In all cases, a high initial friction coefficient was followed by a steady-state regime where extremely low coefficient values were obtained (μ=0.02-0.09), due to a smoother surface. Wear coefficient values are in the order of $\sim 10^{-7}$ mm^3 N^{-1} m^{-1} for the ball and flat specimens, for short and endurance tests, indicate a mild wear regime. The applied loads reported in literature are considerably lower than the ones presented in the present work, for similar test conditions.

As a screening tool for biotribological applications of the present self-mated system based on CVD diamond coated ceramics, sliding tests were conducted under 11 N and 98 N load regimes under fetal bovine serum (FBS) Hank's balanced salt solution (HBSS) lubrication. For the 11 N loads, the wear coefficient values are from one to two orders of magnitude smaller than for similar dry experiments, in the range 10^{-9} to 10^{-8} $mm^3.N^{-1}.m^{-1}$, corresponding to very mild wear regime. These values increase by about one order of magnitude for the 98 N test, due to enhanced fatigue effects, with multilayer films being less sensitive to the speed and load increment than the monolayers. In these tests, μ values vary from 0.015 to 0.081, with the larger values

being obtained for the FBS lubrication, but still inside the range of values found for common hip-joint replacement materials.

Future work will be dedicated to the manufacturing of multilayer diamond coated total hip joint prosthesis. Firstly, dense Si_3N_4 ceramic acetabular cups and femoral heads will be produced and coated with MCD/NCD multilayers. Biotribological testing (according to ISO 14242 standard) will be further carried out at INMETRO (Instituto Nacional de Metrologia, Qualidade e Tecnologia, Brasil). The new hip joints should present a volumetric wear better than the ceramic-on-ceramic ones (0.1 mm^3/million cycles) and also eliminate problems related to periprosthetic osteolysis induced by metallic or UHMWPE debris of the commonly used UHMWPE/metal joints, presenting themselves as a favourable alternative to the currently existing hip joints.